THE JOURNAL OF
PHYSICAL
CHEMISTRY

THE JOURNAL OF

PHYSICAL CHEMISTRY

©Copyright, 1975, by the American Chemical Society. Published biweekly by the American Chemical Society at 20th and Northampton Sts., Easton, Pa. 18042. Second-class postage paid at Washington, D.C., and at additional mailing offices.

All manuscripts should be sent to *The Journal of Physical Chemistry*, Department of Chemistry, University of Minnesota, Minneapolis, Minn. 55455.

Additions and Corrections are published once yearly in the final issue. See Volume 78, Number 26 for the proper form.

Extensive or unusual alterations in an article after it has been set in type are made at the author's expense, and it is understood that by requesting such alterations the author agrees to defray the cost thereof.

The American Chemical Society and the Editor of *The Journal of Physical Chemistry* assume no responsibility for the statements and opinions advanced by contributors.

Correspondence regarding accepted copy, proofs, and reprints should be directed to Editorial Processing Department, American Chemical Society, 20th and Northampton Sts., Easton, Pa. 18042. Department Head: CHARLES R. BERTSCH. Associate Department Head: MARIANNE C. BROGAN, Assistant Editors: CELIA B. McFARLAND, JOSEPH E. YURVATI.

Advertising Office: Centcom, Ltd., 50 W. State St., Westport, Conn. 06880.

Business and Subscription Information

Send all new and renewal subscriptions *with payment* to Office of the Controller, 1155 16th Street, N.W., Washington, D.C. 20036. Subscriptions should be renewed promptly to avoid a break in your series. All correspondence and telephone calls regarding

changes of address, claims for missing issues, subscription service, the status of records, and accounts should be directed to Manager, Membership and Subscription Services, American Chemical Society, P.O. Box 3337, Columbus, Ohio 43210. Telephone (614) 421-7230. For microfiche service, contact ACS Microfiche Service, 1155 16th St. N.W., Washington, D.C. 20036. Telephone (202) 872-4444.

On changes of address, include both old and new addresses with ZIP code numbers, accompanied by mailing label from a recent issue. Allow four weeks for change to become effective.

Claims for missing numbers will not be allowed (1) if loss was due to failure of notice of change in address to be received before the date specified, (2) if received more than sixty days from date of issue plus time normally required for postal delivery of journal and claim, or (3) if the reason for the claim is "issue missing from files."

Subscription rates (hard copy or microfiche) in 1975: $20.00 for 1 year to ACS members; $80.00 to nonmembers. Extra postage $4.50 in Canada and PUAS, $5.00 other foreign. Supplementary material (on microfiche only) available on subscription basis, 1975 rates: $15.00 in U.S., $19.00 in Canada and PUAS, $20.00 elsewhere. All microfiche airmailed to non-U.S. addresses; air freight rates for hard-copy subscriptions available on request.

Single copies for current year: $4.00. Rates for back issues from Volume 56 to date are available from the Special Issues Sales Department, 1155 Sixteenth St., N.W., Washington, D.C. 20036.

Subscriptions to this and the other ACS periodical publications are available on microfilm. For information on microfilm write Special Issues Sales Department at the address above.

17 ନ୍ତ 2513

1A

COMMUNICATIONS TO THE EDITOR

■ Supplementary and/or miniprint material for this paper is available separately, in
photocopy or microfiche form. Ordering information is given in the paper.

* In papers with more than one author, the asterisk indicates the name of the author to
whom inquiries about the paper should be addressed.

AUTHOR INDEX

Chemically Activated ¹⁴CH₃CF₃ from Cross Combination of ¹⁴CH₃ with CF₃. An Introductory Experimental Study

R. R. Pettijohn, G. W. Mutch, and J. W. Root*

Department of Chemistry, University of California, Davis, California 95616   *(Received July 25, 1974; Revised Manuscript Received May 28, 1975)*

The cophotolysis of acetone-*1,3*-¹⁴*C*–hexafluoroacetone mixtures has been used in a study of the unimolecular behavior of chemically activated ¹⁴CH₃CF₃. Conclusive evidence was obtained for the spurious loss of the unimolecular decomposition product ¹⁴CH₂=CF₂ through secondary free-radical addition reactions, and a kinetic procedure was developed for controlling this nuisance problem. Experiments carried out in several bath gases suggested that these ¹⁴CH₂=CF₂ losses could be rendered negligible through the addition to the reaction mechanism of a rapid hydrogen abstraction or olefin addition channel involving CF₃ radicals.

Introduction

During the past decade CH_3CF_3 has been utilized in a variety of experimental studies in unimolecular kinetics.[1-3] The discovery that chemically activated fluorinated ethanes decompose through molecular HF elimination was made by Whittle and coworkers:[4]

$$CH_3 + CF_3 \rightarrow (CH_3CF_3)^\dagger \qquad (1)$$

in which the superscript dagger denotes excess internal energy. Provided that the excitation level is sufficient, the activated molecule can undergo unimolecular reaction (D) vs. collisional stabilization (S):

$$(CH_3CF_3)^\dagger \xrightarrow{\text{D}} CH_2=CF_2 + HF \qquad (2)$$

$$(CH_3CF_3)^\dagger + M \xrightarrow{\text{S}} CH_3CF_3 + M \qquad (3)$$
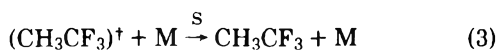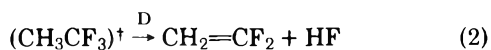
Here the excitation energy has been shown to fall below the reaction threshold in a single "strong" collision with M, a molecule of the bath gas. This "unit deactivation" behavior is often rather well approximated by large efficient colliders in the high-pressure part of the decomposition vs. stabilization competition. As the pressure is reduced deviations from unit deactivation become more apparent and are due to a cascading energy transfer sequence.[2,3] For ineffi-

cient colliders many step deactivation is observed at all pressures.

The pioneering research on the theoretical description of unimolecular hydrogen halide elimination has been carried out at the laboratories of Setser.[2a] In addition to the early work with chloro and bromo alkanes several fluorinated ethanes have also been investigated, and the threshold energy for reaction 2 has been determined as 68 ± 2 kcal mol⁻¹.[5] Other pyrolysis[6] and chemical activation experiments[7] have been carried out on CH_3CF_3, and the related Arrhenius parameters and decomposition thermochemistry have been thoroughly characterized.[5b,8,9]

Berry and Pimentel and Polanyi et al. employed chemical laser techniques to determine the internal energy content of HF produced via reaction 1.[10] Excited vibrational states up to the fourth are populated by reaction 2, but large levels of rotational excitation are apparently not involved. Another series of non-Boltzmann experiments using CH_3CF_3 has been reported by Root and coworkers, who investigated the unimolecular behavior of species formed in high-energy atomic substitution reactions:[11]

$$^3H^* + CH_3CF_3 \rightarrow (CH_2{}^3HCF_3)^\dagger + H \qquad (4)$$

$$^{18}F^* + CH_3CF_3 \rightarrow (CH_3CF_2{}^{18}F)^\dagger + F \qquad (5)$$
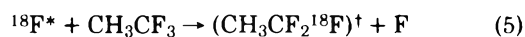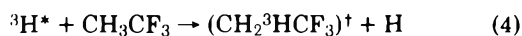
Here $^3H^*$ and $^{18}F^*$ denote fast tritium and fluorine-18 atomic recoils generated through the $^3He(n,p)^3H$ and $^{19}F(n,2n)^{18}F$ nuclear reactions. The newly formed primary

TABLE I: Arrhenius Parameters for Radical Combination Reactions

Product	Temp range, °K	Log A (A in cm^3 mol^{-1} sec^{-1})	E_a, kcal mol^{-1}	$k \times 10^{-13}$, cm^3 mol^{-1} sec^{-1} (at 307 °K)	Ref
C_2H_6	398–448	13.34 ± 0.03	0.0 ± 0.7	2.2 ± 0.2	4c
C_2F_6	298–400	13.36 ± 0.03	0.0 ± 0.5^a	2.3 ± 0.2	4c
CH_3CF_3	296–513	13.75 ± 0.05	0.0 ± 0.5^a	5.6 ± 0.6	4b

^{a} Estimated error limits.
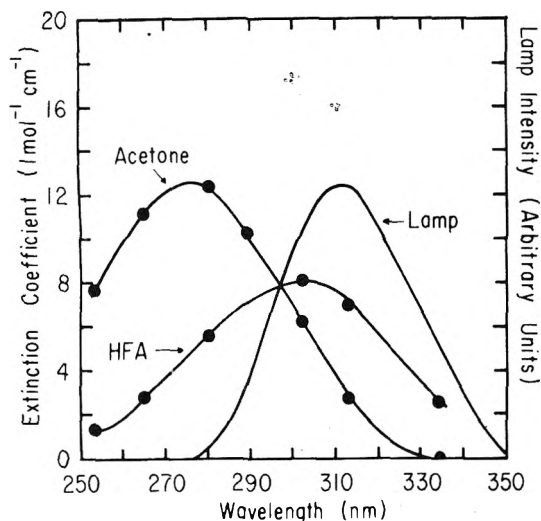
Figure 1. Uv lamp filtered spectral output and extinction coefficient data for acetone and hexafluoroacetone: ●, ref 25.
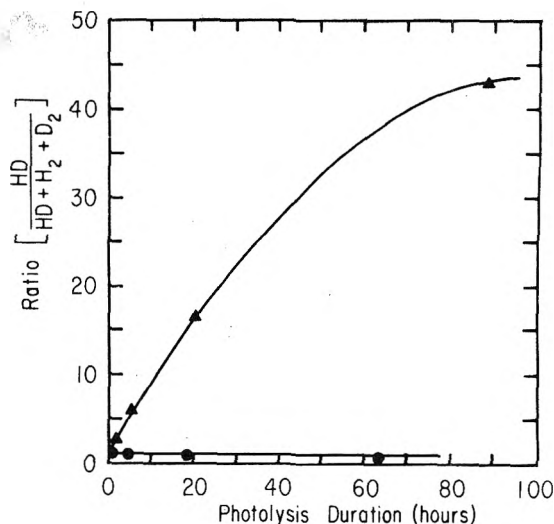
Figure 2. Hg 6^3P_1 photosensitization experiment: ▲, quartz photolysis cell; ●, KG-33 photolysis cell.

products from these activation processes behaved differently from species generated through more conventional chemical activation routes, probably because of angular momentum effects.[11,12]

This paper presents results from a series of experiments with chemically activated $^{14}CH_3CF_3$ generated from the 310-nm cophotolysis of acetone-$1,3$-^{14}C-hexafluoroacetone mixtures followed by the reaction

$$^{14}CH_3 + CF_3 \rightarrow (^{14}CH_3CF_3)^\dagger \qquad (6)$$

Our rationale for initiating this research was threefold. We sought through radiotracer methods to achieve (i) the effective control of secondary CF_3 attack upon the $^{14}CH_2{=}CF_2$ decomposition product following reaction 6; (ii) development of a versatile system for collisional energy transfer experiments;[13,14] and (iii) development of background data for $(CH_3CF_3)^\dagger$ in conjunction with our ongoing nuclear recoil research program.

Whittle et al. proposed that CH_3CF_3 from (1) decomposed via molecular HF elimination, and that near-zero activation energies were involved for the various self- and cross combinations between CH_3 and CF_3.[4] The product ratio $(CH_2{=}CF_2/CH_3CF_3)$ exhibited a systematic dependence upon the photolysis duration at constant pressure, suggesting that "In principle, the addition [of CF_3 radicals] to the olefin could be so fast as to make it impossible to obtain accurate olefin analyses at all." Thus it was indicated that this ketone cophotolysis system was subject to a spurious secondary reaction leading to the consumption of $CH_2{=}CF_2$:

$$CF_3 + CH_2{=}CF_2 \rightarrow \cdot C_3F_5H_2 \qquad (7)$$
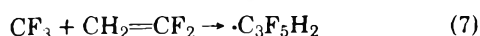
Recently this system has been reinvestigated at 468°K using conventional analytical procedures.[7b] A minimum photolysis conversion of 0.6% was required for reliable analysis, but above 33% conversion tertiary as well as secondary complications became important. Experiments were carried out between the above limits and the measured $(CH_2{=}CF_2/CH_3CF_3)$ product ratios were extrapolated to zero conversion in an effort to correct for the $CH_2{=}CF_2$ losses, which would be serious in energy transfer experiments.

Experimental Section

General. Radiogas chromatography has been used for nearly 2 decades in nuclear recoil chemistry research.[11,15] This method also offers advantages for applications in unimolecular kinetics. Because the radiolabel is confined to the photolysis precursor, the bath gas generally does not interfere with the analysis.[16] For example, CH_3CF_3 itself is one of the colliders investigated in this study. The radiotracer method is highly sensitive so that good counting statistics are easily attained, even with long-lived radioisotopes such as carbon-14.[17] The required photolysis precursor concentration in the samples consistent with good data quality is generally determined by the addition of carrier during the manufacture of the labeled compound. The typical ranges of specific radioactivity for available tagged substances correspond to very small precursor concentrations. No efforts have been made here either to obtain high specific activity acetone-$1,3$-^{14}C or to utilize unusually sensitive counting methods. A final advantage of the radiotracer technique is that small photochemical conversions are required, about 1% in this work.

Materials. Phillips research grade C_2H_6 (99.99%); J. T. Baker $CH_2=CF_2$ (99.0%); Pierce Chemical Co. CF_3COCF_3 (HFA, 99.0%); Peninsular Chemresearch, Inc., CH_3CF_3 (98.0%) and CH_3CH_2F (98.0%); Matheson Gas Products C_2F_6 (99.6%) and CH_3CHF_2 (98.0%) were purified by repeated bulb-to-bulb distillation until gas chromatographic analysis showed less than 1% organic impurities.[18] All materials were stored in heliarc-welded stainless steel canisters provided with Superior type 5030K-A1 packless diaphragm vacuum valves and $\frac{5}{16}$-32 straight-threaded NEF-2 connectors modified through the addition of size 2-031 Viton-A O-ring vacuum gaskets.[9,11b] After transfer to a storage vessel each organic substance received additional purification *via* outgassing and freeze-thaw cycles until less than 1 micron Hg vapor pressure (77°K) was measurable in the closed vacuum system.

International Chemical and Nuclear Corporation supplied acetone-1,3-^{14}C at a specific radioactivity of 8.53 ± 0.01 mCi millimole^{-1} (6.84 ± 0.01 mole % acetone-1,3-^{14}C in unlabeled acetone carrier). Chemical and radioisotopic purities were both in excess of 99.9%. Radiogaschromatographic assay of blanks showed no detectable impurities at the *ca.* 1 ppm absolute sensitivity level used here. A convenient feature of carbon-14 tagged precursors is their minimal tendency to form impurities from decay-induced self-radiolysis.[19]

Preparation of Samples. The vacuum apparatus used for gas phase sample preparation consisted of a Welch model 1402B mechanical forepump; an Eimac 4-inch, 3-stage glass oil diffusion pump provided with a liquid nitrogen trap; a multiple-station model DV-20 Hastings gauge; a Wallace and Tiernan series 1500 differential pressure gauge (0-800 Torr); and several special function manifolds.[9] The Hastings gauge was used for checking the operation of the vacuum system, for monitoring the removal of trace oxygen by outgassing, and for measuring

the ketone mixture aliquot size. The Wallace and Tiernan gauge had a calibrated absolute accuracy of ±6.9 × 10^{-3} atm. In recent experiments it has been superceded by a Barocell model 1174 digital electronic manometer and model 570D-1000T-1B2-H3 differential pressure sensor (0-1000 Torr). The present uses of the Barocell have been to provide a Hastings gauge calibration for our ketone photolysis mixture[20] and sample composition data for the C_2H_6 scavenger experiments.

Precursor blends were prepared through standard volumetric expansion methods and stored in a blackened 1000 cm^3 flask, which was connected to the vacuum apparatus through a pair of Kontes 5 mm bore teflon plug high-vacuum stopcocks. The tubing volume between them provided for the reproducible removal of 0.24% of the reservoir contents per aliquot. Because the Hastings calibration was not available at the beginning of this work, the constant fractional aliquot technique was used to monitor the photolysis mixture concentration in the samples.

The addition of unlabeled $CH_2=CF_2$ or C_2H_6 effectively suppressed secondary reactions leading to the consumption of $^{14}CH_2=CF_2$. The mechanism for this protective scavenging action involved the kinetic control of the CF_3 concentration. Under these conditions it was necessary to maintain roughly constant intersample precursor concentrations. This was accomplished through monitoring the reactant ratio (R) for each sample:

$$R = \frac{PV}{N} \qquad (8)$$

in which P, V, and N denote the sample pressure, volume, and added number of ketone aliquots.[9] An obvious deficiency of this technique is that the quantity of ketone mixture per aliquot decreased slowly during the experiments. All the samples for each series were prepared in succession in order to minimize the importance of this effect.

Photolysis vessels (2000 to 100 cm^3) were fabricated from spherical Kimax KG-33 glass flasks and Kontes high-vacuum O-ring stopcocks. The inlets consisted of 3.0 × 1.5 mm o.d.x.i.d. tubing to facilitate connection to the vacuum apparatus through Burrell type 261-9 silicone seals. New flasks were cleaned, outgassed for 12 hours, and stored under vacuum.

Following this preconditioning samples were routinely prepared as follows: the bath gas was added; the flask was isolated and cooled to 77°K; the ketone mixture was introduced; and, finally, the mixture was subjected to several additional outgassing cycles. The Hastings reading corresponding to each ketone aliquot was recorded.[21] Freshly filled samples were allowed to stand in the dark for six hours in order to insure completeness of mixing.

Three basic types of experiments were performed: (i) The ketone mixture composition was varied in pure CH_3CF_3 bath gas in order to determine optimum photolysis conditions; (ii) Varying concentrations of C_2H_6 or carrier $CH_2=CF_2$ were added to different bath gases at constant total pressure, temperature, and reactant ratio to yield "scavenger curves"; (iii) After the appropriate scavenger concentration had been determined, the total pressure was varied at constant mixture composition, temperature, and reactant ratio to yield pressure falloff curves, which were then subjected to theoretical analysis.[9,13]

Photolysis of Samples. The ultraviolet light source was fabricated from 24 Westinghouse type FS20T12 20-watt sunlamps housed in a cylindrical 18 × 25 inch o.d.x.i. galvanized steel drum, the ends of which were provided with 12-inch circular openings. The effective irradiation length of the FS20T12 is about 21 inches. For ambient temperature runs the lamps were cooled by convective air circulation through the uncovered openings at the ends of the vertically mounted drum. The temperature distribution within the irradiation zone was

measured, and the sample filling data were corrected from the laboratory (295.5 ± 0.5°K) to the mean lamp temperature value (306.8 ± 0.5°K).[9] Anisotropies in the radial photon intensity were minimized through sample rotation.

For high temperature irradiations an oven was installed into a section of 17 × 74 cm i.d.x.i. KG-33 tubing. Heating was provided by a pair of Master type 24-HAS-018K elements driven by a regulated Triac controller. Uniformity within the oven was obtained by forced air circulation. This apparatus, which has been tested to 425°K, exhibited a ± 1°K stability. Rotation was not possible, but the samples were reproducibly located at the center of the irradiation zone. The lamp bank required auxiliary cooling, which was provided by an American Standard model H-105814A squirrel cage blower.

It should be emphasized that this photolysis apparatus constitutes a severe radiation hazard. Exposed personnel should wear protective clothing and uv safety goggles. In addition, our lamps are isolated from the rest of the laboratory by uv-absorbing plastic shielding.

The lamps were powered by 12 General Electric 6G3512 trigger-start ballasts.[22] The Westinghouse FS20T12 lamp operates as an A.C. low-pressure mercury arc with external phosphor coating. The emission ranges from 280-350 nm with maximum intensity at about 310 nm. Extinction coefficients for the ketones are superimposed on the spectral output curve in Figure 1.[25] Rough quantum yield measurements indicated that the lamp intensity remained essentially constant during these experiments. The photochemical conversion, which was occasionally measured as described below, was less than 1%.

Mercury Photosensitization. Since the samples were recovered for analysis by means of a mercury Toepler pump, it was necessary to insure the absence of mercury-sensitized reactions. Roughly 90% of the primary output of the FS20T12 corresponds to 254 nm Hg $6\,^3P_1$

resonance radiation. The phosphor absorbs about 95% of this component, but the residual 254 nm output would induce severe photosensitization complications. This problem was eliminated through the use of KG-33 photolysis flasks and filters. This glass alloy is strongly opaque below about 280 nm.[25] The efficacy of the filtration was assessed through the photolysis of H_2/D_2 mixtures in the presence of added Hg.[26] Sensitized reactions lead to HD formation, which is easily detected *via* mass spectrometry. Several standard flasks and one fabricated from fused quartz were provided with a large Hg droplet and 40 Torr of an equimolar H_2/D_2 mixture. After varying photolysis times each flask was sampled for mass spectrometric analysis (Consolidated Electrodynamics Corp. Model 21-104). The results shown in Figure 2 clearly indicate the effectiveness of this procedure. We strongly emphasize the importance of this precaution. Preliminary results demonstrated severe losses of $^{14}CH_2=CF_2$ in unfiltered samples.

Analysis of Samples. Samples were transferred for analysis by means of a one-liter Toepler pump.[9] Although blanks were processed routinely, no dark or Toepler pump induced reactions were ever detected. Standard radiogaschromatographic techniques were employed. Elution of macroscopic carriers was monitored by a Carle model 1160 thermal conductivity detector (Dimbat-Porter-Stross sensitivity in excess of 1.5×10^4 mV ml mg^{-1}).[9] The photolysis conversion was measured through recovery and radioassay of the undecomposed ketone by reverse flushing. The stationary phase CROT9 was the crotonic acid ester of $H(CF_2)_8CH_2OH$.[11b,27] The column consisted of 150 feet of 0.25 inch o.d. stainless steel beverage tubing packed with 30 weight percent of CROT9 on 30/40 ASTM mesh Chromosorb PA. It was normally operated at 273°K with 50 cm^3 min^{-1} (NTP) of He carrier. The HETP for CH_3CF_3 was 0.24 cm, and the elution times (min.) for the products were as follows: $^{14}CH_4$, 25.5; $^{14}CH_3CH_3$, 32.0; $^{14}CH_2=CF_2$, 41.0; and $^{14}CH_3CF_3$, 73.5.

The radioactivity detector consisted of a mixer,[15] internal flow proportional counter, and associated electronics. The Matheson C.P. propane counting gas was adjusted to provide a total detector flow of 250±5 cm^3 min^{-1} (NTP). The counter was fabricated from a 0.5×12 inch o.d.x.i. length of hardened copper tubing, two 0.50 inch copper sweat tees, two Amphenol type UG-560/U connectors, two 5/32x1 inch stainless steel springs, and a length of nominal 2 mil diameter tungsten wire.[22] Typical detectors had active volumes of about 35 cm^3 with background signal levels in the range of 40-80 cpm when shielded with two inches of lead. During operation the background slowly increased due to the deposition of labeled polymer films as a result of ion-molecule reactions. Contaminated counter bodies were replaced when the background exceeded 150 cpm.

The high voltage power supply, amplifier-discriminator, and scaling equipment were fabricated for this research.[22] The buffered scaler contained four six-decade 15 MHz counters with optional coincidence gating, a readout interval timer (1 to 9.9×10^5 sec), a teletype output format generator, coded oscillographic output pulse generator, and power supplies. Teletype page listings and punched paper tapes and oscillographic outputs (Heathkit model EU-20V recorder) were routinely obtained. The punched tape was employed in data analysis on a Wang Laboratories model 720C programmable electronic calculator provided with model 703 paper tape editor and model 702 plotting output writer. The digital output consisted of a sequence of differential or integral counts detected per time-of-measurement interval. The Wang program provided background-corrected radioactivities for each product, the activity ratio $^{14}CH_2=CF_2/^{14}CH_3CF_3$, and statistical standard errors for all these quantities.[9] Cited standard errors represent single standard deviations (68% confidence level).

Results and Discussion

General Mechanism. The mechanism for the formation of the principal primary photolysis products is as follows:

$$^{14}CH_3CO^{14}CH_3 + h\nu \xrightarrow{0.3} {}^{14}CH_3 + CO^{14}CH_3 \qquad (9)$$

$$\xrightarrow{0.7} 2\,^{14}CH_3 + CO \qquad (10)$$

$$CH_3COCH_3 + h\nu \xrightarrow{0.3} CH_3 + COCH_3 \qquad (11)$$

$$\xrightarrow{0.7} 2CH_3 + CO \qquad (12)$$

$$CF_3COCF_3 + h\nu \rightarrow 2CF_3 + CO \qquad (13)$$
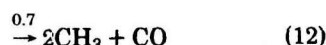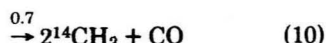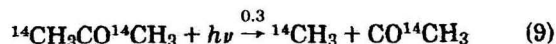
Carbon-14 isotope effects upon the photolysis processes can be taken as negligible, so that the initial concentration ratio for the isotopic methyl radicals is determined by the acetone-1,3-^{14}C specific activity:

$$[CH_3]/[^{14}CH_3] = 13.63 \pm 0.02 \qquad (14)$$

The approximate branching ratios shown above represent 300°K quantum yields.[25] At 373°K the values for channels 10 and 12 are essentially unity. That for HFA at either temperature is reduced because of quenching,[28,29] which caused the inhibition of (6) through reduction of the available CF_3 radical concentration. Although acetyl radicals were present, these rather unreactive species do not interfere.[30]

In the present study (D/S), the ratio of rate constants

TABLE II: Arrhenius Parameters for Elementary Hydrogen Abstraction Reactions

Reaction	Temp range, °K	Log A (A in cm³ mol⁻¹ sec⁻¹)	E_a, kcal mol⁻¹	k, cm³ mol⁻¹ sec⁻¹ (at 307 °K)	Ref
$CH_3 + (CH_3)_2CO \longrightarrow CH_4 + R$	373–573	11.47 ± 0.06	9.69 ± 0.11	3.7×10^4	31
$CF_3 + (CH_3)_2CO \longrightarrow CF_3H + R$	296–588	11.51 ± 0.10	8.14 ± 0.14	5.2×10^5	31
$CH_3 + CH_3CF_3 \longrightarrow CH_4 + CH_2CF_3$		$11.4 = 0.4^a$	12.4 ± 1.0^a	3.7×10^{2a}	9
$CF_3 + CH_3CF_3 \longrightarrow CF_3H + CH_2CF_3$	566–678	12.1 ± 0.1	13.5 ± 1.0	3.1×10^2	31
$CH_3 + CH_4 \longrightarrow CH_4 + CH_3$		$11.4 = 0.4^a$	11.3 ± 0.2	2.3×10^{3a}	9
$CF_3 + CH_4 \longrightarrow CF_3H + CH_3$	303–797	11.87 ± 0.36	10.7 ± 1.0	1.8×10^4	31
$CH_3 + C_2H_6 \longrightarrow CH_4 + C_2H_5$		11.4 ± 0.4^a	10.2 ± 0.2	1.4×10^4	9
$CF_3 + C_2H_6 \longrightarrow CF_3H + C_2H_5$	323–489	11.3 ± 0.3	7.0 ± 0.3	2.1×10^6	31

^{a} Estimated values.

(k_{15}/k_{16}), was used to provide information about the kinetic control of reaction 7:

$$(^{14}CH_3CF_3)^\dagger \xrightarrow{D} {}^{14}CH_2{=}CF_2 + HF \tag{15}$$

$$(^{14}CH_3CF_3)^\dagger + M \xrightarrow{S} {}^{14}CH_3CF_3 + M \tag{16}$$
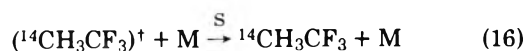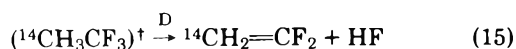
Other elementary reactions requiring brief consideration include combination, abstraction, and addition. Reaction 6 and its isotopic counterpart (1) have already been discussed. Other combination reactions include

$$^{14}CH_3 + CH_3 \rightarrow {}^{14}CH_3CH_3 \tag{17}$$

$$^{14}CH_3 + {}^{14}CH_3 \rightarrow {}^{14}CH_3{}^{14}CH_3 \tag{18}$$

$$CH_3 + CH_3 \rightarrow C_2H_6 \tag{19}$$

$$CF_3 + CF_3 \rightarrow C_2F_6 \tag{20}$$
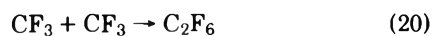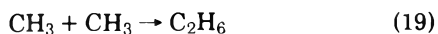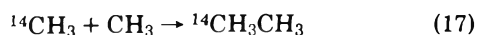
Available Arrhenius parameters for these processes are summarized in Table I. The relative isotopic ethane yields follow from eq 14 as C_2H_6 (1.00), $^{14}CH_3CH_3$ (0.073), and $^{14}CH_3{}^{14}CH_3$ (0.0058).

Important abstraction reactions in CH_3CF_3 bath gas include

$$^{14}CH_3 + CH_3COCH_3 \rightarrow {}^{14}CH_4 + \dot{C}H_2COCH_3 \tag{21a}$$

$$CH_3 + CH_3COCH_3 \rightarrow CH_4 + \dot{C}H_2COCH_3 \tag{21b}$$

$$^{14}CH_3 + CH_3CF_3 \rightarrow {}^{14}CH_4 + \dot{C}H_2CF_3 \tag{22a}$$

$$CH_3 + CH_3CF_3 \rightarrow CH_4 + \dot{C}H_2CF_3 \tag{22b}$$

$$^{14}CH_3 + CH_2{=}CF_2 \rightarrow {}^{14}CH_4 + \dot{C}HCF_2 \tag{23a}$$

$$CH_3 + CH_2{=}CF_2 \rightarrow CH_4 + \dot{C}HCF_2 \tag{23b}$$

$$CF_3 + CH_3COCH_3 \rightarrow CF_3H + \dot{C}H_2COCH_3 \tag{24}$$

$$CF_3 + CH_3CF_3 \rightarrow CF_3H + \dot{C}H_2CF_3 \tag{25a}$$

$$CF_3 + CH_2{=}CF_2 \rightarrow CF_3H + \dot{C}HCF_2 \tag{26}$$
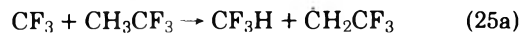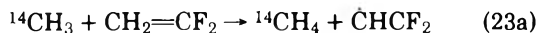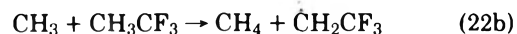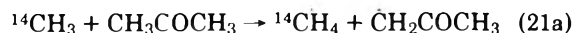
In other hydrogen-containing bath gases (22) and (25) must be generalized:

$$^{14}CH_3 + RH \rightarrow {}^{14}CH_4 + R \tag{22c}$$

$$CH_3 + RH \rightarrow CH_4 + R \tag{22d}$$

$$CF_3 + RH \rightarrow CF_3H + R \tag{25b}$$
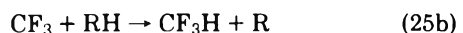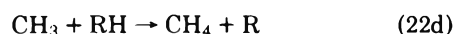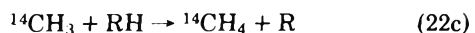
The available Arrhenius parameters are summarized in Table II. No data appear to have been measured for the reactions with $CH_2{=}CF_2$, C_2H_5F, or CH_3CHF_2.

Important olefin addition channels include (7) and (27)

$$^{14}CH_3 + CH_2{=}CF_2 \rightarrow {}^{14}C\dot{C}_2H_5F_2 \tag{27a}$$

$$CH_3 + CH_2{=}CF_2 \rightarrow \dot{C}_3H_5F_2 \tag{27b}$$
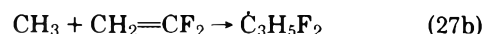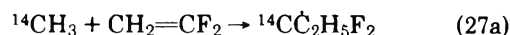
Evidence has been obtained previously favoring the occurrence of (7) in the acetone–HFA cophotolysis system.[4,7b] The Arrhenius parameters listed in Table III indicate that the CF_3 processes characteristically involve small activation energies. A crude estimate for k_{27} (307°K) that neglects polarity effects follows as 9×10^3 cm³ mol⁻¹ sec⁻¹ from the averaged Arrhenius parameters for C_2H_4 and C_2F_4. Although k_7 (307°K) can be estimated from available experimental results as 8.1×10^4 cm³ mol⁻¹ sec⁻¹, these kinetic data may not be reliable.[32] The rate constants for CF_3 reactions with C_2H_4 and C_2F_4 are much larger than this value (1.2×10^7 and 3.2×10^6 cm³ mol⁻¹ sec⁻¹). An estimated k_7 (307°K) of about 6×10^6 cm³ mol⁻¹ sec⁻¹ follows from these latter data.

Finally, ketone addition reactions also require brief consideration. Alcock and Whittle reported that (28) did not occur significantly at temperatures below 358°K.[4a]

$$^{14}CH_3 + CF_3COCF_3 \rightarrow [(CF_3)_2\dot{C}O^{14}CH_3]^\dagger \tag{28}$$
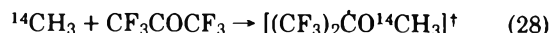
We feel that processes of this type could not have constituted a source of interference.

Optimization of the Photolysis Mixture. The overall mechanism clearly includes several reactions that have not been thoroughly characterized. In the interests of accuracy and sensitivity the yield of $^{14}CH_3CF_3$ must be optimized.[33] The search for optimum photolysis conditions involved experiments in which the HFA concentration in the photolysis mixture was systematically varied. The results (cf. Figure 3) indicate that the products from (6) increase markedly with increasing HFA content. A 25-fold reduction in the product ratio [ethane-$^{14}C/(^{14}CH_3CF_3 + {}^{14}CH_2{=}CF_2)$] accompanied an increase in HFA from 50.0 to 90.9 mol %.[34]

Figure 3 also shows that the sum of $^{14}CH_4$, ethane-^{14}C, $^{14}CH_2{=}CF_2$, and $^{14}CH_3CF_3$ yields was invariably less than 100%. In these experiments an average of $2.2 \pm 0.7\%$ of the *detected* activity was eluted in the C_3-fluorocarbon VPC region, providing direct if not conclusive evidence for the occurrence of

$$CH_3 + {}^{14}CH_2{=}CF_2 \rightarrow {}^{14}CC_2H_5F_2 \tag{27c}$$

or

$$CF_3 + {}^{14}CH_2{=}CF_2 \rightarrow {}^{14}CC_2H_2F_5 \tag{29}$$
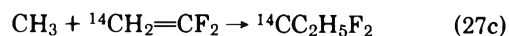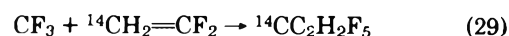
Because VPC standards were not available for the fluorinated propanes, no attempt was made to utilize these re-

TABLE III: Arrhenius Parameters for Olefin Addition Reactions

Reaction	Log A (A in cm³ mol⁻¹ sec⁻¹)	E_a, kcal mol⁻¹	k, cm³ mol⁻¹ sec⁻¹ (at 307 °K)	Ref
$CH_3 + C_2H_4 \longrightarrow C_3H_7$	8.52	7.7		32
	8.1	6.8		4c
	8.9	7.9		4c
	8.5 ± 0.3	7.5 ± 0.4	1.4×10^3	Av[a]
$CF_3 + C_2H_4 \longrightarrow C_3F_3H_4$	8.21	0.95		32
	8.39	2.37		4c
	8.3 ± 0.1	1.7 ± 0.7	1.2×10^7	Av[a]
$CH_3 + C_2F_4 \longrightarrow C_2F_4H_3$	8.05	5.2		32
	8.92	5.7		4c
	8.5 ± 0.5	5.4 ± 0.3	4.5×10^4	Av[a]
$CF_3 + C_2F_4 \longrightarrow C_3F_7$	7.54	1.4		32
	7.5	1.4		4c
	7.5 ± 0.1	1.4 ± 0.1	3.2×10^6	Av[a]
$CH_3 + CH_2{=}CF_2 \longrightarrow C_3F_2H_5$	8.5	6.4	$\sim 8.8 \times 10^3$	Est[b]
$CF_3 + CH_2{=}CF_2 \longrightarrow CF_3CH_2CF_2$	7.86	4.0		32
	7.95	4.37		4c
	7.9 ± 0.1	4.2 ± 0.2	8.1×10^4	Av[a]
$\longrightarrow CF_3CF_2CH_2$		>8.4		4c
$CF_3 + CH_2{=}CF_2 \longrightarrow C_3F_5H_2$	7.9 ± 0.4	1.6 ± 0.2	$\sim 5.8 \times 10^6$	Est[b]

[a] Average of recommended values from current reviews (ref 32 and 4c). [b] Estimated from averaged Arrhenius parameters for C_2H_4 anc C_2F_4.
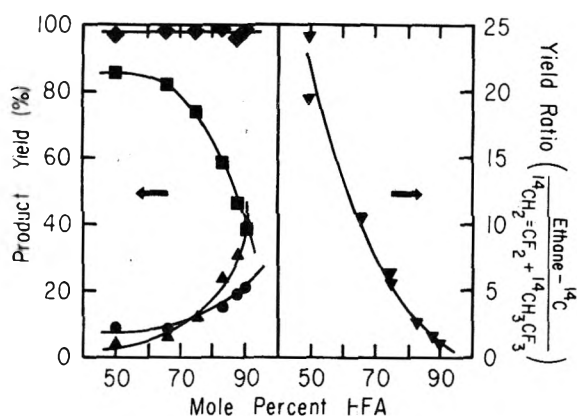
Figure 3. Product distribution vs. HFA concentration in ketone photolysis mixture (pure CH₃CF₃ bath gas): ◆, total; ■, ethane-¹⁴C; ●, ¹⁴CH₄; ▲, ¹⁴CH₂=CF₂ + ¹⁴CH₃CF₃; ▼, ratio (ethane-¹⁴C/ (¹⁴CH₂=CF₂ + ¹⁴CH₃CF₃)).
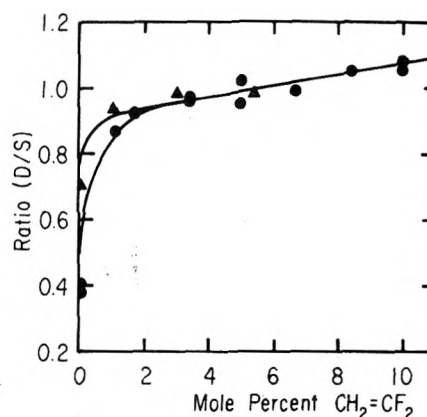
Figure 4. Effect of added CH₂=CF₂ upon experimental (D/S) ratios for CH₃CF₃ bath gas at 307°K and 31.3 Torr total pressure: ●, 0.43–0.59 Torr ketone pressure; ▲, 0.060 Torr ketone pressure.

sults for quantitative purposes.[35] The 90.9 mol % photolysis mixture was adopted for the scavenger and energy transfer experiments. At larger concentrations HFA self-quenching became prohibitively severe.

The Protective Scavenging Method. The (¹⁴CH₂=CF₂/ ¹⁴CH₃CF₃) ratios obtained from the data shown in Figure 3 decreased from 1.17 ± 0.05 to 0.98 ± 0.02 over the range 50.0 to 90.9 mol % HFA (29.8 ± 0.1 Torr total pressure).[34] This finding indicates a significant dependence upon the magnitude of the average CF₃ concentration and constitutes a second source of evidence for the spurious loss of ¹⁴CH₂=CF₂, probably through reaction 29. Similar reductions in (CH₂=CF₂/CH₃CF₃) ratios have been reported previously.[4b,7b] Neely and Carmichael attempted to account for the loss of CH₂=CF₂ through extrapolation of measured (D/S) ratios to 0% photolysis conversion. A rather different procedure has been preferred in this work. We have sought to protect the trace concentration of ¹⁴CH₂=CF₂ through the addition of carrier CH₂=CF₂ to

all the samples. Data obtained from such an experiment (cf. Figure 4) exhibit a marked initial increase in (D/S) with increasing CH₂=CF₂ concentration. These results include runs carried out at two total ketone photolysis mixture concentrations that differed by a full order of magnitude. This range encompasses the ketone aliquot size variation that occurred during this work. Although the protective scavenging effect was more pronounced at the larger ketone concentration, it was also clearly discernable at the lower concentration.

We conclude that the acetone–HFA cophotolysis system is subject to serious systematic errors associated with the occurrence of reaction 7. The mechanism for the protective scavenging action presumably involves suppression of the average CF₃ concentration through (7) itself. The data of Figure 4 indicate that at least 3 mol % of added CH₂=CF₂ is required in order to provide control of the spurious ¹⁴CH₂=CF₂ losses under our conditions.

Other Bath Gases. Similar scavenger curve results ob-

TABLE IV: Regression Analysis Parameters Obtained from Scavenger Plateau Data[a]

Bath gas	Additive	Temp, °K	Pressure, Torr	$(D/S)_0$	γ
CH_3CF_3	$CH_2{=}CF_2$	307	31.3	0.90 ± 0.01	0.017 ± 0.002
CH_3CHF_2	$CH_2{=}CF_2$	307	36.8	0.49 ± 0.02	0.015 ± 0.003
CH_3CH_2F	$CH_2{=}CF_2$	307	37.0	0.99 ± 0.01	0.017 ± 0.001
C_2H_6	$CH_2{=}CF_2$	307	42.2	1.30 ± 0.03	0.013 ± 0.006
C_2F_6	C_2H_6	297	30.0	0.60 ± 0.01	0.010 ± 0.002
C_2F_6	$CH_2{=}CF_2$	307	29.5	0.66 ± 0.02	0.020 ± 0.005
C_2F_6	C_2H_6	373	37.5	0.58 ± 0.01	0.010 ± 0.001
C_2F_6	$CH_2{=}CF_2$	373	37.5	0.91 ± 0.05	0.010 ± 0.013

[a] The quantities γ and $[D/S]_0$ are defined by eq 31.
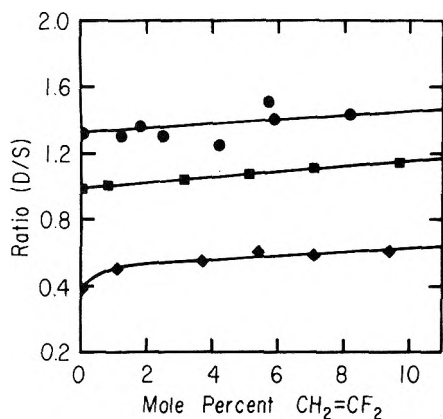
Figure 5. Effect of added $CH_2{=}CF_2$ upon experimental (D/S) ratios for C_2H_6, C_2H_5F, and CH_3CHF_2 bath gases at 307°K: ●, C_2H_6 (42.2 Torr); ■, C_2H_5F (37.0 Torr); ◆, CH_3CHF_2 (36.8 Torr).
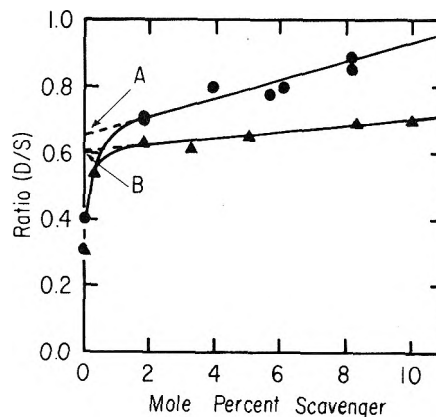
Figure 6. Comparison of $CH_2{=}CF_2$ and C_2H_6 additives in C_2F_6 bath gas: ●, $CH_2{=}CF_2$ (307°K, 29.5 Torr); ▲, C_2H_6 (297°K, 30.0 Torr); A and B, $[D/S]_0$ intercepts.

tained with CH_3CHF_2, C_2H_5F, C_2H_6, and C_2F_6 bath gases are shown in Figures 5 and 6. A qualitative difference from the behavior depicted in Figure 4 arose for C_2H_6 and C_2H_5F. The rapid initial increase in (D/S) was not observed. The behavior exhibited by C_2F_6 strongly resembles that of CH_3CF_3, and CH_3CHF_2 appears to be intermediate between the C_2H_6 and CH_3CF_3 cases. Rapid abstraction reactions in C_2H_6 and C_2H_5F effectively control the average CF_3 concentration. In C_2F_6 and CH_3CF_3, however, this control is provided mainly by reaction 7. Regrettably, the complexity of the overall mechanism precludes a kinetic analysis of greater detail.

Further experiments were carried out in C_2F_6 in order to eliminate altogether the possibility for hydrogen abstraction. As a test of the above arguments C_2H_6 was employed as the CF_3-scavenging moiety:

$$CF_3 + C_2H_6 \rightarrow CF_3H + \dot{C}_2H_5 \qquad (30)$$
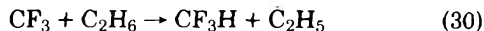
These results are compared in Figure 6 to data obtained from a similar study with $CH_2{=}CF_2$ additive. The C_2H_6–C_2F_6 system (297°K) behaved similarly to the $CH_2{=}CF_2$–C_2F_6 system (307°K). At least 2 mol % of either scavenger was required in order to suppress reaction 29. Both of these scavenger curves exhibited typical saturation or plateau behavior at additive concentrations exceeding 2 mol %. Within the experimental accuracy the (D/S) ratios were directly proportional to the additive concentration (C) throughout the plateau region:

$$[D/S]_C = [D/S]_0 + \gamma C \qquad C \geq 2 \text{ mol } \% \qquad (31)$$

Here $[D/S]_0$ denotes the extrapolated $[D/S]_C$ intercept and γ the slope parameter. This linear plateau behavior has

proven to be rather general. Regression analysis parameters obtained for all the additive–bath-gas systems investigated have been listed in Table IV.

The small positive plateau slopes shown in Table IV indicate differences in the energy transfer characteristics for the bath gases relative to the respective additives. Included in this phenomenological effect are factors that influence the *collision rates* (elastic cross sections and molecular masses for the rigid sphere model) as well as the respective energy transfer *efficiencies*. A full energy transfer analysis requires computer modeling of pressure fall-off data corresponding to the cascade deactivation region. This topic will be treated in detail in subsequent papers.[14] Here we note that under cascade deactivation conditions the energy transfer efficiency is generally an increasing function of molecular complexity as measured, for example, by the available number of vibrational degrees of freedom. Thus in general the efficiencies for our bath gases and scavengers can be anticipated to be different. The observation of positive slopes (cf. Table IV) indicates that the fluorinated ethanes are *stronger* colliders than $CH_2{=}CF_2$ toward chemically activated CH_3CF_3. The parameter $(D/S)_0$ represents the hypothetical (D/S) ratio for the pure bath gas corresponding to (i) the temperature and total pressure of the experiment; (ii) the absence of spurious $^{14}CH_2{=}CF_2$ losses; and (iii) the absence of energy transfer complications.

An important diagnostic criterion follows: well-behaved scavenging substances must yield the same $(D/S)_0$ value for a given bath gas studied at constant temperature and pressure. This test can be applied to the present results for C_2H_6–C_2F_6 (30.0 Torr, 297°K) and $CH_2{=}CF_2$–C_2F_6 (29.5 Torr, 307°K). From Figure 6 the respective intercepts were
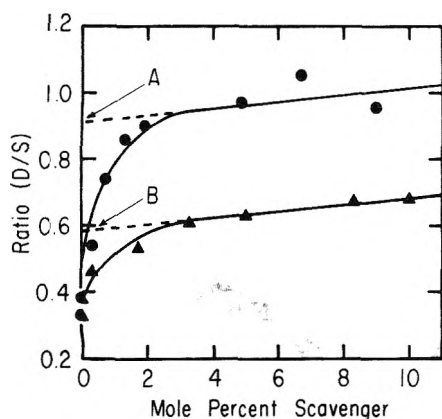
Figure 7. Comparison of CH_2=CF_2 and C_2H_6 additives in C_2F_6 bath gas at 373°K and 37.5 Torr total pressure: ●, CH_2=CF_2; ▲, C_2H_6; A and B, [D/S]₀ intercepts.

Figure 8. Dependence of corrected product yields upon CH_2=CF_2 pressure for C_2F_6 bath gas: ●, $^{14}CH_4$ + ethane-^{14}C (307°K, 29.5 Torr); ▲, $^{14}CH_2$=CF_2 + $^{14}CH_3CF_3$ (same conditions); ◆, $^{14}CH_4$ + ethane-^{14}C (373°K, 37.5 Torr); ■, $^{14}CH_2$=CF_2 + $^{14}CH_3CF_3$ (same conditions).

0.60 ± 0.01 and 0.66 ± 0.02. Stepladder cascade simulations of these systems yielded a predicted (D/S)₀ increase of 0.08 ± 0.03 for CH_2=CF_2-C_2F_6 relative to C_2H_6-C_2F_6 arising from the difference in photolysis temperatures.[3,13] We conclude that the above analysis of the protective scavenging mechanism is strongly corroborated; that the C_2H_6-C_2F_6 and CH_2=CF_2-C_2F_6 systems can be employed for reliable (D/S) ratio measurements at temperatures in the neighborhood of 300°K; and that our postulated rough similarity in rate constants for CF_3 reactions with C_2H_6 (ca. 2.1×10^6 cm^3 mol^{-1} sec^{-1}, 307°K, Table II) and CH_2=CF_2 (ca. 6×10^6 cm^3 mol^{-1} sec^{-1}, 307°K, Table III) has been substantiated.

Experiments at High Temperatures. Temperature variation is of fundamental importance in energy transfer studies.[2,3,5] Thus, we have also evaluated the protective scavenging method at 373°K for both the C_2H_6-C_2F_6 and CH_2=CF_2-C_2F_6 systems (cf. Figure 7). Both 373°K scavenger curves exhibited pronounced sensitivity to small additive concentrations. For CH_2=CF_2 the two sets of results were in semiquantitative agreement: (1) at both temperatures the scavenger curves exhibited saturation behavior above additive concentrations of 2–3 mol %; and (ii) the measured slope parameters were 0.020 ± 0.005 (307°K) and 0.010 ± 0.013 (373°K). As noted above, (D/S)₀ is dependent upon temperature and pressure. The value of 0.91 ± 0.05 observed for CH_2=CF_2-C_2F_6 at 373°K is in good agreement with stepladder predictions based upon the 307°K data. However, the 373°K experimental (D/S)₀ value for C_2H_6-C_2F_6 was only 0.58 ± 0.01, which is significantly smaller than the presumably correct CH_2=CF_2-C_2F_6 result. We conclude that CH_2=CF_2 provides effective protective scavenging at both temperatures, that a minimum of 3 mol % CH_2=CF_2 must be present in order to ensure reliable results, and that at 373°K the C_2H_6 protective mechanism apparently has failed.

This latter observation suggests that k_{30} must be significantly smaller than k_7 at 373°K. Although reliable Arrhenius parameters for (30) have been determined (cf. Table II), the available results for reaction 7 are both controversial[32] and in conflict with our low temperature data. If the literature results for (30) are accepted, and if *all* the error in our estimated parameters for reaction 7 is assigned to the activation energy, then a very crude estimated value of 0.7 kcal mol^{-1} follows from the added assumption that the ratio (k_7/k_{30}) has a value of 2.
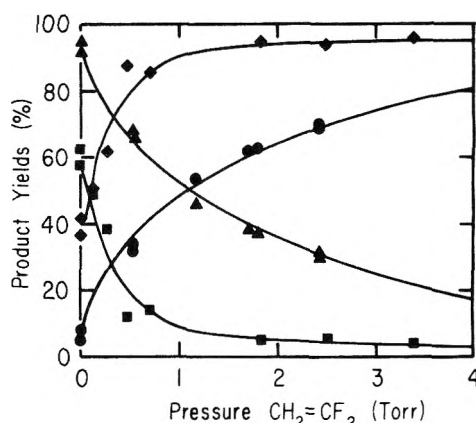
HFA Quenching by CH_2=CF_2 and C_2H_6. Our results can be viewed somewhat differently in order to illustrate another important distinction between the C_2H_6 and CH_2=CF_2 additives. The self- and olefin-induced quenching behavior of primary photoexcited HFA have been extensively studied[28,29]

$$CF_3COCF_3 + h\nu \rightarrow CF_3COCF_3^* \qquad (32)$$

$$CF_3COCF_3^* \rightarrow \text{dissociation products} \qquad (33)$$

$$CF_3COCF_3^* + M \rightarrow CF_3COCF_3 + M \qquad (34)$$

in which the superscripted asterisk denotes electronic excitation.

The 313-nm quantum yield for pure HFA approaches unity at 300°K in the limit of zero pressure. It is a decreasing function of increasing pressure until the high-pressure limiting value of 0.4 is achieved at roughly 45 Torr. The self-quenching is also sensitive to temperature. The high-pressure limiting quantum yield increases to roughly 0.9 at 350°K.[28a] Olefins quench the fluorescence emission with a temperature dependence similar to that for self-quenching.[28] The present results provide evidence for efficient HFA quenching by CH_2=CF_2. For the CH_2=CF_2-C_2F_6 system (cf. Figure 8) the yield of labeled fluorocarbons at constant temperature and pressure decreases with increasing CH_2=CF_2 concentration. In order for these results to be of quantitative significance the data must be corrected for the loss of $^{14}CH_2$=CF_2 from reaction 7. These corrections can be estimated from eq 31 together with the parameters given in Table IV based upon the following assumptions: (i) the energy transfer characteristics can be represented by eq 31; (ii) the stabilized $^{14}CH_3CF_3$ yields are not subject to spurious losses; and (iii) the $^{14}CH_2$=CF_2 losses (0 < C < 3 mol %) can be estimated from eq 31. The estimated [D/S]$_C$ values were then combined with the measured $^{14}CH_3CF_3$ yields to provide corrected $^{14}CH_2$=CF_2 yields. The corrected results shown in Figure 8 demonstrate marked depression of the fluorocarbon yield with increasing CH_2=CF_2 concentration. This evidence is indirect and includes no provision for acetone quenching, but we feel that HFA quenching by CH_2=CF_2 provides the most plausible explanation for the fluorocarbon activity losses.[36] *This analysis points up the most serious drawback to the*
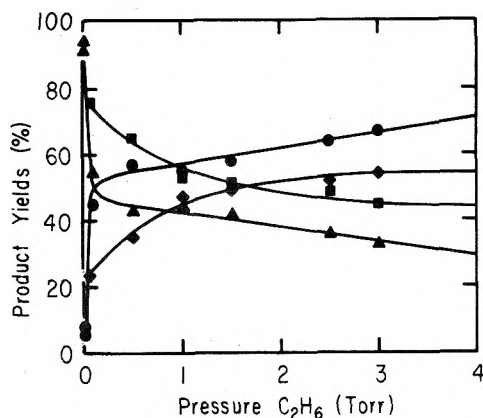
Figure 9. Dependence of corrected product yields upon C_2H_6 pressure for C_2F_6 bath gas: ●, $^{14}CH_4$ + ethane-^{14}C (297°K, 30.0 Torr); ▲, $^{14}CH_2$=CF_2 + $^{14}CH_3CF_3$ (same conditions); ◆, $^{14}CH_4$ + ethane-^{14}C (373°K, 37.5 Torr); ■, $^{14}CH_2$=CF_2 + $^{14}CH_3CF_3$ (same conditions).

present CH_2=CF_2 *technique.* At 6 mol % CH_2=CF_2 the fluorocarbon activity losses shown in Figure 8 are 63 ± 2% (307°K, 29.5 Torr) and 93 ± 1% (373°K, 37.5 Torr).[37] The only important consequence of this nuisance problem is a limitation in experimental accuracy in the high-pressure region through loss of counting statistics. The reliability of the measured (D/S) ratios is not otherwise affected.

A similar C_2H_6 quenching study yielded the results shown in Figure 9. The 297°K results were treated as described above. Since the 373°K C_2H_6 regression analysis parameters are not reliable (vide supra), the $[D/S]_0$ value for CH_2=CF_2-C_2F_6 was used in the corrections. The additional quantitative uncertainty associated with the experimental slope parameter is not of sufficient magnitude to affect the conclusions given below. From Figure 9 it is clear that quenching is much less serious for C_2H_6 additive. The fluorocarbon yield depressions observed under the present conditions were 58 ± 2% (297°K, 30.0 Torr) and 21 ± 2% (373°K, 37.5 Torr).

Conclusions

The attempted generalization of the present mechanistic results to other chemical activation systems would represent a gross oversimplification. The enhanced reactivity of CF_3 radicals toward CH_2=CF_2 may represent an unusual kinetic situation. Unimolecular energy transfer is an important chemical dynamics research area in which virtually the entire emphasis is upon the *quantitative* interpretation of reaction rate data. In our view the practitioners of this discipline would be well advised to assess carefully the possible importance of mechanistic complications in each experimental system.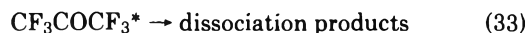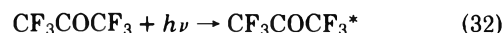 A sophisticated RRKM energy transfer analysis can hardly be expected to compensate for deficiencies in the experimental data.

Supplementary and Miniprint Material Available. The original data tables corresponding to Figures 3–9 and technical details concerning the apparatus will appear following these pages in the microfilm edition of this volume of the journal. Photocopies of the supplementary material and full-size photocopies of the miniprinted material from this paper only or microfiche (105 × 148 mm, 24× reduction, negatives) containing all of the supplementary material for the papers in this issue may be obtained from the Business Office, Books and Journals Division, American Chemical Society, 1155 16th St., N.W., Washington, D.C. 20036. Remit check or money order for $4.50 for photocopy or $2.50 for microfiche, referring to code number JPC-75-2077.

References and Notes

(1) Cf. ref.2 and 3 for recent reviews.
(2) (a) D. W. Setser, *MTP Int. Rev. Sci. Phys. Chem., Ser. One*, 9, 1ff (1972); (b) B. S. Rabinovitch and D. W. Setser, *Adv. Photochem.*, 3, 1 (1964); (c) B. S. Rabinovitch and M. C. Flowers, *Quart. Rev., Chem. Soc.*, 122 (1964).
(3) (a) P. J. Robinson and K. A. Holbrook, "Unimolecular Reactions", Wiley, New York, N.Y., 1972; (b) W. Forst, "Theory of Unimolecular Reactions", Academic Press, New York, N.Y., 1973.
(4) W. G. Alcock and E. Whittle, *Trans. Faraday Soc.*, 61, 244 (1965); (b) R. D. Giles and E. Whittle, *ibid.*, 61, 1425 (1965); (c) E. Whittle, *MTP Int. Rev. Sci., Phys. Chem., Ser. One*, 9, 75ff (1972).
(5) (a) H. W. Chang and D. W. Setser, *J. Am. Chem. Soc.*, 91, 7648 (1969); (b) H. W. Chang, N. L. Craig, and D. W. Setser, *J. Phys. Chem.*, 76, 954 (1972); (c) K. C. Kim and D. W. Setser, *ibid.*, 77, 2021 (1973); (d) K. C. Kim, D. W. Setser, and B. E. Holmes, *ibid.*, 77, 725 (1973).
(6) (a) D. Sanesi, G. Nelli, and R. Fontanelli, *Chim. Ind. (Milan)*, 50, 619 (1968); (b) P. Cadman, M. Day, A. W. Kirk, and A. F. Trotman-Dickenson, *Chem. Commun.*, 203 (1970); (c) P. Cadman, M. Day, and A. F. Trotman-Dickenson, *J. Chem. Soc. A*, 1356 (1971); (d) E. Tschuikow-Roux and W. J. Quiring, *J. Phys. Chem.*, 75, 295 (1971); (e) J. A. Kerr and D. M. Timlin, *Int. J. Chem. Kinet.*, 3, 427 (1971).
(7) (a) G. O. Pritchard and M. J. Perona, *Int. J. Chem. Kinet.*, 2, 281 (1970); (b) B. D. Neely and H. Carmichael, *J. Phys. Chem.*, 77, 307 (1973).
(8) (a) J. R. Lacher and H. A. Skinner, *J. Chem. Soc. A*, 1034 (1968); (b) W. Tsang, *Int. J. Chem. Kinet.*, 5, 643 (1973); (c) A. S. Rodgers and W. G. F. Ford, *ibid.*, 5, 965 (1973).
(9) G. W. Mutch, Ph.D. Dissertation, University of California, Davis, 1973; available from University Microfilms as Dissertation No. 74-8530.
(10) (a) M. J. Berry and G. C. Pimentel, *J. Chem. Phys.*, 49, 5190 (1968); (b) P. N. Clough, J. C. Polanyi, and R. T. Taguchi, *Can. J. Chem.*, 48, 2919 (1970).
(11) (a) C. F. McKnight, N. J. Parks, and J. W. Root, *J. Phys. Chem.*, 74, 217 (1970); (b) K. A. Krohn, N. J. Parks, and J. W. Root, *J. Chem. Phys.*, 55, 2690, 5771, 5785 (1971); (c) R. G. Manning and J. W. Root, *J. Phys. Chem.*, 79, 1478 (1975); (d) R. G. Manning, Ph.D. Dissertation, University of California, Davis, 1975.
(12) D. L. Bunker, *J. Chem. Phys.*, 57, 332 (1972).
(13) R. R. Pettijohn, G. W. Mutch, and J. W. Root, *J. Phys. Chem.*, in press.
(14) Energy transfer experiments based upon conventional analytical procedures are often limited with respect to the identity and range of concentrations of bath gases that can be investigated.
(15) J. K. Lee, E. K. C. Lee, B. Musgrave, Y. N. Tang, J. W. Root, and F. S. Rowland, *Anal. Chem.*, 34, 741 (1962).
(16) Under unfavorable circumstances counter quenching could cause difficulties (ref 15).
(17) (a) Carbon-14 decays via negatron emission with a radioactive half-life of 5720 years and a maximum decay energy of 0.155 MeV (Ref 17b). (b) G. Friedlander, J. W. Kennedy, and J. M. Miller, "Nuclear and Radiochemistry", 2nd ed, Wiley, N.Y., New York, 1964.
(18) The cited purities represent minimum values specified by the manufacturers.
(19) This behavior, which is a consequence of the long radioactive half-life of carbon-14, is in marked contrast to our experience with tritium-labeled precursors. These may require repurification at intervals of a few days.
(20) The Barocell calibration of the Hastings gauge for the acetone–HFA photolysis mixture showed the following differences relative to the manufacturer's nomograph for pure acetone: +25 ± 1% above the corrected reading at 200 mTorr; +53 ± 3% at 400 mTorr; and +270 ± 20% at 600 mTorr.
(21) The photolysis mixture concentration for each sample has been calculated from the recorded Hastings readings together with the Barocell calibration results. These values have been included in the data tables given in the microfilm edition of this journal.
(22) The authors thank Dr. Larry L. Lucas for assistance with the design and fabrication of the lamp and power supply and the counting electronics components. Detailed parts lists, schematic wiring diagrams, and as-

sembly diagrams for everything but the scaler have been included in the microfilm edition of this journal. Additional details are given in ref 23 and 24.

(23) J. W. Root, R. R. Pettijohn, and L. L. Lucas, "Flow Proportional Counting Techniques", AFOSR Technical Report, University of California, Davis, Calif., 1975.

(24) L. L. Lucas, Ph.D. Dissertation, University of California, Davis, 1973; Available from University Microfilms as Dissertation No. 74-8523.

(25) J. G. Calvert and J. M. Pitts, Jr., "Photochemistry", Wiley, New York, N.Y., 1966.

(26) B. M. Mahan and R. Mandal, J. Chem. Phys., 37, 207 (1962).

(27) K. A. Krohn, Ph.D. Dissertation, University of California, Davis, 1971; available from University Microfilms as Dissertation No. 72-3587.

(28) (a) D. A. Whytock and K. O. Kutschke, Proc. R. Soc., Ser. A, 306, 503 (1968); (b) A. Gandini and K. O. Kutschke, ibid., 306, 511 (1968); (c) A. Gandini, D. A. Whytock, and K. O. Kutschke, ibid., 306, 529, 537, 541 (1968).

(29) W. Ware and S. K. Lee, J. Chem. Phys. 49, 217 (1968).

(30) In ref 9 the minimum activation energy paths for reaction of acetyl (reactions 9 and 11) and acetonyl radicals are shown to involve bimolecular radical combination and hydrogen abstraction from acetone itself. The estimated activation energies for these reactions are 18 ± 3 kcal mol^{-1} (acetyl) and 16 ± 3 kcal mol^{-1} (acetonyl). Since the activation energies for olefin additions involving these species can also be anticipated to be large, their principal mode of reaction likely involves bimole-

(31) P. Gray, A. A. Herod, and A. Jones, Chem. Rev., 71, 247 (1971).

(32) J. A. Kerr and M. J. Parsonage, "Evaluated Kinetic Data on Gas Phase Addition Reactions: Reactions of Atoms and Radicals with Alkenes, Alkynes, and Aromatic Compounds", Chemical Rubber Company Press, Cleveland, Ohio 1972.

(33) In addition to considerations of statistical accuracy, it was also expedient to minimize the formation of ethane-^{14}C. When present in large yield, this substance interfered with the assay of $^{14}CH_2=CF_2$.

(34) In these preliminary experiments no attempt had been made to evaluate the importance of spurious $^{14}CH_2=CF_2$ loss through reaction 29. The cited HFA concentrations refer to the ketone mixture itself.

(35) The labeled radicals from (27c) and (29) would likely undergo combination reactions as well as abstraction to form propanes. Thus, other higher molecular weight products probably escaped detection. The present VPC analysis is poorly suited for such products because of their prohibitively large retention volumes.

(36) The HFA quenching behavior shown in Figures 8 and 9 reflects the differences in quenching efficiency between C_2F_6 and the respective additives.

(37) The results do not suggest that the pure C_2F_6 bath gas system would give spurious results at 373°K. However, a 6 mol % C_2H_6 concentration in bath gases such as C_2F_6 or CH_3CF_3 would be inadequate to ensure the control of reaction 29. The indicated temperature dependence for quenching by $CH_2=CF_2$ seems anomalous (ref 28 and 29).

Shock Tube Cis–Trans Isomerization Studies. IV

Wayne M. Marley and Peter M. Jeffers*

Department of Chemistry, State University College, Cortland, New York 13045 (Received March 26, 1975)

Single pulse shock tube relative rate measurements are reported for the cis–trans isomerization of several conjugated olefins. The homogeneous, unimolecular isomerizations were followed in the limiting high-pressure region. Results are k^∞ (crotononitrile) = $10^{13.2}$ exp$(-58,100/4.58T)$ sec^{-1}, (1060–1280°K); k^∞ (1,3-pentadiene) = $10^{13.6}$ exp$(-63,000/4.58T)$ sec^{-1}, (1000–1150°K); k^∞ (3-methyl-1,3-pentadiene) = $10^{14.0}$ exp$(-55,000/4.58T)$ sec^{-1}, (955–1160°K); and imply resonance stabilization energies of 8–12 kcal.

Earlier studies in this series[1-4] covered the cis–trans isomerization of several olefins and halogenated olefins, all with a single unsaturated site. We now report the effects of conjugated unsaturation on the cis–trans isomerization process, as observed in crotononitrile, 1,3-pentadiene, and 3-methyl-1,3-pentadiene. In addition to enlarging the series of cis–trans isomers studied in our laboratory by this method, a previous report[5] of crotononitrile isomerization listed Arrhenius parameters which appeared inconsistent with a simple unimolecular mechanism, and new measurements appeared warranted. The present results do differ significantly from those found by Butler and McAlpine,[5] and are much more easily fitted by reasonable unimolecular isomerization theories.[6] There are no previous literature reports on the thermal geometric isomerization of either 1,3-pentadiene or 3-methyl-1,3-pentadiene.

These measurements were all accomplished using the single pulse shock tube relative rate technique, which we have found[3,4] yields reliable values for the limiting high-pressure unimolecular rate constant with no apparent interference from heterogeneous or homogeneous free-radical processes.

Experimental Section

The shock tube and general procedures remain unchanged from earlier work and have been fully detailed.[1,2]

Shocked gas samples (1 ml) at 250–400 Torr were transferred from the shock tube to the F.I.D. gas chromatograph with a Precision Sampling Co. gas syringe which was vacuum cleaned after each sample injection.

Materials. Eastman crotonitrile and Matheson 1,2-dichloroethylene (both cis–trans mixtures) were resolved using a 1.8 m × 6 mm Carbowax 750 column at 70°. The trans isomers collected were 99.65 and 99.69% pure with the corresponding cis isomer as the only contaminant. The cis-1,3-pentadiene and trans-3-methyl-1,3-pentadiene were supplied by PCR. They contained, respectively, 0.48 and 0.34% trans isomer. Philips research grade cis-2-butene was 99.978% pure. Linde high-purity Ar was used to prepare dilute mixtures of the appropriate isomers.

Analysis. Concentrations were found from triangulation of the chromatogram peaks. The four isomers in crotononitrile–dichloroethylene mixtures were resolved with a 1.8 m × 3 mm Carbowax 750 column at 60°. A 1.8 m × 6 mm diethylene glycol–AgNO$_3$ column operated at room temperature separated mixtures of 1,3-pentadiene and 2-butene. A 1.5 m × 6 mm polyethylene glycol–AgNO$_3$ column at 25° was used for 1,3-pentadiene-3-methyl-1,3-pentadiene mixtures. Usually each shock was analyzed only once, but at times a second sample was also processed.

Shock Experiments. The mixtures listed in Table I were prepared in 5-l. Pyrex bulbs with Ar diluent. Initial pre-

TABLE I

| Mixture | | | | | | Parameters derived[a] for A | | |
A	B	% A	% B	Shocks	T range, °K	log A, sec⁻¹	E_a, kcal	E_a, kJ
trans-Crotononitrile	*trans*-1,2-Dichloroethylene	0.95	0.46	6	1060–1280	13.2 ± 0.3	58.0 ± 2.0	243
		0.20	0.10	10				
		0.005	0.002	8				
cis-1,3-Pentadiene	*cis*-2-Butene	1.14	0.86	9	1000–1150	13.6 ± 0.3	53.0 ± 2.0	222
		0.20	0.15	6				
trans-3-Methyl-1,3-pentadiene	*cis*-1,3-Pentadiene	1.10	0.90	5	955–1160	14.0 ± 0.3	55.0 ± 2.0	230
		0.24	0.19	6				
		0.044	0.041	7				

[a] The Arrhenius parameters assumed for 2-butene and dichloroethylene were those reported in ref 3. The 1,3-pentadiene parameters found were then used for the 3-methyl-1,3-pentadiene study. Error limits include additive errors from the reference system.
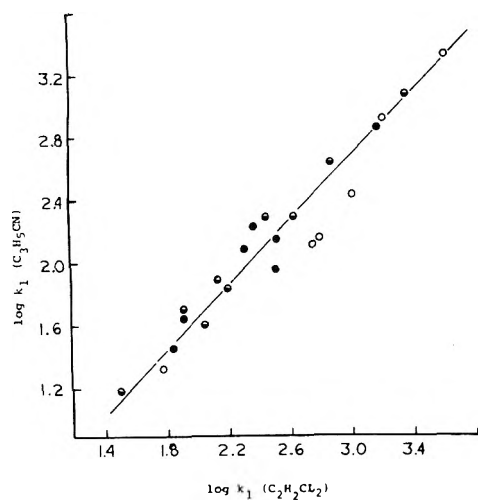
Figure 1. Relative rate plot for crotononitrile with dichloroethylene as reference standard. Filled symbols are highest dilution, half-filled symbols represent intermediate concentration, as listed in Table I.

Figure 2. Relative rate plot for 1,3-pentadiene with 2-butene as standard. Concentrations are listed in Table I with filled circles representing the dilute mixture.

shock pressures were 200–340 Torr. The Mylar diaphragms burst at 88–96 psig. Residence times of about 150 μsec were measured from the flat portion of the pressure trace.

Calculations. The cis → trans rate constants were found, regardless of the starting isomer, using the integrated form of a reversible first-order rate law. The equilibrium constants used in the rate constant calculations were in the range 0.76–1.4. Since conversions were very small and never approached equilibrium levels, the calculation is quite insensitive to the value of K_{eq}. Parts I[1] and II[2] of this series reported values for both $k_{c \to t}$ and $k_{t \to c}$ and indicated good agreement between their ratio and K_{eq}, but since that point has been established and precise values for K_{eq} are not a primary concern or result of this particular investigation, we followed each reaction in only one direction.

Results

Relative rate plots of the experimental results are presented in Figures 1–3. The slope of these plots equals the ratio of the activation energies for the two systems and the intercept can be used to find the Arrhenius A factors. Numerical results deduced from the graphs are listed in Table I. The scatter on the crotononitrile relative rate plot appears larger than that found for the dienes. We feel the source of the greater uncertainty may be in the higher boiling point of crotononitrile (118° vs. 43° for pentadiene)

Figure 3. Relative rate plot for 3-methyl-1,3-pentadiene with 1,3-pentadiene used as reference. Filled circles are highest dilution, empty circles highest concentration, as listed in Table I.

which probably leads to more adsorption on the walls of the shock tube and the other gas-handling equipment.

Discussion

We feel that convincing arguments have been presented[3,4] which imply that these unimolecular reactions are unperturbed by free-radical or heterogeneous contributions, and these facts may be the source of the considerable discrepancy between our Arrhenius parameters for crotononitrile and those reported by Butler and McAlpine (E_a = 51.3 kcal, log A = 11.0). In fact, extrapolation of our results passes nearly through the middle of Butler and McAlpine's rate constants over their temperature range of 573–630°K. All three conjugated olefin systems studied have isomerization rate parameters in line with those we found for halogenated olefins,[1-3] and all of these appear entirely consistent with theoretical estimates based on a biradical intermediate mechanism as proposed by Benson and coworkers.[6] Our previously established rate constant for 2-butene isomerization, log k^∞ = 14.62 − 66,200/4.58T can be compared with the present findings and implies resonance stabilization of the biradical by 8 kcal due to the cyano group, 11 kcal by methyl allyl, and 13 kcal by the allyl interaction. These values are in good agreement with the findings of Sarner et al.,[7] who derived a value of 6 kcal for a CN resonance from thermolysis of substituted cyclobutanes which

also decompose through biradical intermediates. The studies of Walters[8] and Frey[9] on isopropyl- and isopropenylcyclobutane indicate 11.6 kcal resonance stabilization with methyl allyl, while 12.6 kcal is the "standard" resonance stabilization accepted by Benson and O'Neal[6] for allyl. Thus, these isomerization measurements appear to provide a convenient method for determining reliable resonance interaction energies.

References and Notes

(1) P. M. Jeffers and W. Shaub, *J. Am. Chem. Soc.*, **91**, 7706 (1969).
(2) P. M. Jeffers, *J. Phys. Chem.*, **76**, 2829 (1972).
(3) P. M. Jeffers, *J. Phys. Chem.*, **78**, 1469 (1974).
(4) (a) S. M. Bauer, B. P. Yadava, and P. Jeffers, *J. Phys. Chem.*, **78**, 770 (1974); (b) P. Jeffers and S. H. Bauer, *Int. J. Chem. Kinet.*, **VI**, 763 (1974).
(5) J. N. Butler and R. O. McAlpine, *Can. J. Chem.*, **41**, 2487 (1963).
(6) A biradical intermediate theory has been developed by Benson and coworkers and can be found in several forms: (a) S. W. Benson, "Thermochemical Kinetics", Wiley, New York, N.Y., 1968; (b) S. W. Benson and H. E. O'Neal, *Natl. Stand. Ref. Data Ser., Natl. Bur. Stand.*, **No. 21**, 21 (1970); (c) S. W. Benson, K. Egger, and D. M. Golden, *J. Am. Chem. Soc.*, **87**, 468 (1965).
(7) S. F. Sarner, D. M. Gale, N. K. Hall, Jr., and A. B. Richmond, *J. Phys. Chem.*, **76**, 2817 (1972).
(8) M. Zupon and W. D. Walters, *J. Phys. Chem.*, **67**, 1845 (1963).
(9) R. J. Ellis and H. M. Frey, *Trans. Faraday Soc.*, **59**, 2076 (1963).

Photodimerization of 9-Anthroate Esters and 9-Anthramide[1]

Rita Shao-Lin Shon, Dwaine O. Cowan,* and Walter W. Schmiegel[2]

Department of Chemistry, The Johns Hopkins University, Baltimore, Maryland 21218 (Received March 14, 1975)

The photodimerization and fluorescence quantum yields of methyl, ethyl, *n*-butyl, *tert*-butyl, and cyclohexyl 9-anthroates and 9-anthramide were measured as a function of concentration. These efficiencies along with the fluorescence lifetime measurements are used to evaluate rate ratios and individual rate constants for several mechanistic schemes.

In this continuing study[3] on substituent and solvent effects on the photodimerization of anthracene[4] derivatives, we report on the photochemistry and photophysics of 9-anthroate esters (methyl, ethyl, *n*-butyl, *tert*-butyl, and cyclohexyl) and 9-anthramide. Relative fluorescence quantum yields and low-conversion photodimerization quantum yields were determined as a function of concentration. In addition absolute fluorescence quantum yields in dilute solution and fluorescence lifetimes were determined for each of the six 9-substituted anthracene derivatives (1).
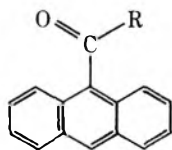
1-6

1, R = -O-methyl	4, R = -O-*tert*-butyl
2, R = -O-ethyl	5, R = -O-cyclohexyl
3, R = -O-*n*-butyl	6, R = -NH₂

Experimental Section

All melting points were measured on a Thomas Hoover melting point apparatus and were not corrected. Infrared spectra were determined with a Perkin-Elmer Model 337 spectrophotometer, ultraviolet and visible spectra were recorded with a Cary Model 14 spectrophotometer, and emission spectra were measured with a Hitachi-Perkin-Elmer MPF-2A fluorescence spectrometer. At high substrate concentrations, 10^{-2} M, fluorescence measurements were determined by the front surface technique previously described.[3] This method uses a cell identical with that used for photodimerization quantum yield studies placed in a solid-sample cell holder such that the intersection of the excitation and emission beams is at the inside front surface of the cell. Typically 99% absorption occurred in less than the first 0.5 mm of solution when 1 × 10^{-2} M solutions were excited at the wavelength corresponding to the lowest vibronic transition. Fluorescence spectra of concentrated solutions were essentially unchanged, except for strong self-absorption of the first vibronic transition of 9-an-

TABLE I: Preparative Photolysis of 9-Anthroate Esters and 9-Anthramide

Compound	Monomer mp, °C	Dimer mp, °C	Remelting mp, °C	Photo-lysis time, hr	Amt photo-lyzed[g]	Dimer,[g] %	Monomer,[g] %	Material balance, %
(1) Methyl ester[a]	111–112	228.5–229.5	111–115					
(2) Ethyl[b,e] ester	112–113	216–217	~110	30	0.100[g]	0.0629 (62.9)	0.0315 (31.5)	94.4
(3) n-Butyl[a,e] ester	43.5–44.5	198–199	44–50	12	0.215	0.128 (60.0)	0.065 (30.0)	90.0
(4) tert-Butyl[a,f] ester	157–158	233–235	155–157	4.5	1.40	1.33 (95.0)	0.05 (3.6)	98.6
(5) Cyclohexyl[a,f] ester	126.2–127.2	208–209	126–127	5.9	0.497	0.454 (91.4)	0.0146 (2.9)	94.3
(6) 9-Anthramide[a,e]	219–219.5 (decomp)	254.5–256	195–200	10	0.332	0.0727 (21.9)	0.259 (78.0)	99.9[d]
(6) 9-Anthramide[c,f]	219–219.5 (decomp)	254.5–256	195–200	6.1	1.599	1.415 (88.4)	0.178 (11.1)	99.5[d]

[a] In 95% ethanol. [b] In benzene. [c] In THF. [d] Small amount (<0.3%) of a yellow material was isolated but not identified. [e] 34 ml degassed solution in cylindrical quartz cell photolyzed on optical bench, same set-up as quantitative studies. [f] 200 ml degassed solution in immersion well set-up with 450-W Hanovia lamp. [g] Range of concentration $1-5 \times 10^{-2}$ M.

thramide, from those at 10^{-5} M. There was no evidence of excimer emission at the concentrations studied.

Low concentration fluorescence measurements were made in the right-angle mode. Absolute fluorescence quantum yields were determined as previously reported.[3] Fluorescence decay lifetimes were measured with a modified TRW nanosecond spectral source system.

The esters were synthesized according to the method of Parish and Stock with prepurified 9-anthroic acid.[5] The melting points of the esters are tabulated in Table I. 9-Anthramide was prepared by the basic hydrolysis of 9-cyanoanthracene in 90% yield.[6] Recrystallization from benzene gave yellow needles, mp 219–219.5°C.

Preparative and Quantitative Photolysis. Preparative photolysis were performed using either a standard 450-W Hanovia immersion photolysis system (available from Ace Glass) with a uranium glass filter or with a 34-ml quartz cylindrical cell on the optical bench used for quantum yield studies.

After irradiation of the 9-substituted anthracene derivatives in 95% ethanol, benzene, or tetrahydrofuran, the dimer precipitates were removed by filtration. The filtrate was evaporated and the resulting residue was extracted with ether. Any remaining solid was combined with the dimer separated previously. The ether solution was examined via thin layer chromatography (silica gel) with at least two solvent systems for possible products other than the dimer. For all 9-anthroate esters studied, only the unreacted monomer was detected in the ether solution. The ether was then removed, and the amount of monomer recovered weighed. For the 9-anthramide a very small amount of an unidentified product was obtained. The results of the photolyses are summarized in Table I.

Quantitative irradiations were carried out on an optical bench consisting of a 4-in. spherical mirror, 1-kW high-pressure mercury–xenon short arc lamp (Hanovia 977-B-1), 2-mm aperture, and 4-in. biconvex quartz collimating lens.[6] The collimated light was filtered via two Corning filters (CS-7-37 and CS-0-52) to isolate the Hg 3650-Å lines. The light then passed through the aperture of a cell holder designed to accommodate 2-cm diameter cylindrical quartz cells. All solutions were preflushed with nitrogen for 15 min, sealed under a positive nitrogen pressure, and stirred using a magnetic stirrer during irradiation. The light intensity was frequently determined using ferrioxalate actinometry. Relative light intensities were monitored before

and after each irradiation by means of a RCA-935 phototube, 120 V battery, microammeter combination. Concentration changes on irradiation were determined by comparing two spectrophotometric solutions of equally diluted, equal volume aliquots of irradiated and unirradiated solution. The quantum yield of dimerization was computed from the disappearance quantum yield. $\Phi_{DIM} = 0.5\Phi_{DIS}$. The extent of photoreaction was limited to 10% monomer disappearance in most cases.

Results and Discussion

Absorption and Fluorescence Spectra. All of the esters of 9-anthroic acid and the 9-anthramide have uv absorption spectra almost identical with the acid, and very similar to anthracene. Figures 1 and 2 present the absorption and emission spectra of a typical anthroate ester and 9-anthramide. Werner and Hercules suggest that the steric interaction of the peri hydrogens and carboxyl group keep the 9 substituent twisted almost 90° out of the place of the anthracene ring and thus preclude extensive conjugation of the carboxyl group and the anthracene π electrons in the ground state. This means that the exciting light used in these dimerization studies (365 nm) is absorbed by an anthracene-like $A \rightarrow {}^1L_a$ transition. The emission spectra of the anthroates consist of Stokes shifted broad structureless bands.

The drastic geometry change in the first excited state required to explain the large Stokes shift is most likely due to rotation of the carboxyl group in the excited state to a geometry suitable for charge transfer interaction with anthracene ring.[7] It is interesting to note, however, that the size of the ester alkyl group has little effect on the extent of the Stokes shift (Me = 5.70×10^3 cm^{-1}; tBu = 5.20×10^3 cm^{-1}).

In contrast to the esters and acid, the sodium 9-anthroate[3] and 9-anthramide (see Figure 2) in polar solvents have a good mirror image relationship between the absorption and fluorescence spectra. The 9-anthramide in benzene exhibits a small Stokes shift (7.9×10^2 cm^{-1}) and some broadening of the vibronic transitions.

Fluorescence quantum yields and singlet lifetimes are summarized in Table II. All measurements were made using 10^{-5} to 10^{-6} M degassed solutions at room temperature.

The reciprocal of the measured fluorescence lifetime (τ_F)
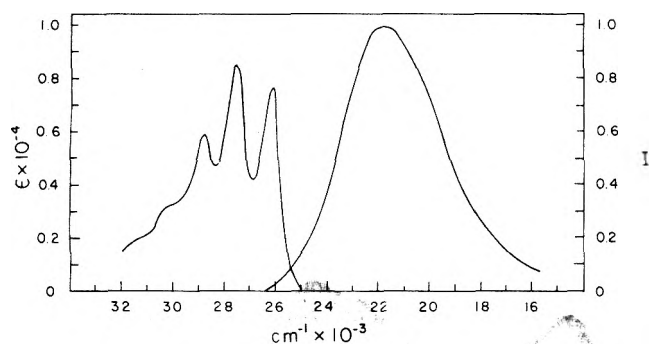
Figure 1. Absorption and fluorescence spectra of cyclohexyl 9-anthroate in benzene.
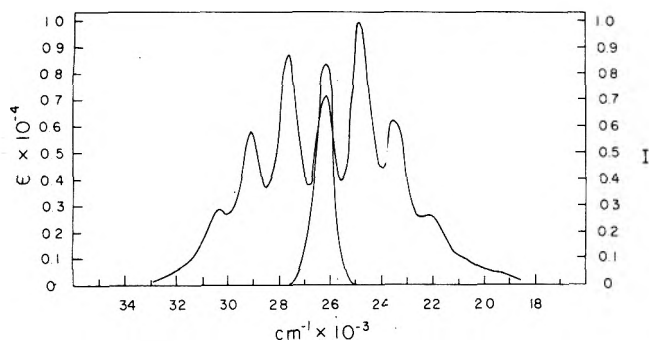
Figure 2. Absorption and fluorescence spectra of 9-anthramide in tetrahydrofuran.

gives the sum of all first-order singlet rate constants

$$\tau_F = 1/(k_{ISC} + k_{IC} + k_F) \tag{1}$$

where k_{ISC}, k_{IC}, and k_F are defined by equations in Chart I. The fluorescence quantum yields at low concentration can be used to calculate the fluorescence rate constant (k_F).

$$\Phi_F^0 = k_F/(k_{ISC} + k_{IC} + k_F) \tag{2}$$

$$k_F = \Phi_F^0/\tau_F \tag{3}$$

Dimerization Quantum Yields. The low-conversion quantum yield of dimerization as a function of concentration was determined using 365-nm exciting radiation. The results are presented graphically in Figures 3–5 and the slope and intercept values are collected in Table III. All of the quantitative photodimerizations were performed using solutions whose concentrations were lower than 0.03 *M*. Because of the extremely low solubilities of 9-anthramide in both benzene and 95% ethanol quantitative photolysis were performed in tetrahydrofuran as well as benzene. The simplest mechanism consistent with these results is shown in Chart I. All intercepts from the 1/Φ_D vs. 1/[A] plots are greater than unity and thus suggest that some bimolecular process or processes other than dimerization are important. The nature of this process, conveniently termed concentra-

Chart I

$$A + h\nu \rightarrow A^s \tag{4}$$
$$A^s \rightarrow A + h\nu \quad k_F \tag{5}$$
$$A^s \rightarrow A \quad k_{IC} \tag{6}$$
$$A^s \rightarrow A^t \quad k_{ISC} \tag{7}$$
$$A^s + A \rightarrow dimer \quad k_D \tag{8}$$
$$A^s + A \rightarrow 2A \quad k_{CQ} \tag{9}$$
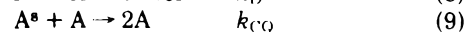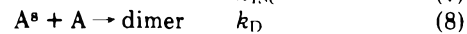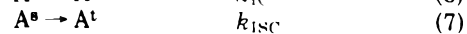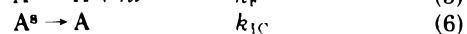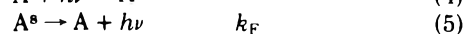
$$1/\Phi_D = (k_D + k_{CQ})/k_D + (k_F + k_{ISC} + k_{IC})/(k_D[A]) \tag{10}$$

TABLE II: Lifetime Measurements, Quantum Yield of Fluorescence, and First Order Rate Constants of 9-Anthroate Esters and 9-Anthramide

Compound	τ_F, nsec	Φ_F^0	k_F, $\times 10^{-7}$ sec^{-1}	$(k_{ISC} + k_{IC})$, $\times 10^{-7}$ sec^{-1}
In Alcohol				
(1) Methyl ester	4.1	0.165	4.02	20.3
(2) Ethyl ester	4.2	0.188	4.48	19.3
(3) *n*-Butyl ester	3.6	0.172	4.78	23.0
(4) *tert*-Butyl ester	4.1	0.183	4.46	19.9
(5) Cyclohexyl ester	4.7	0.195	4.15	17.1
(6) 9-Anthramide	2.5	0.100	4.0C	36.0
In Benzene				
(-) Anthracene	4.15	0.28	6.75	17.4
(2) Ethyl ester	12.9	0.585	4.54	3.22
(5) Cyclohexyl	11.8	0.669	5.67	2.80
(6) 9-Anthramide	8.0	0.172	2.15	10.4
In Tetrahydrofuran				
(6) 9-Anthramide	1.7	0.353	20.7	38.1
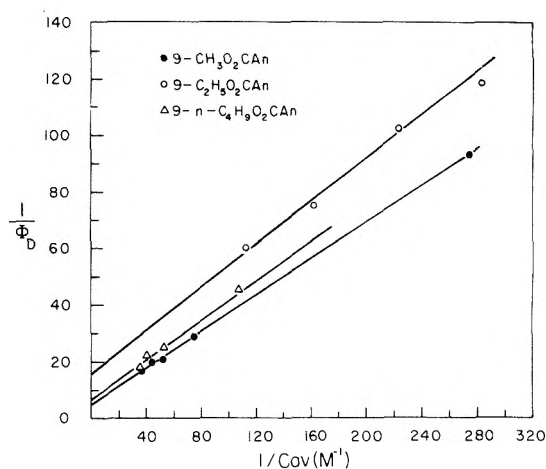
Figure 3. Reciprocal graph of dimerization quantum yield and concentration for methyl, ethyl, and *n*-butyl 9-anthroates in 95% ethyl alcohol.

tion quenching, has been discussed at length by Cowan and Schmiegel.[3] The two most attractive possibilities are the formation of a nonfluorescent excimer or the formation of a σ-bonded complex with a geometry such that head-to-tail dimer formation cannot occur. Other more complex mechanisms will be considered later.

Fluorescence Intensity as a Function of Concentration. The intensity of fluorescence, which is proportional to the fluorescence quantum yield, was measured as a function of substituted anthracene concentration over the concentration range used in the dimerization studies via front surface fluorescence excitation. Typical graphs of 1/I_F vs. [A] are given in Figures 6 and 7 and the slopes and intercepts obtained from the least-squares treatment of the data are given in Table IV. Based on the mechanism given in Chart I, the fluorescence quantum yield should follow the relationship given by

$$1/\Phi_F = (k_F + k_{ISC} + k_{IC})/k_F + (k_D + k_{CQ})/(k_F)[A] \tag{11}$$

TABLE III: Graphical Solutions[a] of the Photodimerization Plot $1/\Phi_D$ vs. $1/C_{av}$

Compound	Solvent	Slope (S_D)	Intercept (I_D)
(1) Methyl ester	Alcohol	0.330	4.52
(2) Ethyl ester	Alcohol	0.379	16.3
(2) Ethyl ester	Benzene	0.180	5.0
(3) n-Butyl ester	Alcohol	0.358	6.01
(4) tert-Butyl ester	Alcohol	0.322	6.45
(5) Cyclohexyl ester	Alcohol	0.338	8.89
(5) Cyclohexyl ester	Benzene	0.160	11.28
(6) 9-Anthramide	Benzene	0.164	2.5
(6) 9-Anthramide	THF	0.411	12.0

[a] All data except those for the ethyl ester are least-squares fit slopes and intercepts. Average error is ±0.3 in intercepts, and ±5% in slopes.
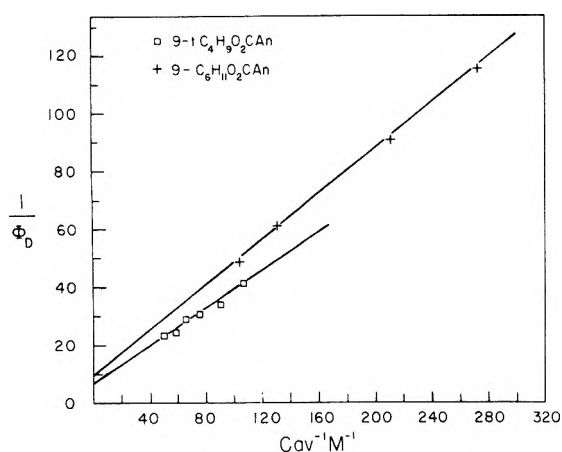
Figure 4. Reciprocal graph of dimerization quantum yield and concentration for *tert*-butyl and cyclohexyl 9-anthroates in 95% ethyl alcohol.
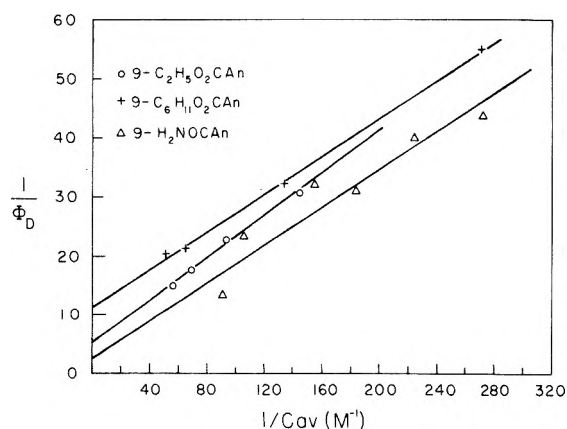
Figure 5. Reciprocal graph of dimerization quantum yield and concentration for ethyl and cyclohexyl 9-anthroates and 9-anthramide in benzene.

It is possible to calculate from fluorescence data ($k_D + k_{CQ}$) by combining the slope of eq 11 (S_F) with the fluorescence lifetime τ_F and the fluorescence quantum yield at low dilution Φ_F^0.

$$(k_D + k_{CQ}) = S_F \Phi_F^0 / \tau_F \qquad (12)$$

The values calculated by this procedure can be compared

with those calculated from the dimerization data using (see Table V)

$$(k_D + k_{CQ}) = I_D / \tau_F S_D \qquad (13)$$

Even though the values of ($k_D + k_{CQ}$) derived from the fluorescence data are much less accurate than those derived from the dimerization data the good quantitative relationship between fluorescence and dimerization data suggests that dimerization from the triplet state can be ruled out as can any mixed dimerization (from the singlet and triplet states).

The specific rate constants for the reactions shown in Chart I can be easily extracted from the data (eq 3, 14, 15, and 16). The specific rate constants based on this mechanism are summarized in Table VI along with values from the literature for related dimerizations.

$$k_{ISC} + k_{IC} = 1/\tau_F - k_F \qquad (14)$$

$$k_D = 1/S_D \tau_F \qquad (15)$$

$$k_{CQ} = (I_D - 1)k_D \qquad (16)$$

The available evidence from photooxidation studies indicates that most, if not all, of the first-order nonradiative decay arises from intersystem crossing. This coupled with the fact that the second triplet level is almost isoenergetic with the first singlet level of anthracene provides a ready explanation for the decrease in the first-order nonradiative rate constants ($k_{ISC} + k_{IC}$) for the Stokes shifted anthracenes (9-anthroic acid and esters) relative to sodium 9-anthroate, 9-anthramide, and anthracene.

We have previously suggested that because of the large Stokes shift, the relaxed singlet state (fluorescent state) of some anthracene derivatives could lie slightly below or at the same level as the second triplet. This should reduce the magnitude of the intersystem crossing rate constant:

		$(k_{ISC} + k_{IC})$
small Stokes shifts	9-anthramide (THF)	$= 37.9 \times 10^7$ sec^{-1}
	sodium 9-anthroate (H$_2$O)	$= 62.1 \times 10^7$ sec^{-1}
large Stokes shifts	9-anthroate esters (ETOH)	$17-23 \times 10^7$ sec^{-1}
	9-anthroic acid (ETOH)	17.2×10^7 sec^{-1}
	9-anthroic acid (PhCN)	2.88×10^7 sec^{-1}

9-Anthramide is particularly interesting because the Stokes shift is very solvent dependent (THF, 1.4×10^2 cm^{-1}; EtOH, 5.4×10^2 cm^{-1}; benzene, 7.9×10^2 cm^{-1}). As could be expected from the previous discussion, the nonradiative rate constants for 9-anthramide in tetrahydrofuran, ethanol, and benzene decrease with increasing Stokes shift (THF, 37.9×10^7 sec^{-1}; EtOH, 36.2×10^7 sec^{-1}; benzene, 10.4×10^7 sec^{-1}).

It is interesting to note that, with the exception of ethyl 9-anthroate, all of the 9-anthroate esters (methyl, n-butyl, tert-butyl, and cyclohexyl) exhibit the same dimerization plot slopes within the error limits of our experiments ($S_D = 0.34 \pm 0.02$). This combined with eq 15 and lifetimes in Table II suggest that the specific rate constants for dimeri-

TABLE IV: Graphical Solutions of Concentration Dependence of Fluorescence

	Relative values		Absolute values[a,b]	
	Slope	Intercept		
Compound	(A)	(B)	$(1/\Phi_F{}^0)$	S_F
a. Alcohol Solutions				
(1) Methyl ester	229.1	16.45	6.06	84.41
(3) n-Butyl ester	227.9	13.80	5.81	95.93
(4) tert-Butyl ester	191.43	11.97	5.46	81.81
b. Benzene Solutions				
(2) Ethyl ester	325	11.25	1.709	49.36
(5) Cyclohexyl ester	670	12.0	1.495	83.75
(6) 9-Anthramide	482.0	30.14	5.81	93.23

[a] $(\Phi_F{}^0)$ is the measured fluorescence quantum yield at low dilution. [b] $S_F = A/(\Phi_F{}^0 B)$.
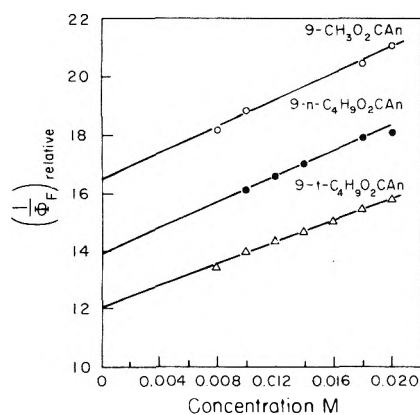
Figure 6. Concentration dependence of reciprocal fluorescence intensity of methyl, n-butyl, and tert-butyl 9-anthroates in 95% ethyl alcohol.
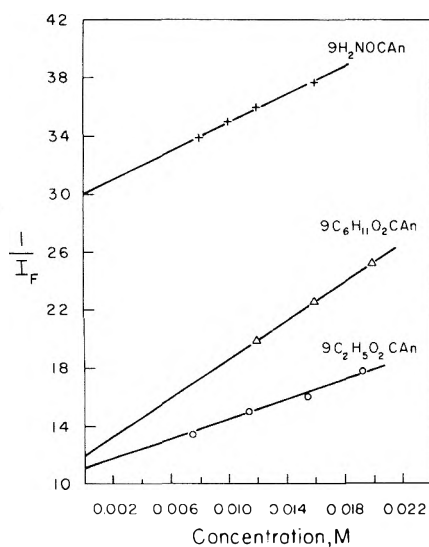
Figure 7. Concentration dependence of reciprocal fluorescence intensity of ethyl and cyclohexyl 9-anthroates and 9-anthramide in benzene.

zation do not vary greatly as the 9-anthroate ester is modified. (See Table VI.) The intercepts of the dimerization plots for the 9-anthroate esters do show a regular trend, again with the exception of the ethyl ester where the data

TABLE V: Comparison of Data from Fluorescence and Photodimerization Studies

Compound	Fluorescence data $(k_D + k_{CQ}) \times 10^{-9} M^{-1} sec^{-1}$ (eq 12)	Dimerization data $(k_D + k_{CQ}) \times 10^{-9} M^{-1} sec^{-1}$ (eq 13)
(1) Methyl ester[a]	3.4	3.34
(2) Ethyl ester[a]		10.24
(2) Ethyl ester[b]	2.24	2.15
(3) n-Butyl ester[a]	4.58	4.66
(4) tert-Butyl ester[a]	3.65	4.89
(5) Cyclohexyl ester[a]		5.60
(5) Cyclohexyl ester[b]	4.75	5.97
(6) 9-Anthramide[b]	2.00	1.91
(6) 9-Anthramide[c]		17.17

[a] In 95% ethanol. [b] In benzene. [c] In tetrahydrofuran.

Chart II

$A + h\nu \rightarrow A^s$		(4)
$A^s \rightarrow A + h\nu$	k_F	(5)
$A^s \rightarrow A$	k_{IC}	(6)
$A^s \rightarrow A^t$	k_{ISC}	(7)
$A^s + A \rightarrow E$	k_E	(15)
$E \rightarrow$ dimer	k_D'	(16)
$E \rightarrow 2A$	k_{CQ}'	(17)
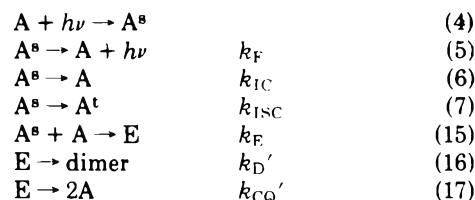
are somewhat less precise. (I_D, Me = 4.5; n-butyl = 6.0; tert-butyl = 6.45; cyclohexyl = 8.89.) Based on the mechanism in Chart I this indicates that the percentage of dimerization, compared to dimerization and concentration quenching, varies from 22 to 11%; decreasing with increasing steric bulk.

Based on the excimer mechanism to be described later (Chart II), this would indicate there is a steric effect on how the excimer decays (eq 16 and 17).

Excimer Mechanism. Chart II gives one of two possible excimer mechanism to be considered.

This mechanism is more costly in the sense that another intermediate, the excimer (E), is involved for which there is no direct evidence. That is, no new excimer fluorescence was observed under the conditions used in this study. However, anthracene and some 9-substituted anthracenes do exhibit excimer fluorescence and it is certainly possible that a nonfluorescent excimer could be the reactive intermediate in this reaction.[10,11] Based on the mechanism given in Chart II, the following expressions can be obtained.

$$1/\Phi_D = \frac{(k_D' + k_{CQ}')}{k_D'} + \frac{(k_D' + k_{CQ}')(k_{ISC} + k_{IC} + k_F)}{k_E k_D'[A]} \quad (18)$$

$$1/\Phi_F = \frac{1}{\Phi_F{}^0} + \frac{k_E[A]}{k_F} \quad (19)$$

consequently

$$k_E = I_D/(S_D \tau_F) \quad (20)$$

$$k_E = S_F \Phi_F{}^0 \tau_F \quad (21)$$

Equations 18 and 19 and the mechanism outlined in Chart II are consistent with the experimental observations. From eq 20 and 21 it is seen that $k_{CQ} + k_D$ in mechanism I

TABLE VI: Derived Rate Constants

Compound	First order, $sec^{-1} \times 10^{-7}$		Second order, $M^{-1} sec^{-1} \times 10^{-9}$		
	k_F	$(k_{ISC} + k_{IC})$	k_D	k_{CQ}	$k_D + k_{CQ}$
In 95% Ethanol					
(−) 9-MeAn[a]	5.56	8.8	2.00	8.5	10.5
(−) 9-EtAn[a]	5.85	9.6	0.646	6.43	7.08
(−) 9-n-PrAn[a]	5.68	9.2	0.364	6.34	6.7
(−) 9-HO_2C An[b]	4.78	17.2	1.02	4.28	5.30
(1) 9-MeO_2C An[c]	4.02	20.3	0.738	2.60	3.34
(2) 9-EtO_2C An[c]	4.48	19.3	0.63	9.61	10.24
(3) 9-n-BuO_2C An[c]	4.78	23.0	0.776	3.89	4.66
(4) 9-t-BuO_2C An[c]	4.46	19.9	0.76	4.13	4.89
(5) 9-Cyclohexyl O_2C An[c]	4.15	17.1	0.63	4.97	5.60
(6) 9-Anthramide[c]	4.00	36.0			
In Benzene					
(−) Anthracene[d]	7.4	24.0	1.0	4.0	5.0
(2) 9-EtO_2C An[c]	4.54	3.22	0.431	1.72	2.15
(5) 9-Cyclohexyl O_2C An[c]	5.67	2.80	0.53	5.44	5.97
(6) 9-Anthramide[c]	2.15	10.4	0.761	1.14	1.90
In THF					
(6) 9-Anthramide[c]	20.7	38.1	1.43	15.7	17.1

[a] From ref 8. [b] From ref 3. [c] This study. [d] From ref 9, the values of k_F and $(k_{ISC} + k_{IC})$ are somewhat larger than those given in Table II.

is equivalent to k_E in mechanism II. The method used to calculate k_D (mechanism I) when applied to mechanism II gives a complex rate ratio (see eq 15 and 22)

$$1/(S_D\tau_F) = (k_E k_D')/(k_D + k_{CQ}') \quad (22)$$

If the dissociative regeneration of the excited anthracene molecule is included in the excimer mode of decomposition (eq 23), the dimerization quantum yield will still have the same functional form (eq 24)

$$E \rightarrow A^s + A \qquad k_{-E} \quad (23)$$

$$1/\Phi_D = \frac{k_D' + k_{CQ}'}{k_D'} + \frac{(k_{-E} + k_D' + k_{CQ}')(k_F + k_{IC} + k_{ISC})}{k_E k_D'[A]} \quad (24)$$

where now $I_D/(S_D\tau_F)$ gives the rate constant for excimer formation reduced by a fraction that depends upon the importance of the excimer dissociation (eq 23).

$$I_D/(S_D\tau_F) = k_E \left| \frac{(k_D' + k_{CQ}')}{(k_{-E} + k_D' + k_{CQ}')} \right| \quad (25)$$

In both the excimer mechanisms the reciprocal of the intercept gives the fraction of the excimers that decay to dimer products.

A number of recent studies suggest that exciplexes from anthracene and either tertiary amines[12-14] or 1,3-dienes[15-17] can act as intermediates in the anthracene dimerization reaction.

$$A^s + X \rightarrow [A^sX] \quad (26)$$

$$[A^sX] + A \rightarrow dimer + X \quad (27)$$

$$[A^sX] + A \rightarrow 2A + X \quad (28)$$

or

$$[A^sX] + A \leftarrow \rightarrow [A^sA] + X \quad (29)$$

$$[A^sA] \rightarrow dimer \quad (30)$$

$$[A^sA] \rightarrow 2A \quad (31)$$
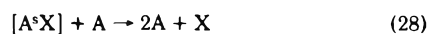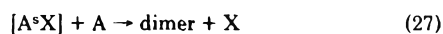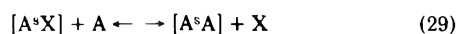
where X = 1,3-diene or amine.

Flash photolysis experiments and temperature quantum yield studies are in progress in an attempt to confirm or reject the excimer mechanisms for the anthracene type dimerization.

References and Notes

(1) Photochemical Reactions XIII, for part XII see D. O. Cowan and J. C. Koziar, *J. Am. Chem. Soc.*, **97**, 249 (1975).
(2) E. I. duPont de Nemours and Co., Inc., Wilmington, Del.
(3) D. O. Cowan and W. W. Schmiegel, *J. Am. Chem. Soc.*, **94**, 6779 (1972); *Angew. Chem.*, **83**, 545 (1971); *Angew. Chem., Intl. Edit.*, **10**, 517 (1971).
(4) For a review of the photodimerization of anthracene and its derivatives, see D. O. Cowan and R. Drisko, "Elements of Organic Photochemistry", Plenum Press, New York, N.Y., Chapter 2, 1975.
(5) R. C. Parish and M. Stock, *J. Org. Chem.*, **30**, 927 (1965).
(6) D. O. Cowan and A. A. Baum, *J. Am. Chem. Soc.*, **93**, 1153 (1971).
(7) (a) T. C. Werner and D. M. Hercules, *J. Phys. Chem.*, **73**, 2005 (1969); (b) *ibid*, **74**, 1030 (1970).
(8) A. S. Cherkasov and T. M. Vember, *Opt. Spectrosc. (USSR)*, **6**, 319 (1959).
(9) R. Livingston in "Photochemistry in the Liquid and Solid States", F. Daniels, Ed., Wiley, New York, N.Y., 1960, p 76.
(10) J. B. Birks and J. B. Aladekomo, *Photochem. Photobiol.*, **2**, 415 (1963).
(11) J. B. Birks, "Photophysics of Aromatic Molecules", Wiley-Interscience, New York, N.Y., 1970.
(12) C. Pac and H. Sakurai, *Tetrahedron Lett.*, 3829 (1969).
(13) R. S. Davidson, *Chem. Commun.*, 1450 (1969).
(14) (a) N. C. Yang and J. Libman, *J. Am. Chem. Soc.*, **95**, 5793 (1973); (b) N. C. Yang and D. M. Shold, *ibid.*, in press.
(15) R. O. Campbell and R. S. A. Liu, *Chem. Commun.*, 1191 (1970).
(16) J. Saltiel and D. E. Townsend, *J. Am. Chem. Soc.*, **95**, 6140 (1973).
(17) I. Bronstein and D. O. Cowan, unpublished observations.

Competitive Free-Electron Scavenging in Liquid Neopentane

Kazuo Mori, Kenji Ito, and Yoshihiko Hatano*

Laboratory of Physical Chemistry, Tokyo Institute of Technology, Meguro-ku, Tokyo 152, Japan (Received April 23, 1975)

The competitive free-electron scavenging of N_2O with various electron scavengers has been studied in the radiolysis of liquid neopentane. The ratio of scavenging rate constant $k(s)$ of a scavenger s to $k(N_2O)$ has been determined by measuring the decreases of $G(N_2)$ upon the addition of s to neopentane solutions of N_2O. These are $k(CCl_4)/k(N_2O) = 31$, $k(CH_3Br)/k(N_2O) = 5$, $k(C_2H_5Br)/k(N_2O) = 0.6$, and $k(biphenyl)/k(N_2O) \simeq 0$. The value of $k(CH_3I)/k(N_2O)$ apparently depends upon the concentration of CH_3I. The possibility of the negative charge transfer from N_2O^- to s has also been discussed. The result shows the scavenging rate to be largely dependent upon the scavenger s, which could not be found in cyclohexane. It seems to indicate that in liquid neopentane the free-electron scavenging process may not necessarily be explained in terms of diffusion kinetics.

Introduction

In recent years, the behavior of electrons in nonpolar liquid has received considerable attention in radiation chemistry. With regard to the electron scavenging process in liquid hydrocarbons, the investigations of cyclohexane and n-hexane were made both experimentally[1] and theoretically.[2] Recently, branched hydrocarbons have also been studied. In neopentane, at lower concentrations of N_2O, $G(N_2)$ gives a constant value of 1.1 ± 0.1[3,4] which is in good agreement with the free-ion yield obtained by the electric conductivity method.[5] This indicates that, at low concentrations of N_2O, $G(N_2)$ arises from the complete scavenging of free electrons. On the basis of the above-mentioned facts, we have already reported[4] a competitive free-electron scavenging study of N_2O with SF_6, CH_3Cl, and CO_2 in liquid neopentane and have indicated[4] for the first time that free-electron scavenging rate constants vary drastically depending upon solutes, which could not be found in cyclohexane.[1] Thus we pointed out that the reaction of free electrons in liquid neopentane cannot be explained by diffusion kinetics. Allen and Holroyd measured[6] free-electron scavenging rate constants in various nonpolar liquids by the electric conductivity method, and also indicated[7] that the rate constants in branched hydrocarbons or in tetramethylsilane are largely dependent upon scavengers.

In this paper, in order to confirm the difference[4] between the behavior of electrons in neopentane and that in cyclohexane, the competitive free-electron scavenging study of N_2O with CCl_4, CH_3Br, C_2H_5Br, CH_3I, and biphenyl in liquid neopentane is reported.

Experimental Section

Neopentane was a Phillips research grade material. Impurities of less than 0.07%, almost all of which was n-butane, were detected by gas chromatography using an activated aluminum column operated at 60°. Nitrous oxide supplied by Takachiho Shoji Co. was thoroughly degassed and stored under vacuum through a −120° cold trap. All the additives except for biphenyl were used after the usual degassing. A given amount of (ca. 10 ml) neopentane was transferred into a tube containing a liquid Na–K alloy distilled in vacuo[8] and was stored for more than 1 week. The dried sample was transferred in vacuo into an irradiation cell, fitted with a break seal, which was baked beforehand

under vacuum. The dead space over the solutions was, at the most, 10% of the total volume.

Biphenyl solutions of neopentane were prepared as described below. Biphenyl was introduced into an irradiation cell as a n-hexane solution of biphenyl, whose concentration was known beforehand, and then n-hexane was removed in vacuo until the measured vapor pressure showed $\sim10^{-2}$ Torr which is the vapor pressure of biphenyl at room temperature. A known amount of the purified neopentane was introduced into the irradiation cell containing the biphenyl stated above. The concentration of biphenyl in the neopentane was confirmed by measuring the optical absorption spectrum[9] of biphenyl in neopentane. The error in concentration was estimated to be less than 5%. It was shown by gas chromatography that only 0.005% of n-hexane was contained in biphenyl–N_2O solutions of neopentane prepared in a way described above.

The concentration of N_2O at room temperature was calculated by using the Ostwald absorption coefficient of 3.[10] The other additives were assumed to be dissolved completely. The temperatures during the γ irradiation of the samples were 20~23° for CCl_4, 23~24° for CH_3Br and C_2H_5Br, and 19° for CH_3I and biphenyl, respectively. The dose rate was $1.03~0.87 \times 10^{17}$ eV/g min, and the total dose was $3.09~2.61 \times 10^{18}$ eV/g. In calculating the dose, $G(Fe^{3+}) = 15.6$ was used in Fricke dosimetry. The product N_2 was analyzed by gas chromatography using a 6 m molecular sieve 5 A column at 40° with helium carrier gas.

Results and Discussion

The γ radiolysis of liquid neopentane containing N_2O gives, as previously reported,[3,4] a constant $G(N_2) = 1.1 \pm 0.1$ at 293 ± 1 K, where the range of concentrations of N_2O was $10^{-6} M \leq [N_2O] \leq 10^{-3} M$. This constant value is in good agreement with the free-ion yield resulting from the electric conductivity method[5] $(G_{fi} = 1.09$ at 294 K). Therefore it may be concluded that in neopentane $G(N_2)$ arises from the complete scavenging of free electrons at $10^{-6} M \leq [N_2O] \leq 10^{-3} M$ and that, at such low concentrations of N_2O, one N_2 molecule is produced per electron scavenged by N_2O. Using this result one can estimate the ratio of the free-electron scavenging rate constant of various solutes to that of N_2O;[4] the ratio $k(SF_6)/k(N_2O)$ in neopentane is much larger than that in cyclohexane. The solutes CH_3Cl

and CO_2 are much more ineffective electron scavengers in neopentane than those in cyclohexane.

Figure 1 shows $G(N_2)$ at various concentrations of CCl_4 in liquid neopentane containing 3.4×10^{-4} M N_2O. The nitrogen yield decreases with an increase in the concentration of CCl_4 and attains nearly zero at a concentration equal to that of N_2O. Since, as was mentioned above, the precursor of the product N_2, at such low concentrations of N_2O, may be the free electron, the decrease of $G(N_2)$ upon the addition of CCl_4 is explained by the competitive free-electron scavenging of N_2O with CCl_4. A reaction mechanism concerning the free electron in this system may be considered as

$$RH \rightsquigarrow M^+ + e_{fi}^-$$

$$e_{fi}^- + N_2O \xrightarrow{k_1} N_2O^- \tag{1}$$

$$e_{fi}^- + CCl_4 \xrightarrow{k_2} CCl_4^- \tag{2}$$

$$N_2O^- + CCl_4 \xrightarrow{k_3} N_2O + CCl_4^- \tag{3}$$

$$N_2O^- \underset{\text{(RH or positive ions)}}{\xrightarrow{\tau^{-1}}} N_2 (+ OH^- \text{ or } OH) \tag{4}$$
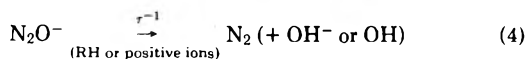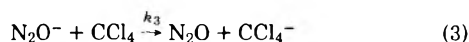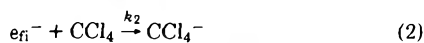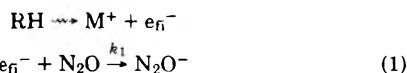
where RH, M^+, and e_{fi}^- represent the parent molecule of neopentane, positive ions produced from RH, and the free electron, respectively. This reaction scheme includes not only the competitive scavenging processes 1 and 2, which have been reported previously,[4] but negative charge transfer process 3. In process 4 N_2O^- may react with solvent molecule or with positive ions producing OH^- or OH, as was reported elsewhere.[3,8]

From a kinetic treatment of the above scheme one obtains

$$\frac{1}{G(N_2)} = \frac{1}{G_{fi}} \left(1 + \frac{k_2[CCl_4]}{k_1[N_2O]}\right) (1 + k_3\tau[CCl_4]) \tag{I}$$

The values of $G(N_2)^{-1}$ are plotted vs. $[CCl_4]$ in Figure 2 giving a linear relationship, which shows that, at such a low concentration of CCl_4 as $\sim 10^{-4}$ M, the negative-charge transfer reaction might be negligible. Taking 20 μsec as the lifetime of N_2O^-, which was obtained in liquid cyclohexane,[11] and assuming that k_3 is the order of diffusion-controlled reaction ($\sim 10^{10}$ M^{-1} sec^{-1}), one can estimate $k_3\tau[CCl_4]$ to be 20 at $[CCl_4] \simeq 10^{-4}$ M. Since, however, the result obtained here shows a good linear relationship, the term $k_3\tau[CCl_4]$ in eq I may be negligible. The lifetime of N_2O^- in neopentane seems to be shorter than 20 μsec in cyclohexane. Thus, $k_2/k_1 \simeq 31$ is obtained from the slope in Figure 2.

In the case of CH_3Br-N_2O and $C_2H_5Br-N_2O$ solutions of neopentane, similar treatment gives $k(CH_3Br)/k(N_2O) \simeq 5$ and $k(C_2H_5Br)/k(N_2O) \simeq 0.6$, respectively.

In the case of CH_3I-N_2O solutions (Figure 3), however, the plots of $G(N_2)^{-1}$ vs. $[CH_3I]$ do not give a good linear relationship. The reason for this result is not clear, but one can estimate $k(CH_3I)/k(N_2O) \simeq 80$ at lower concentrations of CH_3I ($<2 \times 10^{-5}$ M). The values of $k(CH_3I)/k(N_2O)$ decreases apparently with increasing the concentration of CH_3I.

In the case of biphenyl-N_2O solutions, $G(N_2)$ remains constant in the region of biphenyl concentrations from 3.9 $\times 10^{-4}$ to 2.0×10^{-3} M. Thus, $k(\text{biphenyl})/k(N_2O) \simeq 0$. Similar results have also been observed in the case of CO_2 and CH_3Cl.[4] This result indicates that in neopentane the scavenging rate constant of biphenyl is much smaller than
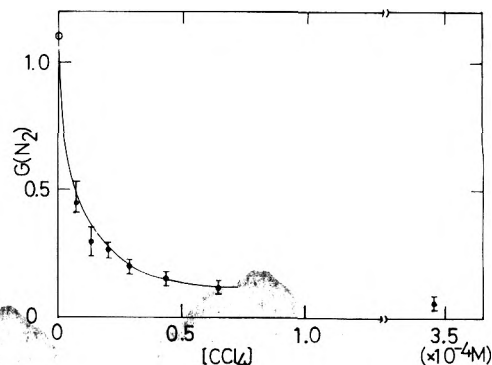
Figure 1. Nitrogen yield as a function of the concentration of CCl_4 at $[N_2O] = 3.4 \times 10^{-4}$ M.
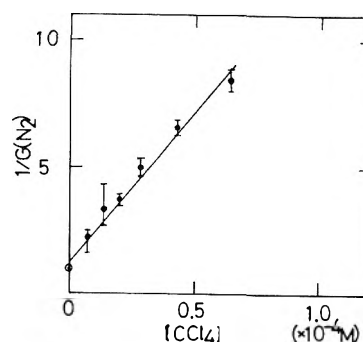
Figure 2. The reciprocal amount of the nitrogen yield as a function of the concentration of CCl_4 at $[N_2O] = 3.4 \times 10^{-4}$ M.
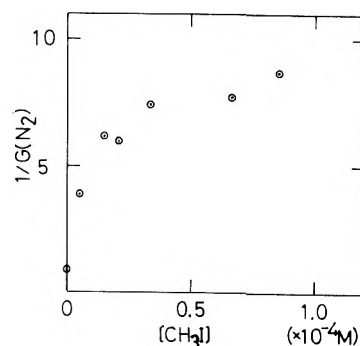
Figure 3. The reciprocal amount of the nitrogen yield as a function of the concentration of CH_3I at $[N_2O] = 3.4 \times 10^{-4}$ M.
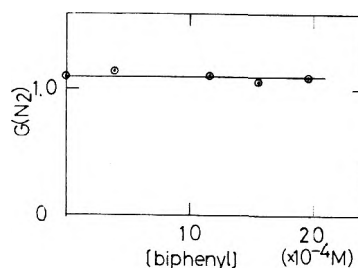
Figure 4. Nitrogen yield as a function of the concentration of biphenyl at $[N_2O] = 3.4 \times 10^{-4}$ M. $G(N_2)$ decreases at 0.4 at $[\text{biphenyl}] = 124 \times 10^{-4}$ M.

that expected[12] from the large electron mobility in neopentane.

Schuler et al.[13] obtained the efficiency of various electron scavengers in cyclohexane by the competitive electron

TABLE I: Summary of Relative Electron Rate Constants in Liquid Neopentane, Electron Scavenging Efficiencies in Liquid Cyclohexane and 2,2,4-Trimethylpentane, Electron Rate Constants in Neopentane, and "Thermal"[i] Electron Attachment Rate Constants in the Gas Phase

Scavenger	$k(s)/k(N_2O)$ in neopentane[a]	$\alpha(s)/\alpha(N_2O)$ in cyclohexane[c]	$\alpha(s)$ in 2,2,4-trimethyl-pentane[d]	$k(s)$ in neopentane,[e] $\times 10^{12}$ M^{-1} sec^{-1}	$k(e_{th}^-)$ in the gas phase, cm^3 molecule^{-1} sec^{-1}	
CCl$_4$	31	1.5		29	4.0×10^{-7}	f
SF$_6$	30	2	65	198	2.2×10^{-7}	g
CH$_3$I	b	2.8			2.5×10^{-8}	h
CH$_3$Br	5	2	24.7		7.0×10^{-12}	i
N$_2$O	1	1	6	2.3	1.2×10^{-13}	j
					6.0×10^{-15}	k
C$_2$H$_5$Br	0.6	1.3	5	0.34	2.8×10^{-13}	i
CH$_3$Cl	~0	0.6			$<1.9 \times 10^{-15}$	i
CO$_2$	~0	1.6		0.55		
Biphenyl	~0	2				

[a] This work and the previous one.[4] [b] See text. [c] Reference 13. [d] Reference 15. [e] Reference 7. [f] Reference 16. [g] Reference 17. [h] Reference 18. [i] Reference 19. [j] Reference 20. [k] Reference 21. [l] Reference 14.

scavenging with alkyl halides. On the basis of their results, $\alpha(CCl_4)/\alpha(N_2O) = 1.5$, $\alpha(CH_3Br)/\alpha(N_2O) = 2$, $\alpha(C_2H_5Br)/\alpha(N_2O) = 1.3$, $\alpha(CH_3I)/\alpha(N_2) = 2.8$, and $\alpha(biphenyl)/\alpha(N_2O) = 2$, where $\alpha(s)$ represents the scavenging efficiency of a scavenger s and is thought to be proportional to the scavenging rate constant. The values of $k(s)/k(N_2O)$ in neopentane obtained in this experiment and those reported previously,[4] and the values of $\alpha(s)/\alpha(N_2O)$ in cyclohexane obtained by Schuler et al.[13] are summarized in Table I. The values of $k(s)/k(N_2O)$ in neopentane exhibit a striking contrast to those of $\alpha(s)/\alpha(N_2O)$ in cyclohexane; $\alpha(s)$ in cyclohexane does not vary appreciably with electron scavengers, while $k(s)$ in neopentane varies markedly with electron scavengers.

Although the thermal electron attachment processes in the gas phase have not been fully investigated, we can tentatively compare our results with the rate constants of "thermal"[14] electron attachment in the gas phase, $k(e_{th}^-)$, cited in Table I. The relative values of $k(s)$ in neopentane seem rather to be qualitatively comparable with those of $k(e_{th}^-)$ in the gas phase.

Rzad and Bansal reported values of $\alpha(s)$ in liquid 2,2,4-trimethylpentane,[15] which are also cited in Table I. These values show a tendency similar to the values of $k(s)$ in neopentane, but the difference of $\alpha(s)$ between various scavengers in 2,2,4-trimethylpentane is not as large as that of $k(s)$ in neopentane. The results concerning these three liquid hydrocarbons indicate that electrons in 2,2,4-trimethylpentane show an intermediate property between those in cyclohexane and neopentane. Rzad and Bansal[15] introduced a parameter f in order to explain $\alpha(s)$ in 2,2,4-trimethylpentane, which shows a different tendency from $\alpha(s)$ in cyclohexane, but it is not obvious what the parameter f means.

Allen and Holroyd measured the rate constants of free electron scavenging in various liquids.[6,7] Their results, which are also cited in Table I, differ quantitatively from ours. This may be, to a certain extent, due to the difference of experimental methods. Further reason of this difference is not clear. Our results, however, are qualitatively consistent

with their results in neopentane; the scavenging rate constant in neopentane varies significantly with scavengers.

The result obtained here, the significant difference of the rate constant of free-electron scavenging between various electron scavengers in liquid neopentane, suggests that at least in the case of liquid neopentane a new theoretical approach taking account of the gaseous character of liquid neopentane as stated above should be introduced instead of diffusion kinetics[2] used in cyclohexane and n-hexane, where there is no appreciable difference in the electron-scavenging rate constant between various electron scavengers.

References and Notes

(1) See, for example, J. M. Warman, K.-D. Asmus, and R. H. Schuler, *Adv. Chem. Ser.*, **No. 82**, 25 (1968), and references cited therein.
(2) See, for example, A. Mozumder, *Adv. Radiat. Chem.*, **1**, 1 (1969); J. P. Dodelet and G. R. Freeman, *Can. J. Chem.*, **49**, 2643 (1971); G. R. Freeman, *Int. J. Radiat. Phys. Chem.*, **4**, 237 (1972).
(3) Y. Hatano, K. Ito, and S. Takao, *Int. J. Radiat. Phys. Chem.*, **7**, 39 (1975).
(4) K. Ito and Y. Hatano, *J. Phys. Chem.*, **78**, 853 (1974).
(5) J.-P. Dodelet and G. R. Freeman, *Can. J. Chem.*, **50**, 2667 (1972).
(6) A. O. Allen and R. A. Holroyd, *J. Phys. Chem.*, **78**, 796 (1974).
(7) (a) A. O. Allen, T. E. Gangwer, and R. A. Holroyd, *J. Phys. Chem.*, **79**, 25 (1975); (b) A. O. Allen, T. E. Gangwer, and R. A. Holroyd, *Chem. Phys. Lett.*, **31**, 520 (1975).
(8) Y. Hatano, K. Takeuchi, and S. Takao, *J. Phys. Chem.*, **77**, 586 (1973).
(9) H. Suzuki, *Bull. Chem. Soc. Jpn.*, **32**, 1340 (1959).
(10) K. Horacek and G. R. Freeman, *J. Chem. Phys.*, **53**, 4486 (1970).
(11) F. S. Dainton, P. O'Neil, and G. A. Samson, *J. Chem. Soc., Chem. Commun.*, 1001 (1972).
(12) G. Beck and J. K. Thomas, *J. Chem. Phys.*, **57**, 3649 (1972).
(13) G. W. Klein and R. H. Schuler, *J. Phys. Chem.*, **77**, 978 (1973), and references therein.
(14) The values of $k(e_{th}^-)$ cited in Table I appear not to be necessarily concerned with completely thermalized electrons.
(15) S. J. Rzad and K. M. Bansal, *J. Phys. Chem.*, **76**, 2374 (1972).
(16) J. M. Warman and M. C. Sauer, Jr., *J. Chem. Phys.*, **52**, 6428 (1970).
(17) R. W. Fessenden and K. M. Bansal, *J. Chem. Phys.*, **53**, 3468 (1970).
(18) R. P. Blaunstein and L. G. Christophorou, *J. Chem. Phys.*, **49**, 1526 (1968).
(19) K. M. Bansal and R. W. Fessenden, *Chem. Phys. Lett.*, **15**, 21 (1972).
(20) R. V. Schindler, *Prog. Prob. Contemp. Radiat. Chem., Proc. Czech. Annu. Meet. Radiat. Chem., 10th, 1970*, **1**, 125 (1971).
(21) J. M. Warman, R. W. Fessenden, and G. Bakale, *J. Chem. Phys.*, **57**, 2702 (1972).

Kinetics of the Oxidation of Sulfite by Hydrogen Peroxide in Acidic Solution

M. R. Hoffmann*

W. M. Keck Laboratories, California Institute of Technology, Pasadena, California 91125

and J. O. Edwards

Department of Chemistry, Brown University, Providence, Rhode Island 02912 (Received November 18, 1974; Revised Manuscript Received June 13, 1975)

The kinetics of the oxidation of sulfite by hydrogen peroxide has been investigated by stopped–flow spectrophotometry over the pH range 4–8. The rate law for the oxidation of sulfite in this pH range is $-d[SO_2]_T/dt = k[H^+][H_2O_2][SO_2]_T\{[H^+]/([H^+] + Ka_2)\} + k'[HA][H_2O_2][SO_2]_T\{[H^+]/([H^+] + Ka_2)\}$ where HA represents all possible proton donors in solution. The reaction probably proceeds via a nucleophilic displacement by H_2O_2 on HSO_3^- to form a peroxomonosulfurous acid intermediate which then undergoes a rate-determining rearrangement.

Control of sulfur dioxide produced in the burning of fossil fuels, in chemical manufacturing, and in paper-pulp processing is presently of great concern. With these environmental considerations in mind, we wish to report the preliminary results of a kinetic study of the oxidation of sulfite in acidic solution by hydrogen peroxide.

Sulfur dioxide is readily soluble in water and the resulting equilibrium relationship is normally written as[1]

$$SO_2 + H_2O \underset{k_2}{\overset{k_1}{\rightleftharpoons}} H^+ + HSO_3^- \tag{1}$$
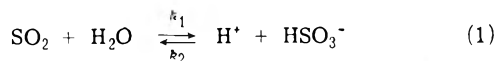
where at 20° and $\mu = 0.1$, $k_1 = 3.4 \times 10^6 \ sec^{-1}$ and $k_2 = 2 \times 10^8 \ M^{-1} \ sec^{-1}$ as determined by ultrasonic absorption. In the present study the reaction between SO_3^{2-} and H_2O_2 was examined in the pH range 8–4. In this range ($pKa_1 = 1.37$, $pKa_2 = 7.0$, $\mu = 0.9$),[2] as the pH decreases, the fraction of total sulfite present as HSO_3^- increases so that at pH 4 the bisulfite ion is the predominant sulfite species in solution. Previous stoichiometric measurements[3–5] have shown that the primary oxidation product is sulfate and only an infinitesimal amount of dithionate is formed.

$$HSO_3^- + H_2O_2 \longrightarrow HSO_4^- + H_2O \tag{2}$$

If a radical pathway was significantly involved in this oxidation then a considerable amount of dithionate should be formed.

Kinetic data for the reaction were obtained from stopped–flow spectrophotometric measurements at 260 nm with a slit width of 1.0 mm. The reaction was studied under pseudo-first-order conditions with $[H_2O_2] > [SO_3^{2-}]_T = 5 \times 10^{-3}$ to $2 \times 10^{-2} \ M$ at 12.0° and $\mu = 1.0$ over the pH range 8–4 using TRIS, TES, phosphate, citrate, pivalate, and acetate buffering systems. Solutions were prepared under nitrogen and EDTA salts were used in all kinetic runs to minimize the effect of trace metal catalysis and the oxidation of sulfite by oxygen.[6] Constant ionic strength was maintained with Na_2SO_4. The reaction rate is first order each in $[SO_2]_T$ and $[H_2O_2]$. Depicted in Figure 1 and listed in Table I are the results of a variation of pH at 12.0° with the sulfite, peroxide, and buffer concentrations held constant. In the pH range 8.3–6.5 the slope of the log k_{obsd} vs. pH plot is roughly −2 whereas in the pH range 6.5–4.5 the slope changes to approximately −1. This pH dependency

indicates that HSO_3^- is the principal reactive sulfite species in solution. Below pH 4.5, with the other conditions held constant the rate of the reaction exceeded the lower limit of detection by the stopped–flow system (i.e., the reaction was completed essentially within the time of mixing ~2 msec). In order to examine the possibility of general acid catalysis as observed by Mader[5] in his kinetic study of the reaction of SO_3^{2-} and H_2O_2 in alkaline solution, a series of kinetic runs was made with the ionic strength, $[H_2O_2]$, $[SO_2]_T$, and pH held constant while the buffer concentration was varied. The results are shown in Figure 2 and listed in Table II for a variation in the phosphate buffer concentration at pH 6.4 $\mu = 1.0$, and 12.0°. The other buffers employed in this study were not tested for possible catalytic behavior.

The results depicted in Figure 2 indicate that the oxidation is definitely subject to general acid catalysis. Mechanistically, this implies that hydrogen ions are transferred from a Brønsted acid (HA) to a substrate in the transition state or that there is an equilibrium protonation of the substrate followed by proton transfer to A^-. In such cases any acidic molecule or ion can act to transfer the proton to the substrate; therefore, a multiterm rate law should be observed.[7] A two-term rate law which accounts for the observed kinetic behavior in the pH range 8–4 is

$$-d[SO_2]_T/dl = k[H^+][H_2O_2][SO_2]_T \{[H^+]/([H^+] + Ka_2)\} + k'[HA][H_2O_2][SO_2]_T \{[H^+]/([H^+] + Ka_2)\} \tag{3}$$

where

$$[SO_2]_T = [HSO_3^-] + [SO_3^{2-}] \tag{4}$$

$$Ka_2 = [SO_3^{2-}][H^+]/[HSO_3^-] \tag{5}$$

In the pH range greater than 6.5, the sulfite is primarily unprotonated in the ground state; therefore, in going from the ground state to the transition state, two protons are needed which is reflected by the slope of approximately −2 in Figure 1. In pH range less than 6.5, the sulfite in the ground state is mostly protonated; therefore, in going from the ground state to the transition state, only one additional proton is required and this is reflected by a slope which is close to −1 in the lower pH range. k and k' have been calculated to be 5.8×10^1 and $7.2 \times 10^2 \ M^{-2} \ sec^{-1}$, respectively, from the data in Table II for the described conditions.

TABLE I: Summary of Kinetic Data for the Oxidation of Sulfite by Hydrogen Peroxide at 12.0° where $[SO_3{}^2]_0$ = 2.0 × 10⁻² M and $[H_2O_2]_0$ = 1.0 × 10⁻¹ M

Buffer	pKa^a	[HA], M	[A⁻], M	pH	k_{obsd}, sec⁻¹	S^b
TRIS	8.3	0.2	0.2	8.25	0.02	
TES	7.5	0.2	0.2	7.45	0.11	
Phosphate	6.8	0.2	0.2	6.52	19.37	1.07
Citrate	5.6	0.2	0.2	5.65	119.98	6.16
Pivalate	5.1	0.2	0.2	5.08	205.01	10.52
Acetate	4.7	0.2	0.2	4.65	381.63	11.91

^{a} At 20.0°. ^{b} Sample standard deviation where $N \geq 5$.
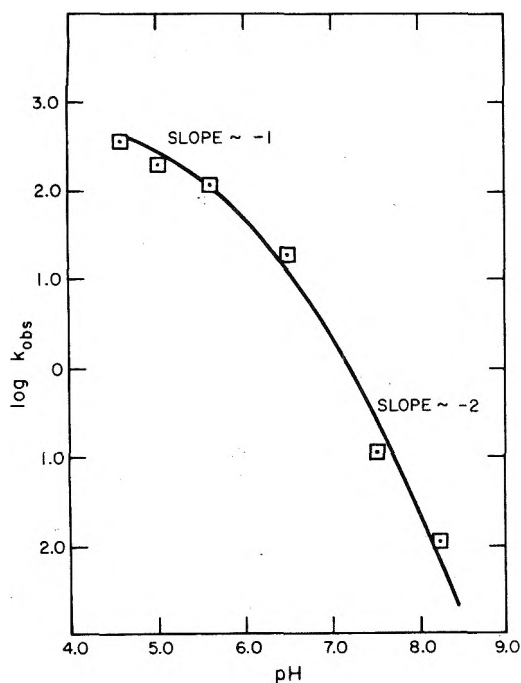
Figure 1. Plot of log k_{obsd} vs. pH for the oxidation of sulfite by hydrogen peroxide.

A mechanism, which is consistent with the present kinetic results, can be written as follows

$$H^+ - SO_3{}^{2-} \xrightleftharpoons{Ka_2{}^{-1}} HSO_3{}^- \tag{6}$$

$$HSO_3{}^- + H_2O_2 \xrightleftharpoons{K} \underset{O}{\overset{-O}{\bigvee}}S{-}OOH + H_2O \tag{7}$$

$$\underset{O}{\overset{-O}{\bigvee}}S{-}OOH + HA \xrightarrow{k} H_2SO_4 + A^- \tag{8}$$

where

$$HA = H_3O^+ \text{ or } H_2PO_4{}^-$$
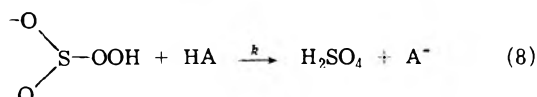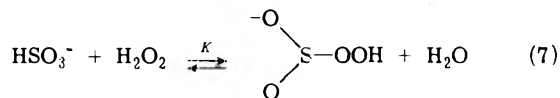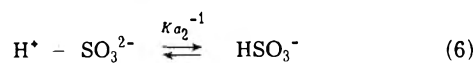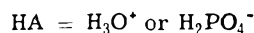
According to this mechanism, the reaction probably occurs via a nucleophilic displacement by H_2O_2 on $HSO_3{}^-$ to form a peroxomonosulfurous acid intermediate which then undergoes a rate-determining rearrangement. Equation 7 is analogous to the reaction of hydrogen peroxide and sulfuric acid to give peroxomonosulfuric acid.[8]

$$H_2O_2 + H_2SO_4 \xrightleftharpoons{K\sim 1} HOOSO_3H + H_2O \tag{9}$$

TABLE II: Summary of Kinetic Data for the Variation of $[H_2PO_4{}^-]$ at pH 6.40, 12.0°, μ = 1.0, $[SO_3{}^{-2}]_0$ = 5.0 × 10⁻³ M and $[H_2O_2]_0$ = 2.5 × 10⁻² M

$[H_2PO_4{}^-]$, M	k_{obsd}, sec⁻¹	$[H_2PO_4{}^-]$, M	k_{obsd}, sec⁻¹
0.32	5.78	0.08	2.28
0.16	3.51	0.04	1.75
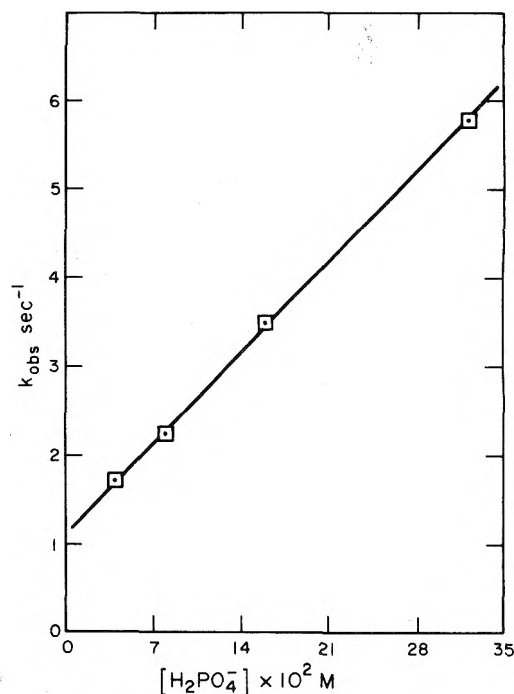
Figure 2. A plot of k_{obsd} as a function of $[H_2PO_4{}^-]$ at 12.0°, μ = 1.0, and pH 6.4.

Alternatively a mechanism in which there would be an equilibrium protonation of the bisulfite followed by a proton transfer to A^- can also be written as follows

$$H^+ + SO_3 \xrightleftharpoons{Ka_2{}^{-1}} HSO_3{}^- \tag{10}$$

$$HSO_3{}^- + HA \xrightleftharpoons{K'} H_2O{\cdot}SO_2 + A^- \tag{11}$$

$$A^- + H_2O_2 + H_2O{\cdot}SO_2 \xrightarrow[slow]{k} \underset{O}{\overset{-O}{\bigvee}}S{-}OOH + HA \tag{12}$$

$$\underset{O}{\overset{-O}{\bigvee}}S{-}OOH \xrightarrow{rapid} HSO_4{}^- \tag{13}$$
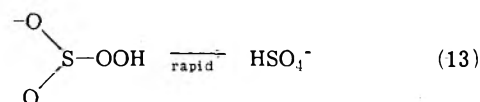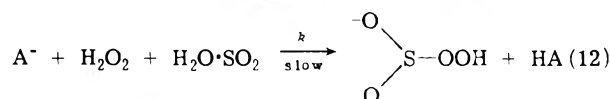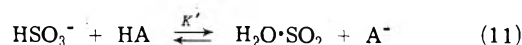
In this scheme, the termolecular step, in which A^-, H_2O_2, and $H_2O{\cdot}SO_2$ react to form peroxomonosulfurous acid, would be rate determining. Both of these mechanisms are consistent with the results of an isotopic labeling study of the reaction between $SO_3{}^{2-}$ and H_2O_2 at pH 5 by Halperin and Taube[9] in which the product sulfate was found to have two ¹⁸O atoms which were present initially in the doubly labeled peroxide even though the stoichiometry requires the net addition of only one oxygen atom. Their results were rationalized in terms of a peroxomonosulfurous acid intermediate which rearranges to form the doubly labeled sulfate. Presently, there is no evidence for participation of the

pyrosulfite ion[2] in the reaction scheme, especially

$$2HSO_3^- \; \underset{k_{-1}}{\overset{k_1}{\rightleftharpoons}} \; S_2O_5^{2-} + H_2O$$

$$k_1 = 7.0 \times 10^2 \; M^{-1} \; sec^{-1}$$

$$k_{-1} = 1.0 \times 10^1 \; sec^{-1}$$

$$(14)$$
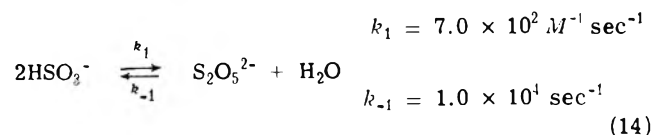
in light of the observed first-order dependence on the total sulfite concentration. Our results do not necessarily preclude a radical mechanism but when combined with the results of Halperin and Taube they seem to favor a polar mechanism. Recently, radical intermediates have been detected by ESR in the reaction of SO_2 and H_2O_2.[10] Contribution of a free-radical pathway in the overall reaction seems unlikely but it definitely cannot be excluded.

References and Notes

(1) M. Eigen, K. Kustin, and G. Maass, *Z. Phys. Chem. (Frankfurt am Main)*, **30**, 130 (1961).
(2) R. H. Betts and R. H. Voss, *Can. J. Chem.*, **48**, 2035 (1970).
(3) H. W. Albu and H. D. Graf von Schweinitz, *Berichte*, **65**, 729 (1935).
(4) W. C. E. Higginson and J. W. Marshall, *J. Chem. Soc.*, 447 (1957).
(5) P. M. Mader, *J. Am. Chem. Soc.*, **80**, 2634 (1958).
(6) K. Meyer and L. Roth, *Z. Wiss. Photogr.*, **49**, 10 (1958).
(7) J. O. Edwards, "Inorganic Reaction Mechanisms", Benjamin, New York, N.Y., 1965, p 17.
(8) F. A. Cotton and G. Wilkinson, "Advanced Inorganic Chemistry", Interscience, New York, N.Y., 1972, p 450.
(9) J. Halperin and H. Taube, *J. Am. Chem. Soc.*, **74**, 380 (1952).
(10) B. D. Flockhart, K. J. Ivin, R. C. Pink, and B. D. Sharma, *J. Chem. Soc. D*, 339 (1971).

Matrix Effects on the Charge Resonance Energy of the Dimer Cations. Low-Temperature Radiolysis of Glassy Aromatic Solutions[1]

R. E. Bühler* [2] **and W. Funk**

Laboratory for Physical Chemistry, Swiss Federal Institute of Technology, 8006 Zürich, Switzerland   (Received February 27, 1975)

Near-infrared absorption bands due to several aromatic hydrocarbons in irradiated organic glasses have been assigned to the charge resonance band of the corresponding dimer cations. The observed drastic changes of these bands with the matrix characteristics are found to correspond to the changes in the structure of the dimer cation: a hard matrix (e.g., methylcyclohexane) strongly distorts the dimer cation, thereby reducing the charge resonance energy, unless steric effects are involved (difference between benzene and *tert*-butylbenzene). On softening the matrix there is a continuous relaxation process with a simultaneous increase in the charge resonance energy, until the conformation of the free dimer cation is reached. It is concluded that benzene and *tert*-butylbenzene do form quite loose complexes, suffering large matrix effects, that the naphthalene dimer cation is a very tight complex with no matrix effects, and that bromobenzene is intermediate. Earlier published band assignments by Ekstrom for systems with benzene are reconsidered in the context of this matrix effects. For a 3MP glass with benzene and CCl_3Br the benzene dimer cation decays isothermally (77 K) into a new transient, absorbing at 740 nm. The corresponding changes in the absorptions cannot be related to a matrix effect. The new 740-nm band was tentatively assigned to a complex between the benzene cation and CCl_3Br. The decay of the bromobenzene dimer cation in 3MP leads to the formation of a new absorption at 570 nm. This is assigned to the (Br·BrPh) charge transfer complex.

Introduction

In the low-temperature radiolysis of organic glasses and polycrystalline samples it is often puzzling that the position of many absorption bands depends rather critically on the matrix involved, the way the matrix was formed, the type of other solutes added, and on the temperature. This is particularly true for systems with aromatic hydrocarbons and with halogenated compounds. This paper discusses the behavior of the absorption bands of aromatic cations, related to the matrix involved.

It is well known that irradiation of aromatic compounds in hydrocarbon glasses, particularly in the presence of an electron scavenger, do yield aromatic cations. Such cations were studied at 77 K by Hamill and coworkers[3] in polycrystalline CCl_4,[4,5] in butyl chloride glasses,[6] and glasses of 3-methylpentane (3MP).[7] Similar information was given by Ekstrom[8] for a 3MP matrix at 77 K, by Willard and Ekstrom[9] for a methylcyclohexane (MCH) matrix at 20 K, and by Louvrier and Hamill[10] in alkane matrices at 77 K. The most detailed information stems from investigations by Badger and Brocklehurst in isopentane–butyl chloride glasses (IP:BuC = 1:1) at 77K.[11-13] These authors detected cationic absorptions for many aromatic compounds: e.g., for benzene a charge-resonance band of the dimer cation $(C_6H_6)_2^+$ at 935 nm, an absorption band of the complexed monomer cation $(C_6H_6)_c^+$ at 470 nm and a band for the noncomplexed (free) cation $C_6H_6^+$ at 555 nm.[11] The

charge-resonance band generally is quite isolated from other transient absorptions. Most of the results in this paper are related to such charge resonance bands. For a particular dimer cation it was found that such bands may vary as much as 300 nm depending on the matrix. It will be shown that this large shift is related to distortions of the cationic complex. For weak complexes the matrix effect can be large, whereas for strong complexes the matrix has little or no influence.

Experimental Section

1. Method. A copper–quartz double cell, filled with degassed solution, was mounted in an evacuated cryostat. One of the two cells was irradiated by 2-MeV electrons from a Febetron 705[14] from both sides for maximum dose uniformity, through thin aluminum windows of the cryostat and the quartz windows of the cell. The second cell was shielded to serve as a reference cell. The double cell holder was then rotated by 90° so that the cell quartz window became parallel to the cryostat quartz window. Spectra were then recorded with a Beckman spectrograph Model DK2.

2. Cryostat (Figure 1). The cryostat was made from an evacuated, vertical brass cylinder carrying a thin stainless steel inner tube (R) to hold liquid N_2. From the copper bottom of this inner tube two copper fingers (H) extend downward to embrace the cell block (Figure 2), which was tightly fastened for each experiment to guarantee good thermal contact. The copper fingers were partly hollow for liquid N_2. The cell holder (H) was surrounded by a rectangular blackened brass box to fit into the cell compartment of the spectrograph. The access of the electron beam (0.01 mm Al foil) and spectrographic light beam (2 mm quartz plate) were at right angles. Correspondingly the cell holder could be rotated on ball bearings under vacuum. The temperature was measured by a thermocouple T fitted tightly into the cell block. The temperature difference between the cell block and the solution was less than 0.1 K for isothermal measurements, but was estimated to be about 1 K during warming experiments.

3. The Cell (Figure 2). The two cells are filled together through the copper–glass connection R and the channels U and K. Each cell is cut from the copper block leaving a central spacer with a sharp edge N on which a Teflon gasket T_1 (0.2 mm thick) ensured tightness for the quartz windows Q (1 mm thick). For vacuum tightness the edges of the quartz plates were sealed with Silastic-731-RTV from Dow Chemical from the outside. The optical path length was 3.1 mm.

The cell block was usually cleaned by washing with distilled acetone and ether, drying in an oven at 110° for 4 hr, washing with concentrated H_2SO_4, rinsing eight times with doubly distilled water, again drying in an oven, and then evacuating for at least 2 days to ensure outgasing of the Teflon gaskets. After about three to four experiments or whenever the chemical system was altered the Teflon gaskets were replaced.

4. Sample Freezing. Different to the usual dip-freezing, the temperature of the probe was lowered slowly by adding liquid N_2 in small portions into the cryostat. Complete freezing to 77 K within about 30 min resulted in better glass quality than by rapid freezing with a completely filled cryostat. The glass sample was irradiated after a minimum of 25 min of standing at 77 K for matrix relaxation.

5. Irradiation. An equal number of electron pulses were
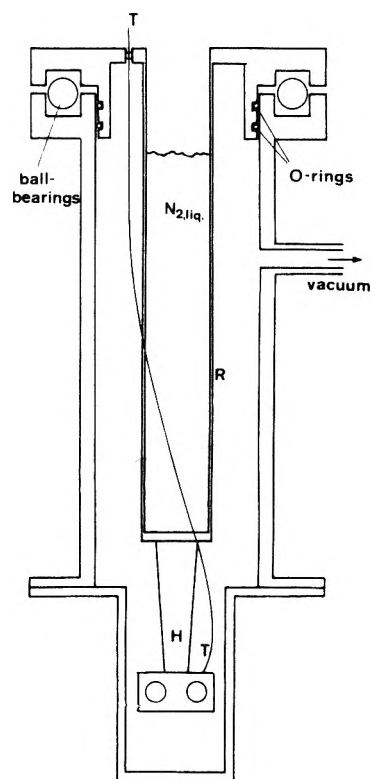
Figure 1. Cryostat for sample irradiation and spectroscopy. (R, thin stainless steel inner tube for liquid nitrogen; H, copper cell holder; T, thermocouple.)
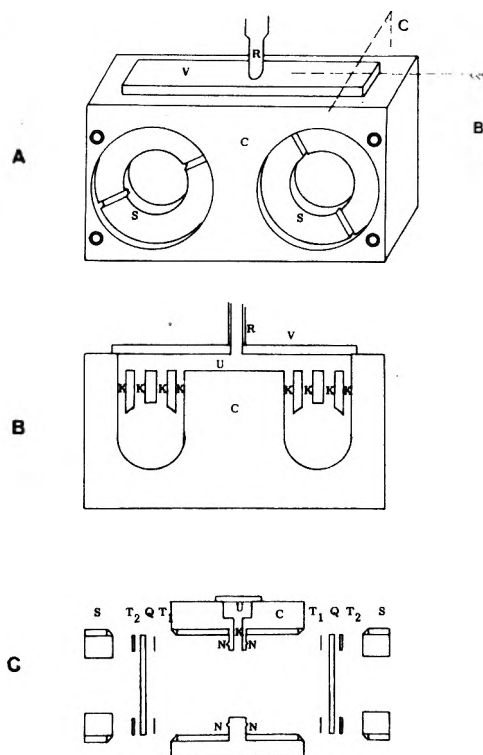
Figure 2. The copper cell block with two cross sections (see text). R, U, and K, channels for filling with solution; N, edge for the Teflon seals; T, Teflon gaskets; Q, quartz windows; S, tightening nut; C, copper cell block; V, copper plate to cover the filling channel U.

applied from both sides to one of the two cells for a high uniformity of dose (Figure 3). The second cell was shielded
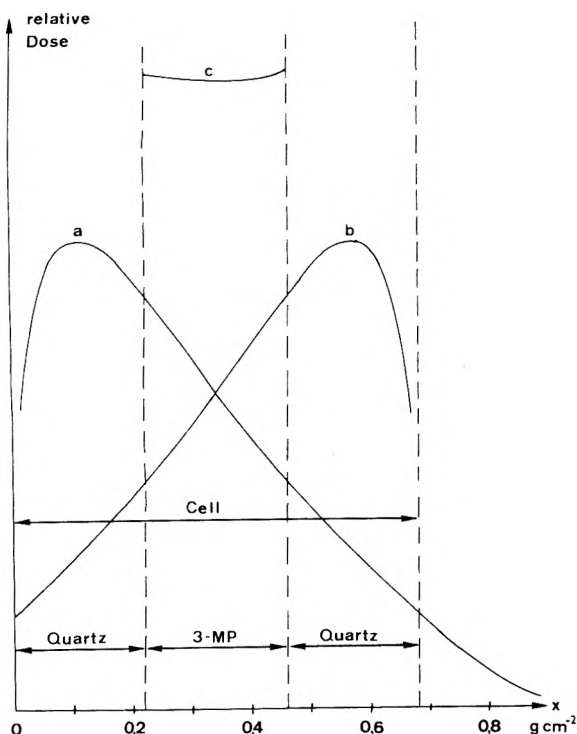
Figure 3. Dose distribution with equal irradiation of the cell from both sides. The sum of the mirror images of the dose depth curves a and b yields curve c, the dose distribution within the cell. Dose uniformity is better than about 2%.

by the thick brass wall and the copper cell holder. The dose was determined by calorimetry[15] with an aluminum probe and by correcting for the density of the material. Corrections for differences in the dose–depth curves (different nuclear charge) and back-scattering at the interface quartz–solution vs. quartz–aluminum were neglected.[15] For all experiments reported in this paper a total of eight pulses were applied, corresponding to a dose of 200 ± 12 krads in 3-MP at 77 K.

6. Spectral Analysis. The 100% transmission was calibrated at 77 K, but on warming of the matrix this 100% transmission could change due to matrix changes. No corrections were applied for these changes. Since most spectra were recorded over a rather narrow temperature range (typically −196 to −180°) this error was small. The warming rate of the sample was 1.7 K min^{-1} from 77 K to about 140 K. Hence, there was a temperature drift of up to 1 K from low to high wavelength in the recorded spectra. Any small wavelength shifts of the absorption maxima, due to fast scanning, were corrected for. In most cases the correction was less than about 10 nm.

7. Chemicals. 3-Methylpentane (3MP) and methylcyclohexane (MCH) were preirradiated with about 2 Mrad from a ^{60}Co source, then purified by pushing the solvent three times through a silica gel column and once through an alox column[16,17] (length 45 cm, diameter 2.5 cm), and finally by distillation. For 3MP the only detectable impurity was 0.4% of 2-methylpentane, an isomer which could not interfere with the experiments. CCl_4, benzene, *tert*-butylbenzene, and bromobenzene were first treated with concentrated sulfuric acid, then NaOH or soda, then dried with $CaCl_2$, and finally distilled from molecular sieve type A4. All other solutes (Fluka puriss.) were used without further purification.

Results

Benzene, *tert*-butylbenzene, bromobenzene, naphthalene, and biphenyl have been studied alone or together with small halocarbons such as CCl_4, CCl_3Br, CBr_4, C_2Cl_6, and $CClF_2$–CCl_2F (Freon 113) in 3MP and MCH glasses. The radiation-induced transient absorptions have been recorded at 77 K (−196°) and on warming of the matrix to their complete disappearance. Generally there were at least two typical regions of transient absorptions: an infrared band in the range from 800 to 1100 nm and absorption bands in the visible region from 400 to 600 nm. The infrared band is related to the aromatic compound, the visible bands mostly to the halogenated compound. Both have similar band widths on an energy scale and suffer wavelength shifts on warming of the matrix, though in opposite directions. The visible absorption will be the subject of a separate study. In this paper the behavior of the infrared band will be reported with a selection of typical transient spectra.

(a) *Aromatic Solutes Alone.* Aromatic hydrocarbons are known to form cations as well as anions, their spectra being closely related (alternant hydrocarbons). As a result naphthalene and biphenyl do show many close lying bands.[3,12,13] The spectra of benzene and substituted benzenes are less specific: Figure 4 for benzene (Bz), Figure 5 for *tert*-butylbenzene (*t*-BuBz). These absorptions are relatively weak. Due to the fact that benzene is a slow electron scavenger, many of the initially produced cations are neutralized again by the relatively mobile electron in the hydrocarbon matrix. The dominant infrared bands clearly correspond to the charge resonance bands of the dimer cations:[11] $(Bz)_2^+$ at 930 nm and $(t$-$BuBz)_2^+$ at 1030 nm. On warming of the hydrocarbon matrix the spectra due to naphthalene or to biphenyl slowly decay without changing their band positions. At −180° all transient absorptions between 300 and 1100 nm have disappeared. The spectra due to benzene and *tert*-butylbenzene do behave differently; simultaneous to the decay of the charge-resonance band a strong apparent blue shift occurs, so that on disappearance at −180° the absorption maxima are found at about 750 nm for benzene and at 850 nm for *tert*-butylbenzene. Details of this shift are much better seen in systems with high concentrations of electron scavengers, when most of the cation–electron neutralizations are stopped by the formation of immobile anions (see below).

(b) *Aromatic Solutes with Added Electron Scavengers.* Systems with both aromatic and halocarbon solutes did not show new absorption bands at 77 K than have already been seen with each solute alone. However the cation spectra were generally much more intense, and absorptions due to aromatic anions disappeared. Typically the spectra for *tert*-butylbenzene with CCl_4, CCl_3Br, and C_2Cl_6 are shown in Figures 6, 7, and 8, respectively. In all cases the charge resonance band of the dimer cation at 77 K lies between 1000 and 1035 nm with an optical density of 0.30–0.38 (200 krads). On warming, the absorption slightly increases first before decaying rapidly under simultaneous blue shift toward 800 nm, where the charge-resonance band disappears at a temperature of about −180°. Obviously this behavior is not dependent on the choice of electron scavengers. In a few systems new absorption bands appear in the visible region on warming, not seen in systems with the individual solutes alone. They seem to be related to the cation decay.

(c) *Bromobenzene (Figure 9).* Bromobenzene is both an
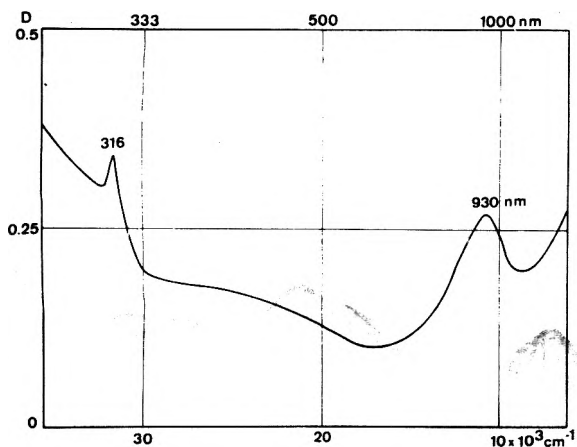
Figure 4. Spectrum for 2 mol % benzene in 3MP at 77 K.
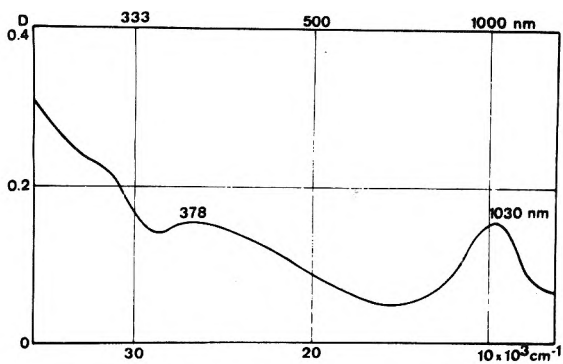
Figure 5. Spectrum for 1 mol % *tert*-butylbenzene in 3MP at 77 K.
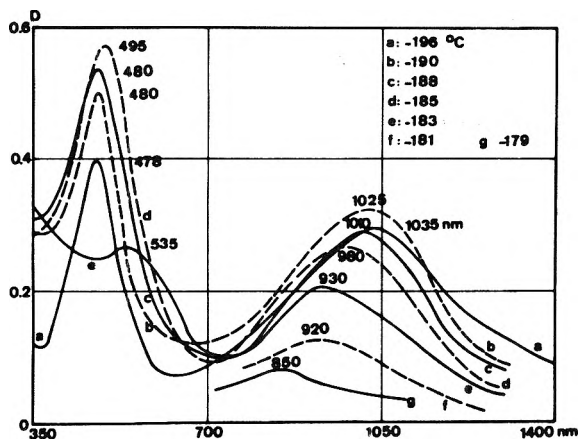
Figure 6. Spectra for 1 mol % *tert*-butylbenzene and 1 mol % CCl₄ in 3MP at 77 K and on warming.

Figure 7. Spectra for 1 mol % *tert*-butylbenzene and 0.4 mol % CCl₃Br in 3MP at 77 K and on warming.
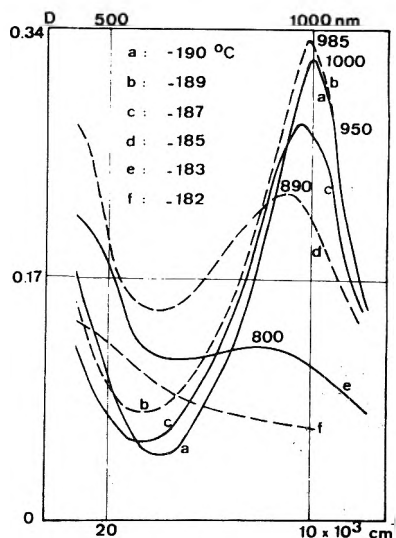
Figure 8. Spectra for 2 mol % *tert*-butylbenzene and 0.2 mol % C₂Cl₆ in 3MP at 77 K and on warming.
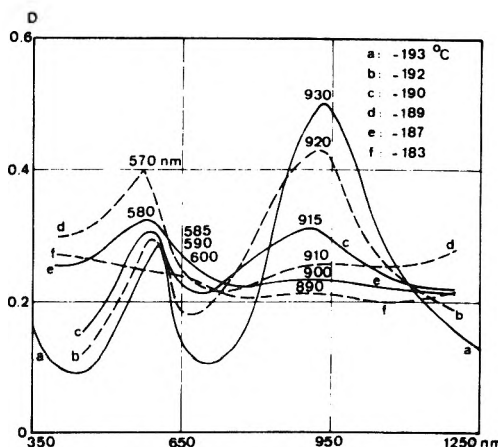
Figure 9. Spectra for 2 mol % bromobenzene in 3MP at 80 K and on warming.

electron scavenger and a positive trap. Consequently the absorptions are also intense, the optical density at 930 nm even being higher by about 50% than comparable mixtures of aromatic and halogenated compounds (higher yield of dimer cation or higher extinction coefficient for the charge resonance band). On warming, the infrared band shifts from 930 to 890 nm, disappearing at about −182°. This is a rather small shift relative to the systems with benzene and *tert*-butylbenzene. The visible band at 600 nm (77 K) also shifts to the blue on warming, but with a strong increase in absorption. After reaching the maximum at 570 nm the band disappears without further shift, indicating that the 570-nm band must be due to a new species.

(d) *Matrix Viscosity.* In Figures 10 and 11 the effect of the matrix viscosity at 77 K is shown: the MCH glass is about 10⁷ times harder than the 3MP glass (η(MCH, 77 K)
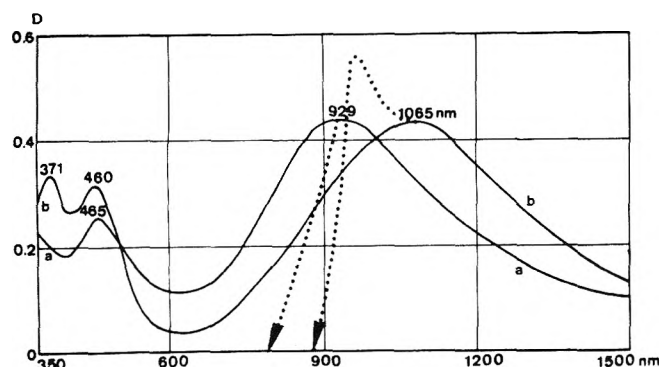
Figure 10. Spectrum for benzene and CCl_4 in 3MP and MCH at 77 K. The dotted arrow indicates the shift of the maximum optical density on warming: (a) 2 mol % benzene, 0.12 mol % CCl_4 in 3MP; (b) 1 mol % benzene, 0.12 mol % CCl_4 in MCH.
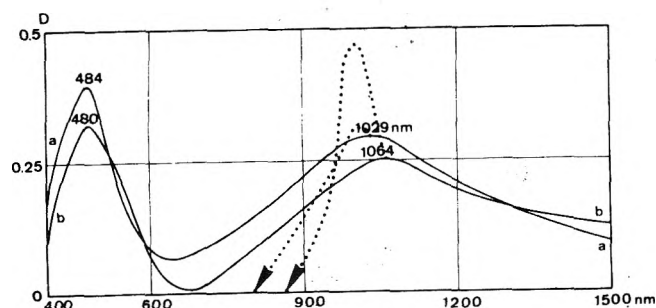
Figure 11. Spectrum for 1 mol % tert-butylbenzene and 0.12 mol % CCl_4 in 3MP (a) and in MCH (b) at 77 K. The dotted arrow indicates the shift of the maximum optical density on warming.

Figure 12. Isothermal change of the spectrum for 1 mol % benzene anc 1 mol % CCl_3Br in 3MP at 77 K.

$= 2 \times 10^{19}$ P, $\eta(3MP, 77 \text{ K}) = 2 \times 10^{12}$ P).[44] On going from a soft to a hard matrix the charge resonance band for benzene cations suffers a red shift of 136 nm (929–1065 nm), while for tert-butylbenzene cations the shift is only 35 nm (1029–1064 nm). On warming of the soft 3MP matrix both charge resonance bands initially increase in optical density by a few percent (e.g., Figure 6). In MCH matrices however the charge resonance band for tert-butylbenzene almost doubles and for benzene increases by about 25% to reach a maximum at about $-180°$ before decaying at higher temperature (see the arrows in Figure 10 and 11). In all four cases the blue shifts on warming (for hard and soft matrices) amount to about 160–200 nm.

(e) *Isothermal Effect.* In all systems studied, the radiation-induced transient spectra were stable as long as the matrix was held at 77 K. However there was one exception: with benzene and CCl_3Br as solutes (Figure 12) the charge resonance band slowly decreased with a simultaneous increase of absorption in the 650–800-nm region, showing a well reproducible isosbestic point at 810 nm. The charge resonance band seems to shift again to the blue, but this is merely the effect of the two overlapping bands, centered at 920 nm (charge resonance band) and at about 740 nm. Therefore the isothermal spectral changes shown in Figure 12 cannot have the same origin as the blue shift of the charge resonance band as discussed in previous sections.

By warming the benzene–CCl_3Br–3MP matrix the isothermally initiated change is accelerated and the 740-nm band decreases rapidly, disappearing without wavelength shift at a relatively low temperature of $-189°$. This behavior contrasts to the results for the similar system tert-butylbenzene–CCl_3Br–3MP (Figure 7).
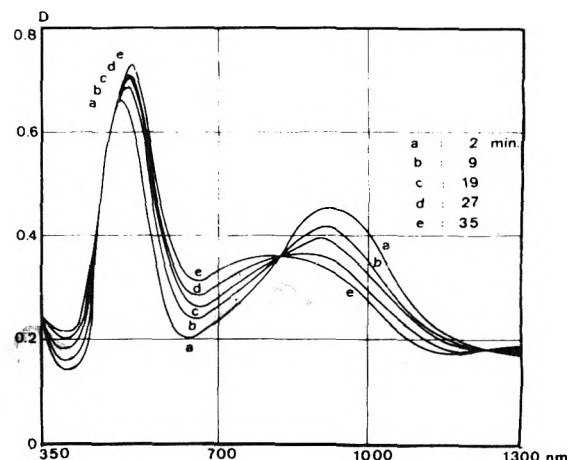
Discussion

1. Spectral Assignment. The infrared absorption as measured in this study at 77 K (Table I) compared to the known absorptions of aromatic cations[11] must clearly be identified as the charge resonance bands of the aromatic dimer cations. The fact that the band shifts to the blue on softening of the matrix could either be explained by the formation of a new transient, absorbing at a shorter wavelength with simultaneous combined decay or by a real band shift due to changing structure of the dimer cation. Since the shift is very large the first argument would seem to be more realistic. However, assuming comparable band widths for both bands and taking into account that in no instance the two bands can be resolved, the second band should appear in the region of 800–900 nm for the tert-butylbenzene systems or 700–800 nm for the benzene system, irrespective of the halocarbons present. The monomer cations, absorbing typically at shorter wavelengths ($\lambda_{max}(Bz^+{}_{free})$ 555 nm, $\lambda_{mix}(Bz^+{}_c)$ 470 nm),[11] cannot be responsible for that band. The appearance of an isosbestic point in the benzene–CCl_3Br system (Figure 12) is not indicative of such a second band as this system constitutes a special case (see below). The red shift occurring in harder matrices (see below) also cannot be explained by this second band. It is believed therefore that the strong blue shifts are real and due to changes in the dimer cation structure. This is supported by a recent paper by Irie et al.[18] concerning a charge transfer band for the complex between a benzyl radical and a chloride ion. This band at 360 nm appears in low-temperature glass matrices if the benzyl chloride anion is caged. In a softer matrix this charge transfer band shifts to the blue and disappears as the benzyl radical is separating from the chloride ion. The present dimer cations also relax on warming the matrix, resulting in a blue shift of the charge resonance band with simultaneous reduction of dimer cation concentration, due to ion neutralization and changes in the monomer–dimer cation equilibrium.

2 Matrix Effects. Changing from the soft matrix (3MP) to the hard matrix (MCH) the charge resonance band shifts by +135 nm for the benzene dimer cation, and +35 nm for the tert-butylbenzene dimer cation (Table I). For bulky molecules the complex cannot be distorted much by a hard matrix, contrary to the locally more mobile benzene molecule. An increase of the halocarbon concentration in 3MP also yields a red shift, as seen for the benzene–CCl_4 system:

TABLE I: Charge Resonance Energies of Aromatic Dimer Cations

Dimer cation[a]	Solvent	Halocarbon solute, mol %	Aromatic solute, mol %	Charge resonance band at 77 K, λ_{max}, nm	Ref
$(t\text{-BuBz})_2{}^+$	3MP glass		t-BuBz (1)	1030	Figure 5
		CCl₄ (0.12)	t-BuBz (1)	1029	Figure 11
		CCl₄ (1)	t-BuBz (1)	1035	Figure 6
		CCl₃Br (0.4)	t-BuBz (1)	1030	Figure 7
		C₂Cl₄ (0.2)	t-BuBz (2)	1000	Figure 8
	MCH glass	CCl₄ (0.12)	t-BuBz (1)	1064	Figure 11
$(Bz)_2{}^+$	3MP glass		Bz (2)	930	Figure 4
		CCl₄ (0.12)	Bz (2)	929	Figure 10
		CCl₄ (2)	Bz (1)	960	b
		CCl₄ (5)	Bz (2.8)	1030	c
		CCl₃Br (1)	Bz (1)	920	Figure 12
		CBr₄ (0.2)	Bz (2)	910	b
	MCH glass	CCl₄ (0.12)	Bz (1)	1065	Figure 10
$(BrPh)_2{}^+$	3MP glass		BrPh (2)	930	Figure 9

[a] t-BuBz = tert-butylbenzene; Bz = benzene. [b] W. Funk, unpublished results. [c] Reference 8.

5 mol % of CCl₄ shifts the charge resonance band to 1010 nm[8] (Table I). Presumably this effect is not related to the viscosity of the matrix but rather to the molecular CCl₄–benzene associations at low temperatures.

The blue shift of the charge resonance band on warming the matrix is large for benzene (Figure 10) and tert-butylbenzene (Figure 6–8), small for bromobenzene (Figure 9), and negligible for naphthalene. This implies that the structure of the dimer cation of naphthalene is stable, irrespective of the surrounding matrix. For benzene and substituted benzenes the dimer cation has a weak bond and the matrix effect is dominant. It is so dominant that the shift of a benzene, toluene, m-xylene, and mesitylene charge resonance band in a 1:1 n-butyl chloride–isopentane matrix on warming slightly is cancelled on refreezing to 77 K.[11,19]

3. Cation Formation and Decay. All systems in a 3MP matrix show an initial increase of the charge resonance band by a few percent on warming. In the hard matrix (MCH) however this initial increase is quite large (Figure 10 and 11). It probably is the result of additional complex formation due to the presence of excess monomer cations. It indicates that in a MCH matrix the association of molecular benzene is far from complete. Badger and Brocklehurst found a similar shift for the monomer–dimer cation equilibrium on softening a n-butyl chloride–isopentane matrix (see Figure 2 in ref 11).

4. Comparison with Theory. Further support for our assignments stems from a theoretical study on monomer and dimer cation absorptions by Badger and Brocklehurst.[20] From their calculations for benzene and naphthalene the charge resonance transitions are expected in the far visible to near-infrared region, well separated from other absorptions. This agrees with the experiments. Unfortunately the theory yields but an order of magnitude, and the model cannot easily be optimized, as too many parameters are involved. However for the present findings of a blue shift for charge resonance bands on softening the matrix, it is interesting to note that the theory also predicts a strong blue shift, if the intermolecular orbital overlap in the dimer cation is reduced to zero.[20] Badger and Brocklehurst[20] also found that both the calculated and experimental monomer cation transitions suffer a blue shift on complexation

(dimer formation), however, that the experimental shift is much larger. They suggested that the dimers must considerably be distorted from the calculated perfect sandwich conformation. Such distortions can be critically dependent on the matrix involved. As the matrix structure changes with increasing temperature, the distortion changes, and consequently the monomer cation band and the charge resonance band shift. We could not observe the monomer cation band (see section 6), but the charge resonance bands clearly show these shifts.

If a neutral dimer molecule has a different conformation than the corresponding dimer cation, the latter should be formed first with the preformed neutral dimer conformation. It will relax on softening the matrix, together with a charge resonance band shift. However from the fact that the charge resonance bands for various dimer cations return to their initial positions on refreezing (see section 2), one has to conclude that the matrix effect (cage effect) is dominant.

The distortion of the dimer cation by the matrix is large if the complex is weak (benzene, tert-butylbenzene). For polar molecules the dimer cations are expected to have stronger bonds with correspondingly less matrix effect (bromobenzene). For naphthalene the interaction in the dimer cation is large through the extended π system (no matrix effect).

5. The Benzene–CCl₃Br System (Figure 12). The isothermal spectral changes observed in this system, together with a rather pronounced isosbestic point cannot result from a matrix effect. A new species absorbing at about 740 nm must be formed from the dimer cation decay. The necessary condition for this process is the presence of CCl₃Br since the dimer cation is stable with all other halocarbons at 77 K. On warming, the CCl₃Br–benzene system does not show a blue shift of the charge resonance band. Instead the dimer cation decays through the new 740-nm transient. It is suggested, rather tentatively, that the new band may be assigned to the charge-transfer band of the ionic complex (Bz⁺·CCl₃Br). Because of the high solute concentrations and the expected molecular associations at low temperature, the aromatic dimer cation will mostly find CCl₃Br molecules close by. It is then assumed that the dimer cation

$(Bz)_2^+$ is weaker than the postulated complex of the benzene cation with CCl_3Br. In systems with the other nonpolar halocarbons the existence of similar complexes, e.g., $(t$-$BuBz)^+ \cdot CCl_4$, cannot be excluded. However they must be weaker and could not be detected in our experiments.

6. Other Transient Absorptions. The absorption of the complexed monomer cation (e.g., $\lambda_{max}(Bz_c)$ 470 nm) should shift toward the free monomer cation band ($\lambda_{max}(Bz^+_{free})$ 555 nm) while the charge resonance band shifts to the blue. It is tempting to correlate this effect with the apparent red shift of the visible absorptions in all mixtures of halocarbons and aromatic solutes, as illustrated by Figure 6. However the results from Badger and Brocklehurst[11] suggest that the intensity of the complexed monomer cation band should be about a factor of 5 smaller than the charge resonance band. Consequently the monomer cation absorption must be hidden within the visible absorption which actually is due to some yet unknown halocarbon transients.

For bromobenzene in 3MP the dimer cation decay is paralleled by the formation of a new transient absorption at 570 nm. It is assigned to the bromine atom charge transfer complex with bromobenzene (Br·BrPh), already known in the literature.[21-23] This result agrees with a similar spectrum published by Noda et al.[24] (Figure 6 in ref 24). Although not correctly interpreted their spectrum clearly shows the 560-nm charge transfer band and an additional band at 340 nm due to the bromine adduct radical ($Br_2C_6H_6 \cdot$).

The transient spectra of the pure aromatic hydrocarbons in 3MP (Figures 4 and 5) do show the charge resonance band, but are rather unspecific otherwise. For benzene (Figure 4) the 316-nm absorption is assigned to the $C_6H_7 \cdot$ radical. The broad 410-nm band must be due to the benzene anion (see Gardner[25]), probably with mixed-in absorption from the complexed monomer cation at 470 nm. The band assignment for the *tert*-butylbenzene system (Figure 5) is quite similar: the 320-nm band due to the H-adduct radical, the 378-nm absorption due to the anion, with the absorption of the complexed monomer cation mixed into the red slope of the anion absorption.

7. Comments to Previously Published Band Assignments. Even though Badger and Brocklehurst have published[11,20] quite extensive proof for the cation assignments, some other conclusions published in the same year by Ekstrom[8] are still debated.[26] It will be shown here to what extent that controversy[27] is solved in the authors opinion.

In a system of benzene in 3MP Ekstrom[8] assigned bands at 525 and 930 nm to the benzene monomer and benzene dimer *anion*, respectively. In a similar system with additional 5 mol % CCl_4 he found bands at 320, 465, and 1030 nm, which he assigned to the benzene monomer *cation*, some unknown species due to CCl_4, and to the benzene dimer *cation*, respectively. In the view of our results the 930-nm band and the 1030-nm band are not due to different species. Both bands must be assigned to the charge resonance band of the benzene dimer cation, merely shifted due to the presence of a high concentration of CCl_4 (see Table I and section 2). The monomer–dimer equilibrium studied with these two bands are also identical (Figures 2 and 5 in ref 8). The 525-nm band, which disappears with increased concentration of benzene, corresponds to Brocklehurst's 555-nm band, i.e., the uncomplexed monomer cation band of benzene. As the dimer cation is formed (930 nm) the monomer cation band (525 nm) disappears or rath-

er is replaced by the complexed monomer cation band at 465 nm.[11] In systems without any additional electron scavengers this band however is hidden under the broad benzene anion band, which is expected in the region of 410 nm (Figure 4 and results by Gardner;[25] see also section 6).

Ekstrom's bleaching experiment for the 525- and 930-nm bands with tungsten light probably means that the benzene anion (absorbing at about 410 nm) can be ionized and the freed electron then neutralizes any cations (monomer at 525 nm or dimer at 930 nm) in the system.

Ekstrom assigned the 320-nm band in the benzene–3MP system with high concentration of CCl_4 to the monomer cation. That means that its behavior should be identical with the other monomer cation band at 525 nm, as supported by its disappearance when the dimer cations are formed (Figure 5 in ref 8). However other facts make the assignment less clear: e.g., Figure 3 of ref 8 displays a strong 320-nm band but no 525-nm band. The strong 320-nm absorption was only detected in systems with high concentration of CCl_4. We believe that it is due to a yet unknown species, which is different from our 316-nm band (Figure 4) in the benzene–3MP system. The latter we assigned to the C_6H_7 radical (see section 6). The fact that we do not see the known fine structure for that radical (316.5 nm:311 nm with intensity ratio of 2:1[28]) is due to the experimental conditions which did not allow us to resolve the weak 311-nm band.

Conclusions

The observed dependence of the charge resonance energy on the matrix characteristics corresponds to changes in the structure of the dimer cation: a hard matrix strongly distorts the dimer cations, thereby reducing the charge resonance energy, unless steric effects block further distortion (e.g., *tert*-butylbenzene). On softening the matrix there is a continuous relaxation process with a simultaneous increase in the charge resonance energy, until the conformation of the free dimer cation is reached (unless it first disappears by neutralization or by a shift of the monomer–dimer cation equilibrium). For benzene and *tert*-butylbenzene this free state is quite loose, but stable, since it had been detected by high-pressure mass spectrometry in the gas phase.[29] Due to the small shift observed for bromobenzene, its free dimer cation cannot be much different from the one in a matrix at 77 K. Naphthalene dimer cations are obviously tight enough so that no matrix effect can be seen.

References and Notes

(1) This work was supported by the Schweizerischer Nationalfonds zur Förderung der wissenschaftlichen Forschung.
(2) Author to whom correspondence should be addressed.
(3) W. H. Hamill in 'Radical Ions'', E. T. Kaiser and L. Kevan, Ed., Interscience, New York, N.Y., 1968.
(4) T. Shida and W. H. Hamill, *J. Chem. Phys.*, **44**, 2369 (1966).
(5) T. Shida and W. H. Hamill, *J. Chem. Phys.*, **44**, 2375 (1966).
(6) T. Shida and W. H. Hamill, *J. Chem. Phys.*, **44**, 4372 (1966).
(7) J. B. Gallivan and W. H. Hamill, *J. Chem. Phys.*, **44**, 2378 (1966).
(8) A. Ekstrom, *J. Phys. Chem.*, **74**, 1705 (1970).
(9) A. Ekstrom and J. E. Willard, *J. Phys. Chem.*, **74**, 1708 (1970).
(10) P. W. F. Louvrier and W. H. Hamill, *J. Phys. Chem.*, **73**, 1707 (1969).
(11) B. Badger and B. Brocklehurst, *Trans. Faraday Soc.*, **65**, 2582 (1969).
(12) B. Badger and B. Brocklehurst, *Trans. Faraday Soc.*, **65**, 2588 (1969).
(13) B. Badger, B. Brocklehurst, and R. D. Russell, *Chem. Phys. Lett.*, **1**, 122 (1967).
(14) Febetron 705: 2-MeV electron accelerator from Field Emission Corp., McMinnville, Oregon, now a subsidiary of Hewlett-Packard.
(15) R. E. Bühler and J. M. Bossy, *Int. J. Radiat. Phys. Chem.*, **6**, 95 (1974).
(16) G. Hesse, I. Daniel, and G. Wohlleben, *Angew. Chem.*, **64**, 103 (1952).
(17) M. F. Ronayne, J. G. Guarino, and W. H. Hamill, *J. Am. Chem. Soc.*, **84**, 4230 (1962).

(18) M. Irie, M. Shimizu, and H. Yoshida, *Chem. Phys. Lett.*, **25**, 102 (1974).
(19) Badger and Brocklehurst[11] did not measure the spectra at elevated temperature before refreezing, and the viscosity of the 1:1 *n*-butyl chloride–isopentane matrix is not known relative to our 3MP and MCH matrices. However the slight warming mentioned in ref 11 is large enough to equilibrate the monomer–dimer equilibrium (Figure 2 for toluene in ref 11). In such conditions our analogous systems with benzene and *tert*-butylbenzene always showed a charge resonance band shift.
(20) B. Badger and B. Brocklehurst, *Trans. Faraday Soc.*, **66**, 2939 (1970).
(21) J. M. Bossy, R. E. Bühler, and M. Ebert, *J. Am. Chem. Soc.*, **92**, 1099 (1970).
(22) J. M. Bossy and R. E. Bühler, *Int. J. Radiat. Phys. Chem.*, **6**, 85 (1974).
(23) R. E. Bühler, *Radiat. Res. Rev.*, **4**, 233–258 (1972).
(24) S. Noda, K. Fueki, and Zen-ichiro Kuri, *Bull. Chem. Soc. Jpn.*, **41**, 2882 (1968).
(25) C. L. Gardner, *J. Chem. Phys.*, **45**, 572 (1966).
(26) Thanks are due to the referee who pointed out that this controversy still persists in the view of many chemists.
(27) B. Brocklehurst, *J. Phys. Chem.*, **75**, 1177 (1971); A. Ekstrom, *ibid.*, **75**, 1178 (1971).
(28) T. Shida and W. H. Hamill, *J. Am. Chem. Soc.*, **88**, 3689 (1966).
(29) S. Wexler and L. G. Pobo, *J. Phys. Chem.*, **74**, 257 (1970).

Partial Volume Expansibility of Simple Organic Solutes from the Temperature of Maximum Density of Aqueous Solutions

James R. Kuppers

Department of Chemistry, The University of North Carolina at Charlotte, Charlotte, North Carolina 28223 (Received May 9, 1975)

Partial volume expansibility of some representative organic solutes, in aqueous solution at 3.98° and infinite dilution, were computed from shifts in the temperature of maximum density. Interplay of electrostrictive disruption of solvent structure by polar groups and the solvent ordering effects associated with the hydrocarbon moiety of solute molecules are thereby brought into focus.

Introduction

An acceptable model of solution structure must be consonant with a set of fundamental thermodynamic properties which includes solute partial volumes and partial thermal expansibilities. There is a unique experimental method for acquiring thermal expansibility data on dilute aqueous solutions near 3.98° which is attributable to the existence of maximum solution density near this temperature. Earlier work on this topic was reviewed by Franks.[1]

The shift in the temperature of maximum density under the influence of solute in dilute aqueous solution was expressed by Wada and Umeda[2] as

$$\Delta\theta = -1/(1 - x)2\beta V_1^*[x\alpha V_2^0 + \partial\Delta V^M/\partial T] \quad (1)$$

where x is solute mole fraction, α is the thermal coefficient of expansion of pure solute, β is the coefficient in the parabolic relation to temperature of the molar volume of water in the vicinity of 3.98°, V_2^0 is the molar volume of pure solute at 0°, V_1^* is the molar volume of water at 3.98°, and ΔV^M is the excess volume of mixing.

Frank[3] identified an approximate relationship between the apparent molal expansibility, Φ, and $\Delta\theta$

$$\Phi = -\Delta\theta/m[\partial^2 V/\partial T^2] \quad (2)$$

where m is the molality and where the second derivative is to be evaluated at 3.98° and infinite dilution. Subsequently it has been shown[4] that eq 1 can be cast into a form which provides a direct link between experiment and a value for the partial molal expansibility of solute at 3.98° and infinite dilution

$$\partial\bar{V}_2^*/\partial T = -2\beta V_1^*[\Delta\theta/x]_L \quad (3)$$

or the thermal coefficient of partial volume expansion of solute

$$\bar{a}^* = -2\beta V_1^*/\bar{V}_2^*[\Delta\theta/x]_L \quad (4)$$

where $[\Delta\theta/x]_L$ is the limiting value of $\Delta\theta/x$ at infinite dilution and $\bar{V}_2^*$ is the partial molal volume of solute at 3.98° and infinite dilution. The reliability of such solute expansibility data will be limited by the precision of extrapolation from experimental measurements. $\Delta\theta/x$ is quite insensitive to solute concentration for a large number of electrolytes[4] at high dilution. However, nonlinear extrapolation functions may be needed for other cases in which this is not true.

This is a report of some experimental measurements of $\Delta\theta/x$ and the calculation of partial expansibility data from these, and from other experimental measurements reported in the literature, for some simple organic solutes in aqueous solution.

Experimental Section

Measurements of $\Delta\theta$ were made by the method of Wada and Umeda[2] with the following modifications. Matched dilatometers, one containing the aqueous solution and the other water, were immersed side by side in a controlled temperature water bath. This type of differential measurement eliminated the need for glass expansion corrections and rendered less critical errors in thermal equilibration or temperature measurement.

The temperature of maximum density, T_{MD}, was calculated from at least eight data points (height, h, of liquid in dilatometer arms) taken over a range of $T_{DM} \pm 2°$. Multilinear regression was used to find the best fit to the equa-

TABLE I: Partial Specific Volumes, Shifts in Temperature of Maximum Density Vs. Concentration, and Thermal Coefficients of Partial Volume Expansion for Some Simple Organic Solutes in Water at Infinite Dilution and 3.98°

		$\bar{v}^*$, ml g^{-1}	$[\Delta\theta/x]_L$, deg mole fraction^{-1}	$10^3\bar{\alpha}^*$, deg^{-1}
CH_4O	Methanol	1.186[a]	42[e]	−0.32
CH_2O_2	Formic acid	0.760[d]	−418	3.44
C_2H_6O	Ethanol	1.187[a]	141[e]	−0.74
$C_2H_6O_2$	Ethanediol	0.864	−189[e]	1.02
			−172	0.92
$C_2H_4O_2$	Acetic acid	**0.833**[d]	−413	2.38
$C_2H_5O_2N$	Glycine	0.530	−548	3.99
C_3H_8O	2-Propanol	1.188[a]	140[e]	−0.56
	1-Propanol	1.165[a]	117[e]	−0.48
$C_3H_8O_2$	1,2-Propanediol	0.926	46[e]	−0.19
$C_3H_8O_3$	Glycerol	0.768	−164[e]	0.67
C_3H_6O	2-Propanone	1.121	−120[e]	0.53
$C_3H_6O_2$	Propanoic acid	0.877	−407	1.80
$C_3H_7O_2N$	α-Alanine[f]	0.657	−399	1.96
	β-Alanine	0.640	−501	2.53
$C_4H_{10}O$	2-Methyl-2-propanol	1.185[b]	393[e]	−1.29
	2-Butanol	1.160[a]	140[e]	−0.47
	2-Methyl-1-propanol	1.159[a]	71[e]	−0.24
	1-Butanol	1.156[a]	71[e]	−0.24
	Diethyl ether	1.093	−44	0.16
C_4H_8O	Tetrahydrofuran	1.050[c]	−223[e]	0.85
			−238	0.91
$C_4H_8O_2$	2-Methylpropanoic acid	0.917	−408	1.46
	1,4-Dioxane	0.895[c]	−410[e]	1.50
			−414	1.51
	1,3-Dioxane	0.724	−451	2.04
$C_5H_{10}O_2$	3-Methylbutanoic acid	0.957	−438	1.29
$C_5H_{11}O_2N$	Valine	0.756	−368	1.20
$C_6H_{13}O_2N$	Leucine	0.760	−580	1.67
	Isoleucine	0.794	−485	1.34
$C_5H_{10}O_3N_2$	Alanylglycine	0.610	−618	1.81
$C_6H_{12}O_3N_2$	Alanylalanine	0.670	−628	1.69
$C_8H_{16}O_3N_2$	Glycylleucine	0.714	−894	1.91

[a] Reference 6. [b] Reference 7. [c] Reference 8. [d] Reference 5. [e] Reference 2. [f] Amino acids are all in the *dl* form.

tion, $h - h_{MD} = c(T - T_{MD})^2$, where c is a constant. This interpolation equation is based upon the empirical parabolic relation between temperature and volume of water and dilute aqueous solutions near 3.98°. A corresponding value of T_{MD}^0 for water in the matched dilatometer was found and $\Delta\theta/x = (T_{MD} - T_{MD}^0)/x$ was recorded for each solution. Values of $\Delta\theta/x$ for a number of solutes were taken from the literature, subject to the condition that they could be extrapolated to infinite dilution with the desired precision.

It was possible to obtain a limiting value of $\Delta\theta/x$ at infinite dilution, $[\Delta\theta/x]_L$, for most solutes by use of a linear extrapolation function, $\Delta\theta/x = ax + b$, where a and b are constants. Better extrapolation for alcohols, as a class, was achieved with $\Delta\theta/x = ax^{1/2} + b$. In either case the reliability of the extrapolated value was within ±5%.

Standard pycnometric methods were employed to measure densities used in the calculation of partial specific volumes within error limits no greater than ±1%, but where possible, values were interpolated from density measurements reported in the literature.

Results

Three comparisons between values of thermal coefficients of partial volume expansion, $\bar{\alpha}^*$, computed from the measurements of Wada and Umeda[2] and those from my measurements are available in Table I, i.e., ethanediol, tetrahydrofuran, and 1,4-dioxane. Agreement is within the confidence limits of ±5% deduced from my own measurements.

The values of $\bar{\alpha}^*$ listed in Table I draw particular attention to monohydric alcohols in this set, all of which are negative, and to the highly symmetrical 2-methyl-2-propanol standing in a class by itself. The dramatic effect of additional hydroxy groups is apparent: compare ethanol with ethanediol and 1-propanol, or 2-propanol with 1,2-propanediol and glycerol. Conformational relationships among tetrahydrofuran (THF), 1-butanol (BA), and diethyl ether (EE) suggest the following consideration. If THF is thought of as cyclized EE with concomitant restriction on freedom of reorientation of the hydrocarbon portion of the molecule, then one sees a significant increase in $\bar{\alpha}^*$. If, on

the other hand, the hydroxy group of BA is replaced by an ether linkage with ring closure to form THF, there is a much greater increase in $\bar{\alpha}^*$.

The series of carboxylic acids included in this set starts with formic acid which has a value of $\bar{\alpha}^*$ comparable with ammonium halides.[4] Increasing size of the hydrocarbon moiety in the progression formic, acetic, propanoic, 2-methylpropanoic, and 3-methylbutanoic acid is accompanied by an uninterrupted decline in $\bar{\alpha}^*$ values, ranging from 3.44×10^{-3} to 1.29×10^{-3}.

The effect of increasing size of the hydrocarbon moiety upon the value of $\bar{\alpha}^*$ for a sequence of amino acids is even more pronounced, ranging from 3.99×10^{-3} for glycine to 1.20×10^{-3} for valine. However, the values for the six-carbon isoleucine and leucine are greater than the sequence minimum of valine. The effect of a hydrocarbon tail, unrestricted by hydrophylic substituents or by ring closure, is again illustrated in the comparison of β-alanine and α-alanine.

The three dipeptides in this set have values of $\bar{\alpha}^*$ less than the average of the respective amino acids from which they are formed.

Discussion

Although some insight into aqueous solution structure was provided by a separation of measured shifts of T_{MD} into $\Delta\theta_{ideal}$ and $\Delta\theta_{structural}$,[2] further significance of these measurements is revealed by the computation of partial volume expansibilities of the solute. When comparing solutes of vastly different partial molal volumes, it is especially advantageous to remove the volume dimension from expansibility data, as done in defining $\bar{\alpha}^*$, the thermal coefficient of partial volume expansion.

The concept of a cage-like solvent structure, involving an increase in hydrogen bonding in the solvation sphere, is supported by a variety of properties of many dilute aqueous solutions.[1] Especial attention has been focused on the alcohols since it appears that, among relatively soluble organic solutes, they have the most profound effect.[1,9,10] To the extent that such a clathrate-like structure exists, it must be associated with increased short-range order in the solvent near the guest molecule. One can expect that this type of structure would be more favored at the T_{MD} than at higher temperatures. Thus a rise in temperature would cause some disruption of the short-range order, and an accommodation of the guest molecule in a somewhat more limited space.

Formal electric charge or electric polarity on a guest molecule produces quite a different effect: solvent electrostriction, disruption of the normal hydrogen-bonded structure of liquid water, with the guest molecule occupying a relatively small volume element. This volume element, of course, will expand as the thermal energy of the water molecules increases.

When a polar organic molecule with a hydrocarbon moiety is placed in an aqueous environment, each of these two effects of the solvent will be manifest to a greater or less extent, and the partial volume expansibility should reflect the manner in which these two solution-structuring effects are balanced against each other: electrostrictured solvent contributing to greater thermal expansibility and quasi-clathrate formation causing a reduction. Moreover, if expansibility data relate to infinite dilution, the complications of solute–solute interactions and their effect on solution structure are eliminated.

If the integration of concepts considered in this discussion is accepted, the collection of data in Table I then illustrates the manner in which these contrasting effects on solvent structure balance out in some representative classes of organic solutes. In any event such data should be useful in testing any solution structure model.

References and Notes

(1) F. Franks and D. S. Reid, "Water, A Comprehensive Treatise", Vol. 2, F. Franks, Ed., Plenum Press, New York, N.Y., 1973, Chapter 1, p 26, Chapter 5, pp 364–365.
(2) G. Wada and S. Umeda, *Bull. Chem. Soc., Jpn.*, **35**, 646 (1962); **35**, 1797 (1962).
(3) H. S. Frank, unpublished work as cited by F. Franks, *Ann. N.Y. Acad. Sci.*, **125**, 287 (1965).
(4) J. R. Kuppers, *J. Phys. Chem.*, **78**, 1041 (1974).
(5) E. W. Washburn, Ed., "International Critical Tables", Vol. III, McGraw-Hill, New York, N.Y., 1933, pp 122–123.
(6) M. E. Friedman and H. A. Scheraga, *J. Phys. Chem.*, **69**, 3795 (1965).
(7) F. Franks and H. T. Smith, *Trans. Faraday Soc.*, **64**, 2962 (1968).
(8) F. Franks, M. A. J. Quickenden, D. S. Reid, and B. Watson, *Trans. Faraday Soc.*, **66**, 582 (1970).
(9) J. R. Kuppers, *J. Magn. Reson.*, **4**, 220 (1971); **8**, 201 (1972).
(10) J. R. Kuppers and N. E. Carriker, *J. Magn. Reson.*, **5**, 73 (1971).

Coenzyme Model Studies. II. Polyelectrolyte Influence on the Complexation Equilibrium between Model Compounds of Nicotinamide Adenine Dinucleotide and Indole Derivatives[1]

Tsuneo Okubo, Tsutomu Ishiwatari, Kazuei Mita, and Norio Ise*

Department of Polymer Chemistry, Kyoto University, Kyoto, Japan (Received November 18, 1974; Revised Manuscript Received April 17, 1975)
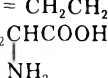
Publication costs assisted by the Department of Polymer Chemistry, Kyoto University

Complex formation of analogs of nicotinamide adenine dinucleotide (NAD+), namely, 3-carbamoylpyridinium compounds quaternized with chloroethylated adenine (NAA), thymine, and theophylline, with indole derivatives were studied in the presence of simple and polyelectrolytes and a surfactant, and in their absence. The indoles are indoleacetate, indolepropionate, indolebutyrate, L-tryptophan, and tryptamine. The polyelectrolytes were sodium poly(ethylenesulfonate), sodium poly(styrenesulfonate) and a copolymer of diethyldiallylammonium chloride and sulfur dioxide. The surfactant was cetyltrimethylammonium bromide. All electrolytes decreased the association constants between the model compounds and indoleacetate, and increased those between the model compounds and tryptamine. Complex formation of the model compounds with L-tryptophan was not influenced with addition of simple and polyelectrolytes. These effects were discussed theoretically in terms of the *secondary salt effect* using the Debye–Hückel theory and Manning's theory on polyelectrolytes, suggesting that electrostatic forces were thus most important to the stability of the complex. The thermodynamic quantities of the complex formation between NAA and indoleacetate, i.e., the free energy (ΔG), enthalpy (ΔH), and entropy (ΔS) were derived. ΔH and ΔS were found to decrease by addition of salts, which was also successfully explained theoretically by using the Debye–Hückel and the Manning theories.

Introduction

In a preceding paper,[2] we synthesized analogs of nicotinamide adenine dinucleotide, NAD+, namely, 3-carbamoylpyridinium compounds quaternized with chloroethylated adenine (NAA), thymine (NAT), and theophylline
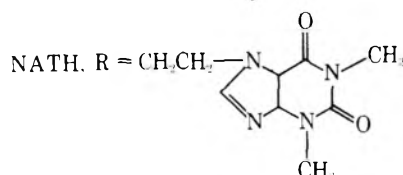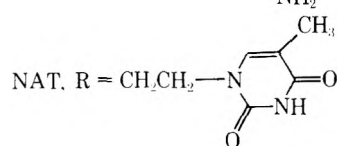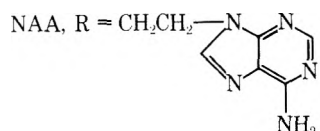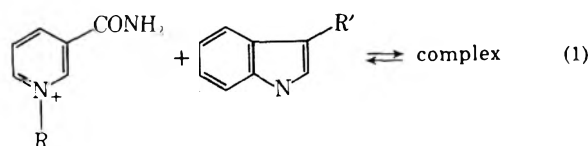
indoleacetic acid (IA), R' = CH$_2$COOH
indolepropionic acid (IP), R' = CH$_2$CH$_2$COOH
indolebutyric acid (IB), R' = CH$_2$CH$_2$CH$_2$COOH
tryptophan (Try), R' = CH$_2$CHCOOH
　　　　　　　　　　　　　　|
　　　　　　　　　　　　　　NH$_2$
tryptamine (TA), R' = CH$_2$CH$_2$NH$_2$

(NATH) and examined their equilibria and reaction rates with cyanide ions. These kinds of analogs which contain neither phosphate nor carbohydrate residues but nucleic acid bases only are very interesting for investigation of charge-transfer interactions.[3-8]

In the present paper, systematic studies were carried out on the influence of polyelectrolyte addition to the complex formations of the model compounds, NAA, NAT, and NATH with indole derivatives, i.e., L-tryptophan, indole-3-acetic acid, tryptamine, etc. The phenomena that interionic complex formation between similary charged ionic species is facilitated by increasing the concentration of simple electrolytes, or ionic strength, whereas that between ionic species of the opposite signs is retarded, are well established as the secondary salt effect.[9] However, the influence of polyelectrolytes on the association phenomena have not been reported. As continuation of our previous work on polyelectrolyte "catalysis" on the reaction rates,[10-14] we wished to investigate this point and to clarify the important contribution of the *electrostatic* forces to the stability of the complexes between the model compounds and indole derivatives which may be inferred from previous work[3-8] to interact with each other by charge-transfer forces.

Experimental Section

Materials. The coenzyme model compounds, NAA, NAT, and NATH, were prepared by the Menschutkin reaction of nicotinamide with N-chloroethyladenine, thymine, and theophylline. The details of the preparation were reported in preceding papers.[2,15] Indole-3-acetic acid (IA) and indole-3-butyric acid (IB) from Merck (for biochemical use) were used without further purification. Indole-3-pro-
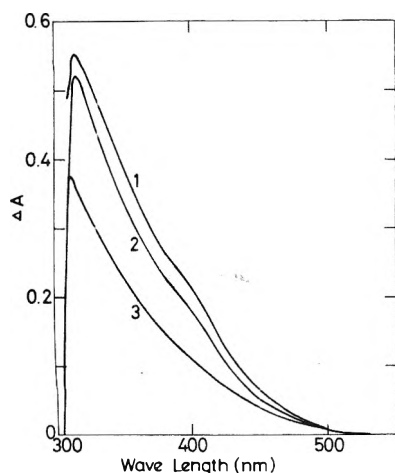
Figure 1. Charge-transfer difference spectra of NAA (curve 1), NAT (curve 2), and NATH (curve 3) with indoleacetate at 25°: [NAA] = [NAT] = [NATH] = 2 mM, [IA] = 30 nM (curves 1 and 2); 16 mM at 340 nm, pH 6.0 in H_2O.

pionic acid (IP), L-tryptophan (Try), tryptamine (TA) hydrochloride, KCl, and $CaCl_2$ were guaranteed reagents.

Sodium poly(ethylenesulfonate) (NaPES), degree of polymerization 770, was a gift from the Hercules Powder Co., Wilmington, Del. Sodium poly(styrenesulfonate) (NaPSt) was kindly donated by the Dow Chemical Co., Midland, Mich. The molecular weight was 6,300,000. The purification of these anionic polyelectrolytes was described in the preceding paper.[2] The copolymer of diethyldiallylammonium chloride and sulfur dioxide (DECS) is a strongly basic polyelectrolyte prepared by Harada et al.[16,17] n-Cetyltrimethylammonium bromide (CTABr) was commercially available. Deionized water was further distilled using a Yamato automatic still (Model WAG-21) for the preparation of aqueous solutions of the model compounds, indole derivatives, and polyelectrolytes.

Equilibrium Constants. The apparent association constant, K, in the absence of foreign salts was evaluated using the Foster–Hammick–Wardley method[18] and the Behme–Cordes method[19] from the slope of the $(\epsilon - \epsilon_0)/N$ vs. ϵ plot, where ϵ_0 is the sum of absorbances of indole derivative and the coenzyme model compound, ϵ the absorbance of the equilibrium mixture, and N the concentration of the indole derivative. The association constant in the presence of the added salt was derived from the equation, $K^{-1} = N[a\beta/(\epsilon - \epsilon_0) - 1]$, where a is the concentration of the coenzyme model compound, and β the molar extinction coefficient of the charge-transfer complex at a given wavelength (340 or 350 nm). There were no salt perturbations of the band maxima under the present experimental conditions. The calculated values of K at three different wavelengths (330, 340, and 350 nm) were the same within experimental error for the systems of NAA, NAT, or NATH and indoleacetate. The reproducibility of the value of K was about 5% both in the presence and absence of polyelectrolytes. The association constants were determined using a Hitachi spectrophotometer (Model EPS-3T) equipped with a thermostated cell holder.

Results

When the coenzyme models were added to a solution of indoleacetate (pH 6.0 in pure water), a faint yellow color appeared instantaneously. As is seen from Figure 1, the difference spectra indicate the appearance of a quite diffuse
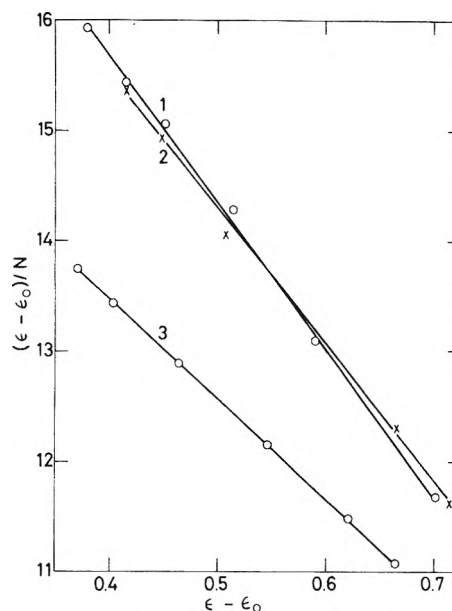
Figure 2. Foster–Hammick–Wardley plots for NAA (curve 1), NAT (curve 2), and NATH (curve 3) complexes with indoleacetate at 25°: [NAA] = [NAT] = [NATH] = 2 mM, [IA] = 27–60 mM, at 340 nm, pH 6.0.

TABLE I: Association Constants of Model Compounds of Coenzyme I with Indole Derivatives at 25° [a]

		K, M^{-1}		
Indole derivative	pH	NAA	NAT	NATH
Indoleacetate[b]	6.0	11.8 (860)	9.7 (940)	13.3 (790)
Indolepropionate[c]	6.8			13.5 (700)
Indolebutyrate[c]	6.5			10.1 (870)
Tryptamine hydrochloride[b]	6.0			1.08 (2000)
L-Tryptophan[b]	6.0			5.63 (750)

[a] [NAA] = [NAT] = [NATH] = 2 mM, [indole derivative] = 24–96 mM, in H_2O. The values in parentheses are molar extinction coefficients of charge-transfer complexes at 340 or 350 nm. [b] At 340 nm. [c] At 350 nm.

band as a long tail to the longer wavelength. The spectra are quite similar to those found for NAD^+–indoleacetate and other coenzyme models–indoleacetate mixtures.[5,6,8] It may be quite plausible that indoleacetate is charge donor and the pyridinium moieties of NAA, NAT, and NATH are charge acceptors.

The representative Foster–Hammick–Wardley plots are given in Figure 2. The $(\epsilon - \epsilon_0)N$ vs. $(\epsilon - \epsilon_0)$ plots yielded in all cases straight lines which imply the formation of 1:1 reversible complexes. The K values were obtained from the plot (see Table I). The K values of nicotinamide adenine dinucleotide (β isomer, βNAD^+) with tryptamine and L-tryptophan were reported by Alivisatos et al.[5] as 14.55 and 13.40 M^{-1}, respectively, in water at 27° and ionic strengths of 0.02–0.1 M. The K values of the present model compounds with tryptamine are fairly small compared with those of NAD^+, because of electrostatic repulsive forces between the donor and acceptor. The K values of the model compound, NATH, decreased in the order indole acetate (anionic) > L-tryptophan (neutral) > tryptamine (cationic). The salt effects on the K value of the NATH–IA complex are shown in Figure 3. As is clearly seen, K decreased
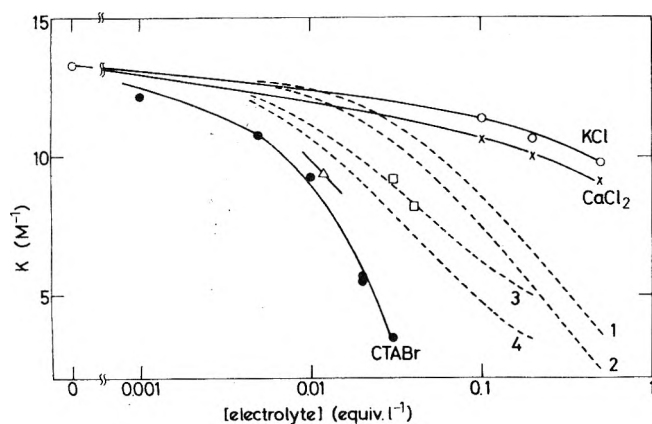
Figure 3. Electrolyte effects on complex formation between NATH and indoleacetate at 25°: [NATH] = 2 mM, [IA] = 30 mM, at 340 nm, pH 6.0; experiment (O) KCl, (X) CaCl$_2$, (□) DECS, (△) NaPSt, (●) CTABr; theory broken curve (1) KCl, (2) CaCl$_2$, (3) DECS (ξ = 1.4), (4) NaPSt (ξ = 2.85).

by addition of the simple, poly- and micelle electrolytes. The effects of poly- and micelle electrolytes were larger than those of simple electrolytes, which should be ascribed to high electrostatic potential of the micelles and macroions. The retarding actions of KCl and CaCl$_2$ are the so-called "secondary salt effect" on the equilibrium constant.[9] A quantitative discussion will be given later.

In Figure 4 the retarding effects of an anionic polyelectrolyte, NaPES, on the NATH-IA, NATH-IP, and NATH-IB complexations at 25° are shown. The changes of the equilibria are mainly due to the electrostatic interactions between NaPES and NATH, or between NaPES and indole derivatives. It should be mentioned that the retarding actions of NaPES or CTABr did not depend on the model compounds as is clearly shown in Figure 5.

The spectra of the NATH-Try system did not show any change by addition of NaPES or DECS, when the concentrations of NATH, Try, NaPES, and DECS were 2 mM, 96 mM, 20 mequiv l^{-1}, and 20 mequiv l^{-1}, respectively, and pH was 6.0. This may be due to the interactions between the polyelectrolytes and neutral tryptophan being very weak under the experimental conditions.

When the anionic polyelectrolyte, NaPES, was added to the NATH-TA·HCl system, the solution turned yellow and turbid. This shows that NaPES adsorbs both of NATH and TA by electrostatic attractive forces and strikingly enhances the complexation. The determination of the association constants in the presence of NaPES was not possible, of course.

The complexation of NATH-TA system was slightly enhanced by cationic polyelectrolyte, DECS, and KCl, as is seen in Table II. The calculated values were obtained using theories to be mentioned later (eq 7 and 17). The reason for the enhancement will be described later.

Discussion

Now let us discuss the influence of simple and polyelectrolytes on the association constant in terms of the "secondary salt effect" theoretically. First, the "secondary salt effect" of simple electrolyte is considered. When a complex is formed between ions D and A

$$D + A \rightleftarrows D{\cdot}A \tag{2}$$

the thermodynamic equilibrium association constant, K_0, is defined by
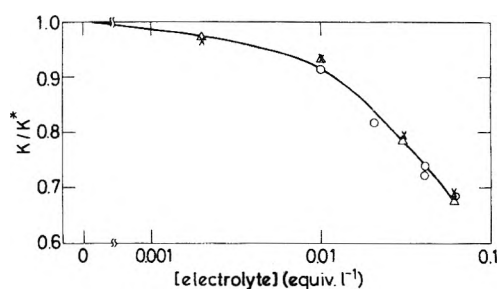
Figure 4. Retarding effect of NaPES on complex formation between NATH and indole derivatives at 25°: (O) IA, (△) IP, (X) IB; [NATH] = 2 mM, [IA] = [IP] = [IB] = 30 mM, at 340 nm, pH 6.0.
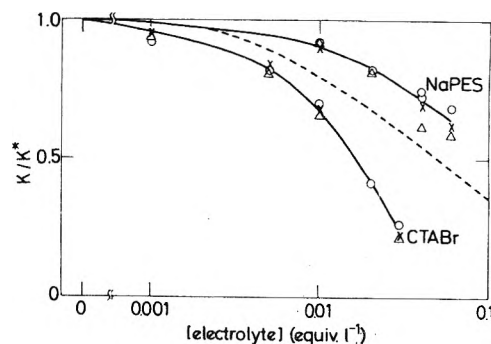
Figure 5. Retarding effect of NaPES and CTABr on complex formation between coenzyme model compounds and indoleacetate at 25°: [NAA] = [NAT] = [NATH] = 2 mM, [IA] = 30 mM, at 340 nm, pH 6.0; (O) NATH, (△) NAA, (X) NAT; (broken curve) Manning's theory for NaPES (ξ = 2.85).

TABLE II: Enhancing Effect of KCl and DECS on Complex Formation between NATH and Tryptamine Hydrochloride at 25°

Electrolyte	Electrolyte concn. equiv l^{-1}	K/K^* (obsd)[a]	K/K^* (calcd)[b]
KCl	0.02	1.04	1.18
	0.1	1.24	1.84
	0.2	1.41	2.73
DECS	0.0535	1.08	1.46
	0.0764	1.12	1.59
	0.115	1.18	1.76
	0.153	1.23	1.89
	0.191	1.30	1.98

[a] [NATH] = 2 mM, [TA·HCl] = 30 mM, at 340 nm, pH 6.0. The K value in the absence of foreign salt (K^*) is 1.08 M^{-1} (see Table I). [b] From eq 7 for KCl and eq 17 for DECS.

$$K_0 = a_{D{\cdot}A}/a_{D}{\cdot}a_{A} \tag{3}$$

where a denotes the activity. The activity is the product of the activity coefficient, f, and the concentration. Thus, eq 4 and 5 are obtained.

$$K_0 = \frac{[D{\cdot}A]}{[D][A]} \frac{f_{D{\cdot}A}}{f_D f_A} = K \frac{f_{D{\cdot}A}}{f_D f_A} \tag{4}$$

$$K = K_0 \frac{f_D f_A}{f_{D{\cdot}A}} \tag{5}$$

We can observe only the ratio of the *concentrations* of D, A, and D·A (not the ratio of the activities); the K values (not K_0) can be obtained by experiments. In very dilute

aqueous solutions, the activity coefficients, f_D, f_A, and $f_{D \cdot A}$, can be safely estimated by the Debye–Hückel theory as follows:

$$\log f_i = -0.509\ z_i{}^2 I^{1/2} \qquad \text{at } 25° \qquad (6)$$

where z_i is the valency of the ionic species, i, and I the ionic strength. From eq 5 and 6 we obtain

$$\log K = \log K_0 + 1.018 Z_D Z_A I^{1/2} \qquad (7)$$

Comparison of the observed K values for complex formation between unlikely charged ionic species in the presence of KCl and CaCl$_2$ with values calculated from eq 7 is demonstrated in Figure 3. It is seen that the observed retarding effect by CaCl$_2$ is larger than that by KCl, though the agreements between the observed and calculated K/K^* values are not so good, especially at high concentrations. This deviation may be due to (1) the ionic strength being so high (0.1–1) that the application of the Debye–Hückel theory is difficult and (2) both reactants, the donor and acceptor ions, being too large to be assumed as point charges.

Next, we discuss the "secondary salt effect" of polyelectrolytes on the interionic association constants between ionic species with unlike charges. In this case, $\log f_{D \cdot A}$ can safely be neglected compared with $\log f_D$ or $\log f_A$, because the activity coefficients of the electrically neutral complex are not sensitive to changes in ionic concentration. We, therefore, obtain the following relation from eq 5

$$\log K = \log K_0 + \log (f_D f_A) \qquad (8)$$

In discussing the polyelectrolyte effect, it is convenient to use the association constant without added salt, K^*, as a reference. K^* is then given as follows

$$\log K^* = \log K_0 + \log (f_D{}^* f_A{}^*) \qquad (9)$$

where the asterisk denotes the reference state. From eq 8 and 9, eq 10 is derived

$$\log K/K^* = \log (f_D f_A / f_D{}^* f_A{}^*) \qquad (10)$$

Since the mean activity coefficient, $f_\pm$, of the electrolyte $D^- A^+$ is given by $(f_D f_A)^{1/2}$, the following is obtained.

$$\log K/K^* = 2 \log f_\pm / f_\pm{}^* \qquad (11)$$

Manning developed a theoretical expression for $f_\pm$ of added simple salts in dilute polyelectrolyte solutions as follows (eq 48 of ref 20)

$$f_\pm{}^2 = \frac{\xi^{-1} n_e + n_s}{n_e + n_s} \exp\left[\frac{-\xi^{-1} n_e}{\xi^{-1} n_e + 2 n_s}\right] \qquad \xi > 1 \qquad (12)$$

where ξ is the charge density parameter given by the relation

$$\xi = e_0{}^2 / D k T b \qquad (13)$$

where b is the distance between the neighboring charges on an infinite linear line charged macroion, D the dielectric constant of solvent, and e_0 denotes the electronic charge. n_e and n_s are the equivalent concentrations (number of ions per cm^3) of macroions and the number of added simple salts per cm^3. Equations 11 and 12 are combined and the following relation is obtained.[21]

$$\ln K/K^* = \ln \frac{1 + \xi^{-1} X}{X + 1} - \frac{X}{X + 2\xi} \qquad (14)$$

where X is $n_e/(n_s + n_{R_1} + n_{R_2})$ and n_{R_1} and n_{R_2} denote the numbers of reactant 1 and reactant 2, respectively.

In Figure 5, a theoretical curve (broken line) for the retardation by NaPES calculated by eq 14 is shown. The parameter value of ξ was taken to be 2.85 for NaPES (b was calculated as 2.5 Å from the molecular structure). The dielectric constant, D, of water was estimated to be 78.54 from Wyman's data.[23] The theory fairly well predicts the observed strong retarding effect of polyelectrolytes. The observed K/K^* values were, however, a little larger than the calculated, which may be due to the fact that the complexation reactions occurred between comparatively large and complicated ions for which the theory is not valid. The comparison for the CTABr containing system with theory was not carried out, since the CTABr micelle is spherical,[24] for which theory is not valid either.

Figure 3 shows a comparison of the K values of the NATH–IA system with the theory in the presence of DECS and NaPSt. In the case of DECS the agreement between the theory (curve 1) and the observed values (open circle) is good. As is seen from the figure, the observed retarding effect of NaPSt is larger than that obtained from the theory (eq 14). This could be due to the strong hydrophobic nature of NaPSt;[12] the NATH molecules accumulate around the PSt macroion because the electrostatic and hydrophobic attractive forces between the hydrophobic PSt macroanion and the hydrophobic NATH univalent cation are extremely strong and are retarded from complexation with indoleacetate anions, which are far from the PSt macroion on account of the electrostatic repulsive forces between them.

We note here that eq 14 is also valid for the cyanide addition reaction of NAA studied earlier in the presence and absence of polyelectrolytes.[2] In Figure 6, the observed equilibrium association constant, K, was compared with the theory (eq 14). A good agreement between the theory and the experiment was obtained, particularly at low polymer concentration regions. Deviations at high polymer concentration regions may be due to the imperfection of Manning's limiting law in such a concentration range.

Now, we discuss the "secondary salt effect" of cationic polyelectrolytes on interionic association constants between cationic charged ionic species, such as between a coenzyme model compound and tryptamine. In this case, all activity coefficients, f_D, f_A, and $f_{D \cdot A}$, in eq 5 are those of coions of macroion given by (see ref 20)

$$f_D = f_A = \exp\left[-\frac{\xi^{-1} n_e}{2(\xi^{-1} n_e + 2 n_s)}\right] \qquad \xi > 1 \qquad (15)$$

and

$$f_{DA} = \exp\left[-\frac{2\xi^{-1} n_e}{\xi^{-1} n_e + 2 n_s}\right] \qquad \xi > 1 \qquad (16)$$

Thus, the $\ln K/K^*$ is expressed as follows:

$$\ln K/K^* = 1 \Big/ \left[1 + \xi\left(\frac{2}{X_1} + \frac{2}{X_2}\right)\right] \qquad (17)$$

where $X_1 = n_e/n_{R_1}$ and $X_2 = n_e/n_{R_2}$. n_{R_1} and n_{R_2} denote the numbers of reactant 1 and 2. The calculated values for the NATH–TA complexation in the presence of DECS using eq 17 are shown in Table II. The calculated values in the presence of KCl were derived using the Debye–Hückel theory (eq 7). As is seen from the table, the observed enhancing effect of simple and polyelectrolytes is supported by the theories, though the agreements between the observed and the calculated K/K^* values are not so good for both KCl and DECS. This deviation may be attributed to
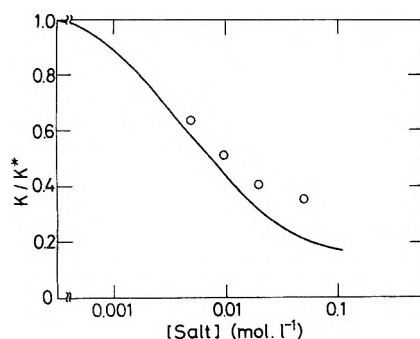
Figure 6. Comparison of observed and calculated K values for NAA–CN$^-$ reaction in the presence of NaPES at 25°: [NAA] = 0.198 mM, [KCN] = 4 mM, [KOH] = 1 mM; (O) NaPES added, observed (from ref 2); (——) calculated.

NATH and TA being too large to be assumed as point charges and the high concentrations of KCl and DECS.[25]

Next, we discuss the temperature dependence of the association constants. The K value for the NAA–IA system decreased with increasing temperature. This reflects the fact that reaction 1 is exothermic. Table III gives the free energy (ΔG), enthalpy (ΔH), and entropy (ΔS) of NAA–IA complex formation. By addition of simple or polyelectrolytes, ΔG increased, which is in agreement with the observed changes of K. Both ΔH and ΔS decreased with added electrolytes, though slightly.

The thermodynamic parameters for the interionic complexation can be computed theoretically from the Debye–Hückel theory and from the Manning theory; ΔG and ΔH in the presence of polyelectrolyte were obtained from eq 14 as follows:

$$\Delta G - \Delta G^* = RT\left[-\ln\frac{\xi^{-1}X+1}{X+1} + \frac{X}{X+2\xi}\right] \quad (18)$$

$$\Delta H - \Delta H^* = RT\left[\frac{X}{X+\xi} - \frac{2\xi X}{(X+2\xi)^2}\right]\left(1+\frac{T}{D}\frac{dD}{dT}\right) \quad (19)$$

where the asterisk denotes the absence of added polyelectrolyte. The changes in ΔG and ΔH of the complex formation by the addition of simple electrolytes (KCl or CaCl$_2$ in the present case) are given by the Debye–Hückel theory.

$$\Delta G - \Delta G^* = -2RT\sqrt{2\pi N/1000}\left(\frac{e_0^2}{DkT}\right)^{3/2} \times$$

$$(\sqrt{n_{R_1}+n_{R_2}+[(z^2+z)/2]n_s} - \sqrt{n_{R_1}+n_{R_2}}) \quad (20)$$

$$\Delta H - \Delta H^* = 3RT\sqrt{2\pi N/1000}\left(\frac{e_0^2}{DkT}\right)^{3/2}\left(1+\frac{T}{D}\frac{dD}{dT}\right) \times$$

$$(-\sqrt{n_{R_1}+n_{R_2}+[(z^2+z)/2]n_s} - \sqrt{n_{R_1}+n_{R_2}}) \quad (21)$$

ΔS can be determined by

$$\Delta G = \Delta H - T\Delta S \quad (22)$$

In Table III, the calculated values are also compiled. The structural parameter, ξ, was taken to be 1.37 for DECS (b was estimated as 5.2 Å from the molecular structure). As is clear from the table, the agreement between theory and experiment was excellent; particularly the observed ΔH values were accurately predicted by the electrostatic interaction theories, that is, eq 19 and 21. The larger changes of ΔG, ΔH, and ΔS by the addition of CaCl$_2$ compared with KCl are also accounted for by eq 21. From the agreements, we can state that the *electrostatic interactions* between

TABLE III: Thermodynamic Constants of Complexation between NAA and Indoleacetate at 25° [a]

Elec-trolyte	ΔG [b]		ΔH [b]		ΔS [b]	
	Obsd	Calcd	Obsd	Calcd	Obsd	Calcd
None	−1.47	(−1.47)	−4.44	(−4.44)	−10.0	(−10.0)
KCl	−1.34	−1.05	−4.67	−4.68	−11.2	−12.2
CaCl$_2$	−1.30	−0.88	−4.80	−4.75	−11.7	−12.9
DECS	−1.20	−1.24	−4.48	−4.49	−11.0	−10.9
NaPES	−1.19	−1.10	−4.44	−4.47	−10.9	−11.4

[a] [NAA] = 2 mM, [IA] = 30 mM, at 340 nm, pH 6.0. [b] The units of ΔG and ΔH are in kcal mol^{-1}, and ΔS in eu. The experimental uncertainty is believed to be ±0.05 for ΔG, ±0.2 for ΔH, and ±2 for ΔS.

the complex-forming ions and added electrolyte are most significant for complex formation in the present cases.

From the above theoretical considerations, it is possible to conclude that the polyelectrolyte influence under consideration on the complex formation constant is due to the changes of the activities of the complex forming ions, i.e., the "secondary salt effect". This conclusion implies that the accumulation or condensation effect of ions in the polymer domain in the narrow sense of the term is not basically an appropriate factor. It should be noted that the same conclusion has been reached from a theoretical consideration (on the bases of the Debye–Hückel theory and the Manning theory) on the rate-enhancing effect of a *cationic* polyelectrolyte on ionic reactions between *cationic* species.[26]

References and Notes

(1) Presented at the 22nd Annual Meeting of the Society of High Polymers, Kyoto, Japan, May 1973.
(2) T. Okubo and N. Ise, *J. Am. Chem. Soc.*, **95**, 4031 (1973).
(3) B. Pullman, Ed., "Molecular Association in Biology", Academic Press, New York, N.Y., 1968.
(4) M. A. Slifkin, "Charge-Transfer Interactions of Biomolecules", Academic Press, London, 1971.
(5) S. G. A. Alivisatos, F. Ungar, A. Jibril, and G. A. Mourkides, *Biochim. Biophys. Acta*, **51**, 361 (1961).
(6) G. Cilento and P. Tedeshi, *J. Biol. Chem.*, **236**, 907 (1961).
(7) S. Shifrin, *Biochemistry*, **3**, 829 (1964).
(8) D. A. Deranleau and R. Schwyzer, *Biochemistry*, **9**, 126 (1970).
(9) See, for example, J. N. Brønsted, *J. Chem. Soc.*, **119**, 574 (1921); V. K. LaMer and H. B. Friedman, *J. Am. Chem. Soc.*, **52**, 876 (1930); A. R. Olson and T. R. Simonson, *J. Chem. Phys.*, **17**, 348 (1949).
(10) N. Ise, *Adv. Polym. Sci.*, **7**, 536 (1971).
(11) T. Okubo and N. Ise, *Proc. R. Soc. (London)*, *Ser. A*, **327**, 413 (1972).
(12) T. Okubo and N. Ise, *J. Am. Chem. Soc.*, **95**, 2293 (1973).
(13) N. Ise and Y. Matsuda, *J. Chem. Soc., Faraday Trans. 1*, **69**, 99 (1973).
(14) T. Okubo and N. Ise, *J. Biol. Chem.*, **249**, 3563 (1974).
(15) T. Okubo and N. Ise, *Tetrahedron Lett.*, 321 (1973).
(16) S. Harada and K. Arai, *Makromol. Chem.*, **107**, 78 (1967).
(17) Y. Negi, and S. Harada, and O. Ishizuka, *J. Polym. Sci.*, **5**, 1951 (1967).
(18) R. Foster, D. L. Hammick, and A. A. Wardley, *J. Chem. Soc.*, 3817 (1953).
(19) M. T. A. Behme and E. H. Cordes, *Biochim. Biophys. Acta*, **108**, 312 (1965).
(20) G. Manning, *J. Chem. Phys.*, **51**, 924 (1969).
(21) The similar equation was derived for the reaction rate coefficients in the presence of polyelectrolyte ("primary salt effect").[22]
(22) K. Mita, S. Kunugi, T. Okubo, and N. Ise, *J. Chem. Soc., Faraday Trans. 1*, **71**, 936 (1975).
(23) J. Wyman, *Phys. Rev.*, **35**, 623 (1930).
(24) K. Shinoda, T. Nakagawa, B. Tamamushi, and T. Isemura, Ed., "Colloidal Surfactants", Academic Press, New York, N.Y., 1963.
(25) At first sight, it is perplexing to find the enhancement of complexation between cationic species by a cationic polyelectrolyte. However, we recall that complexation can be enhanced by an increase in ionic strength, which can be accomplished by additions of not only 1–1 type simple electrolytes, but also salts of multivalent cations and monovalent anions, in other words, the symmetry of the electrolytes does not matter in the observed enhancement. Polyelectrolytes are highly unsymmetrical electrolytes.
(26) K. Kim, M. Shikata, and N. Ise, to be submitted for publication.

Application of Passynsky's Method for Determination of Hydration Numbers of Electrolytes in Water–Organic Mixtures

Stefan Ernst and Bogusława Jeżowska-Trzebiatowska*

*University of Wrocław, Institute of Chemistry, Wrocław, Poland (Received November 27, 1974;
Revised Manuscript Received May 19, 1975)*

Passynsky's method was applied for the determination of hydration numbers of uranyl salts in aqueous solutions from ultrasonic velocity and density measurements. The hydration numbers of uranyl salts in water–dioxane mixtures were determined by a modification of the above method. Two different procedures were applied and discussed for water–dioxane mixtures.

In order to obtain some information on the structure of uranyl compounds in water and mixed water–dioxane solvents, especially the hydration of ions and ion associates in those systems, the latter have been studied by means of ultrasonic measurements. This paper presents the treatment of data based on the well-known Passynsky's method (in the case of aqueous solutions) and on a modification of it for the determination of hydration numbers of electrolytes in water–dioxane mixtures.

The compressibilities of solutions of uranyl sulfate and nitrate in water and water–dioxane mixtures have been calculated from sound velocity and density measurements. The measurements were carried out with an ultrasonic interferometer at 1 MHz and at constant temperature of 25 ± 0.05°. All other experimental details were described elsewhere.[1] Typical results obtained for uranyl sulfate in aqueous solutions are given in Figure 1. Similar curves have been obtained for all other systems investigated.

The sound velocity decreases with increasing electrolyte concentration both in aqueous solutions and in water–dioxane mixtures. Aqueous solutions of a few other salts of heavy metals also show such an abnormal behavior which according to Allam and Lee[2] may be due, among other things, to ion pair formation. Nevertheless, the β values decrease with increasing electrolyte concentration similarly as in the case of all other known electrolyte solutions. This decrease reflects the compressibility change of the solvent caused by solvation and affords possibilities for computation of hydration numbers.

Treatment of Data and Results

Aqueous Solutions. The hydration numbers for aqueous solutions were determined using Passynsky's method[3] based on the following assumptions: (1) The compressibilities of electrolyte ions and molecules together with their hydration spheres are equal to zero, $\beta_2 = 0$. (2) The apparent molar compressibility of the dissolved electrolyte is equal to the loss of the compressibility of water, i.e., to the number of moles of water bound by one electrolyte mole times the molar compressibility of pure water

$$\varphi_k = \frac{V\beta - n_1 \bar{V}_1{}^0\beta_1{}^C}{n_2} = -n_h \bar{V}_1{}^0\beta_1{}^0$$

where φ_k is the apparent molar compressibility of the electrolyte; V, $\bar{V}_1{}^0$ are the volume of solution and the molar volume of water, respectively; β, $\beta_1{}^0$ are the compressibility coefficients of the solution and water, respectively; n_2, n_1

are the numbers of electrolyte and water moles in volume V; and n_h is the hydration number of the electrolyte. Thus n_h can be calculated from the formula

$$n_h = \frac{n_1}{n_2}\left(1 - \frac{V\beta}{n_1\bar{V}_1{}^0\beta_1{}^0}\right) \tag{1}$$

Equation 1 yields true hydration numbers when extrapolated to infinite dilution. However, hydration numbers calculated from eq 1 often prove to be concentration independent up to moderate electrolyte concentrations (1.5 N for monovalent ions,[4] as well as for the uranyl salts investigated). In this case a graphical method may also be employed according to the following equation:

$$\frac{10^3\beta}{c_1} = \bar{V}_1{}^0\beta_1{}^0 - n_h\frac{\bar{V}_1{}^0\beta_1{}^0M_1}{10^3}m \tag{2}$$

where c_1 is the molarity of water (moles of water per liter of solution); m is the molality of the electrolyte (moles of electrolyte per 1000 g of solvent); and M_1 is the molar weight of water. A plot of this type for an aqueous uranyl sulfate solution is shown in Figure 2.

Electrolyte Solutions in Water–Dioxane Mixtures. In the case of mixed solvents, some difficulties arise since both solvent components may participate in the formation of solvation shells. In order to calculate hydration numbers from experimental data, we have used a method similar to that of Passynsky making two additional assumptions. (1) Ions and ion pairs are solvated exclusively, or at least mainly, by the stronger solvating component (water). (2) Even if the organic component does participate in the formation of the first layer around the ion, the electrostriction of its molecules by the ions does not markedly influence the compressibility of the solvent. Both of the above assumptions seem to be justifiable in the case of the solutions studied containing 20 and 45 wt % of dioxane for the following reasons. (1) Dioxane is a much weaker solvating agent than water. (2) The mole ratio dioxane:water equals approximately 1:18 and 1:6 in the solvent mixtures containing 20 and 45 wt % dioxane, respectively. (3) Because of the size and structure of the dioxane molecules, their electrostriction in the electric field of the ions should be small in comparison with the electrostriction of water molecules, i.e. according to the model of Bockris and Reddy[5] dioxane molecules, although contributing to the coordination number (CN), are not associated with the ions such as water molecules and therefore do not contribute to the solvation number (SN) of the electrolyte.
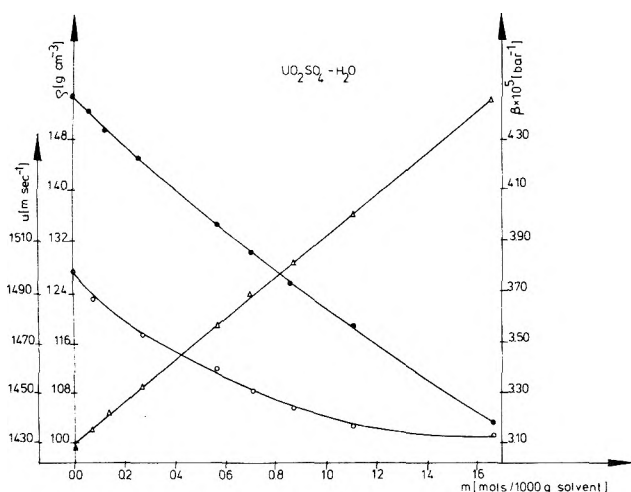
Figure 1. The concentration dependence of density ($\triangle$), ultrasonic velocity (O), and compressibility ($\bullet$) of aqueous UO_2SO_4 solutions.
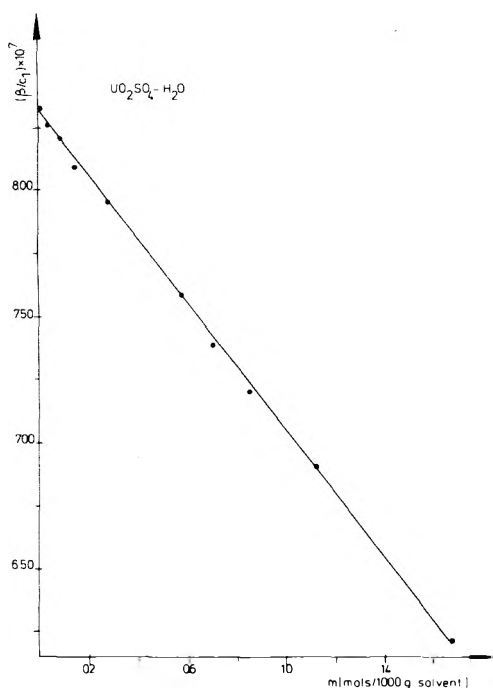
Figure 2. The graphical determination of the hydration number of UO_2SO_4 in aqueous solutions according to eq 2. The slope equals $-n_h \bar{V}_1^0 \beta_1^0 M_1 \times 10^{-3}$.

The assumptions of Passynsky together with the two additional ones lead to the following equation:

$$\varphi_k \equiv \frac{V\beta - V_s\beta_s}{n_2} = \frac{V\beta - (n_3\varphi_{k3} + n_1\bar{V}_1^0\beta_1^0)}{n_2} = -n_h\bar{V}_1^0\beta_1^0$$

where φ_k is the apparent molar compressibility of the solute (electrolyte); $V_s\beta_s$ is the compressibility of the solvent; φ_{k3} is the apparent molar compressibility of dioxane in the solution; and n_3 is the number of moles of dioxane in volume V. Thus

$$n_h = \frac{c_1}{c_2} + \frac{c_3\varphi_{k3} - 10^3\beta}{c_2\bar{V}_1^0\beta_1^0} \qquad (3)$$

where c_i, c_2, and c_3 are the concentrations of water, electrolyte, and dioxane in moles per liter solution, respectively. In general, φ_{k3} depends on the solvent composition and on
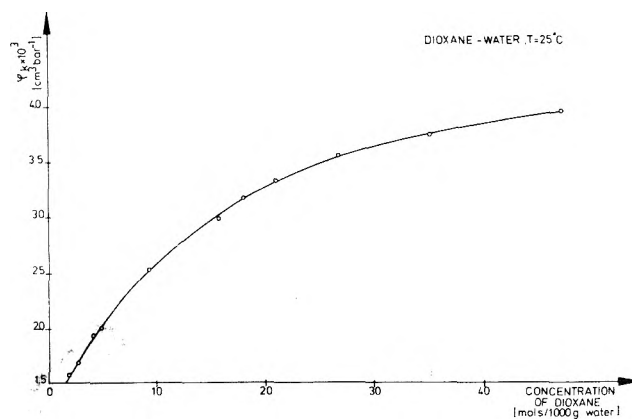
Figure 3. Apparent molar compressibility of dioxane in aqueous solutions.

the electrolyte concentration. In order to determine this value and its dependence on solvent composition, ultrasonic velocities of water–dioxane mixtures as well as their densities have been measured and the apparent molar compressibilities of dioxane calculated at different concentrations of the organic component. The apparent molar compressibilities of dioxane corresponding to the solvent compositions, φ_{k3}^0, have been determined from the plot shown in Figure 3.

Two different procedures may be used for the calculation of hydration numbers from eq 3.

Procedure 1. Because of the relatively slow variation of φ_{k3} with solvent composition, the approximation $\varphi_{k3} \approx \varphi_{k3}^0$ seems to be justified, i.e., the apparent molar compressibility of dioxane in the pure solvent mixture (without the electrolyte) may be used instead of the true φ_{k3} value. Assuming a hydration number of 10, the changes in φ_{k3} caused by hydration do not exceed 1% of φ_{k3}^0 even for the highest uranyl salt concentrations studied. Thus, if φ_{k3} is considered to be independent of the electrolyte concentration, the hydration numbers may be calculated from eq 3, by setting $\varphi_{k3} = \varphi_{k3}^0$. For a concentration range in which n_h remains constant (i.e., does not change with electrolyte concentration), a graphical method (Figure 1) may be applied according to the following equations:

$$\frac{10^6\beta}{c_3M_3 + c_1M_1} = \frac{10^3(n_3\varphi_{k3} + n_1\bar{V}_1^0\beta_1^0)}{n_3M_3 + n_1M_1} - n_h\bar{V}_1^0\beta_1^0m \qquad (4)$$

or

$$10^3\beta = (c_3\varphi_{k3} + c_1\bar{V}_1^0\beta_1^0) - n_h\bar{V}_1^0\beta_1^0c_2 \qquad (5)$$

where M_3 is the molar weight of dioxane and all the other symbols have the same meaning as before.

Procedure 2. If the variation of φ_{k3} with the electrolyte concentration is taken into account (an amount of water proportional to the electrolyte concentration is "removed" from the solvent which results in an increase of the organic component concentration) an iteration procedure may be applied. The concentration dependence of the apparent compressibility of the organic component in the vicinity of φ_{k3}^0 (Figure 3) can be represented by a polynomial: $\varphi_{k3} = \bar{\varphi}_{k3}^{(0)} + \bar{\varphi}_{k3}^{(1)}(m_3^0 - m_3) + \bar{\varphi}_{k3}^{(2)}(m_3^0 - m_3)^2 + \bar{\varphi}_{k3}^{(3)}(m_3^0 - m_3)^3$, where m_3^0 is the molality of the organic component in the pure solvent and m_3 is the molality of the organic component in a certain vicinity of m_3^0. Starting with the approximation $\varphi_{k3} \approx \varphi_{k3}^0$, n_h is calculated using eq 3. In the next approximations φ_{k3} is corrected taking into ac-
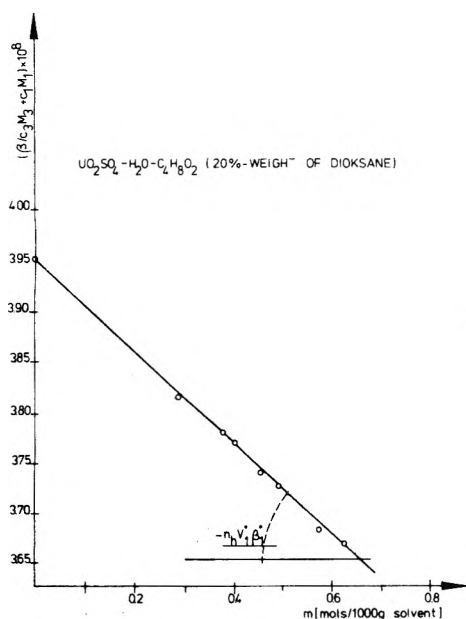
Figure 4. The graphical determination of the hydration number of UO_2SO_4 in a water–dioxane mixture containing 20 wt % dioxane according to eq 4. The slope equals $-n_h \bar{V}_1^0 \beta_1^0$.

TABLE I: Hydration Numbers of Uranyl Sulfate and Uranyl Nitrate in Water and Water–Dioxane Mixtures

wt % dioxane	UO_2SO_4 Procedure 1	UO_2SO_4 Procedure 2	$UO_2(NO_3)_2$ Procedure 1	$UO_2(NO_3)_2$ Procedure 2
0	10.3 ± 0.60^a		11.9 ± 0.71	
20	6.3 ± 0.07	6.7 ± 0.30	6.3 ± 0.15	6.6 ± 0.30
45	4.8 ± 0.06	5.5 ± 0.18	5.8 ± 0.17	7.1 ± 0.43
70				~ 10.9

^{a} Mean values for the concentration range studied with confidence limits corresponding to the 95% confidence level.

count the corrected solvent composition (i.e., and the amount of water in the solvent decreased by the amount bound by the electrolyte) according to the scheme:

1. approximately $\varphi_{k3}^{(1)} = \varphi_{k3}^0 \rightarrow n_h^{(1)}$

2. approximately $n_h^{(1)} \rightarrow \varphi_{k3}^{(2)} \rightarrow n_h^{(2)}$

.

.

n. approximately $n_h^{(n-1)} \rightarrow \varphi_{k3}^{(n)} \rightarrow n_h^{(n)}$

A computer program was prepared for the iteration procedure. Our results indicate that the application of procedure 1 leads to hydration numbers somewhat smaller than those obtained by procedure 2 (Table I).

The constancy of the hydration numbers in the whole concentration range studied (except of the $UO_2(NO_3)_2$ solution in the 70% dioxane–water mixture where the hydration number varies with the electrolyte concentration from about 14 to 9.8) suggests a predominantly outer-sphere association not accompanied by any (or only by an insignificant) loss of hydration water molecules. Also in the case of other divalent metal monosulfate complexes, the predomi-

Figure 5. Hydration numbers of UO_2SO_4 and $UO_2(NO_3)_2$ in water–dioxane mixtures. The hydration number of $UO_2(NO_3)_2$ in the mixture containing 70 wt % dioxane decreases from 14 to 9.8 in the concentration range studied.

nation of outer-sphere association is indicated by the results obtained from a kinetic analysis of the multiple relaxation spectra.[6] The mean hydration numbers found for aqueous solutions agree relatively well with those obtained by other authors for the uranyl ion (7.35^7 and 4^8), for the sulfate anion ($6,^9$ 7.9, and 8.8^2), and for the nitrate anion ($6^{10,11}$).

No comparative data are available for water–dioxane solutions, but the decrease of the hydration numbers with increasing dioxane concentration seems to be quite reasonable since the water structure is markedly promoted by dioxane up to the mole fraction of the organic component $X \simeq 0.2$.[12-15] Dioxane molecules may also partially replace water molecules in the coordination sphere of the ions decreasing the number of solvating molecules (SN) if the coordination number (CN) remains constant or even decreases because of steric factors. The enhancement of the water structure by dioxane is opposed by the electrolyte provided it contains a structure breaking ion (e.g., NO_3^{-} [16]) which leads to a slight increase of hydration at higher dioxane concentrations (45 wt %, i.e., still below $X = 0.2$), while the hydration of UO_2SO_4 containing the structure ordering anion SO_4^{2-} decreases continuously up to 45 wt % of dioxane (Figure 5).

It should be noted that the above method may be useful only for studying electrolyte solutions in water–organic mixtures containing an organic component of low solvating properties compared to those of water. Also, some difficulties may arise in the case of very small hydration numbers because the hydration number is then calculated as a small difference between two much greater values (eq 4).

References and Notes

(1) S. Ernst and B. Jeżowska-Trzebiatowska, *Z. Phys. Chem.*, in press.
(2) D. S. Allam and W. H. Lee, *J. Chem. Soc.* 6049 (1964); 5 (1966).
(3) A. C. Passynsky, *Zhur. Fiz. Khim.* **11**, 608 (1938); **20**, 981 (1946).

(4) J. O'M Bockris and P. P. S. Saluja, *J. Phys. Chem.*, **76**, 2140 (1972).
(5) J. O'M Bockris and A. K. N. Reddy, "Modern Electrochemistry", Vol. I, Plenum Press, New York, N.Y., 1970.
(6) N. Purdie and M. M. Farrow, *Coord. Chem. Rev.*, **11**, 189 (1973).
(7) E. Glueckauf, *Trans. Faraday Soc.*, **51**, 1235 (1955).
(8) A. Fratiello, V. Kubo, R. E. Lee, and R. E. Schuster, *J. Phys. Chem.*, **74**, 3726 (1970).
(9) J. Stuehr and E. Yeager in "Physical Acoustics", Vol. II, W. P. Mason, Ed., Academic Press, New York and London, 1965.
(10) A. J. Rutgers and Y. Hendrikx, *Trans. Faraday Soc.*, **58**, 2184 (1962).

(11) A. J. Rutgers, W. Pigole, and Y. Hendrikx, *Chem. Weekbl.*, **59** 33 (1953).
(12) J. C. Clemett, *J. Chem. Soc.* 455 (1966); 458, 761 (1969).
(13) T. Erdey-Grúz and B. Lévay, *Acta Chim. Acad. Sci. Hung.*, **69**, 215 (1971).
(14) A. M. Shkodin, N. K. Levitskaya, and V. A. Lozhnikov, *Zh. Struct. Khim.*, **38**, 1006 (1968).
(15) J. R. Goates and R. J. Sullivan, *J. Phys. Chem.*, **62**, 188 (1958).
(16) E. R. Nightingale, Jr., in "Chemical Physics of Ionic Solutions", B. E. Conway and R. C. Barradas, Ed., Wiley, New York, N.Y., 1966, p 87.

A Plastic–Crystalline Phase of Ethane

D. F. Eggers, Jr.

Department of Chemistry, University of Washington, Seattle, Washington 98195   (Received June 16, 1975)

Visual and dilatometric observations are reported for the solidification of liquid ethane. A plastic–crystalline phase has been detected, and it is stable from the solidification temperature of the liquid to a temperature $0.4_5°$ lower. The melting point of ethane, as reported by the majority of earlier workers, agrees with our transition temperature between the low-temperature solid and the plastic crystal. All crystals of the low-temperature solid observed in polarized light showed sharp extinctions, and this means the crystal cannot be uniaxial as is presently accepted.

Introduction

We had done some infrared spectroscopic work on ethane, and found some definite evidence that the crystal structure could not be that which was reported by Mark and Pohland.[1] In seeking further evidence regarding solid ethane, we observed the slow solidification of the liquid. A new phase, which we believe to be a plastic crystal, was observed; this has apparently not been previously reported. We record here some optical and dilatometric observations on the two solid phases of ethane and briefly discuss the implications concerning the structure of the low-temperature solid.

Experimental Section

Phillips research grade ethane was used, with stated purity of 99.92%. We were unable to detect any impurities in it by infrared spectroscopy, and the only purification employed was to pump several times on the frozen solid. The dilatometer was made from a Pyrex tube of 1.94 mm i.d. with an attached bulb to permit condensation of about 0.5 ml of liquid. The position of the meniscus was measured with a cathetometer through the walls of a clear glass dewar that contained liquid oxygen or oxygen–nitrogen mixtures. Slow raising of the coolant level around the dilatometer sufficed to freeze the sample.

Visual observations were conducted with the ethane condensed in a cell made entirely of fused quartz; the sample thickness was 0.15 mm. This cell was connected through a quartz–Pyrex graded seal to a bulb of about 400 ml volume; a stopcock and ground joint allowed filling of the system. To ensure a more uniform temperature, the quartz cell was enclosed in a split aluminum cylinder of 2.4 cm diameter and 12 cm long; there were holes drilled through both halves of the cylinder in the vicinity of the cell to permit observation of its contents. The halves of the cylinder were held together with bolts, and the mating faces were milled out to fit fairly snugly around the cell. The aluminum cylinder and ethane cell were placed in a special clear glass dewar whose inner diameter was only 0.5 mm larger than the aluminum cylinder. There was also a thermometer well in the cylinder for a silicon diode that was used as the main device for recording temperature and temperature changes. The dewar was provided with a heating coil between the inner and outer walls.

This special dewar was immersed in liquid nitrogen contained in a larger, conventional clear glass dewar. The well of the inner dewar contained liquid oxygen to promote thermal contact; the heater was supplied with a small ac voltage from a variac and transformer. Adjustment of the variac permitted the temperature of the sample to be maintained constant to within 0.01°, or it could be very slowly warmed or cooled.

The silicon diode was a 1N5614 Semtech unit. A simple circuit was constructed for supplying the diode with a small dc current of 0.4 mA that was carefully regulated. The resulting voltage drop across the diode near 90 K was only slightly less than the voltage of a standard cell; this difference voltage was balanced against the voltage across some precision resistors carrying a known current. The net voltage was directly recorded on a 10-mV strip-chart recorder. Since the diode voltage under these conditions changes by 2.14 mV/deg, it is easily possible to see a change of 0.01°. The nonlinearity of the voltage as a function of temperature is negligible over the small temperature range of interest here. The calibration of the diode was carried out by comparing it with a platinum resistance thermometer that

was supplied by Leeds and Northrup and certified by the National Bureau of Standards.

One problem with the use of the diode is sensitivity to light. In earlier exploratory work the diode was not enclosed in a thermometer well; simply turning on and off the observation light bulb produced voltage changes equivalent to temperature changes of several tenths of a degree. With proper shielding from light the diode has been found to be remarkably stable and reproducible as a thermometer.

Only enough ethane was used to half-fill the quartz cell, and it was tilted with the long axis almost horizontal during the cool-down and freezing process. Upon returning the cell to the vertical position, we had the solid ethane confined to one side of the cell. The melting could then be readily observed since the liquid as formed would flow to the bottom of the cell. Pieces of sheet polaroid were placed in back and in front of the outer clear glass dewar; the ethane in the cell was viewed through the polaroids with the aid of a light bulb in back of the assembly. The polaroids were kept in the crossed position by rotating them simultaneously.

Results

Careful cooling of the liquid invariably first produced a solid that appeared uniformly dark for all rotations of the (crossed) polaroids; the liquid phase yielded similar results. Further cooling transformed the solid to another form that produced definite directions of sharp extinctions in small areas as the polaroids were rotated. By a careful adjustment of the temperature, regions of single crystal with areas of several mm^2 could be produced; they displayed striking first-order interference colors. This anisotropic solid is presumed to be the familiar solid form.

Careful warming of the anisotropic solid invariably produced the isotropic solid before the liquid phase was formed. The isotropic solid phase must therefore be thermodynamically stable and not a metastable phase formed only under certain special conditions.

The dilatometer showed a decrease in volume accompanying the change from liquid to isotropic solid of about 2.7 ± 0.2%. We also attempted a direct measurement of the volume decrease from liquid to anisotropic solid, but on repeated attempts these solids displayed numerous large cracks. The value that we obtained, about 9%, is thus a lower limit to the true magnitude. This may be compared with a value of 11.1% deduced from the measured values for the heat of fusion, the change of melting temperature with pressure, and use of the Clapeyron equation.[2,3]

It is interesting that we have never, in the course of many solidifications of ethane, either in the quartz cell, in quartz tubes of several millimeter diameter, or in Pyrex tubes, observed fractures of any type in the isotropic solid. Very careful observation of the solidification in the quartz cell showed some faint needles at the liquid–isotropic solid interface; however, after the entire sample had solidified, only the perfectly clear solid could be seen. These observations, together with the absence of any rotation of plane-polarized light, strongly suggest that this form is a plastic crystal.

The temperature of the solid–solid transition was found to be 89.82 ± 0.02 K; the melting point of the isotropic solid was found to be 90.27 ± 0.02 K. The indicated uncertainties reflect mainly the difficulty of telling exactly when the sample was entirely transformed to isotropic solid or to liquid upon warming, rather than uncertainty in measured

temperature. It is interesting to note that Witt and Kemp[2] gave 89.87 K as the melting point; more recently Burnett and Muller[4] reported 89.82 K based on an NMR method. Both of these values agree quite well with our temperature of the solid–solid transition. On the other hand, Clusius and Weigand reported a melting point of 90.35 K; our value is in essential agreement.

Discussion

The apparent absence of earlier observations of the plastic–crystalline phase is puzzling. Witt and Kemp[2] found a substantial increase in the heat capacity of solid ethane from about 67 K up to the melting point, and they ascribed the increase to a premelting phenomenon due to about 0.5% impurity. Apparently no analysis of the sample was done to verify the existence of the impurity. It is possible that their sample was actually more pure, and that the rising heat capacity is associated with increased motions of the molecules as the solid–solid transition temperature is approached. It is also noteworthy that the heat capacity of the solid was always measured by Witt and Kemp with sufficient heat input to raise the temperature by approximately 2 or 3°. The initial temperature of the highest such measurement on the solid was 86.73 K; the final temperature was 88.63 K. Thus the sample would not have reached the solid–solid transition temperature.

Many years ago Wahl[5] reported his observations on the freezing of ethane to form the anisotropic solid. He deduced that it was uniaxial since he found some crystal sections that remained dark as the crossed Nicol prisms of his polarizing microscope were rotated. We have tried to repeat this observation numerous times, omitting the microscope, and had no success. That is, in a sample completely converted to the low-temperature phase, all parts were observed to have definite extinction directions. We attempted to convert a large part of the sample to one single crystal but were never successful; however, the presence of a number of different single crystals at the same time provided more opportunity to verify the uniaxial nature of the solid, if indeed it were. We can only report the consistent failure to observe even one small crystal that did not rotate polarized light.

We suggest that Wahl might very well have had part of his sample transformed into the isotropic solid, and this would of course lead to the erroneous conclusion that the (single) solid phase was uniaxial. It should be noted that Mark and Pohland[1] used Wahl's result, together with their X-ray powder pattern from solid ethane, to deduce the crystal symmetry of space group $D_{6h}{}^4$. However, if the crystal is not uniaxial, a space group of such high symmetry can no longer be a possibility. Mark and Pohland's work was done at a time when the true symmetry of the isolated ethane molecule was not firmly established. Thus the site symmetry for ethane molecules in the $D_{6h}{}^4$ space group is D_{3h}; we now know that the molecular symmetry is D_{3d}.

The infrared-active fundamentals of pure solid ethane show splittings in the spectrum near 60 K.[6] We have also studied isotopic mixtures and found that most of the degenerate fundamentals are still split even when the molecule of interest, e.g., C_2D_6, is isolated in a large excess of C_2H_6. This observation conclusively rules out the existence of a threefold rotation symmetry axis that passes through the ethane molecule in the crystal; it is in agreement with our failure to observe evidence of uniaxial crystals in the anisotropic solid.

We have made some attempts to observe the infrared and Raman spectra of the isotropic solid; thus far we were not successful. In the infrared there is a problem arising from the nonzero vapor pressure of the ethane; it sublimes to a slightly colder region of the conventional low-temperature cell. We have designed a special infrared cell that incorporates two cold windows with provision for introducing ethane between them and isolating the sample from the insulating vacuum. For Raman work the sample was contained in a quartz tube connected to an expansion bulb; cooling was done by a stream of cold nitrogen gas. It was not possible to hold the sample temperature in the 0.4° range of stability for the isotropic phase for more than a few minutes. A different cell, with provision for much better temperature control, has been designed; we plan to report the infrared and Raman spectra of the isotropic solid phase in a separate paper.

In some work on condensed phases of ethane at high pressures, Webster and Hoch[7] reported a solid–solid phase transition; solid I, which lies between the liquid and solid II, has a range of stability of about 5° at a pressure of 1 kbar. These workers suggested that there must be a solid I–solid II–liquid triple point between 0 and 1 kbar; they were unable to conduct measurements in this region. We believe that the isotropic solid phase that we have observed

is the same as their solid I phase, and that there is no triple point involving these phases in the range of pressures from 0 to 5 kbars, the upper limit of their measurements.

It would be most interesting to have additional measurements of the heat capacity of highly purified ethane in the vicinity of the solid–solid transition temperature as well as near the melting point. We suspect that the enthalpy change of the solid–solid transition may be substantially larger than the enthalpy change of melting.

References and Notes

(1) H. Mark and E. Pohland, *Z. Kristallogr.*, **62**, 103 (1925).
(2) R. K. Witt and J. D. Kemp, *J. Am. Chem. Soc.*, **59**, 273 (1937).
(3) K. Clusius and K. Weigand, *Z. Phys. Chem.*, **B46**, 1 (1940).
(4) L. J. Burnett and B. H. Muller. *J. Chem. Eng. Data*, **15**, 154 (1970).
(5) W. Wahl, *Z. Phys. Chem.*, **88**, 133 (1914).
(6) S. B. Tejada and D. F. Eggers, Jr., to be submitted for publication.
(7) D. S. Webster and M. J. R. Hoch, *J. Phys. Chem. Solids*, **32**, 2663 (1971). We are grateful to Professor W. A. Steele for pointing out the relation of this work to ours.

Effect of the Potential Correlation Function on the Physical Adsorption on Heterogeneous Substrates

P. Ripa and G. Zgrablich*

Departamento de Física, Universidad de San Luis, San Luis, Argentina (Received April 21, 1975)

A model for heterogeneous substrates with a multivariate gaussian distribution for the adsorption potential is proposed. The evaluation of second and third virial coefficients shows a considerable dependence on the correlation length, in the range of the other parameters where heterogeneity plays an important role. The model has as limiting cases the homogeneous and large patches models; but the behavior at finite correlation lengths is by no means intermediate between that corresponding to those extremes.

1. Introduction

The most commonly used model for the adsorption of gases on heterogeneous substrates depicts the adsorption potential (U_{ad}) as being constant through large patches of the surface.[1] Another model was also proposed in which the surface is partitioned in an infinity of single adsorbing sites and U_{ad} is randomly distributed on them with no correlation between the values of U_{ad} for neighboring sites.[2] For both models, the best distribution for the values of U_{ad} was found to be gaussian.[2,3]

We propose here a model in which U_{ad} is considered to have a chaotic (stochastic) structure with a *finite* correlation length. The potential has a multivariate gaussian distribution and, therefore, all its statistical properties are given in terms of its mean value and covariance function.

The usual formulae for the evaluation of the two-dimensional virial coefficients (reviewed in section 2) are used in

section 3 with the distribution of the present model to obtain a general expression for the nth coefficient.

The second and third coefficients are evaluated in section 4 for a square well parametrization of the interparticle potential, while the conclusions are discussed in section 5.

We include an Appendix with the deduction of the multivariate gaussian distribution for the sake of completeness.

2. Virial Expansion of the Adsorption-Isotherm Equation

We are interested in those adsorption processes that can be pictured in terms of an ideal nonadsorbed phase (NAP), a two-dimensional adsorbed phase (AP), and an inert solid substrate, responsible for the adsorption force. For simplicity we take both phases to have one component.

The NAP is macroscopically described by means of its absolute temperature T, the volume particle density ρ_0,

and the pressure p (equal to $kT\rho_0$ in our case), while the AP is described by T, the surface adsorbed particle density ρ, and the two-dimensional or spreading pressure ϕ. The latter can be expanded in powers of ρ giving

$$\phi = kT\rho\left(1 + \sum_{n\geq 2} B_n(T)\rho^{n-1}\right) \qquad (1)$$

where $B_n(T)$ is the nth two-dimensional virial coefficient.

Using this expansion in Gibbs equation $\rho_0 \, d\phi = \rho \, dp$, which gives the condition for statistical equilibrium between the NAP and the AP, yields

$$p = K(T)\rho \exp\left[\sum_{n\geq 2} \frac{n}{n-1} B_n(T)\rho^{n-1}\right] \qquad (2)$$

where $K(T)$ is an integration constant.

We further assume that the potential energy of the system of adsorbed particles can be written as the sum over all pairs of the interparticle potentials $U_{gg}(|\tilde{x}_i - \tilde{x}_j|)$, plus the sum over all particles of the particle–solid potential[4]

$$U_{ad}(z_i, \tilde{x}_i) = \frac{1}{2} k_Z(z_i - z_m)^2 + V(\tilde{x}_i) \qquad (3)$$

In the above equation $\tilde{x} = (x, y)$ denotes the two-dimensional position vector.

Under these assumptions, the coefficients $K(T)$ and $B_n(T)$ can be evaluated as

$$K(T) = (kTk_Z/2\pi)^{1/2}\langle\exp(-V/kT)\rangle^{-1}$$

$$B_n(T) = -I_n/(n(n-2)!I_1^n) \qquad (4)$$

with

$$I_n = \int_A \cdots \int d\tilde{x}_1 \ldots d\tilde{x}_n \delta(\tilde{x}_1 + \ldots + \tilde{x}_n) \times$$

$$S_{1,\ldots,n}' \left\langle \prod_{i=1}^{n} \exp(-V(\tilde{x}_i)/kT) \right\rangle$$

where

$$S_{1,2}' = f_{12} = \exp(-U_{gg}(|\tilde{x}_i - \tilde{x}_j|)/kT) - 1$$

$$S_{1,2,3}' = f_{12}f_{13}f_{23}$$

$$S_{1,2,3,4}' = f_{12}f_{13}f_{14}f_{23}f_{24}f_{34} + 6f_{12}f_{13}f_{14}f_{23}f_{34} +$$

$$3f_{12}f_{23}f_{34}f_{14}$$

and in general $S_{1,\ldots,n}'$ is the sum over all completely connected diagrams (see Figure 1).

In the above formulae we denote by $\langle F(\tilde{x}_1, \ldots, \tilde{x}_k)\rangle$ the average of F over the surface

$$\langle F(\tilde{x}_1, \ldots, \tilde{x}_k)\rangle = \lim_{A\to\infty} \frac{1}{A} \times$$

$$\int_A d\tilde{R}\, F(\tilde{x}_1 + \tilde{R}, \ldots, \tilde{x}_k + \tilde{R}) \qquad (5)$$

Hill[6] used eq 4 and 5 to evaluate B_2 with $V(\tilde{x})$ a periodic function of $\tilde{x}$. The case of a heterogeneous potential is treated in next section.

3. Adsorption on a Heterogeneous "Gaussian" Surface

In order to use eq 4 when the adsorption potential has a chaotic structure we must postulate the validity of the *statistical homogeneity hypothesis*

$$\langle F(\tilde{x}_1 + \tilde{a}, \ldots, \tilde{x}_k + \tilde{a})\rangle = \langle F(\tilde{x}_1, \ldots, \tilde{x}_k)\rangle \qquad (6)$$

i.e., averages must be functions of the differences of coordinates. Physically this hypothesis means that any macro-
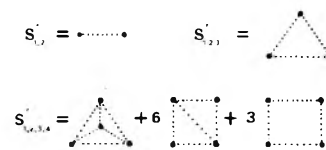
Figure 1. Interparticle interaction contribution for the integrand of I_n in eq 4, for $n = 2, 3,$ and 4. Each dotted line represents a factor f_{ij}.

scopic portion of the total surface has all the meaningful information.

Now, all statistical information about the surface is given by the multivariate potential distribution Φ_n for all values of n, where $\Phi_n \, dV_1 \ldots dV_n$ is the fraction of the surface such as the potential at the point $\tilde{x}_i$ is between V_i and $V_i + dV_i$, for $i = 1, 2, \ldots, n$.

Equation 4 shows that to evaluate $K(T)$ we need only Φ_1, whereas to calculate $B_n(T)$ we must know the interparticle interaction and Φ_n. $B_n(T)$, however, does not depend on the mean value of $V(\tilde{x})$.

For the distribution of $V(\tilde{x})$ over the surface it has been common to use a gaussian form

$$\Phi_1(V) = [kT_s(2\pi)^{1/2}]^{-1} \exp\left[-\frac{1}{2}\left(\frac{V + kT_a}{kT_s}\right)^2\right] \qquad (7)$$

where $-kT_a$ and kT_s are the mean value and standard deviation of $V(\tilde{x})$, respectively

$$\langle V(\tilde{x})\rangle = -kT_a; \quad \langle(V(\tilde{x}) + kT_a)^2\rangle = (kT_s)^2 \qquad (8)$$

This distribution gives $K(T) = (kTk_Z/2\pi)^{1/2} \exp[-T_a/T - \frac{1}{2}(T_s/T)^2]$

For the evaluation of $B_n(T)$ we propose for Φ_n a multivariate gaussian form (see Appendix)

$$\Phi_n(V_1, \ldots, V_n; \tilde{x}_1 - \tilde{x}_2, \ldots, \tilde{x}_{n-1} - \tilde{x}_n) =$$

$$[(2\pi)^n \det H]^{-1} \exp\left[-\frac{1}{2} \sum_{i,j=1}^{n} (V(\tilde{x}_i) + kT_a) \times \right.$$

$$\left. (H^{-1})_{ij}(V(\tilde{x}_j) + kT_a)\right] \qquad (9)$$

where $H_{ij} = \langle(V(\tilde{x}_i) + kT_a)(V(\tilde{x}_j) + kT_a)\rangle = (kT_s)^2 C(\tilde{x}_i - \tilde{x}_j)$, is the covariance matrix.

Thus Φ_n can be evaluated for any set of positions $\tilde{x}_i$, in terms of T_a, T_s, and a single function, namely, the correlation function $C(\tilde{r})$. The latter satisfies $C(0) = 1$, $C(\infty) = 0$ and $|C(\tilde{r})| < 1$ for $|\tilde{r}| \neq 0$.

Using (9) in (4) gives

$$B_n(T) = -\frac{1}{n(n-2)!} \int_A \cdots \int d\tilde{x}_1 \ldots d\tilde{x}_n \times$$

$$\delta(\tilde{x}_1 + \ldots + \tilde{x}_n) S_{1,\ldots,n}' \prod_{i>j=1}^{n} \exp[(T_s/T)^2 C(\tilde{x}_i - \tilde{x}_j)] \qquad (10)$$

The above equation can be diagrammatically represented as in Figure 2.

One could pose the question whether it is correct or not to average the integrand of I_n, which is not a directly measurable quantity. If we call

$$Z_n = \int d\tilde{x}_1 \ldots d\tilde{x}_n \, \delta(\tilde{x}_1 + \ldots + \tilde{x}_n) \times$$

$$S_{1,\ldots,n}' \prod_{i=1}^{n} \exp[-V(\tilde{x}_i)/kT]$$

it can be easily proved that the vanishing limit of $f(\tilde{r})$ and $C(\tilde{r})$ as $|\tilde{r}| \to \infty$ (short range of interparticle potential and

Figure 2. B_n for heterogeneous substrates, for $n = 2$, 3, and 4 (eq 10). A solid line represents a factor $f_{ij} \exp(H_{ij}/(kT)^2)$ and a wiggly line denotes a factor $\exp(H_{ij}/(kT)^2)$.

adsorptive potential correlation) leads to $\langle Z_n Z_m \rangle = I_n I_m$, i.e., the Z_n are deterministic variables (standard deviation zero) with mean value I_n.

We have then constructed a model in which all the necessary information about the adsorption potential is given by its mean value, $-kT_a$, and the covariance function $(kT_s)^2 C(\bar{r})$. In the spirit of this model, indeed, this is all the physically meaningful information, i.e., the adsorptive potential of two substrates with identical macroscopic properties (for instance, two carbon blacks graphitized at the same temperature) will very likely have different detailed structures, but identical mean values and covariances.

In next section we calculate B_2 and B_3 using

$$C(\bar{r}) = \exp[-\tfrac{1}{2}(r/r_0)^2] \quad (11)$$

We do not intend to take eq 11 as a realistic parametrization of the correlation function. We rather use it as a useful form to study the effect of the correlation length r_0.

We also want to discriminate the influence of the repulsive core and attractive part of the interparticle potential. This can be easily achieved using a "square well" parametrization

$$U_{gg}(r) = \begin{cases} \infty \text{ for } r < a \\ -kT_{gg} \text{ for } a < r < b \\ 0 \text{ for } b < r \end{cases} \quad (12)$$

for this potential.

4. $B_n(T)$ for the Square Well Potential

Using (11) in (10) we find that

$$\lim_{r_0 \to 0} B_n = \lim_{T_s \to 0} B_n = \bar{B}_n$$

$$\lim_{r_0 \to \infty} B_n = \exp\left[\frac{n(n-1)}{2}\left(\frac{T_s}{T}\right)^2\right]\bar{B}_n \quad (13)$$

where $\bar{B}_n$ is the virial coefficient for a constant, and then homogeneous, adsorptive potential. For a fixed value of n the first limit is reached (roughly speaking) for (T_s/T) $\exp(-nb/2r_0) \ll 1$, and the second one for $T_s n^2 b/4Tr_0 \ll 1$, where b is the range of interparticle potential. Therefore, $(T_s/T) \exp(-b/r_0)$ somehow indicates the degree of heterogeneous behavior of the surface at temperature T.[9]

We calculated B_2 and B_3 using the square well potential (12), in the form

$$B_2 = \frac{\pi a^2}{2}(J_1^{(2)} - \gamma J_2^{(2)})$$

$$B_3 = \left(\frac{\pi a^2}{2}\right)^2 (J_1^{(3)} - \gamma J_2^{(3)} + \gamma^2 J_3^{(3)} - \gamma^3 J_4^{(3)}) \quad (14)$$

with $\gamma = \exp(T_{gg}/T) - 1$. The integrals $J_i^{(j)}$ are functions of r_0/a, T_s/T, and, except for $J_1^{(j)}$, of $R = b/a$. The $J_1^{(j)}$ have only the contribution of the hard core and the $J_i^{(j)}$ (for $i > 1$) have the contribution of the pure attractive part. The above decomposition allows an independent variation

of T_s/T and T_{gg}/T without increasing considerably the computation time.

The limiting values when $T/T_s \to \infty$ (or $r_0 \to 0$) are

$$J_1^{(2)} = 1; J_2^{(2)} = R^2 - 1$$

$$J_1^{(3)} = \frac{4}{3} - \frac{3^{1/2}}{\pi}; J_2^{(3)} = \frac{8}{\pi}(R^2 - 1)\psi_1 -$$

$$\frac{2}{\pi}\sin\psi_1 R(R^2 + 2) + \frac{3(3)^{1/2}}{\pi}$$

$$J_4^{(3)} = \frac{8}{\pi}(R^2 - 1)(R^2\psi_2 + \psi_1) +$$

$$\frac{2R}{\pi}[\sin\psi_2(2R^2 + 1) - \sin\psi_1(R^2 + 2)] +$$

$$\left(\frac{8}{3} + \frac{3^{1/2}}{\pi}\right)(1 - R^4) \quad (15)$$

where

$$\psi_1 = \begin{cases} \cos^{-1}(R/2) & R < 2 \\ 0 & R \geq 2 \end{cases}$$

and

$$\psi_2 = \cos^{-1}(1/(2R))$$

In any range of the parameters the easiest way to calculate $J_3^{(3)}$ is through the relation

$$\sum_{i=1}^{4} J_i^{(3)}(r_0/a, R, T/T_s) = R^4 J_1^{(3)}(r_0/b, 1, T/T_s) \quad (16)$$

The second virial coefficient can be evaluated analytically in terms of the exponential integral function $E_i(x)$[7] in the form

$$J_1^{(2)} = \frac{1}{2}\left(\frac{r_0}{a}\right)^2\left\{E_i[(T_s/T)^2] - E_i\left[(T_s/T)^2\exp\left(-\frac{1}{2}(a/r_0)^2\right)\right]\right\}$$

$$J_2^{(2)} = \frac{1}{2}\left(\frac{r_0}{a}\right)^2\left\{E_i\left[(T_s/T)^2\exp\left(-\frac{1}{2}\left(\frac{a}{r_0}\right)^2\right)\right] - E_i\left[(T_s/T)^2\exp\left(-\frac{1}{2}\left(\frac{b}{a}\right)^2\right)\right]\right\}$$

The $J_i^{(3)}$ were calculated using a three-dimensional Simpson integration subroutine with a 1% precision.

$B_2^* = B_2/(\pi a^2/2)$ and $B_3^* = B_3/(\pi a^2/2)^2$ are shown in Figure 3a–c as functions of T/T_{gg} for $T_s/T_{gg} = 0.5$ (quite homogeneous), $T_s/T_{gg} = 2$ and $T_s/T_{gg} = 2.5$ (very heterogeneous), for $r_0/a = 0$, 1, and ∞, and for $R = 1.85$.

For heterogeneous substrates (Figure 3b, c) the behavior for finite values of r_0 is quite different from the behavior at $r_0 = 0$ (homogeneous) and $r_0 = \infty$ (large patches). Indeed, as $T \to 0$, B_2 and B_3 tend to $-\infty$ for $r_0 = 0$ or $r_0 = \infty$; but they tend to $+\infty$ for $0 < r_0 < \infty$ (predominance of the repulsive core).

The reason for this is very simple: at very low temperatures the particles are trapped in wells of very large (negative) adsorptive potentials (wells narrower the deeper they are), and thus the main contribution comes from the hard core. Although the portion of total surface with such deep wells is very small, the probability of finding a particle there is enhanced at small T by the Boltzmann factor $\exp(-U_{ad}/kT)$ (for instance, the average potential energy
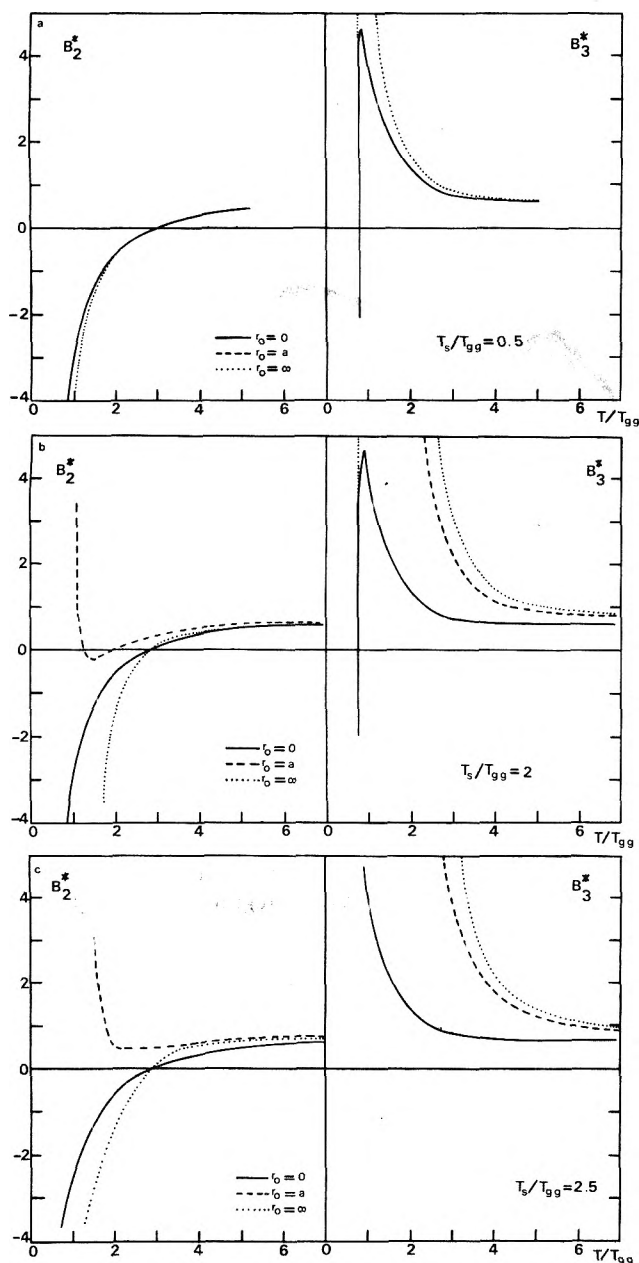
Figure 3. Second and third virial coefficients (for a square well potential) as a function of the reduced temperature T/T_{gg}, for different values of the correlation length r_0 and standard deviation of the adsorptive potential kT_s.

per particle in the absence of interparticle interaction is $-kT_a - kT_s{}^2/T$ which goes to $-\infty$ as $T \to 0$).

5. Conclusions

We have succeeded in constructing a stochastic model of heterogeneous substrates in terms of two parameters: the standard deviation of the absorption potential, kT_s, and the correlation length for the values of U_{ad} at two points of the surface, r_0. At a given temperature heterogeneity effects will be more important for larger values of T_s/T $\exp(-(b/r_0)^2)$, where b is the range of interparticle potential. For the coefficient $K = \lim_{\rho \to 0} (p/\rho)$, however, the scale of temperature for heterogeneous behavior is $T_s{}^2/T_a$, $-kT_a$ being the mean value of the adsorption potential.

A numerical calculation of the second and third two-dimensional virial coefficients shows a considerable influ-

ence of r_0 for values of T_s of the order of the strength of the interparticle attraction.

We thus conclude the importance of introducing the correlation function to understand adsorption phenomena on heterogeneous substrates. A fit to experimental data, actually being carried out, will show, though, the sensitivity of the adsorption isotherms to simultaneous variation of r_0 and T_s. Further developments of the model will appear elsewhere.[8]

We are also constructing an approximate model valid at any temperature, including phase transition range, and any coverage in order to see the importance of correlation effects in the whole equation of state.

Appendix. Multivariate Gaussian Distribution

The gaussian probability distribution for a random variabe $\hat{x}$, with mean value $\langle \hat{x} \rangle = \bar{x}$ and standard deviation $\langle (\hat{x} - \bar{x})^2 \rangle = \sigma^2$ is

$$\Phi_1(x) = (2\pi\sigma^2)^{-1/2} \exp\left[-\frac{1}{2}\left(\frac{x - \bar{x}}{\sigma}\right)^2\right] \quad (A1)$$

The corresponding generating function is given by

$$f(\alpha) = \langle e^{\alpha(\hat{x}-\bar{x})} \rangle = \exp(\tfrac{1}{2}\alpha^2\sigma^2) \quad (A2)$$

Alternatively (A2) can be taken as defining the distribution, since from it we can get back (A1) performing the integral

$$\frac{1}{2\pi} \int_{-\infty}^{\infty} d\beta f(i\beta) \exp(-i\beta x) = \langle \delta(\hat{x} - x) \rangle = \Phi_1(x)$$

$$(A3)$$

For n random variables $\hat{x}_i$ with mean values $\bar{x}_i$ the generating function is

$$f(\alpha_1, \ldots, \alpha_n) = \langle \exp[\alpha_1(\hat{x}_1 - \bar{x}_1) + \ldots + \alpha_n(\hat{x}_n - \bar{x}_n)] \rangle = \exp(\sum_{i,j}\alpha_i H_{ij}\alpha_j) \quad (A4)$$

where H, which can be shown to be the covariance matrix $H_{ij} = \langle (\hat{x}_i - \bar{x}_i)(\hat{x}_j - \bar{x}_j) \rangle$, must satisfy $\det H \geq 0$ (when the determinant vanishes the $\hat{x}_i$ are not all linearly independent). The probability distribution, when $\det H > 0$, can be calculated from (A4), giving

$$\Phi_n(x_1, \ldots, x_n) = \left\langle \prod_{i=1}^{n} \delta(\hat{x}_i - x_i) \right\rangle = (2\pi \det H)^{-1/2} \times$$

$$\prod_{i,j=1}^{n} \exp\left[-\frac{1}{2}(x_i - \bar{x}_i)(H^{-1})_{ij}(x_j - \bar{x}_j)\right] \quad (A5)$$

Finally, if we have a continuously infinite set of random variables $\hat{x}(t)$ which are functions of a parameter t (stochastic process), we define the generating functional

$$\mathcal{F}(\alpha) \equiv \left\langle \exp\left[\int dt\, \alpha(t)(\hat{x}(t) - \bar{x}(t))\right] \right\rangle =$$

$$\exp\left[\frac{1}{2}\int\int dt\, dt'\, \alpha(t)H(t,t')\alpha(t')\right] \quad (A6)$$

where $H(t,t') = \langle (\hat{x}(t) - \bar{x}(t))(\hat{x}(t') - \bar{x}(t')) \rangle$.

If we select n points t_i with an appropriate function $\alpha(t)$ we obtain eq A4.

In our case, the adsorptive potential must satisfy the hypothesis 6, therefore we obtain the generating functional

$$\mathfrak{F}(\alpha) = \left\langle \exp\left[\int d\tilde{x}\, \alpha(\tilde{x})(V(\tilde{x}) - V(\tilde{x})) \right] \right\rangle =$$

$$\exp\left[\frac{1}{2} \int d\tilde{x}\, d\tilde{y}\, \alpha(\tilde{x})H(\tilde{x} - \tilde{y})\alpha(\tilde{y}) \right] \quad (A7)$$

References and Notes

(1) S. Ross and J. P. Olivier, "On Physical Adsorption", Wiley, New York, N.Y., 1964.

(2) W. A. Steele, *J. Phys. Chem.*, **67**, 2016 (1963).

(3) S. Ross, *Adsorption Technol.*, **67**, 1 (1971).

(4) W. A. Steele in "The Solid-Gas Interface", Vol. 1, E. A. Flood, Ed., Marcel Dekker, New York, N.Y., 1967.

(5) T. L. Hill, "Statistical Mechanics", McGraw-Hill, New York, N.Y., 1956.

(6) T. L. Hill and S. Greenschag, *J. Chem. Phys.*, **34**, 1538 (1961).

(7) M. Abramowitz and I. A. Stegun, "Handbook of Mathematical Functions", National Bureau of Standards, Applied Mathematical Series-55, 1964.

(8) G. Zgrablich, submitted for publication.

(9) The second limit corresponds to large (macroscopic) patches with uniform adsorption potentials. In this limit ρ and ϕ are not constant through the surface. Furthermore, the radius of convergence of the series in (2) is very likely to be zero. However, eq 2 is still valid if we take it as an asymptotic (formal) expansion that should be summed up by some extrapolating method such as, for instance, Padé approximants.

Surface Viscosity of Sodium Dodecyl Sulfate Solutions with and without Added Dodecanol

Alan M. Poskanzer and F. C. Goodrich*

Institute of Colloid and Surface Science, Clarkson College of Technology, Potsdam, New York 13676 (Received July 1, 1974; Revised Manuscript Received March 24, 1975)

Using a new, high sensitivity surface viscometer, the surface shear viscosity of sodium dodecyl sulfate solutions is studied as a function of increasing bulk concentration. The surface viscosity is shown to exhibit an abrupt rise beginning at 1.5 g l.$^{-1}$, well below the critical micelle concentration. This rise continues through the critical micelle concentration until at a bulk concentration of 2.4 g l.$^{-1}$ the surface viscosity attains a near plateau value. The addition of dodecanol to sodium dodecyl sulfate solutions can greatly increase the surface viscosity due to a synergistic interaction in the interface between the two surface active components, but the proper balance of components in the interface depends sensitively upon competition for these components by mixed micelles formed in the bulk solution.

1. Introduction

In two recent communications[1,2] from this laboratory we have described the construction and hydrodynamic interpretation of a new, highly sensitive surface viscometer and demonstrated its usefulness in measuring the surface viscosity of an insoluble monolayer (stearic acid). The instrument is absolute in the sense that full consideration is given in the theory to the hydrodynamic coupling of viscous interactions between an interface bearing an adsorbed film and its bulk substrate exhibiting ordinary internal or bulk viscosity. If the general theory is correct, then surface viscosities determined with its use should be independent of the geometry of the instrument employed, just as surface tensions determined by different experimental methods are independent of the apparatus used. We thus anticipate that the surface viscosity, known for over a century to exist for films adsorbed at liquid interfaces, will in the future come to be accepted as an absolute surface transport property of the same interest and reliable reproducibility as the surface tension itself.

In the present article we demonstrate the application of our viscometer to the elucidation of the surface structure of solutions of soluble surface active agents.

2. Surface Viscometer

Our instrument has been described elsewhere.[2] Briefly it consists of a thermostated, cylindrical, steel vessel into whose wall has been machined a narrow, circular slot in such a way that the cylinder is divided into upper and lower halves. Into the slot is inserted a knife edge ring coaxial with the cylinder and flush with its wall. The ring rotates with steady angular velocity ω, and when the cylinder is filled to the level of the ring with a suitable liquid, the rotating knife edge makes contact with the perimeter of the viscous interface and tends to twist it with respect to the supporting bulk substrate. This twisting motion is opposed by the viscous drag of the underlying fluid, and it is from the momentum balance attained between these forces that a steady pattern of fluid angular velocity develops at the interface.

The experimental technique consists in floating a Teflon dust particle on the interface near the axis of the cylinder and in measuring its period of revolution around the axis. After subtracting from the motion of the dust particle a substrate contribution ("calibrating" the instrument), the contribution Ω of the surface film to the total angular velocity of the particle may be determined, after which the
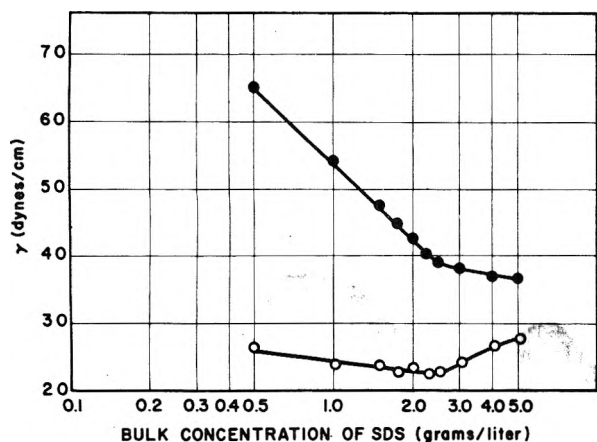
Figure 1. Surface tension vs. bulk concentration curves of aqueous SDS solutions: O, commercial SDS; ●, after purification.

Figure 2. Density of aqueous SDS solutions at 22.0°C.

Figure 3. Bulk viscosity of aqueous SDS solutions at 22.0°C.

dimensionless ratio Ω/ω is formed. The surface viscosity η is then

$$\eta = 0.5631(\Omega/\omega)\mu a \qquad (1)$$

in which μ is the internal viscosity of the substrate in poise and a is the radius of the cylinder. Equation 1 is an asymptotic approximation to an exact relationship given in ref 1, and for the case of aqueous substrates should not be used if η exceeds 0.008 g sec^{-1} = 8 surface millipoise. For all of the work reported here, however, eq 1 is adequate.

Procedures for cleaning and aligning the surface viscometer and details of the quality of the water used are described in ref 2.

The viscometer has mounted above it a Cahn electrobalance from whose arm a Wilhelmy plate is suspended for surface tension measurements in situ in the viscometer. No attempts to measure surface viscosity were made until the solution under study had achieved· a condition of stable surface tension equilibrium.

3. Surface Viscosity of Sodium Dodecyl Sulfate Solutions

Sodium dodecyl sulfate (SDS) has been exhaustively investigated with respect to its surface and micellar properties.[3-10] In many ways it has become a standard soluble surface active agent in the same way that stearic acid has become a standard monolayer forming material. In this section we present data on the surface viscosity of aqueous SDS solutions as a function of bulk concentration.

Our sample of SDS was purchased from Eastman Kodak, catalogue no. 5967. A plot of the surface tension vs. aqueous concentration at 22°C of the material as received is shown in Figure 1 as well as the same plot after the commercial sample had been extracted with anhydrous diethyl ether for 48 hr in a Soxhlet extractor. It is evident that the commercial sample was grossly impure. The surface tension vs. concentration curve of the purified material shows no minimum and agrees well with the similar plot published by Elworthy and Mysels.[3] From the abrupt change in slope of the plot we infer a critical micelle concentration (cmc) of 2.4 g l.$^{-1}$.

In order to calculate surface viscosities from eq 1, it is evident that the internal viscosity μ of the bulk phase must be known. To measure μ we used an Ostwald capillary viscometer, but the use of the Ostwald viscometer in turn requires that the density of the solution be known, and these
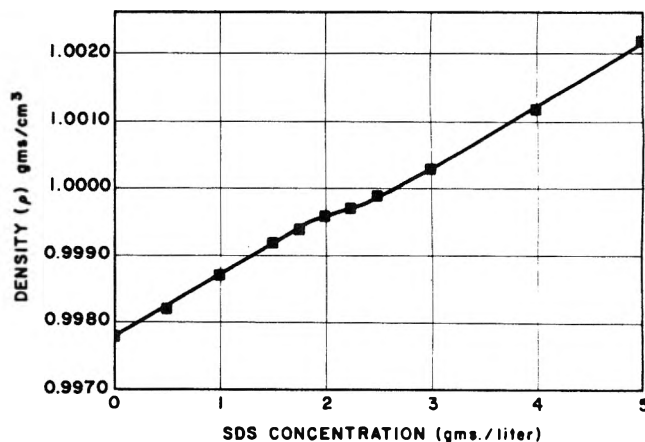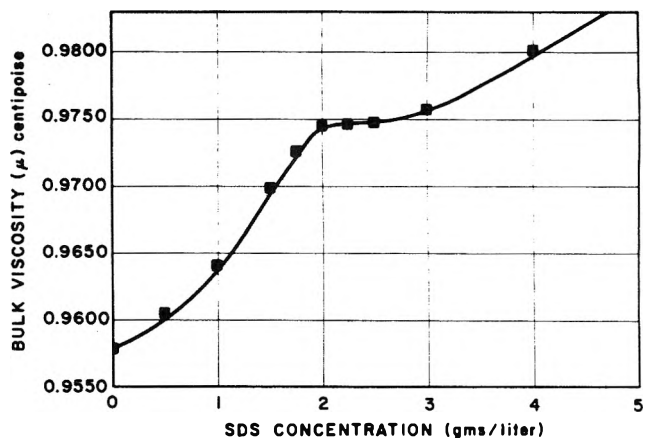
densities were measured using a Weld pycnometer. Both the Ostwald viscometer and the Weld pycnometer were calibrated at 22.0°C using distilled water. The results for aqueous SDS solutions are plotted in Figures 2 and 3. It is evident that neither the internal viscosity nor the density of the solutions changes by more than 2% over the concentration range studied. This is the same as the precision obtainable in measurements of the surface viscosity itself, so that with negligible error we might have used in eq 1 the viscosity of pure water. The measurements are nonetheless interesting, for both the density and the viscosity curves show a change in slope at 2.0 g l.$^{-1}$ and inflection points at 2.2 g l.$^{-1}$. If the inflection points are identified as critical micelle concentrations, then this value is to be compared with the cmc of 2.4 g l.$^{-1}$ determined from Figure 1. Williams, Phillips, and Mysels[4] report a cmc of 2.34 g l.$^{-1}$ for SDS taken as an average of conductivity, dye solubilization, and light scattering techniques; and it is thus evident that different physical properties of solutions of surface active agents are affected to slightly different degrees by the formation of micelles. Indeed, Figures 2 and 3 suggest that micelle formation in SDS starts at a concentration as low as 2.0 g l.$^{-1}$.

Finally our results for the surface viscosity at 22°C of solutions of SDS are plotted in Figure 4. The interface is without detectable viscosity until a bulk concentration of 1.5 g l.$^{-1}$ is achieved, meaning that the surface viscosity is 10^{-6} surface poise or less. Between 1.5 and 2.4 g l.$^{-1}$ the surface viscosity rises steeply, following which it levels off
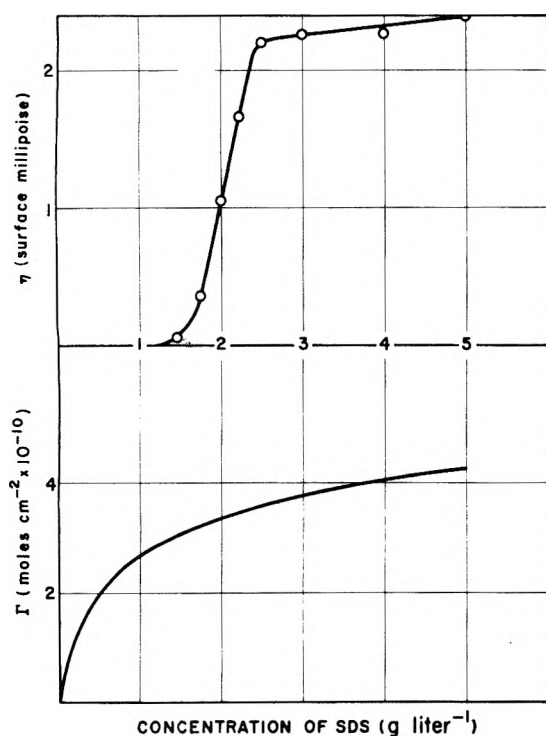
Figure 4. (Upper curve) surface viscosity of aqueous SDS solutions; (lower curve) surface excess of SDS as reported by Nilsson.[5]

to a near plateau value. In the lower half of Figure 4 is plotted the surface excess concentration Γ taken from the work of Nilsson.[5] These values were measured by a radioactive counting technique, and are thus free from the usual errors involved in the use of an approximate Gibbs adsorption isotherm with concentrations substituted for thermodynamic activities.[6,7]

By comparing the plots, one can calculate that the area per lauryl sulfate ion in an adsorbed monolayer is 53 Å^2 when the surface viscosity begins its initial rise at 1.5 g l.$^{-1}$, is 50 Å^2 at 2.0 g l.$^{-1}$ when the first micelles start to form, and is 45 Å^2 at 2.4 g l.$^{-1}$ when the surface viscosity achieves its plateau value and the surface tension ceases to fall rapidly with increasing bulk concentration. At higher concentrations the surface is nearly saturated, and further SDS added to the solution is largely consumed in the formation of new micelles with only small subsequent changes in the surface tension and surface viscosity.

To our knowledge this is the first time that anyone has succeeded in measuring the surface viscosity of uncontaminated SDS solutions. Both McBain and coworkers[8] and Gupta and Wasan[9] report the surface viscosity of SDS solutions to be zero at all concentrations. Using an instrument not all of whose hydrodynamic characteristics could be measured or controlled, Ewers and Sack[10] claimed surface viscosities of the order 10^{-4} surface poise for SDS solutions more dilute than any studied here. Their acknowledged experimental difficulties render their results questionable.

4. Discussion

Our data clearly indicate that the initial abrupt rise in surface viscosity at 1.5 g l.$^{-1}$ (53 Å^2 per lauryl sulfate ion in the interface) occurs before the appearance of the first micelles at 2.0 g l.$^{-1}$ (50 Å^2 per detergent ion in the interface). At neither of these points does the surface tension show

any deviation from its steady fall with increasing concentration, nor do Nilsson's data[5] over this range show any alteration in the smooth rise in surface excess. Any attempt to explain the initial rise in η in terms of a "two surface phase" model is hence inadmissible, being inconsistent with the phase rule. Thus our data on stearic acid monolayers[2] also reveal an abrupt rise in surface viscosity beginning at about 25 Å^2 per stearic acid molecule. This is coincident with the well-known abrupt rise in surface pressure as the surface area is reduced. For films more dilute than 25 Å^2 per molecule it is well recognized[11–13] that stearic acid exists in the surface as floating islands of condensed film in chemical equilibrium with a dilute, two-dimensional stearic acid surface "vapor". Compression of such two phase films on a film balance takes place without change in either the surface pressure or the chemical potential of the stearic acid so long as the two surface phases are both present.

Once, however, the surface vapor phase has been eliminated, the surface pressure and the chemical potential of stearic acid rise steeply upon compression, as does the surface viscosity. In the latter case one can interpret the rheological effect as due to the difficulty of shearing a coherent sheet of condensed stearic acid film. A two phase film would be expected to yield easily to shear stresses, for the floating islands of condensed film would remain largely intact with rheological distortion occurring locally in the easily sheared portions of vapor covered interface.

For adsorption films of SDS, however, the two surface phase model is eliminated by virtue of the fact that the chemical potential of SDS changes smoothly over the whole concentration range, albeit more slowly above the cmc. From the phase rule it is thus impossible to have present more than one surface phase. It would seem then that the rise in surface viscosity at 53 Å^2 per long chain ion in a homogeneous adsorption film is due to the sensitivity of the surface viscosity to the increasingly dominant van der Waals attraction between the paraffin chains; but it is at the same time remarkable that it is only the transport property η which is affected dramatically by these forces while the thermodynamic properties γ and Γ remain seemingly indifferent. In a three-dimensional, bulk phase system, the equivalent effect would be to find a marked change in the viscosity of a dense gas at some point along an isotherm above the critical point of the gas, without any special irregularity in the isotherm itself. In three-dimensional systems we know of no such experimental effect.

5. Surface Viscosity of SDS–Dodecanol Mixtures

It has been known for a long time that the presence of dodecanol in solutions of SDS has a striking affect upon the surface properties.[5,6,8,9,14,15,17] A synergistic interaction takes place in which a mixed adsorption film of considerable stability is formed. In this section we present data concerning the rheological properties of these mixed films.

Our dodecanol sample was fractionally distilled under vacuum and then recrystallized from n-hexane, being heated to drive off the last traces of hexane. It had a melting point of 24.4° (handbook values 22–26°). Before adding it to SDS solutions, we examined it alone in an aqueous solution of 1.0 mg/l. The surface tension was 59 dyn cm^{-1} and the surface viscosity 0.13 surface millipoise. Higher concentrations were not studied because of the low solubility of dodecanol in water.

For our viscosity measurements we prepared three stock
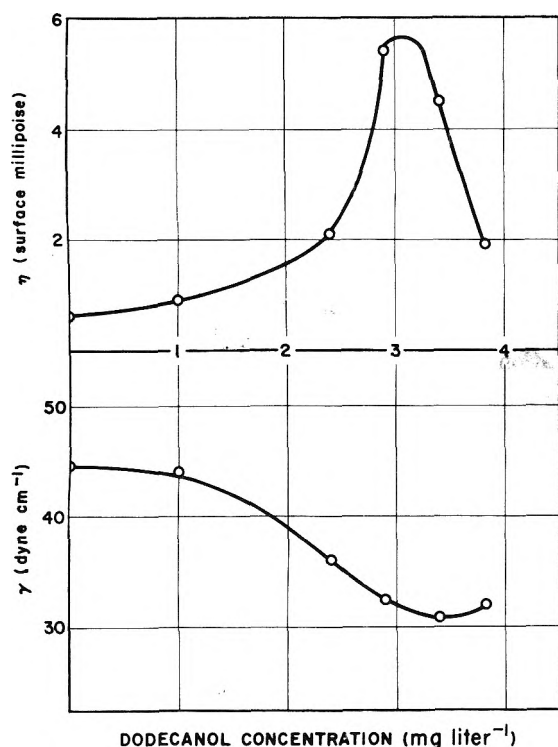
Figure 5. Surface viscosity and surface tension of a solution containing 1.75 g l.$^{-1}$ of SDS as a function of increasing dodecanol concentration.
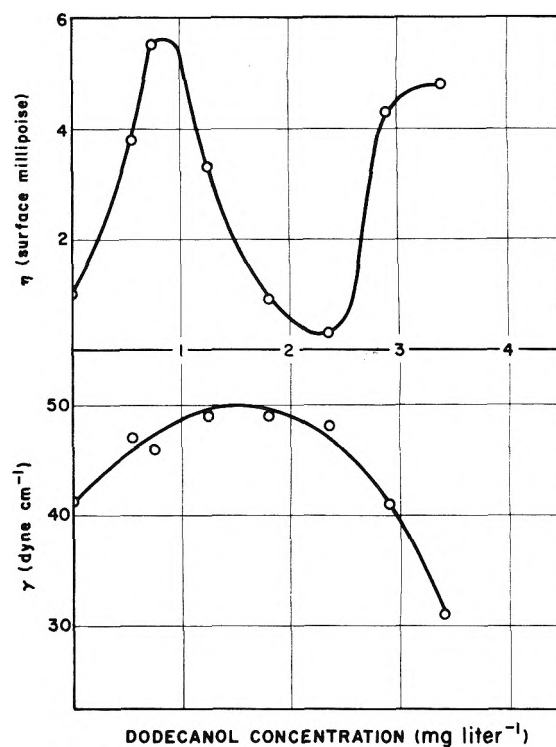
Figure 6. Surface viscosity and surface tension of a solution containing 2.00 g l.$^{-1}$ of SDS as a function of increasing dodecanol concentration.

solutions of SDS at 1.75 g l.$^{-1}$, 2.00 g l.$^{-1}$, and 2.50 g l.$^{-1}$. For pure SDS solutions these correspond respectively to a micelle free solution, to a solution just at the beginning of its micelle forming range, and to a solution in excess of the cmc. Into each of these stock solutions was dissolved increasing quantities of dodecanol, and the surface tensions and viscosities of these mixed solutions were determined. The time required to form a stable interface was much longer here than for pure SDS solutions, with up to 1 hr necessary for the surface tension to achieve an equilibrium value.

The data at 22.0°C are presented in Figures 5–7. Surface viscosities η were calculated from eq 1 using for μ the bulk viscosity of the corresponding SDS solution ignoring any effect due to added dodecanol.

6. Discussion

The surface viscosity shows a remarkable variation with the concentration of added dodecanol. Let us discuss Figure 6 first, for it exhibits features common to the other two plots. In Figure 6 the bulk concentration of SDS is 2.00 g l.$^{-1}$, just below the cmc. Injection of dodecanol at first rapidly increases the surface viscosity, a feature which we interpret as the formation of a "plastic" film through synergistic interaction between SDS and dodecanol adsorbed into the interface. During this process the surface tension rises somewhat, suggesting that the adsorption of dodecanol is accompanied by a partial desorption of SDS. This result is in agreement with the radio tracer experiments of Nilsson[5] on mixed SDS–dodecanol films. Finally, a maximum in the surface viscosity is achieved, and further additions of dodecanol serve only to depress the surface viscosity. We interpret this maximum as due to the formation of mixed micelles in the bulk solution, meaning that the addition of about 0.8 mg l.$^{-1}$ of dodecanol into an SDS solution
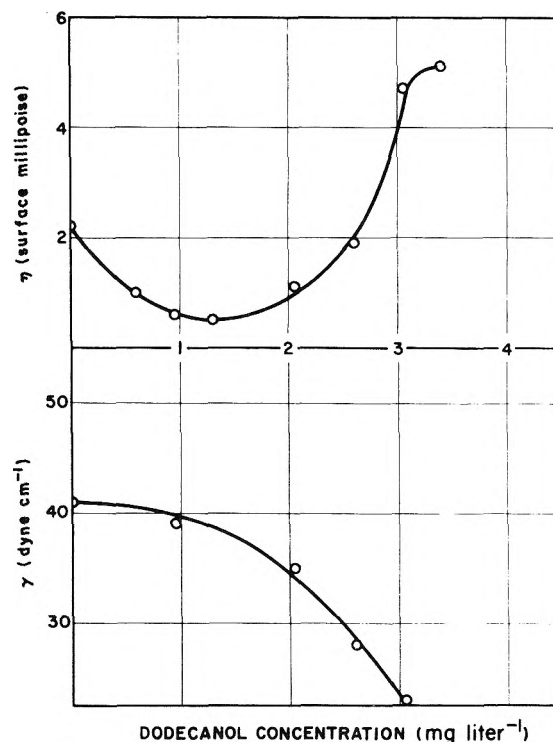
Figure 7. Surface viscosity and surface tension of a solution containing 2.50 g l.$^{-1}$ of SDS as a function of increasing dodecanol concentration.

depresses the cmc from 2.3 to 2.0 g l.$^{-1}$ of SDS. Independent support for this interpretation is obtained by plotting the surface tension of solutions containing 0.76 mg l.$^{-1}$ of dodecanol as a function of the concentration of added SDS.[16] A minimum appears in the surface tension at an SDS concentration of 2.0 g l.$^{-1}$.

As dodecanol is added beyond the cmc, desorption continues from the interface, for the surface tension continues to rise slightly. According to Tajima, Muramatsu, and Sasaki,[17] it is the SDS which is still being desorbed, and in any case the rapid fall in surface viscosity indicates that the synergistic balance in the interface necessary to form the plastic film has been upset. The minimum in surface viscosity at 2.3 mg l.$^{-1}$ of dodecanol is lower than that for the pure SDS adsorption film but at the same time higher than the 0.13 surface millipoise which we found for the pure dodecanol adsorption film, so that our results are consistent with the hypothesis of Tajima, Muramatsu, and Sasaki.

Finally, additions of dodecanol beyond 2.3 mg l.$^{-1}$ result in another rapid rise in the surface viscosity, accompanied by a sharp drop in the surface tension. This can only mean that the micelles are no longer able to compete successfully for SDS, so that SDS repenetrates the interface to reform the synergistic, plastic film.

Dodecanol can be successfully dispersed in SDS at higher concentrations than the points plotted in Figures 5–7, but the solutions have a cloudy appearence quite unlike the optical clarity of the solutions employed in these experiments. It is largely with such concentrated solutions that previous investigations of this system[8,9] have been concerned.

Having dealt with Figure 6, let us now turn to Figure 5 in which the SDS concentration is submicellar at 1.75 g l.$^{-1}$. The initial surface viscosity maximum of Figure 6 is reproduced here, but it is postponed until the addition of about 3.1 mg l.$^{-1}$ of dodecanol. Interpreting the maximum as due to the break up of the synergistically plastic surface film because of the formation of micelles in the bulk solution, we conclude that a dodecanol concentration of 3.1 mg l.$^{-1}$ lowers the cmc of SDS to 1.75 g l.$^{-1}$. The surface tension data are concordent with this interpretation, for γ falls as η rises, achieving a minimum coincident with the maximum in surface viscosity.

In Figure 7 the concentration of SDS at 2.50 g l.$^{-1}$ is above the cmc, and there are thus micelles present from the start of dodecanol addition. The initial surface viscosity maxima of Figures 5 and 6 are thus absent from Figure 7, and dodecanol enters the micelles preferentially, although from the falling surface viscosity it would appear that to some extent it also replaces SDS in the interface. Finally with micelle saturation, the plastic film reforms and the surface viscosity rises. Throughout this process the surface tension falls, at first slowly and then with increasing rapidity.

7. Non-Newtonian Effects

It is shown in ref 1 that a newtonian surface film is characterized by a strict proportionality between the angular velocity Ω of the floating dust particle and the angular velocity ω of the driving ring. For all films examined by us this proportionality is exact for sufficiently low ring speeds, and all viscosities herein reported were calculated from linear plots of Ω against ω in the newtonian regime. At the highest ring speeds, however ($\omega = 10$ rpm), some deviation was occasionally noted from this newtonian law. In every case the deviation was such as to make Ω lower than expected, meaning that the film tends to become more fluid at higher shear rates.

The appearance of non-newtonian behavior in every case correlated with the formation of the plastic surface film in

SDS–dodecanol mixtures. Thus in Figure 6 the plastic film formed near the first maximum in surface viscosity was markedly non-newtonian at high shear rates, while the rheological behavior of the film at the surface viscosity minimum was newtonian at all shear rates available to us. Films of intermediate surface viscosity displayed intermediate non-newtonian behavior. This is further evidence for the synergistic effect to which in section 6 we attributed the surface viscosity maxima. Because the plastic films tend to become more fluid at higher shear rates, it follows that the synergistic structure of mixed SDS–dodecanol films deteriorates upon sufficiently rapid mechanical deformation.

8. Summary

Surface shear viscosity is shown to be a parameter highly sensitive to the structure of adsorbed surface films. When accompanied by measurements of the surface tension, it can throw much light upon changes in the physical condition of an interface.

In this paper we have shown that adsorption films of sodium dodecyl sulfate behave in a manner entirely analogous to insoluble monomolecular layers of stearic acid in that the surface viscosity is immeasurably small (less than 10^{-6} surface poise) at low surface coverages, but rises abruptly when the area per surfactant molecule in the interface is less than a certain critical value. For SDS this rise in surface viscosity occurs at 53 Å^2 per long chain ion, well before the formation of micelles in the bulk solution and continues through the critical micelle concentration, after which it ceases (area per lauryl sulfate ion $\doteq$ 45 Å^2). Presumably it ceases only because the surface concentration Γ above the cmc increases but slowly.

Injection of dodecanol into an SDS solution can cause profound increases in the surface viscosity, but only if the bulk concentrations are properly balanced so as to produce surface concentrations favorable to the creation of a synergistically plastic surface film. The proper ratio of components in the surface needed to produce the plastic film is sensitive to competition for these components by mixed micelles formed in the bulk phase.

References and Notes

(1) F. C. Goodrich, L. H. Allen, and A. Poskanzer, *J. Colloid Interface Sci.*, in press.
(2) A. Poskanzer and F. C. Goodrich, *J. Colloid Interface Sci.*, in press.
(3) P. H. Elworthy and K. J. Mysels, *J. Colloid Interface Sci.*, **21**, 331 (1966).
(4) R. J. Williams, J. N. Phillips, and K. J. Mysels, *Trans. Faraday Soc.*, **51**, 728 (1955).
(5) G. Nilsson, *J. Phys. Chem.*, **61**, 1135 (1957).
(6) E. Hutchinson, *J. Colloid Sci.*, **3**, 413 (1948).
(7) B. A. Pethica, *Trans. Faraday Soc.*, **50**, 413 (1954).
(8) A. G. Brown, W. C. Thuman, and J. W. McBain, *J. Colloid Sci.*, **8**, 491 (1953).
(9) L. Gupta and D. T. Wasan, *Ind. Eng. Chem., Fundamen.*, **13**, 26 (1974).
(10) W. E. Ewers and R. A. Sack, *Aust. J. Chem.*, **7**, 40 (1954).
(11) N. K. Adam, "The Physics and Chemistry of Surfaces", Oxford University Press, London, 1941, pp 43–46.
(12) G. L. Gaines, "Insoluble Monolayers at Liquid-Gas Interfaces", Interscience, New York, N.Y., 1966, pp 156–162.
(13) N. L. Gershfeld and R. E. Pagano, *J. Phys. Chem.*, **76**, 1231 (1972).
(14) M. B. Epstein, A. Wilson, J. Gershman, and J. Ross, *J. Phys. Chem.*, **60**, 1051 (1956).
(15) J. Ross, *J. Phys. Chem.*, **62**, 531, 533 (1958).
(16) A. M. Poskanzer, Ph.D. Dissertation, Clarkson College of Technology, Potsdam, N.Y., 1974, Figure 57.
(17) K. Tajima, M. Muramatsu, and T. Sasaki, *Bull. Chem. Soc. Jpn.*, **42**, 2472 (1969).

Infrared Study of the Nature of the Copper Ion–Alkyne Bond in Y Zeolite

Pierre Pichat

Institut de Recherches sur la Catalyse, CNRS, 69626, Villeurbanne, France (Received March 14, 1975)

Publication costs assisted by Centre National de la Recherche Scientifique

From the infrared spectra of acetylene, deuterated acetylene, propyne, and but-2-yne, chemisorbed in Cu, Na-Y zeolites, which have undergone various treatments, it is inferred that (i) the OH groups interact only with the weakly adsorbed molecules, (ii) the Cu^+ ions are not involved, (iii) the acetylenic hydrogen atoms do not take part in the bonding, (iv) the Cu^{2+} ion–alkyne bond results mainly from π donation from the unsaturated hydrocarbon to the metallic ion.

Introduction

Within the last few years, attempts have been made to anchor coordination complexes on solid supports for practical as well as for theoretical reasons. Zeolites, owing to the mobility of protons, cations, and adsorbed molecules in their lattice, may be considered as a choice material to compare homogeneous and heterogeneous catalysis. Nevertheless, to our knowledge, works on unsaturated hydrocarbon complexes in zeolites have not hitherto been published.

Previous reports on Y zeolites[1,2] showed that dehydrated or partly dehydrated cations with an even number of half-filled d orbitals are capable of cyclotrimerizing C_2H_2, whereas the formation of a more stable complex was pointed out in the case of copper cations.[2] Here is presented an infrared study of the nature of the bonding formed between copper cations and some alkynes in Y zeolites.

Bonding between metal cations and acetylenes may be formed either by replacement of an acetylenic hydrogen by the metal cation or via the $C\equiv C$ bond.[3,4] The latter bonding mode has been found with certain transition cations, whereas, usually, copper acetylides correspond to the former mode or to coordination polymers combining both types.[4] It was of interest to determine the type of bonding present in Y zeolites, since the alkyne reactivity depends upon it.

Experimental Section

The Cu^{2+}, Na-Y zeolite was prepared from the commercial material Linde SK-40 by repeated exchanges, using 0.3% $Cu(NO_3)_2$ aqueous solutions. Samples containing 2.5, 15.5, and 24.5 Cu^{2+} ions per unit cell were obtained. Care was taken to prevent precipitation of the metal hydroxides or deterioration of the zeolite structure which can occur if an unsuitable pH is used. Chemical analyses for copper and sodium (flame spectroscopy) yield cation equivalents of 56 ± 3 per unit cell. Retention of the faujasite structure was checked by studying the ir spectra in the 1300–350-cm^{-1} region.[5-10]

Acetone was removed from cylinder C_2H_2 by passing the gas through concentrated sulfuric acid. Deuterated acetylene contained more than 99.5 atom % of deuterium. All the alkynes were vacuum distilled and thoroughly dried over molecular sieves.

For ir measurements, the zeolites were compressed at a pressure of 10^3 kg cm^{-2}. The resulting disks ($\simeq 5$ mg cm^{-2}) were mounted in a quartz sample holder and treated in a cell similar to that described previously[11] but with no joint or stopcock. Greaseless vacuum systems were used, since it has been observed that grease is a very effective reducing agent for cations in zeolites.[12] Dehydroxylated samples were obtained after the following treatment. Under vacuum, the temperature was raised stepwise up to 450° in 5 hr. Then, O_2 was admitted, and the cell, connected to a liquid nitrogen trap, was maintened at this temperature for 4–5 hr. Finally, the zeolite was evacuated overnight at 550°. Despite the oxygen treatment, formation of CuO was not observed for similar samples, as shown by X-ray diffraction patterns[13] and EPR spectra.[14] Hydroxylated zeolites resulted from a mere evacuation at 200° for 15 hr. Treatment in CO at 450° for 15 hr before the final above evacuation partially reduced the Cu^{2+} ions into Cu^+ ions.[15]

To obtain spectra at wave numbers lower than 1200 cm^{-1}, powders were treated in the same way as the disks, then impregnated with nujol under vacuum.

Spectra were scanned on a Perkin-Elmer Model 125 grating spectrophotometer (Model 225 for the region below 400 cm^{-1}). The reference beam was attenuated.

Results

Figure 1 shows the spectra of C_2H_2 adsorbed on a dehydroxylated sample. Table I indicates the wave numbers of the observed bands for C_2H_2 and the other alkynes. In the OH region of the spectra, no band occurs. The absorption maxima of C_2D_2 corroborate the assignment of the C_2H_2 bands. No OD band is found.

Admission of C_2H_2 onto a hydroxylated Cu^{2+}, Na-Y zeolite causes the OH band near 3630 cm^{-1} to diminish, whereas that near 3550 cm^{-1} remains unchanged. The easily accessible OH groups corresponding to the 3630-cm^{-1} band are weakly hydrogen bonded to C_2H_2 molecules. The formation of new OH bands is not observed. On evacuation at room temperature, the 3630-cm^{-1} band is restored. These phenomena are similar to those pointed out for C_2H_4 adsorption in decationated Y zeolites.[16]

If a small quantity of H_2O is introduced after C_2H_2 adsorption, C_2H_2 is not removed from the surface, but higher quantities of H_2O produced C_2H_2 desorption. In a partly hydrated zeolite, C_2H_2 bonding to Cu^{2+} ions is possible. In contrast, molecules which form more stable complexes with the copper ions in Y zeolite are capable of displacing C_2H_2. This is the case for methyl isocyanide.[17] These experiments give an idea of the stability of the C_2H_2–Cu^{2+} ion bond.

The influence of the Cu content was examined for acetylene. Even for the sample containing only 2.5 Cu^{2+} ions per

TABLE I: Frequencies (in cm^{-1}) of Acetylene, Deuterated Acetylene, Propyne, and But-2-yne

Alkynes	Vibrations	Free state (gas or liquid)	Adsorbed in Cu. Na-Y zeolite^d	Frequency shift free-adsorbed
C$_2$H$_2$			3250	49
	≡CH	3289	3190 sh	99
			3170^b	129
	C≡C	1974^a	1820 sh	154
			1810^b	164
C$_2$D$_2$	≡CD	2427	2365 sh	62
			2345^b	82
	C≡C	1763^a	1650 sh	113
			1640^b	123
C$_3$H$_4$	≡CH	3365	3230 sh	135
			3200^b	165
	C≡C	2142	1975	167
C$_4$H$_6$	C≡C	2233^{a,c}	2045	188

^{a} Raman. ^{b} Most intense band in its spectral region. ^{c} Reference 30. ^{d} sh = shoulder.
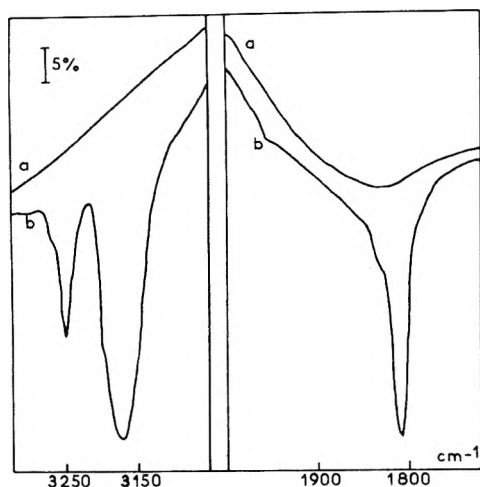
Figure 1. Ir spectra of chemisorbed acetylene: (a) dehydroxylated Cu, Na-Y zeolite containing 24.5 Cu^{2+} ions per unit cell; (b) after adsorption of 50 Torr of C$_2$H$_2$ at 25° for 15 hr, then desorption at 25° for 5 min.

unit cell, C$_2$H$_2$ bands resistant to evacuation were found, though their intensity was very weak. This confirms that Cu^{2+} ions, located in the small cavities of the zeolite after treatment at high temperature, migrate to the supercages because of the presence of unsaturated hydrocarbons.[18] The sample containing 15.5 Cu^{2+} ions per unit cell gives rise to C$_2$H$_2$ bands whose intensity does not differ a great deal from that observed in the case of the sample containing 24.5 Cu^{2+} ions.

For C$_2$H$_2$ and C$_2$D$_2$, attempts were made to detect the CH (or CD) deformation mode and the Cu–C stretching mode, using nujol mulls. Unfortunately, no band was observed down to 250 cm^{-1}, although the bands corresponding to the CH and C≡C stretching modes were visible.

A decrease in intensity but no change in frequency of the C$_2$H$_2$ and C$_3$H$_4$ bands were observed for the partially reduced samples as compared with the unreduced ones. It is inferred that no Cu$^+$ ion–alkyne interaction takes place.

Discussion

Possibility of Formation of Cu–C≡CR Species. If C$_2$H$_2$, C$_3$H$_4$, and C$_2$D$_2$ loose a hydrogen or deuterium atom on adsorption, this atom will most likely react with a lattice oxygen and yield an OH or an OD group. This was found in the case of ZnO.[19] The appearance of new OH bands, which increased on standing, was also pointed out for C$_2$H$_2$ and C$_3$H$_4$ adsorbed on silica-supported CuCl$_2$.[20] Here, formation of OH or OD bands was not observed.

The absence of OH bands casts a doubt on the possible formation of RC$_2$Cu species. Other data are also in agreement with this conclusion. (i) For propyne, which has only one acidic hydrogen atom, the CH stretching vibration subsists in the adsorbed state and the stability of the CH and C≡C ir bands on desorption are comparable, which shows that these two bands refer to the same chemisorbed species. (ii) But-2-yne, which has no labile hydrogen atom, is also chemisorbed on the copper ions, as evidenced by thermally stable ir bands. (iii) The frequency shifts found for the C–H and C≡C stretching vibrations are more important than those noted for RC$_2$M acetylides.

The CH stretching frequency of the acetylides HC$_2$M is in the 3215–3290-cm^{-1} region[21,22] which corresponds to the bands previously observed for C$_2$H$_2$ chemisorbed on ZnO[19] and for the mixture C$_2$H$_2$–O$_2$ chemisorbed on MgO–NiO.[23] The 3170-cm^{-1} band found in the present case is far below this region. Also the C≡C stretching vibration is at 1810 cm^{-1}, outside the 1850–1961-cm^{-1} range reported for the acetylides HC$_2$M[21,22] but close to that observed for μ,π-bonded acetylene on silica-supported CuCl$_2$ (1818 cm^{-1}) whose ≡CH bands are at 3290 and 3205 cm^{-1}.

In the case of propyne, however, the wave number of the C≡C band does not allow such a clear cut distinction, since this band is shifted 167 cm^{-1} from its position in the gas, compared with 187 cm^{-1} for C$_6$H$_5$C$_2$H and C$_6$H$_5$C$_2$Cu[24] and 277 cm^{-1} for propyne probably chemisorbed as a (CH$_2$–C≡CH) species bonded to Zn atoms on ZnO.[19] Nevertheless, as pointed out above, the presence of the CH stretching band suffices to rule out the formation of CH$_3$C$_2$Cu species. Moreover, a 180-cm^{-1} shift was found for μ,π-bonded propyne on silica-supported CuCl$_2$,[20,25] whereas it was suggested that the CH$_3$C$_2$Cu species, formed on standing, cause a 96-cm^{-1} shift toward high wave numbers.[20]

Formation of π-Acetylenic Complexes. Bonding between alkynes and metals or cations may be depicted as intermediate between the two extreme cases[26] I and II. The
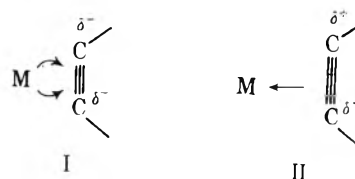
respective importance of electron donation from the hydrocarbon to the cation and back donation from the cation to the hydrocarbon depends upon the relative positions of the energy levels of the alkyne π and π^* orbitals on the one hand and the bonding s, p, and d orbitals in the cation on the other hand. Also, a complex close to type II is favored by electron-donating substituents on the alkyne (such as CH$_3$ groups) and electron-withdrawing ligands on the metal or cation.

Due to the transfer of electron from the cation into the π orbitals of the alkyne, the C≡C bond order is greatly decreased in I and hence the (C≡C) band is considerably

lowered (from 2260–2190 cm^{-1} to 1845–1740 cm^{-1}).[26] In II the C≡C frequency is in the 2046–1994-cm^{-1} region.[26] For but-2-yne in Cu, Na-Y zeolite, the C≡C band is displaced from 2233 cm^{-1} in the Raman spectrum of the liquid to 2045 cm^{-1}, which refers to a type II bonding. In contrast no band due to the C≡C bond was found for but-2-yne adsorbed on silica[27] and alumina.[27,28] The shifts observed for C_2H_2 (164 cm^{-1}) and C_3H_4 (167 cm^{-1}) in the Cu, Na-Y zeolites are not very large and may be accounted for by a type II complex, though data on such complexes of acetylene and simple monosubstituted alkynes are missing. The appearance of an ir active C≡C band is due to a cis configuration. It is not possible to determine accurately the bond order from the ν(C≡C) frequency, because this frequency also depends upon the C≡C-R angle.[29]

Similar bondings have not been pointed out for those simple alkynes in Cu^{2+} ion solutions. Their formation in Y zeolite may be due to the lattice electrostatic field and/or to the electron transfers with the framework. It is worth noting that the Cu^+ ions which are less electron deficient do not give complexes stable at room temperatures with acetylene and propyne.

Because of its relative weakness, the Cu^{2+} ion–acetylene bond described above may correspond to intermediates in catalytic reactions in which the acetylene molecule is not dissociated, since a nucleophilic attack at the acetylenic carbons is favored.

References and Notes

(1) P. Pichat, J. C. Vedrine, P. Gallezot, and B. Imelik, *J. Catal.*, **32**, 190 (1974).
(2) T. Besoukhanova, P. Pichat, M. V. Mathieu, and B. Imelik, *J. Chim. Phys.*, **71**, 751 (1974).
(3) See, for example, F. L. Bowden and R. B. P. Lever, *Organometal.*

Chem. Rev., **3**, 227 (1968); G. E. Coates, M. L. H. Green, and K. Wade, "Organometallic Compounds", Vol. 2, "Transition Elements", Methuen, London, 1968, pp 271–311; F. R. Hartley, *Chem. Rev.*, **69**, 799 (1969); R. D. N. Kemmit in "Inorganic Chemistry Series One", Vol. 6 "Transition Metals—Part 2", M. J. Mays, Ed., Butterworths, London, 1972, pp 227–272.
(4) M. A. Bennett, *Chem. Rev.*, **59**, 611 (1961).
(5) E. M. Flanigen, H. Khatami, and H. A. Szymanski, *Adv. Chem. Ser.*, **No. 101**, 201 (1971).
(6) P. Pichat, R. Beaumont, and D. Barthomeuf, *C. R. Acad. Sci., Ser. C*, **272**, 612 (1971).
(7) O. Lahodny-Sarc and J. L. White, *J. Phys. Chem.*, **75**, 2408 (1971).
(8) D. Ballivet, P. Pichat, and D. Barthomeuf, *Adv. Chem. Ser.*, **No. 121**, 469 (1973).
(9) A. A. Kubasov, K. V. Topchieva, and A. N. Ratov, *Russ. J. Phys. Chem.*, **47**, 1023 (1973).
(10) P. Pichat, R. Beaumont, and D. Barthomeuf, *J. Chem. Soc., Faraday Trans. 1*, **70**, 1402 (1974).
(11) M. V. Mathieu and P. Pichat In "La Catalyse au Laboratoire et dans l'Industrie", B. Claudel, Ed., Masson and Cie, Paris, 1967, p 319.
(12) C. Naccache and Y. Ben Taarit, *J. Chem. Soc., Faraday Trans. 1*, **69**, 1475 (1973).
(13) P. Gallezot, Y. Ben Taarit, and B. Imelik, *C. R. Acad. Sci., Ser. C*, **272**, 261 (1971).
(14) C. Naccache and Y. Ben Taarit, *Chem. Phys. Lett.*, **11**, 11 (1971).
(15) C. Naccache and Y. Ben Taarit, *J. Catal.*, **22**, 171 (1971).
(16) B. V. Liengme and W. K. Hall, *Trans. Faraday Soc.*, **62**, 3229 (1966).
(17) P. Pichat in "Catalysis, Heterogeneous and Homogeneous", B. Delmon and G. Jannes, Ed., Elsevier, Amsterdam, 1975, p 183.
(18) P. Gallezot, Y. Ben Taarit, and B. Imelik, *J. Catal.*, **26**, 295 (1972).
(19) C. C. Chang and R. J. Kokes, *J. Catal.*, **28**, 92 (1973).
(20) D. M. Smith, P. M. Walsh, and T. L. Slager, *J. Catal.*, **11**, 113 (1968).
(21) A. N. Rodionov, G. V. Timofeyuk, T. V. Talalaeva, D. N. Shigorin, and K. A. Kocheshkov, *Isv. Akad. Nauk. SSSR, Ser. Khim.*, 42 (1965).
(22) D. M. Adams, "Metal-Ligand and Related Vibrations", Edward Arnold, London, 1967, p 212.
(23) T. Z. Tabasaranskaya and A. A. Kadushin, *Kinet. Catal.*, **12**, 1334 (1971).
(24) P. W. R. Corfield and H. M. M. Shearer, *Acta Crystalogr.*, **21**, 957 (1966).
(25) D. M. Smith, J. R. Brainard, M. E. Grant, and C. A. Lieder, *J. Catal.*, **32**, 148 (1974).
(26) E. O. Greaves, C. J. L. Lock, and P. M. Maitlis, *Can. J. Chem.*, **46**, 3879 (1968); P. M. Maitlis, "The Organic Chemistry of Palladium", Vol. 1 "Metal Complexes", Academic Press, New York, N.Y., 1971, pp 123–130.
(27) D. J. C. Yates and P. J. Lucchesi, *J. Chem. Phys.*, **35**, 243 (1961).
(28) M. M. Bhasin, C. Curran, and G. S. John, *J. Phys. Chem.*, **74**, 3973 (1970).
(29) E. G. Gal'pern, *Izv. Akad. Nauk. SSSR, Ser. Khim.*, **No. 9**, 2114 (1970).
(30) I. M. Mills and H. W. Thompson, *Proc. R. Soc. (London), Ser. A*, **226**, 306 (1954).

Infrared Spectrum and Structure of Matrix-Isolated Sulfur Tetroxide

Roger Kugel and Henry Taube*

Department of Chemistry, Stanford University, Stanford, California 94305 (Received February 18, 1975)

Publication costs assisted by Stanford University

The reaction of SO_3 with atomic oxygen was explored using the matrix isolation method. A new species was observed by infrared spectroscopy having peaks at 1434, 1267, 925, 777, 611, 498, and 490 cm^{-1} in an Ar matrix at 15°K. Similar spectra to within small matrix shifts were observed in Xe, N_2O, SF_6, and CO_2 matrices. The species giving rise to these spectra is identified as neutral, monomeric SO_4. Both ^{34}S and ^{18}O isotope labeling studies were carried out with this new species. The results of these indicate that the structure is of either C_1 (or C_s) symmetry having a sulfuryl group and an open SOO group or of C_{2v} symmetry having a sulfuryl group and a SOO three-membered ring. The latter of these two structures is preferred on the basis of the positions of certain infrared bands. The mechanism of formation of SO_4 is discussed and evidence for its photo and thermal decomposition presented.

Introduction

Neutral sulfur tetroxide has previously been proposed as an intermediate in a variety of sulfur oxide reaction systems. It has been suggested as the active oxidizing species in persulfate oxidations[1] and as a transient species produced by the action of a silent electric discharge over sulfuric acid solution.[2] The SO_4 molecule has also been invoked as an intermediate in the reaction of sulfur trioxide with atomic oxygen,[3,4] and as an atmospheric intermediate in the photoinduced oxidation of sulfur dioxide by molecular oxygen.[5-8] However, in none of these studies was SO_4 directly observed.

Some early work was reported in which sulfur tetroxide was produced by the action of a silent electric discharge (6500–8000 V) on mixtures of SO_2 and O_2.[9,10] The product is isolated as a white solid which melts at 3° with decomposition. Later work[11] characterized this solid as a polymeric species of composition $SO_{3.5-4.0}$, the exact product composition depending on the S:O ratio in the discharge reaction mixture. Wannagat and Schwarz[12] give a theoretical discussion of the existence of monomeric SO_4 and argue that such a molecule would be unstable relative to polymerization.

In the present work we report the synthesis and characterization of a molecular species identified as monomeric SO_4. This was accomplished by the reaction of SO_3 with atomic oxygen at low temperatures (15–78°K) in several inert matrices. The atomic oxygen was produced in situ by the photolysis of matrix-isolated ozone, nitrous oxide, or sulfur trioxide at various wavelengths. The oxygen atoms produced were free to diffuse through the matrix and react with coisolated SO_3 molecules. The product SO_4 thus isolated in a rigid support was unable to polymerize. The infrared absorption spectrum of matrix-isolated SO_4 was observed and ^{34}S and ^{18}O isotope labeling studies were carried out on it from which its most probable structure was inferred.

Experimental Section

A modular liquid helium dewar Model MHD-3L-15N manufactured by Andonian Associates was used for the low-temperature experiments. The design has been described previously.[13] This dewar could be used with liquid nitrogen, solid nitrogen, or liquid helium as the primary coolant giving matrix sample block temperatures of 78, 65, 15°K, respectively.

Matrix samples were made by deposition of gas mixtures onto the cold window in several (5–10) pulses of 0.05–0.1 mmol. This method gave matrix deposits sufficiently glassy for spectroscopic work and obviated long deposition times needed in the slow spray-on method of matrix deposition.

Gas samples were prepared on an all-glass vacuum line using halocarbon stopcock grease from the Halocarbon Corp. This grease was inert to all the gases sampled except for sulfur trioxide which was handled in a separate manifold equipped with greaseless, Kel-F bore, high vacuum stopcocks from the Kontes Co. The gas mixtures were measured out using a quartz spiral null manometer from Texas Instruments Co. and condensed into 1-l. bulbs containing glass beads. These mixtures were stirred by shaking the bulbs causing an agitation of the glass beads.

Ozone was prepared by silent electric discharge (15,000 V) through oxygen in a closed system cooled with liquid nitrogen. This setup gave 99+% conversion of oxygen to ozone. Ozone enriched in ^{18}O was prepared in the same way using 94.0 atom % ^{18}O-enriched oxygen obtained from Yeda Research and Development Co. Sulfur trioxide was isolated from 30% fuming sulfuric acid by bubbling with helium at 110° and condensing the effluent with liquid nitrogen. The SO_3 was then purified by repeated bulb-to-bulb distillations under vacuum and several freeze–pump cycles at −78° to remove residual SO_2. Sulfur trioxide enriched in ^{18}O was prepared by heating elemental sulfur and an excess of ^{18}O-enriched oxygen in a quartz ignition tube to a temperature of ca. 500° for 24 hr. The resulting ^{18}O-enriched sulfur dioxide was transferred to another ignition tube containing an excess of ^{18}O-oxygen and Pt-black catalyst and was heated to 400° for about 1 week. The product $S^{18}O_3$ was purified by the method that was used for isotopically normal sulfur trioxide described above. The overall yield of $S^{18}O_3$ was 90%. Sulfur trioxide enriched in ^{34}S was prepared similarly by using ^{34}S-enriched elemental sulfur and isotopically normal oxygen. The ^{34}S content of the enriched sulfur obtained from Oak Ridge National Laboratory was 67.5 atom %.

Infrared spectra were recorded between 4000 and 200 cm^{-1} using a Perkin-Elmer Model 621 grating spectropho-

tometer. The spectra were calibrated to within 1.0 cm^{-1} using atmospheric water vapor[14] and indene liquid[15] as standards.

Photolyses were carried out with a 450-W medium-pressure mercury lamp (Ace Glass Inc.) used together with chemical filters for the isolation of various regions of the spectrum. These filters have been described previously.[16,17] For photolyses at 1849 Å in which it was desirable to exclude 2537-Å light, a γ-irradiated LiF plate was used. Such a filter has a sharp intense absorption band centered at 2480 Å ($A \sim 3.6$) but transmits at 1849 Å.[18]

Results

The reaction of sulfur trioxide with atomic oxygen was investigated in the matrix phase at temperatures between 15 and 78°K. The product of this reaction gives rise to an infrared absorption spectrum previously unobserved in sulfur oxide chemistry, with bands at 1434, 1267, 925, 777, 611, 498, and 490 cm^{-1} in an argon matrix at 15°K.

This new species was produced in various matrices by several methods. In the first of these methods, ozone and sulfur trioxide were dispersed in argon, in xenon, or in carbon dioxide matrices. The ozone was subsequently photolyzed with 5780-Å light producing only $O(^3P)$ as the atomic fragment, with 2537-Å light producing $O(^1D)$, or with 3130-Å light producing a mixture of $O(^1D)$ and $O(^3P)$ in the ratio of about 1:10.[19] These atomic species, being free to diffuse through the matrix, react with isolated SO₃ molecules. Surprisingly, the reaction producing the new sulfur oxide was observed to occur even with ground state $O(^3P)$ in an argon matrix at 15°K. This indicates a very low activation energy (≤ 0.03 kcal/mol) for this process. However, the most efficient production of the new species by this method was observed when 3130-Å light was used. The infrared spectra of such an ozone photolysis experiment in an argon matrix are shown in Figure 1. In the second method used to produce the new species, sulfur trioxide was isolated in a nitrous oxide matrix at 77°K. Photolysis of the nitrous oxide at 1849 Å produces $O(^1D)$, and the reaction of $O(^1D)$ with the SO₃ isolated in this matrix produced the new species. However, the yield for this reaction was quite low and only the two most intense bands in the infrared spectrum of the new product were observed at 1434 and 1260 cm^{-1}. A third means of synthesizing the new compound under consideration was also employed. In this method, sulfur trioxide was isolated in either a carbon dioxide, sulfur hexafluoride, or argon matrix. Photolysis of the SO₃ itself at 1849 Å produces $O(^3P)$ and SO₂[20] and $O(^3P)$, as already has been noted, was found to react with isolated SO₃ molecules. The product of this reaction has an infrared spectrum that was very similar to that of the new species produced by the other methods. A spectrum for this reaction in a CO₂ matrix is shown in Figure 2. It should be pointed out that when neat deposits of SO₃ were irradiated under these conditions, only polymeric products were observed.

The infrared data from the above experiments are given in Table I. The small shifts in the infrared absorption maxima among these matrix experiments are attributed to different environments in the lattice sites of the various hosts.

Other syntheses which were attempted, though they did not meet with such gratifying success, merit brief mention here. In the first of these, sulfur dioxide was isolated in an oxygen matrix at 15°K. The matrix was subsequently irradiated with 2537 Å for 4.75 hr. The idea behind this experi-
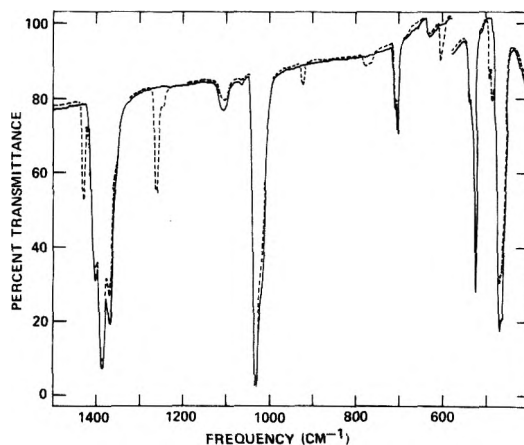
Figure 1. Infrared spectra for the photolysis of O_3 in the presence of SO₃ in an Ar matrix at 15°K: (solid line) deposit before photolysis, SO₃ bands centered at 1389, 1070w, 529, and 486 cm^{-1}, O_3 bands centered at 1110, 1043, and 705 cm^{-1}; (broken line) after 1.5 hr of irradiation at 3120 Å, SO₄ bands centered at 1434, 1267, 925, 777, 611, 498, and 490 cm^{-1}.
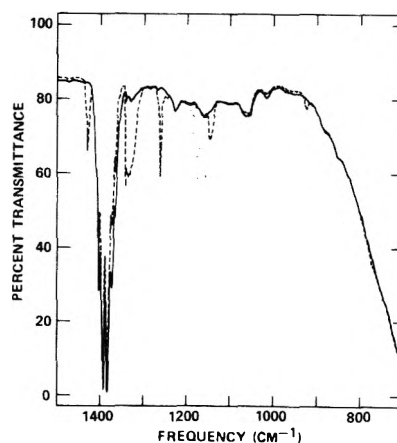
Figure 2. Infrared spectra for the photolysis of SO₃ in a CO₂ matrix at 78°K: (solid line) deposit before photolysis, SO₃ band centered at 1391 cm^{-1}, cutoff at 700 cm^{-1} due to BaF₂ windows used on the low-temperature dewar; (broken line) after 1.5 hr of irradiation with the unfiltered light from a low-pressure mercury lamp, SO₂ bands centered at 1329 and 1148 cm^{-1}, SO₄ bands centered at 1437, 1268, 929, and 779w cm^{-1}. These spectra give direct evidence for the photodisproportionation reaction: $2SO_3 + h\nu(1849$ Å$) = SO_2 + SO_4$.

ment was to elevate SO₂ to an excited state which might react with an adjacent O₂ molecule in the matrix. However, no reaction was observed by infrared spectroscopy to occur under these conditions. An attempt was also made to isolate the new sulfur oxide species directly from the gas phase. A radiofrequency discharge (7.37 MHz) was passed through pure SO₃ and through mixtures of SO₂ and O₂ immediately prior to freezing at 15°K. The infrared spectra of these deposits, however, showed no peaks attributable to the new sulfur oxide species observed above.

Several isotope labeling experiments were carried out with this new molecule in order to obtain more information about its structure and mechanism of formation. In the first of these experiments, $^{32}S^{16}O_3$ and $^{18}O_3$ (94.0 atom % ^{18}O) were isolated in an argon matrix. Photolysis of the $^{18}O_3$ at 3130 Å generated the new compound containing one ^{18}O statistically distributed in the molecule. This is evidenced in the infrared spectrum in which each peak due to the new species shows an ^{18}O isotope shifted peak at lower

TABLE I: Infrared Data on the Product of the Reaction of Sulfur Trioxide with Atomic Oxygen

Experiment	IV	XIII	XLIII	LVI	XLIX	XLVIII	LX	LII
Matrix host	CO_2	CO_2	Xe	Ar	N_2O	CO_2	SF_6	Ar
Temp, °K	78	78	65	15	78	78	78	15
O source	O_3	O_3	O_3	O_3	N_2O	SO_3	SO_3	SO_3
New infrared	1438	1430	1431	1434	1434	1437	1436	1433
stretching	1267	1265	1264	1267	1260	1268	1266	1262
frequencies,				1263				
cm^{-1}	928	927		925		929		924
	777	776		777		779	782	772
	608	608		611				607
	497	496		498			497	497
	491	490		490			492	

TABLE II: Infrared Isotope Data and Relative Isotope Shifts for $^{34}SO_4$ and $S^{18}O_4$

ν $^{32}S^{16}O_i$, cm^{-1}	ν $^{34}S^{16}O_i$, cm^{-1}	Relative shift, %	ν $^{32}S^{18}O_4$, cm^{-1}	Relative shift, %
1434	1418	1.12	1387	3.28
1267	1256	0.868	1223	3.47
925	924	0.108	881	4.76
777	767	1.29	746	3.99
611	610	0.164	582	4.75
498	(487)[a]	2.21	(481)	3.41
490				

[a] Values in parentheses questionable due to their close proximity to intense SO_3 bands.

frequency. In the second of these isotope studies, $^{32}S^{18}O_3$ and $^{18}O_3$ (both 94.0 atom % ^{18}O) were isolated in an argon matrix. Photolysis in this case at 3130 Å resulted in the formation of the new molecule in which all of the oxygen atoms are replaced by ^{18}O as well as a smaller percentage of the new species which is less completely labeled. In the third of these isotope labeling experiments $^{34}S^{16}O_3$ (67.5 atom % ^{34}S) and $^{16}O_3$ were isolated in an argon matrix. Photolysis of the ozone in this matrix generated the new species enriched in ^{34}S. The results of these isotope labeling experiments are summarized in Table II.

No evidence was seen for the photodecomposition of the new product with visible light. A slight amount of decomposition was observed however when SO_4 samples were irradiated with the unfiltered light of the medium-pressure mercury lamp. These observations indicate that SO_4 may have an absorption maximum in the ultraviolet. Unfortunately, attempts at measuring the uv-visible spectrum of this new species were inconclusive. No absorption peak was seen in the region from 8000 to 2000 Å which might be attributed to this compound, but, since the amount of product in this experiment was relatively small, a weak absorption may have gone unnoticed. To form this product in greater quantity, thicker matrix deposits were required and the high degree of light scattering from these deposits interfered with the uv-visible measurement.

Electron spin measurements were made on the product of the reaction of SO_3 with $O(^3P)$ using SO_3 as the atomic oxygen source by self-photolysis at 1849 Å. The reaction was carried out in both CO_2 and SF_6 matrices. These experiments showed no detectable ESR signal attributable to the new molecule under consideration. When these samples

were warmed to room temperature after photolysis and refrozen, the vacuum inside the cell degenerated and the characteristic ESR spectrum of O_2 gas was observed, indicating thermal decomposition of SO_4.

Infrared measurements indicated that the new species is stable at least up to the softening point of a carbon dioxide matrix (100–150°K). Above this temperature the matrix became frosty and began to sputter away and further infrared measurements were impossible.

Discussion

Seven new infrared absorption maxima have been observed attributable to the product of the reaction of SO_3 with atomic oxygen. These peaks (see Table I) are the only new features which are observed when the infrared spectrum is scanned from 4000 to 200 cm^{-1} using CsI windows on the low-temperature dewar. They have been observed when the reaction was run in five different matrix hosts (Ar, Xe, N_2O, CO_2, SF_6) and the positions of the infrared maxima are the same, apart from small matrix shifts in these different media. Furthermore, the relative intensities of these peaks remain constant during their growth and disappearance. This behavior indicates that these peaks arise from the production of only one new species and not the simultaneous production of two or more new species.

The positions and relative intensities of the new infrared absorption peaks were also found to be independent of the mode of production of atomic oxygen. Therefore, neither the atomic oxygen source nor the matrix host molecules are responsible directly or indirectly through adduct formation for any of the new infrared bands. That is, the only reactants essential for the production of this new entity are sulfur trioxide and atomic oxygen.

A comparison of infrared absorption band intensities in the spectrum of the new product (see Figure 1) gives an indication of the number of fundamentals present. The two high-energy peaks at 1434 and 1267 cm^{-1} are also the most intense. These peaks are probably due to fundamental vibrational transitions in the new molecule since overtone and combination bands are characteristically of diminished intensity. The rest of the bands in this infrared spectrum are between 490 and 925 cm^{-1}. If any of these were due to overtone or combination bands, one would expect to see strong fundamentals at lower energy. Since no such low-frequency fundamentals were observed down to 200 cm^{-1}, it is likely that the five remaining bands between 490 and 925 cm^{-1} are also fundamentals. If this is true, seven infrared active fundamental vibrations are observed for the new product.

Since sulfur trioxide itself shows a tendency to polymerize and since it has been argued that sulfur tetroxide should be unstable relative to polymerization,[12] the question of the number of sulfur atoms per new molecule is an important one. That the species is not polymeric is evidenced by the sharpness of the infrared peaks, since even at low temperatures polymers characteristically show broad peaks in the infrared. Moreover, the new species has been produced both in the presence and absence of polymeric SO$_3$ with no observable difference in the infrared spectra. Furthermore, the new product was made using 67.5% enriched ^{34}SO$_3$. In this case no peak assigned to the new species showed more than one ^{34}S isotope shifted peak. This is strong evidence in favor of the ratio of the one sulfur atom per new product molecule, indicating that it is a monomeric species.

Sulfur trioxide and atomic oxygen may react at low temperatures by one or more of the following reactions:

$$SO_3 + O(^3P) \longrightarrow SO_2 + O_2 \tag{1}$$

$$SO_3 + O(^3P) \longrightarrow OSOO + O(^3P) \tag{2}$$

$$SO_3 + O(^3P) \xrightarrow{M} SO_4 \tag{3}$$
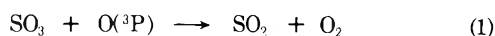
where the role of the third body molecule M is played by the matrix. Reaction 1 has been observed at room temperature in the gas phase.[4] However in this study, no SO$_2$ formation as a result of reaction 1 was observed in the matrix phase at low temperatures. Reaction 2 involves the formation of a peroxy isomer of SO$_3$. Such tetratomic species would show only six infrared active fundamentals whereas seven are observed in this study. Reaction 2 is in any case impossible unless O(^{3}P) possesses much excess kinetic energy, and energy loss to the matrix should be efficient. Thus the most likely of these reactions is reaction 3 involving the addition of atomic oxygen to sulfur trioxide in the matrix to form sulfur tetroxide.

Spectrum and Structure of SO$_4$. A variety of molecular structures involving one sulfur and four oxygen atoms can be drawn. Some of the structures which might arise from the reaction of sulfur trioxide with atomic oxygen are shown in Figure 3. Structure I (together with its corresponding resonance forms) represents a molecule having tetrahedral symmetry. Such a molecule would have only two infrared active fundamentals. A C_{3v} structure (II) would have six fundamentals which are infrared active. A C_{2v} structure such as III would show eight infrared active fundamentals. A molecule of C_{2v} symmetry such as structure IV as well as one of C_1 (or C_s) symmetry (V) would have nine fundamentals, all of them infrared active.

On the basis of the observed spectrum, structures I and II are ruled out immediately, since seven fundamentals are observed in the infrared spectrum, and these structures are compatible with only two and six, respectively. Structure IV is unlikely since the infrared spectrum of the new species shows two intense bands in the S=O stretching region at 1434 and 1267 cm^{-1}. This implies that the species contains more than one sulfur–oxygen double bond, while structure IV has only one such group. Thus the remaining likely structures are C_{2v} structure III and C_1 (C_s) structure V.

A comparison of the infrared data on isotopic substitution collected for the 1434- and 1267-cm^{-1} bands of SO$_4$ with the isotope data for ν_3 and ν_1 of SO$_2$ isolated in Kr matrices[21] shows that the relative observed isotope shifts follow the same patterns. This comparison is shown in Table III. The implication of this correlation is that the SO$_4$ bands at 1267 and 1434 cm^{-1} are due to the symmetric and antisymmetric stretches of a SO$_2$ moiety.
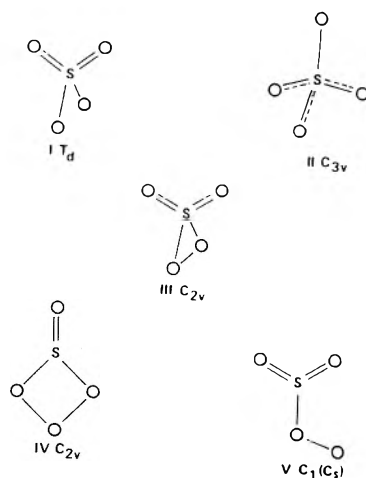
Values for the characteristic frequencies of the sulfuryl group in various compounds are given in Table IV. The correlation between the symmetric and asymmetric stretching frequencies is consistent with the presence of the SO$_2$ moiety in SO$_4$. A comparison of the SO$_2$ bending frequencies in these compounds gives a strong indication that the corresponding frequency in SO$_4$ should be at about 530 cm^{-1}. Unfortunately a product peak was never observed in this region since SO$_3$, which is always present in these experiments, has an intense absorption which peaks at 529 cm^{-1}. Thus whether or not SO$_4$ actually has a 530-cm^{-1} band must remain open to question.

The band at 925 cm^{-1} is assigned to a vibration which is mainly O–O stretching. This assignment was made on the basis of the observed isotope data. Table II revealed that this band shows the largest relative ^{18}O isotope shift of all the observed SO$_4$ bands. Furthermore, the O–O stretching frequencies of peroxides[25] and of transition metal dioxygen complexes[26] are located in this general region from 800 to 1200 cm^{-1}. The relation between structures and O–O vibrational frequencies in the latter may have a bearing on the structure-frequency relationship in SO$_4$. Two classes of transition metal dioxygen complexes have been observed.

class I   class II

The O–O vibrational frequencies for class I complexes range from 820 to 909 cm^{-1}, whereas the corresponding frequencies for class II complexes lie between 1120 and 1140 cm^{-1}. Since the assigned O–O vibrational frequency in SO$_4$ is at 925 cm^{-1}, the above structure-frequency relationship in metal dioxygen complexes provides indirect support for the C_{2v} structure III of SO$_4$. The assignment of the two low-energy bands of SO$_4$, namely, those at 498 and 490 cm^{-1}, was made primarily on the basis of their proximity to the out-of-plane deformation mode of SO$_3$. These bands are assigned to the wagging and rocking modes of the sulfuryl group, respectively, although this assignment may also be reversed. Finally, the bands at 777 and 611 cm^{-1} are assigned to the antisymmetric and symmetric stretches of

Figure 3. Some possible structures for SO$_4$.

TABLE III: A Comparison of the Isotope Data for the 1267- and 1434-cm⁻¹ Bands of SO₄ with Corresponding Data for ν_1 and ν_3 of SO₂

	$^{32}S^{16}O_2$	$^{32}S^{16}O^{18}O$	$^{32}S^{18}O_2$	$^{34}S^{16}O_2$
$\nu_1(SO_2)^a$	1149.8	1121.4	1098.9	1142.4
$\Delta\nu_1/\nu_1$	0	0.025	0.044	0.0064
$\nu(O_2SO_2)^b$	1267	1244	1223	1256
$\Delta\nu/\nu$	0	0.018	0.035	0.0087
$\nu_3(SO_2)^a$	1350.9	1331.8	1307.6	1334.0
$\Delta\nu_3/\nu_3$	0	0.014	0.032	0.013
$\nu(O_2SO_2)^b$	1434	1417	1387	1418
$\Delta\nu/\nu$	0	0.012	0.033	0.011

^{a} Frequencies measured in a Kr matrix, ref 21. ^{b} Frequencies measured in an Ar matrix, this work.

TABLE IV: Sulfuryl Group Frequencies of Various Compounds Frequencies in cm⁻¹

	$\nu_A(OSO)$	$\nu_S(OSO)$	$\delta(OSO)$	Ref
F_2SO_2	1502	1269	545	22
Cl_2SO_2	1414	1182	560	22
OSO_2	1391	1068	529	22
SO_2	1362	1151	518	22
S_3O_9	1515	1270	534	23
$(CH_2)_7SO_2$	1310	1168		24
O_2SO_2	1434	1267		This work

the S–O single bonds in the three-membered ring of the C_{2v} structure III. However since this ring does not exist in the C_1 structure V, these bands are assigned to the S–O single bond stretch and the S–O–O bend in this structure. The relative isotope shifts for these two bands seem to be more consistent with the former assignment to a symmetric and antisymmetric pair of S–O vibrations. Furthermore 611 cm⁻¹ is quite high for an S–O–O bending mode. This also favors the C_{2v} assignment for the structure of SO₄.

On the basis of the isotope data, the above assignments, and chemical intuition, both structures III and V are possible for SO₄, but the C_{2v} structure III is favored for the aforementioned reasons. A theoretical test of these assignments using the Teller–Redlich product rule was impossible to carry out due to the incompleteness of the isotope data. A matrix isolation Raman or high-resolution infrared study, particularly in the 450–550-cm⁻¹ region, may be helpful in obtaining further isotope data on SO₄. With sufficient information on the vibrational frequencies of the various isotopic species of SO₄ and a successful application of the product rule, it should be possible to distinguish between these two remaining possibilities for the structure of SO₄.

Mechanism of Formation of SO₄. Since the sulfur atom in SO₃ is slightly electron deficient, initial attack of SO₃ by O(³P) probably takes place on the nonbonding electrons of an SO₃ oxygen atom or on the electron density of an S=O double bond. This will produce SO₄ in some triplet state as shown, for example, in the reaction

$$SO_3 + O(^3P) \longrightarrow O_2\dot{S}\text{—}O\text{—}\dot{O} \qquad (4)$$
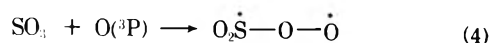
The ring may subsequently close by the spin forbidden process

$$O_2S\text{—}O\text{—}O \longrightarrow O_2S\overset{O}{\underset{O}{\diagdown}} \qquad (5)$$
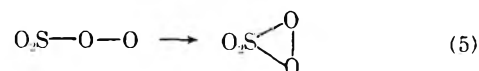
From this point the added oxygen atom may be equilibrated with the other three merely by shifting electrons. This accounts for the isotopic scrambling observed when $S^{16}O_3$ reacts with ^{18}O. It should be pointed out that even if the ground state of SO₄ is the open $C_1(C_s)$ structure V, the scrambling of oxygen atoms can only be explained by a mechanism in which at some point all four oxygen atoms are bound to the sulfur.

The production of SO₄ was found to be more efficient when the photolysis of ozone was carried out at 3130 Å instead of 2537 Å. It is not known whether the inefficiency of production using 2537-Å light is due to cophotolysis of SO₄ at 2537 Å, via the reaction

$$SO_4 + h\nu(2537\,\text{Å}) \longrightarrow SO_3 + O(^3P) \qquad (6)$$

or to the contribution of the reaction

$$SO_3 + O(^1D) \longrightarrow SO_4^* \longrightarrow SO_3 + O(^3P) \qquad (7)$$
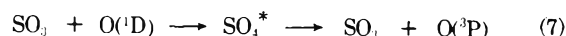
which describes net deactivation of O(¹D) by SO₃. The fact that isotope exchange was observed in the SO₃ when $^{18}O(^1D)$ was used is consistent with both reactions 3 and 4. Attempts at measuring the uv-visible spectrum of SO₄ to assess the contribution of reaction 3 were inconclusive.

After long photolysis times, when the steady-state concentration of SO₄ is reached, reaction 8 may also be occur-

$$SO_4 + O(^3P),(^1D) \longrightarrow SO_3 + O_2 \qquad (8)$$
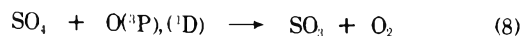
ring. This reaction also accounts for the observed isotope exchange.

References and Notes

(1) L. Levitt, *Can. J. Chem.*, 31, 915 (1953).
(2) J. B. Martinez and B. R. Rios, *An. R. Soc. Esp. Fis. Quim.*, Ser. B, 49, 193 (1953).
(3) B. G. Reuben, J. Linnett, and M. Barber, *Symp. (Int.) Combust.*, [Proc.], 8th, 97 (1962).
(4) A. Jacob and C. A. Winkler, *J. Chem. Soc., Faraday Trans. 1*, 68, 2077 (1972).
(5) H. W. Sidebottom, C. C. Badcock, G. E. Jackson, J. G. Calvert, G. W. Teinhardt, and E. K. Damon, *Environ. Sci. Technol.*, 6, 72 (1972).
(6) E. R. Allen, R. D. McQuigg, and R. D. Cadle, *Chemosphere*, 1, 25 (1972).
(7) R. A. Cox, *J. Phys. Chem.*, 76, 814 (1972).
(8) K. G. Vohra, P. V. N. Nair, and T. S. Muraleedharan, *J. Aerosol. Sci.*, 3, 225 (1972).
(9) J. F. Meyer, G. Baileul, and G. Henkel, *Ber. Dtsch. Chem. Ges. B*, 55, 2923 (1922).
(10) R. Schwarz and H. Achenbach, *Z. Anorg. Allg. Chem.*, 219, 271 (1934).
(11) V. Wannagat and J. Rademachers, *Z. Anorg. Allg. Chem.*, 286, 6 (1956).
(12) V. Wannagat and R. Schwarz, *Z. Anorg. Allg. Chem.*, 288, 180 (1956).
(13) E. Weissberger, W. H. Breckenridge, and H. Taube, *J. Chem. Phys.*, 47, 1764 (1967).
(14) "IUPAC Tables of Wavenumbers for the Calibration of Infrared Spectrometers", Butterworths, Washington, D.C., 1961.
(15) R. N. Jones and A. Nadeau, *Spectrochim. Acta*, 20, 1175 (1964).
(16) P. R. Jones and H. Taube, *J. Phys. Chem.*, 77, 1007 (1973).
(17) J. G. Calvert and J. N. Pitts, Jr., "Photochemistry", Wiley, New York, N.Y., 1966, p 728 ff.
(18) J. Weeks, S. Gordon, and G. Meaburn, *Nature (London)*, 191, 1186 (1961).
(19) C. L. Lin and W. B. DeMore, *J. Photochem.*, 2, 161 (1973).
(20) No O(¹D) was observed in the photolysis of SO₃ at 1849 Å. When this reaction was carried out in a CO₂ matrix, the presence of any O(¹D) would have resulted in the formation of carbon trioxide. Since no carbon trioxide appeared in this experiment, the conclusion is that the photolysis of SO₃ under these conditions yields only O(³P) as the atomic fragment.

(21) M. Allavena, R. Rysnik, D. White, V. Calder, and D. Mann, *J. Chem. Phys.*, **50**, 3399 (1969).

(22) K. Nakamoto, "Infrared Spectra of Inorganic and Coordination Compounds", Wiley, New York, N.Y., 1963.

(23) R. J. Gillespie and E. A. Robinson, *Can. J. Chem.*, **39**, 2189 (1961).

(24) G. Hesse, E. Reichold, and S. Majmudar, *Ber. Dtsch. Chem. Ges.*, **90**, 2106 (1957).

(25) F. J. Blunt, P. J. Hendra, and J. R. Mackenzie, *Chem. Commun.*, 278 (1969).

(26) J. S. Valentine, *Chem. Rev.*, **73**, 235 (1973).

Optical Transitions to the Rydberg-Like and Ionized States of an Organic Molecule in Nonpolar Organic Media

Yoshihiro Nakato and Hiroshi Tsubomura*

Department of Chemistry, Faculty of Engineering Science, Osaka University, Toyonaka, Osaka, Japan   (Received February 10, 1975)

Absorption spectra assigned to transitions to the Rydberg-like and ionized states from an organic molecule (1,1',3,3'-tetramethyl-2,2'-biimidazolidinylidene) in nonpolar organic media are studied. The spectrum changes strongly with temperature, but little with solvent in wavelength and intensity. On the other hand, the photocurrent thresholds shift definitely with solvent. From these experimental results, the energy of the electron in the bottom of the conduction band of the solvent, the electron–cation binding energy in the lowest Rydberg state, and the absorption intensity of the "Rydberg" band are evaluated. It is found that these quantities are well correlated with the molecular sphericity of the solvent. The similar correlation has been reported already for the excess electron mobility. It is also predicted from this correlation that very high-mobility electrons exist in tetramethylsilane matrices at 77 K.

Introduction

It is well known that an electron ejection from organic molecules into solvents occurs by excitation in the near-ultraviolet region. Recently, the ionization thresholds of some organic compounds in solutions were determined by the method of photocurrent measurements.[1-4] The values obtained are about 1.1–1.8 eV lower than the gas-phase ionization potentials of the same molecules, but still above the low-lying $(\pi-\pi^*)$-type excited states. This is one of the reason why no direct measurement of the optical absorption spectrum corresponding to the electron ejection in solution has ever been made.

Recent experiments have shown that mobile, excess electrons exist in liquid hydrocarbons.[5,6] The magnitude of the electron mobility in these liquids varies over a wide range from 0.07 for n-hexane to 90 cm^2 V^{-1} sec^{-1} for tetramethylsilane, increasing with the molecular sphericity of the solvent. It has also been found that the energy of the excess electron varies with media, increasing with decreasing electron mobility.[7]

We reported previously[2,8] that some of the low-lying absorption bands of tetrakis(dimethylamino)ethylene (TMAE) and 1,1',3,3'-tetramethyl-2,2'-biimidazolidinylidene (TMBI) could be assigned to the transitions to the
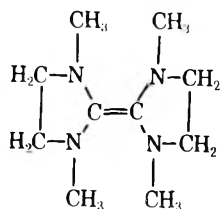
Rydberg-like states and even to the ionized states. In the present paper, we will report and discuss the results of detailed measurements of the absorption spectra, together with the photocurrent yield curves and the fluorescence excitation spectra of TMBI in nonpolar organic media.

Experimental Section

Merck spectrograde cyclopentane and isooctane (2,2,4-trimethylpentane) and Merck NMR grade tetramethylsilane were dried with Na–K mirrors just before use. Other materials were prepared and purified in the same way as described previously.[2,8]

Absorption spectra were measured with a Cary Model 15 or a Shimadzu MPS-50L spectrophotometer. Fluorescence and its excitation spectra were measured with an Aminco-Bowman spectrophotofluorimeter. The temperature of the sample solution was controlled by using quartz dewars containing isopentane or methanol cooled with nitrogen gas. 3-Methylpentane (3-MP) gave clean, transparent solutions throughout the temperature range, but tetramethylsilane (TMS) crystallized and became completely opaque at about 178 K when cooled gradually. Glassy, cracked TMS solutions at 77 K, which were used for measurements, were obtained by cooling rapidly in a thin cell. The Shimadzu MPS-50L spectrophotometer was used for measurements of absorption spectra of such slightly opaque samples. The determination of the molar extinction coefficient of TMBI, reactive with atmospheric oxygen, was made by weighing TMBI in vacuo by use of glass ampoules with breakable seals.

The steady-state photocurrents were measured by using a quartz cell equipped with two platinum-plate electrodes. The details were described elsewhere.[2]

TMBI

Results

The absorption and fluorescence spectra of TMBI in 3-MP and TMS are shown in Figures 1 and 2, respectively. The absorption spectra in solutions are greatly different from the gas-phase spectrum and also change with temperature. This change in the spectral shape by the environment and temperature is quite anomalous and one might be tempted to think of an isomeric equilibrium. However, as there are no geometric isomers having different ultraviolet absorption spectra conceivable for TMBI, such an idea is of course not feasible. The blue shift at the onset of the absorption from the gas phase to the solution is typical of the behavior of Rydberg bands of organic molecules.[2,8] Also, its intensity obtained here ($\epsilon \sim$ 2000–3000) is reasonable for Rydberg transitions. The blue shift of the fluorescence spectrum of the 3-MP solution with decreasing temperature also shows that the fluorescent state is of Rydberg character.[2] These results suggest that the absorption spectra of TMBI in the region lower than 45 kK are assigned to the transitions to the Rydberg-like and ionized states. The steeply rising absorptions in the region higher than 45 kK both in solutions and in the gas-phase are assigned to the transition to the lowest $(\pi-\pi^*)$-type excited state of TMBI, as discussed previously.[8]

The photocurrent yield (the photocurrent divided by illumination intensity) is shown in Figure 3, together with the fluorescence excitation spectra and the absorption spectra. The photocurrent yield is correlated with the probability of the transition to the ionization continuum in solutions, while the fluorescence excitation spectrum can be correlated with transitions to Rydberg-like states. These interpretations are supported by the fact that the absorption spectrum can be regarded as a composition of the photocurrent yield curve and the fluorescence excitation spectrum for each solution, as seen from Figure 3A.[9]

Based on the above interpretation, the relatively sharp peak appearing at 36.5 kK in the 3-MP solution spectrum at 77 K can be assigned to the transitions to Rydberg-like states (Figure 3B). The peak at 36.5 kK observed in the TMS solution at 77 K is also probably of the same character. To determine the ionization thresholds in these solutions at 77 K, the formation of TMBI$^+$ was investigated spectroscopically. On excitation of the TMS solution with monochromatic light from an Aminco-Bowman spectrophotofluorimeter, it rapidly became yellow at short wavelengths and a new absorption band assigned to TMBI$^+$ at 407 nm[10] appeared. The threshold of the action spectrum lay at 350 ± 10 nm, almost the same as the onset of the absorption spectrum of TMBI. This very efficient photoionization seems to be in good harmony with the fact that the TMS rigid solution at 77 K shows no detectable fluorescence. The colored sample showed no thermoluminescence.

The similar uv irradiation of TMBI in the 3-MP solutions at 77 K yielded no new band.

Absorption spectra and photocurrent yield curves were also obtained in other solvents. The results are summarized in Table I. It is seen that the absorption spectra shift very little with solvent, while the ionization threshold definitely shifts.

Discussion

As stated in the preceding section, the near-ultraviolet absorption spectra of TMBI have been assigned to transitions from the ground state to the Rydberg-like and ionized states in solutions, or, by analogy with the photoionization
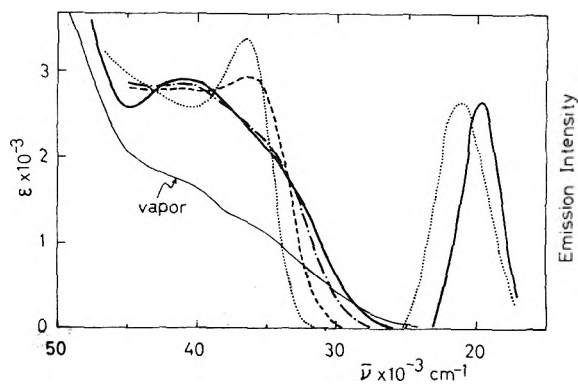
Figure 1. Absorption (left) and fluorescence (right) spectra of TMBI in 3-MP at (—) 293, (–·–·–) 231, (- - - - -) 134, and (·····) 77 K. ϵ is the molar extinction coefficient (M^{-1} cm^{-1}), the error of which is estimated to be less than 5%. The curve denoted by vapor is the vapor-phase absorption spectrum of TMBI, with an arbitrary unit for the ordinate.
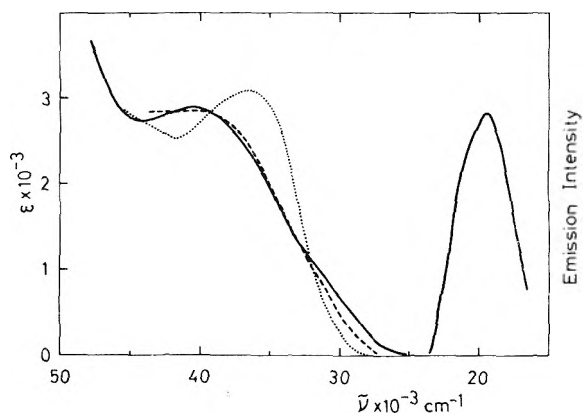
Figure 2. Absorption (left) and fluorescence (right) spectra of TMBI in TMS at (—) 293, (- - - - -) 216, (·····) 77 K.

of impurity states in inorganic crystals, to transitions to the Wannier-type impurity states and conduction bands of solvents.

The hot electron, formed by photoexcitation, relaxes with time, losing its kinetic energy through the collisional interaction with randomly oriented solvent molecules, until it comes to thermal equilibrium with the solvent inside or outside the sphere of the coulombic well of the parent cation. From electron mobility measurements,[11,12] it is suggested that such a thermalized electron can be described as a quasi-free particle with a mobility of about 150 cm^2 V^{-1} sec^{-1}, which is halted briefly from time to time by groups of solvent molecules. The trap depth ranges from 0.18 for n-hexane to 0.02 eV for neopentane.

The absorption spectra of TMBI in solutions (Figures 1–3) show that the part of the absorption assigned to transitions to Rydberg-like states is sharpened with decreasing temperature.[13] This part is thought to consist of numerous transitions to Rydberg-like states. The spectral sharpening mentioned above can be explained as follows. As discussed in a previous paper,[2] the lowest Rydberg band is blue shifted by change from the vapor phase to the solution phase, and further to the solid solution, while the ionization threshold is not shifted as much, or rather red shifted. The Rydberg states therefore become more condensed. This condensation is also understood by taking into account that the stabilization of Rydberg-like states by the electronic polarization of the solvent is small for the lower state

TABLE I: Relation between the Excess Electron Mobility and Some Quantities Concerning the Photoelectron Ejection Process of TMBI in Various Organic Media[a]

Solvent	T	μ^d	ϵ_0	ϵ_{max}	$E_{th}{}^b$	$E(e)$	E_b
n-Pentane	293	0.1	3.23	5.10	4.29	−0.11	1.06
3-Methylpentane	293		3.26	5.11	4.24	−0.12	0.98
Cyclopentane	293	1.1	3.18	5.04	4.08	−0.23	0.90
Isooctane	293	7	3.24	5.06	3.99	−0.35	0.75
Tetramethylsilane	293	90	3.18	5.04	3.66	−0.69	0.48
3-Methylpentane	77		3.87	4.51			
Tetramethylsilane	77		3.44	4.54	3.54^c	−0.66	0.10
TMBI vapor	323		2.95^e		5.41^e	0.00	2.46

[a] T, temperature in K. μ is the excess electron mobility $(cm^2\ V^{-1}\ sec^{-1})$. ϵ_0, ϵ_{max}, and E_{th} are the energies (in eV) at the absorption onset, the absorption maximum, and the photocurrent threshold, respectively. $E(e)$ is the energy (in eV) of the excess electron. E_b is the electron binding energy (in eV). [b] Determined from plots of log (photocurrent)/(light intensity) vs. photon energy. [c] From the threshold of the TMBI$^+$ production monitored spectroscopically. [d] References 5 and 6. [e] Reference 8.
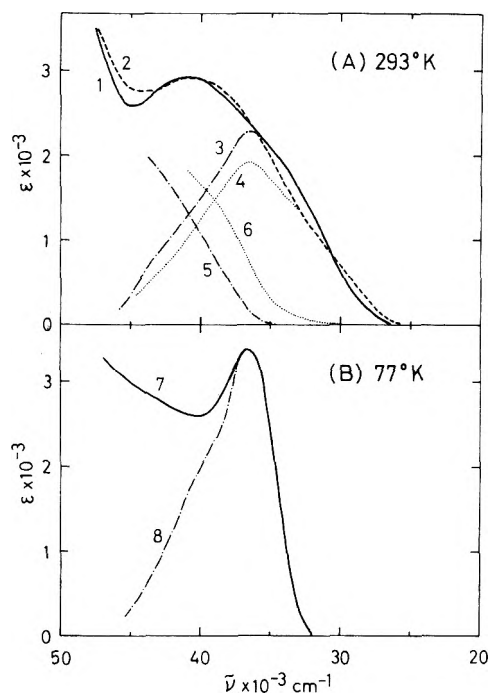
Figure 3. Photocurrent yield curves and fluorescence excitation spectra of TMBI in solutions. Curve 1 is the absorption spectrum of the 3-MP solution and curve 2 that of the TMS solution. Curve 3 is the fluorescence excitation spectrum of the 3-MP solution and curve 4 that of the TMS solution. Curve 5 is the photocurrent yield curve of the 3-MP solution and curve 6 that of the TMS solution. Curves 7 and 8 are the absorption and the fluorescence excitation spectrum of the 3-MP solution at 77 K, respectively. The fluorescence excitation spectra are so adjusted as to agree with the corresponding absorption spectra in the lower energy region.

Figure 4. The energy level diagram showing the photoelectron ejection of a molecule, M, in a gas phase (left) and in a nonpolar solution (right). The subscripts g and s represent the gas phase and the solution, respectively.

but large for the higher one with increasing size of the Rydberg orbital, while the repulsive interaction between the Rydberg electron and the solvent molecules corresponding to the large, negative electron affinity of the solvent molecule is relatively indifferent to the size of the Rydberg orbital. Both effects increase with the density of solvent. It is also pointed out as another factor influencing the sharpening of the Rydberg band that the local distribution of the solvent molecules around TMBI becomes more homogeneous at low temperature as the solvent becomes more compact.

As discussed in previous papers,[2,4] the ionization potential of a molecule, M, in solution, $I_s(M)$, is related to that in the gas phase, $I_g(M)$, as follows (Figure 4).

$$I_s(M) = I_g(M) + S(M) - \{S(M^+) + S'(M^+)\} + E(e) \quad (1)$$

where $S(M)$ is the solvation energy for M; $S(M^+) + S'(M^+)$ are the solvation energies for M^+, in which $S(M^+)$ gives only the part relevant to the monopositive charge on M^+ and $S'(M^+)$ the remaining part; and $E(e)$ is the energy of an electron in the bottom of the conduction band of the solvent relative to the vacuum level. Under the approximation that $S(M)$ is nearly equal to $S'(M^+)$,[4] the above equation becomes

$$I_s(M) = I_g(M) - S(M^+) + E(e) \quad (2)$$

$S(M^+)$ can be calculated by use of Born's equation,[4] and $I_s(M)$ is taken as equal to the photocurrent threshold, $E_{th}(M)$.[14] We can, therefore, calculate the values of $E(e)$ in various solvents. The results, obtained by using $I_g(TMBI)$ = 5.41 eV[8] and $a(TMBI^+)$ = 3.25 Å,[4] the average radius assumed for M^+ in the Born's equation, are listed in Table I. The $E(e)$ values thus calculated are in good agreement with those reported.[3,7]

The binding energy between M^+ and the electron in the lowest Rydberg-like state, E_b, which can be taken as the energy difference between the ionization threshold and the absorption onset (ϵ_0), is also included in Table I. The value of E_b obtained for TMBI in the gas phase, ~2.5 eV, is in good agreement with that expected for large molecules,[15] and of reasonable magnitude. The large decrease of E_b for TMBI in solutions is a consequence of the great lowering of the ionization threshold and the slight destabilization of the lowest Rydberg state in solutions.

The main aspects of our experimental results on the sol-

vent dependence of the photoelectron ejection process at room temperature are now summarized as follows. With the increasing electron mobility, (1) the electron energy in the bottom of the conduction band, $E(e)$, is lowered, (2) the electron binding energy, E_b, decreases, and (3) the intensity of the absorption band assigned to the transitions to Rydberg-like states becomes weak, as can be seen from Figure 3A.[16]

The change of E_b seems to be caused by the difference in the microscopic structure of the solvent, because the optical dielectric constant, ϵ_{op}, and hence the coulombic interaction between the ejected electron and the parent cation, $-e^2/\epsilon_{op}r$, is almost the same in TMS and 3-MP. It may further be concluded that all the changes mentioned above originate from the difference of the molecular sphericity of the solvent.

Theoretical interpretations on the shifts of the electron mobility and energy were made.[11,17,18] The aforementioned correlations may be understood by using an effective-mass (m^*) approximation.[19] Since the relation, $E_b \propto m^*$, is expected by analogy of the impurity levels and also since the electron mobility (μ) increases with decreasing m^*, it follows that E_b decreases with increasing μ. In addition, as E_b gets smaller, the radius of the electron orbital becomes larger, and the transition probability becomes smaller.

It should be noted that E_b and $E(e)$ at low temperature also depend on the molecular sphericity of the solvent. Especially, it is very interesting that the magnitude of E_b in the rigid TMS solution at 77 K is extremely small. According to the above-mentioned correlations, it is expected that very high-mobility electrons exist in this matrix. Such a property is unique in organic media.

References and Notes

(1) R. C. Jarnagin, *Acc. Chem. Res.*, **4**, 420 (1971).

(2) Y. Nakato, M. Oazki, and H. Tsubomura, *J. Phys. Chem.*, **76**, 2105 (1972).

(3) R. A. Holroyd, *J. Chem. Phys.*, **57**, 3007 (1972).

(4) Y. Nakato, T. Chiyoda, and H. Tsubomura, *Bull. Chem. Soc. Jpn.*, **47**, 3001 (1974).

(5) W. F. Schmidt and A. O. Allen, *J. Chem. Phys.*, **52**, 4788 (1970).

(6) R. M. Minday, L. D. Schmidt, and H. T. Davis, *J. Chem. Phys.*, **54**, 3112 (1971).

(7) R. A. Holroyd and M. Allen, *J. Chem. Phys.*, **54**, 5014 (1971).

(8) Y. Nakato, M. Ozaki, and H. Tsubomura, *Bull. Chem. Soc. Jpn.*, **45**, 1299 (1972). The absorption spectra of TMBI in *n*-pentane reported in this paper (Figure 3, curves b and c) were found to be erroneous by recent experiments. It seems that part of TMBI was oxidized by a small amount of atmospheric oxygen contained as an impurity in the cell.

(9) Since photocurrents are measured under steady illumination, they may involve the effect of recombination of free charge carriers, especially in the region of large current. The effect of this recombination on the fluorescence excitation spectrum may, however, be neglected because a rigid TMS solution at 77 K containing TMBI⁺ and trapped electrons shows no thermoluminescence, as mentioned later in the text.

(10) This assignment is supported by the following facts. A cation radical of tetrakis(dimethylamino)ethylene, whose absorption band with a peak at 405 in *n*-decane,[10a] at 385 in acetonitrile,[10b] and at 383 nm in ethanol.[10c] (a) C. A. Heller and A. N. Fletcher, *J. Phys. Chem.*, **69**, 3313 (1965); (b) K. Kuwata and D. H. Geske, *J. Am. Chem. Soc.*, **86**, 2101 (1964); (c) M. Hori, K. Kimura, and H. Tsubomura, *Spectrochim. Acta, Sect. A*, **24**, 1397 (1968). The 407-nm band is observed only in TMS solutions, in which the photocurrent yield at room temperature is much larger than in other hydrocarbons. This suggests strongly that the product is due to photoionization.

(11) H. T. Davis, L. D. Schmidt, and R. M. Minday, *Chem. Phys. Lett.*, **13**, 413 (1972); R. M. Minday, L. D. Schmidt, and H. T. Davis, *J. Phys. Chem.*, **76**, 442 (1972).

(12) J.-P. Dodelet, K. Shinsaka, and G. R. Freeman, *J. Chem. Phys.*, **59**, 1293 (1973).

(13) Similar behaviors were observed in absorption bands of impurity states in inorganic crystals, for example, in KI diluted in KCl crystals; H. Mahr, *Phys. Rev.*, **125**, 217 (1962).

(14) A question might arise whether $E_{th}(M)$ agrees with $I_s(M)$, because the ejected electron might lose part of its kinetic energy while it migrates away from the parent cation. The fact that the values of $E(e)$, calculated by using eq 2 and $E_{th}(M) = I_s(M)$, are in good agreement with those determined by the method of photoelectron injection from metals to hydrocarbons[7] seems to show its validity.

(15) M. B. Robin, "Higher Excited States of Polyatomic Molecules", Vol. 1, Academic Press, New York, N.Y., 1974, pp. 51-65.

(16) In relation to this, it is to be noted that the shape of the absorption spectrum of the 3-MP solution at room temperature is slightly different from that of the TMS solution.

(17) K. Fueki, D.-F. Feng, and L. Kevan, *Chem. Phys. Lett.*, **13**, 616 (1972).

(18) N. R. Kestner and J. Jortner, *J. Chem. Phys.*, **59**, 26 (1973).

(19) C. Kittel, "Introduction to Solid State Physics", Wiley, New York, N.Y., 1953.

Vibrational Spectra and Structure of Bicyclo[2.1.0]pentane[1]

J. Bragin* and D. Guthals

Department of Chemistry, California State University, Los Angeles, Los Angeles, California 90032 (Received January 8, 1975; Revised Manuscript Received July 11, 1975)

Vibrational spectra of bicyclo[2.1.0]pentane are presented for the molecule in the gaseous, liquid, and solid states and assignments for all vibrational fundamentals are proposed. The transannular bond results in an unusual potential function for puckering of the five-membered ring. This and other structural features are discussed, qualitatively, in terms of the proposed vibrational assignments.

Introduction

Recent interest in transition metal complex promoted rearrangements of strained hydrocarbons[2a] has promoted an investigation of the mechanism and intermediates in reactions of this type involving bicyclo[2.1.0]pentane using low-temperature vibrational spectroscopy as a probe. Since no vibrational assignments for this molecule were found in the literature the complete spectrum of vibrational fundamentals was obtained and is presented herein along with a proposed assignment.[2b]

Relatively few assignments of the vibrational spectra of highly strained molecules have been reported yet such data has found wide application in elucidating the quantitative relationships between the structure, energy, and reactivities of small acyclic systems.[2c] Also, there has been considerable recent interest in spectra–structure relationships for the conformation changing vibrations of small rings[3] yet few polycyclic or highly strained molecules have been included in such studies. For these reasons it is felt that the vibrational data and analysis presented here are of sufficiently general interest to warrant publication as a separate paper.

Experimental Section

Bicyclo[2.1.0]pentane was prepared by the method of Gassman and Mansfield.[4] Sample purity was checked by comparing the infrared spectrum of this compound with that reported by Criegee and Rimmelin.[5] In addition, since the major impurity of the synthetic reaction is known to be cyclopentene, a careful search was made for spectroscopic evidence of that molecule in the sample. The low-temperature infrared spectrum of solid bicyclo[2.1.0]pentane (Figure 1) shows no sign of absorption in regions in which solid cyclopentene exhibits its most intense vibrational bands.[6] Since the two compounds boil within 1°C of each other, the failure to observe any cyclopentene is not due to any purification by fractional sublimation resulting from the deposition and annealing processes accompanying preparation of the solid film at low temperatures. Furthermore, the Raman spectrum of gaseous bicyclo[2.1.0]pentane (Figure 2) showed no evidence of cyclopentene impurity.

Infrared spectra were recorded on a Beckman IR-12 double-beam grating spectrophotometer which was purged with a continuous stream of dry nitrogen gas and calibrated in the usual manner.[7] The spectrum of the gaseous molecule at 90 mm pressure (Figure 3) was obtained in a 10-cm Pyrex cell fitted with CsI windows and viton O ring vacuum seals. Polycrystalline films of bicyclo[2.1.0]pentane were prepared in a modified Wagner–Hornig cold cell[8] by permitting the vapors to slowly distill onto a CsI substrate in good thermal contact with a dewar of liquid nitrogen at its normal boiling point. The solid samples were repeatedly annealed until no further change in the spectrum was observed. The use of a silicon wedge as a substrate gave spectra identical with those obtained for the sample deposited on CsI and there were no differences in the spectra of several different depositions on CsI.

The Raman spectrum of liquid bicyclo[2.1.0]pentane (Figure 4), degassed and sealed under vacuum in a Pyrex capillary, was excited with 150 mW (measured at sample) of 488.0-nm radiation from an Ar$^+$ laser and recorded on a Cary Model 82 spectrometer. The sample capillary was illuminated and viewed normal to its long axis and depolarization ratios were obtained by rotating a piece of polaroid in the scattered beam which subsequently passed through a polarization scrambler before entering the monochromter. The Raman spectrum of the gaseous molecule at 85 mm pressure was obtained with the same equipment by focussing 10 passes of a 1-W (measured at sample) 514.5-nm Ar$^+$ laser beam at the center of a quartz cell fitted with quartz windows set at Brewster's angle. The Raman spectrometer was calibrated with atomic emission lines. The spectral data are summarized in Table I.

Assignment

The microwave substitution structure of bicyclo[2.1.0]pentane[9] is shown in Figure 5. The molecule exhibits only a plane of symmetry which bisects both the cyclobutyl and cyclopropyl rings, and is normal to the planes of both rings. The angle between the ring planes is 112.67°. Under the C_s point symmetry of the molecule, all 33 vibrational modes are both Raman and infrared active. Of these, 18 are symmetric (a') and 15 are antisymmetric (a'') with respect to the molecular symmetry plane. The a' modes may give rise to a maximum of 18 polarized Raman lines all of which may have infrared counterparts. The microwave study of bicyclo[2.1.0]pentane[9] has shown that the rotation axes of least and greatest moment of inertia (A and C, respectively) lie in the molecular symmetry plane. Therefore, in the spectrum of the gaseous molecule the a' modes will give rise to bands with sharp single Q branches whereas the a'' modes will be distinguished by the absence of a single central Q branch. The calculated[10] PR separations are 23 and 31 cm^{-1} for ideal A and C type bands, respectively. This is

TABLE I: Observed Frequencies[a] of Bicyclo[2.1.0]pentane

Infrared		Raman		
Vapor	Solid	Liquid	Vapor	Assignm
		280 vw brd dp	265 vw brd dp	33
403 P				
416 Q vw A	424 m	418 w p	417 Q m p	18
427 R				
698 vw		678 vw brd dp		18 + 33
743 P				
755 Q m A/C	755 s	755 m brd p?	755 Q w p	17
769 sh				
			765 P	
774 Q m A/C	767 w	775 w brd p?	774 Q w p	16
			781 R	
783 Q m B	777 s			
790 Q m B	782 s	781 m brd dp	790 w brd dp	32
799 R				
870 P	881 w			
883 Q m A/C	885 w	880 w brd dp	883 Q w dp	15
903 P				
914 Q m B	917 m	914 m brd dp		31
918 Q m B				
927 Q m B	924 w		925 w brd dp	30
962 P			961 sh	
968 Q m A/C	966 m	966 vs p	967 Q vs p	14
974 Q m B				
981 Q m B	978 m		978 brd sh	29
1012 Q vw A/C	1006 w	1009 m p	1012 Q m	13
1017 P				
1026 Q w B				
1033 Q w B	1028 s			28
1039 P				
1049 Q w B				
1056 Q w B	1047 m			27
1066 R				
	1096 w			
	1098 w			
1094 P	1101 w			
1106 Q w A	1104 w	1104 s p	1107 Q s	12
1117 R	1108 w			
		1170 sh p	1179 Q w	18 + 32
	1188 w		1191 Q ms	
	1190 w	1188 s p	1195 Q ms	11
	1198 w			26
1207 P				
1218 Q w C	1210 w brd			10
	1217 w			29 + 33
1234 Q w B				
1242 Q w B	1235 w		1237? vw brd	25
1264 P				
1274 Q m B	1265 sh			
1280 Q m A/C	1270 s	1275 vw brd dp	1283? vw brd	9
1284 Q m B				24
1295 R				
		1296 vw brd p	1300 Q vw	15 + 18
1320 Q vw B		1323 vw dp		
1329 Q vw B	1324	(obsd in ⊥)		23
1332 Q vw A/C		1326 m p	1330 Q m	8
1341 R			1335 sh	
1384 Q vw A/C				14 + 18
1434 P	1435 sh w			
1446 Q mw A	1438 m	1441 w brd dp	1445 w brd	7

Table I (*Continued*)

| Infrared | | Raman | | |
Vapor	Solid	Liquid	Vapor	Assignm
1458 R	1440 m			
1461 Q mw B				
1468 Q mw B	1457 w	1450 sh		22
1470 Q m A/C	1466 w	1464 w dp	1470 Q w	6
1481 R				
1508 sh				16 + 17
1638 p				15 + 16
1648 Q vw				
1656 R				
1674 Q? vw B?				
1685 Q? vw B?				16 + 31
1707 p				
1715 Q vw A/C				14 + 17
1723 R				
1772 sh				
1777 p				13 + 16
1793 R				
1800 sh				
1825 P				
1835 Q vw A/C				14 + 15
1846 R				
2016 P				
2029 Q vw A/C				9 + 17
2040 R				
2074 Q vw A/C				10 + 15
2098 Q vw A/C				9 + 17
2215 Q vw A/C				6 + 16
2682 Q vw A/C				6 + 10
2866 P				
2874 Q s A/C	2861 s	2862 s p	2875 Q vs	5
2885				
	2880 w			2 × 22
		2898 sh p?		6 + 22
2907 P				
2921 Q s A/C	2910 m	2909 s p	2922 Q vs	4
2932 Q s B				
2939 Q s B	2929 s	2926 sh dp?	2936 Q m	21
2946 Q vs A/C	2939 s	2937 s p	2945 Q vs	3
2966 Q vw B?	2961 sh	2957 sh dp	2965 w brd	20
2970 P				
2982 Q vs A/C	2974 s	2975 s p	2982 Q vs	2
2993 R				
3051 Q s B				
3058 Q s B	3045 s	3051 sh dp	3058 Q vs	19
3070 Q s A/C	3056 s	3060 s p	3070 Q vs	1

a Frequencies in cm^{-1}. vw = very weak, w = weak, mw = medium weak, m = medium, s = strong, vs = very strong, sh = shoulder, brd = broad, p = polarized, dp = depolarized, A = A-type band, B = B-type band, C = C-type band.

in good agreement with the observed separations of 22 and 31 cm^{-1}, respectively. The calculated[10] QQ separation for B type bands is 8 cm^{-1} and the observed separations for such bands average 8 cm^{-1}.

C–H Stretches. The structure of the representation formed by the eight CH stretches is 5a′ + 3a″. The approximate descriptions of these modes and their assignments are given in Table II. In view of the expected s character in the bonds and the correlation between this quantity and vibrational frequency the CH stretching frequencies should

occur in the order: 1-bridge methylene > bridgehead methine > 2-bridge methylene. The proposed assignments are consistent with this expectation and also with the infrared and Raman band contours of the gaseous molecule and the Raman depolarization data obtained for the compound as a neat liquid (cf. Table I). In addition, the assignments are consistent with those proposed for cyclopropane,[11] substituted cyclopropanes,[12] cyclobutane,[13] cyclobutene,[14] bicyclobutane,[15] norbornane,[16] and bicyclo[1.1.1]pentane.[17]

CH Deformations. The CH$_2$ deformations should give
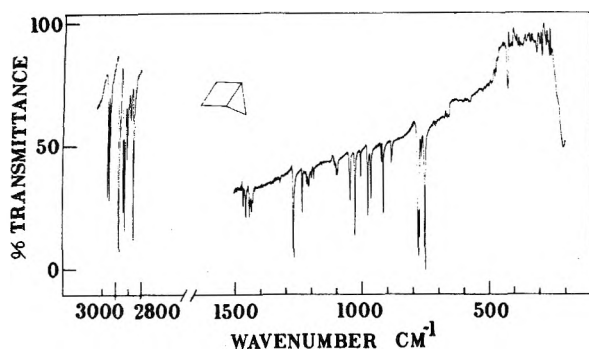
Figure 1. The infrared spectrum of polycrystalline bicyclo[2.1.0]pentane at $-175°C$.
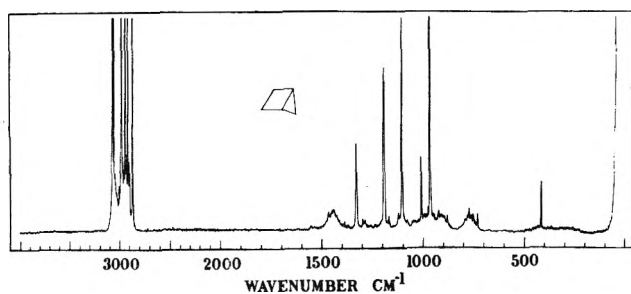
Figure 2. The Raman spectrum of gaseous bicyclo[2.1.0]pentane at 85 mm pressure excited by 1 W of 514.5-nm Ar^+ laser radiation.
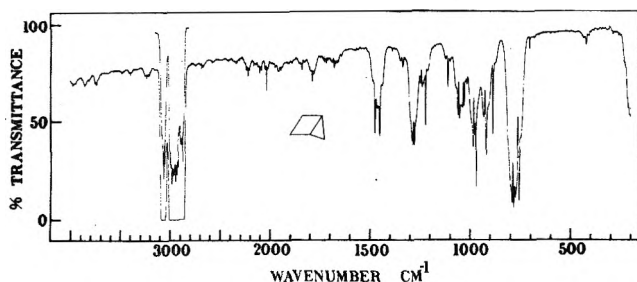
Figure 3. The infrared spectrum of gaseous bicyclo[2.1.0]pentane at 90 mm pressure (insert, 18 mm pressure) and 10 cm absorption path.

Figure 4. The Raman spectrum of liquid bicyclo[2.1.0]pentane excited with milliwatts of 488.0-nm Ar^+ laser radiation.
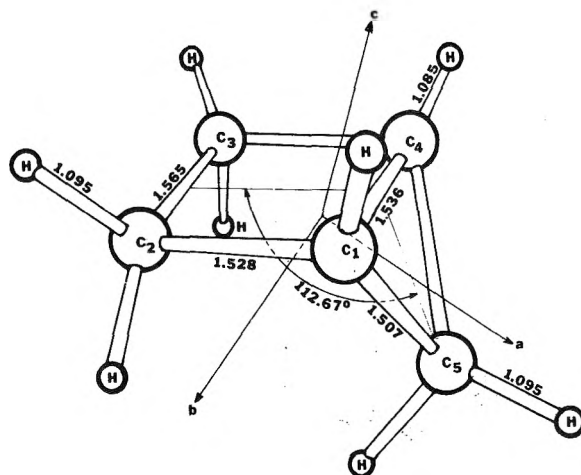
Figure 5. The microwave substitution structure of bicyclo[2.1.0]pentane (ref 9).

rise to two A/C hybrid bands and one B-type band in the 1400–1500-cm^{-1} range of the infrared spectrum of gaseous bicyclo[2.1.0]pentane. This prediction is confirmed (cf. Table I) and the assignments are straightforward. The extent of mixing between the a' CH_2 deformations cannot be determined with the present data and we have chosen to describe these two modes as pure 1-bridge and 2-bridge CH_2 scissoring motions.

The bridgehead deformations should give rise to two symmetric and two antisymmetric modes. Thus ν_8 and ν_9 are described as a' bridgehead deformations and ν_{23} and ν_{24} as a'' bridgehead deformations. Analogous modes have been assigned at 1228 cm^{-1} in bicyclo[1.1.1]pentane[17] and in the range 1145–1317-cm^{-1} in norbornane.[16] Thus, the assignments (cf. Table II) proposed here are consistent with those of analogous modes in other bicyclic molecules as well as with the band contours and Raman depolarization ratios expected for the bridgehead deformations.

There are nine CH_2 deformations remaining unassigned and these may be described (in order of decreasing frequency) as twists, wags, and rocks. The structure of the representation formed by these modes is twist (a' + 2a''),

wag (a' + 2a''), and rock (2a' + a''). The extent of mixing of the 1- and 2-bridge a'' methylene deformations is not known and these modes will not be characterized further.

The twisting modes of cyclobutane[13] have been assigned at 1225 cm^{-1} in good agreement with the assignment of ν_{10} to the weak C type band observed at 1218 cm^{-1} in the infrared spectrum of gaseous bicyclo[2.1.0]pentane. It should be noted that ν_{10} cannot involve any 1-bridge methylene twisting due to the symmetry of the molecule. The antisymmetric methylene twists, ν_{25} and ν_{26}, are assigned to a weak B-type band observed at 1238 cm^{-1} in the infrared spectrum of the gaseous molecule and to a weak band observed at 1198 cm^{-1} in the infrared spectrum of the solid, respectively.

There are four polarized bands observed in the Raman spectrum of liquid bicyclo[2.1.0]pentane in the frequency range expected for the a' methylene wag (ν_{12}). The most intense of these correlate well with the ring breathing frequencies in cyclopropane[11] and cyclobutane.[13] Of the remaining two, ν_{12} is described as a cyclobutylmethylene wag although the possibility of extensive mixing with ν_{13} cannot be excluded in the absence of data for the perdeuterated molecule. Reasons for this assignment will be given in the following section

Of the five, as yet unassigned B type infrared bands in the range expected for the a'' methylene wags, those at 1030, 978, and 922 cm^{-1} are assigned to the skeletal deformations as described in the following section. The two a'' methylene wags (ν_{27} and ν_{31}) are assigned at 1053 and 917 cm^{-1}, respectively.

The methylene rocking modes (ν_{16}, ν_{17}, ν_{32}) should give

TABLE II: Vibrational Assignments
of Bicyclo[2.1.0]pentane

Vibrn no.	Approx description of vibrn[a]	Infrared Vapor	Infrared Solid	Raman Liquid	Raman Vapor
		a'			
1	Cp CH$_2$ (−)	3070	3056	3060	3070
2	Cp CH$_2$ (+)	2982	2974	2975	2982
3	Bh CH	2946	2939	2937	2945
4	Cb CH$_2$ (−)	2921	2910	2909	2922
5	Cb CH$_2$ (+)	2874	2861	2862	2875
6	CH$_2$ def	1470	1466	1564	1470
7	CH$_2$ def	1446	1440	1441	1445
8	Bh CH def	1332	1324*	1326	1330
9	Bh CH def	1280	1270	1275*	1283*
10	Cb CH$_2$ tw	1218	1210		
11	Cp ring breathe		1190	1188	1195
12	Cb CH$_2$ wag	1106	1098	1104	1107
13	Cb ring def	1012	1006	1009	1012
14	Cb ring breathe	968	966	966	967
15	Cp ring def	883	885	880	883
16	CH$_2$ rock	774	767	775	774
17	CH$_2$ rock	755	755	755	755
18	Envelope flap	416	424	418	417
		a''			
19	Bh CH	3054	3045	3051	3058
20	Cb CH$_2$ (−)	2966	2961	2957	2965
21	Cb CH$_2$ (+)	2936	2929	2926	2936
22	CH$_2$ def	1465	1457	1450	
23	Bh CH def	1325	1324*	1323	
24	Bh CH def	1279	1265	1275*	1283*
25	CH$_2$ tw	1238	1235		1237
26	CH$_2$ tw		1198		
27	CH$_2$ wag	1053	1047		
28	Cb ring def	1030	1028		
29	Cb ring def	978	978		978
30	Cp ring def	922	924		925
31	CH$_2$ wag	914	917	914	915
32	CH$_2$ rock	787	782	781	790
33	Cb ring pucker			280	280

[a] Cp = cyclopropyl, Cb = cyclobutyl, Bh = bridgehead. (−) = out-of-phase, (+) = in-phase, def = deformation, tw = twist. * = assigned to more than one vibration.

rise to an infrared band with a B-type contour and two with A, C, or A/C hybrid contours. The Raman counterparts of the latter two may be polarized. Since there are only two A-type infrared bands in the frequency range of the methylene rocks and these have polarized Raman counterparts, they may be assigned to ν_{16} and ν_{17} with confidence. Similarly, the B-type infrared band centered at 787 cm^{-1} with a depolarized Raman counterpart may be assigned to ν_{32}.

Skeletal Modes. The structure of the representation formed by the skeletal vibrations of bicyclo[2.1.0]pentane is 5a' +4a''. The five totally symmetric skeletal motions may be described as ring breathing (two modes), ring deformation (two modes), and envelope flap (bending around the transannular bond).

Breathing modes always give rise to the most intense Raman lines and these motions in cyclopropane[11] and cyclobutane[13] have been assigned at 1188 and 1004 cm^{-1}, re-

spectively. Similarly, the three- and four-membered ring breathes (ν_{11} and ν_{14}) are assigned to the bands at 1195 and 967 cm^{-1}, respectively, in the Raman spectrum of gaseous bicyclo[2.1.0]pentane.

There has been some controversy as to the deformation frequencies of the cyclopropyl ring.[11] Recent analyses of these vibrations[11e,f] indicate that ν_{11} of C$_3$H$_6$ (868 cm^{-1}) has a much larger skeletal component than ν_{10} (1028 cm^{-1}). In the present assignment the description of ν_{15} and ν_{30} as the symmetric and antisymmetric components of the analog of ν_{11} in the three-membered ring in bicyclo[2.1.0]pentane is consistent with the cyclopropane analyses.

One symmetric and two antisymmetric skeletal modes expected above 800 cm^{-1} remain unassigned. These may all be described as cyclobutyl deformations. Two of the three may be considered as arising from a degenerate mode, in an analogous cyclobutyl ring of higher symmetry, which is split in bicyclo[2.1.0]pentane. Thus a pair of closely spaced fundamentals is expected. One of these gives rise to a B-type band in the infrared spectrum of the gaseous molecule and a depolarized Raman counterpart whereas the other exhibits an A/C type band contour and a polarized Raman counterpart. These criteria best fit the assignment of ν_{13} and ν_{28} to the modes under consideration. Although it is possible to assign 1106 cm^{-1} to the a' mode in question, such an assignment presents several difficulties. In the first place this assignment would result in an average cyclobutyl stretching frequency of 1020 cm^{-1} for bicyclo[2.1.0]pentane compared with 975 cm^{-1} for cyclobutane,[13a] whereas the present assignment gives a value of 997 cm^{-1} for this quantity. Some increase in electron density of the cyclobutyl ring in bicyclo[2.1.0]pentane over that in cyclobutane is consistent with the average bond lengths of these two cyclobutyl rings,[9] however, this effect is a small one. Moreover, the alternative assignment would require overlap of the frequency ranges of the cyclobutyl wags and skeletal motions whereas in cyclobutane the methylene wags appear to be firmly assigned at appreciably higher frequencies than the skeletal modes.[13a] The third cyclobutyl ring deformation presently under consideration is of a'' symmetry and may be assigned to ν_{29} (978 cm^{-1}) by analogy with the 999-cm^{-1} assignment for the B$_2$ ring mode in cyclobutane.[13a]

Only two vibrational modes of bicyclo[2.1.0]pentane are expected to be below 500 cm^{-1} and only the a' envelope flap (ν_{18}) may be assigned to a polarized Raman line. Of the two frequencies observed below 500 cm^{-1}, in the vibrational spectrum of bicyclo[2.1.0]pentane, only the Raman counterpart at 417 cm^{-1} is polarized and, therefore, it must be assigned to ν_{18}. The last mode to be assigned is ν_{33} and this must be described as the puckering of the four-membered ring. The only band observed below 500 cm^{-1} in the vibrational spectrum of bicyclo[2.1.0]pentane which may be assigned to an a'' fundamental is the depolarized band at 280 cm^{-1} in the Raman spectrum of the liquid molecule. Therefore, this frequency is assigned to ν_{33}. As will be discussed in detail below, the analogous mode in cyclobutane has been reported at 199 cm^{-1}.[13]

Discussion

In the infrared spectrum of polycrystalline bicyclo[2.1.0]pentane the splitting of ν_7, ν_{11}, ν_{12}, ν_{15}, and ν_{32} is thought to be due to coupling of the motions of at least two symmetry related molecules in the unit cell. Since the multiplet spacing does not appear to be approximately propor-

tional to the absolute intensity of the bands, the intermolecular forces are not primarily dipolar.

Harris et al.[18] have discussed five-membered ring puckering potentials in terms of mixed series in even powers of the two puckering coordinates (applicable to molecules having C_{2v} symmetry in the planar state). Due to the contribution of angle strain, the anharmonic terms in such series may be significant.[19] Such a situation has a number of consequences for the vibrational spectrum. In the first place, significant anharmonicity of the bending and twisting modes (ν_{18} and ν_{33}, respectively) will shift the frequency of hot bands of these vibrations relative to their respective fundamentals. If the upper states of these low-energy motions are appreciably populated, a band progression may be observed assuming the components are sharp enough to be distinguished. A second consequence of significant anharmonicity in the puckering modes is that higher order cross terms can be large enough to couple ν_{18} and ν_{33}.[20,21]

In the present work, a very broad featureless band, approximately centered at 265 cm^{-1}, was observed in the Raman spectrum of gaseous bicyclo[2.1.0]pentane with a weak depolarized counterpart appearing at 280 cm^{-1} in the Raman spectrum of the liquid. This frequency has been assigned to the a$''$ twisting fundamental (ν_{33}), whereas the bending fundamental (ν_{18}) has been assigned to the very weak A-type band observed at 416 cm^{-1} in the infrared spectrum of the gas with Raman counterparts at 418 cm^{-1} (liquid, w, p) and 417 cm^{-1} (gas, m, p). A search for overtones and for additional features on the fundamental infrared and Raman bands of the gaseous molecule was limited by the amount of material available and a tendency toward increasingly rapid decomposition at higher laser powers.

The failure to observe sharp features on the 265-cm^{-1} Raman band in gaseous bicyclo[2.1.0]pentane and the absence of any appreciable sample scattering in the 100–200-cm^{-1} region favor assignment of this feature to the fundamental twisting transition. The single sharp feature observed at 416 ± 1 cm^{-1} in both the infrared and Raman spectrum of the gaseous molecule, and the absence of a feature near 200 cm^{-1}, favors assigning this frequency to a highly harmonic fundamental. Thus the two-dimensional puckering potential well for bicyclo[2.1.0]pentane has a deep, double minimum contour along the bending coordinate which closely approximates a parabola in the region of the equilibrium structure. The contour along the twisting coordinate must be a single minimum but its curvature cannot be further characterized without assignments for upper state twisting transitions.

Direct comparisons of the puckering frequencies of bicyclo[2.1.0]pentane with those reported for other five-membered rings[22] will not be valid if the comparison molecule exhibits some degree of pseudorotation (i.e., the puckering normal modes are not pure bending or pure twisting). However, the five-membered ring in bicyclo[2.1.0]pentane is unique in that its bending frequency is higher than its twisting frequency. This may be attributed to the high barrier to inversion at the bridgehead carbon (estimated to be 30 kcal/mol)[23] which results in a bending potential function with a high curvature near the equilibrium value of that coordinate. The twisting frequency of the five-membered ring in bicyclo[2.1.0]pentane is higher than those reported for methylenecyclopentane[24] and cyclopentanone.[25] Although this may merely reflect a higher degree of quartic angular strain resulting from a twisting deformation of the

equilibrium structure, it probably includes a significant contribution from steric repulsion of the 1-bridge and 2-bridge methylene groups.

Harmony[9] has pointed out that the average length of the skeletal bonds in three-, four-, and five-membered rings in a number of different molecules is quite similar, suggesting that a fixed amount of electron density is available for C–C bonding in such structures and that it will be distributed around the ring in a manner which minimizes the molecular energy. The close correspondence between the present assignments for the breathing modes of the three- and four-membered rings in bicyclo[2.1.0]pentane and the analogous modes in cyclopropane and cyclobutane seems consistent with this idea.

References and Notes

(1) Abstracted from the thesis of D. Guthals submitted in partial fulfillment of the requirements for the degree of Master of Science (Chemistry), California State University, Los Angeles, 1975.
(2) (a) P. G. Gassman, T. J. Atkins, and J. T. Lamb, *J. Am. Chem. Soc.*, **94**, 7757 (1972); (b) Reference 26 appeared in Chemical Abstracts after the present manuscript was submitted for review. (c) J. E. Williams, P. J. Stang, and P. v. R. Schleyer, *Ann Rev. Phys. Chem.*, **19**, 531 (1968).
(3) See, for example, ref 22.
(4) P. G. Gassman and K. T. Mansfield, *Org. Syn.*, **49**, 1 (1969).
(5) R. Criegee and A. Rimmelin, *Chem. Ber.*, **90**, 414 (1957).
(6) A. Le Roy and J. C. Thouvenot, *C. R. Acad. Sci., Paris, Ser. B*, **265**, 545 (1967).
(7) (a) IUPAC, "Tables of Wavenumbers for the Calibration of Infrared Spectrometers", Butterworths, Washington, D.C., 1961; (b) R. T. Hall and J. M. Dowling, *J. Chem. Phys.*, **47**, 2454 (1967); **52**, 1161 (1970).
(8) E. L. Wagner and D. F. Hornig, *J. Chem. Phys.*, **18**, 296 (1950).
(9) R. D. Suenram and M. D. Harmony, *J. Chem. Phys.*, **56**, 3837 (1972).
(10) I. Haller, Research Paper No. RC-1152, IBM Watson Research Center, 1964.
(11) (a) J. L. Duncan and D. C. McKean, *J. Mol. Spectrosc.*, **27**, 117 (1968); (b) J. B. Bates, *J. Chem. Phys.*, **58**, 4236 (1973); (c) Hs. H. Gunthard, R. C. Lord, and T. K. McCubein, Jr., *ibid.*, **25**, 768 (1956); (d) A. W. Baker and R. C. Lord, *ibid.*, **23**, 1636 (1955); (e) J. L. Duncan and G. R. Burns, *J. Mol. Spectrosc.*, **30**, 253 (1969); (f) T. Hirokawa, M. Hayashi, and H. Murata, *J. Sci. Hiroshima Univ., Ser. A, Phys. Chem.*, **37**, 271 (1973).
(12) (a) R. W. Mitchell and J. A. Merritt, *Spectrochim. Acta, Part A*, **27**, 1609 (1971); (b) R. W. Mitchell and J. Nakovich, Jr., *ibid.*, **29**, 1153 (1973); (c) R. C. Lord and C. J. Wurrey, *ibid.*, **30**, 915 (1974); (d) L. H. Daly and S. E. Wiberley, *J. Mol. Spectrosc.*, **2**, 177 (1958); (e) T. Hirokawa, M. Hayashi, and H. Murata, *J. Sci. Hiroshima Univ., Ser. A, Phys. Chem.*, **37**, 301 (1973).
(13) (a) F. A. Miller, R. J. Capwell, R. C. Lord, and D. G. Rea, *Spectrochim. Acta, Part A*, **28**, 603 (1972); (b) R. C. Lord and I. Nakagawa, *J. Chem. Phys.*, **39**, 2951 (1963).
(14) R. C. Lord and D. G. Rea, *J. Am. Chem. Soc.*, **79**, 2401 (1957).
(15) I. Haller and R. Srinivasan, *J. Chem. Phys.*, **41**, 2745 (1964).
(16) I. W. Levin and W. C. Harris, *Spectrochim. Acta, Part A*, **29**, 1815 (1973).
(17) K. B. Wiberg, D. Sturmer, T. P. Lewis, and I. W. Levin, *Spectrochim. Acta, Part A*, **31**, 59 (1975).
(18) D. O. Harris, G. G. Engerholm, L. A. Tolman, A. C. Luntz, R. A. Keller, H. Kim, and W. D. Gwinn, *J. Chem. Phys.*, **50**, 2438 (1969).
(19) R. P. Bell, *Proc. R. Soc., Ser. A*, **183**, 328 (1945).
(20) T. Ikeda and R. C. Lord, *J. Chem. Phys.*, **56**, 4450 (1972).
(21) L. A. Carreira, I. M. Mills, and W. B. Person, *J. Chem. Phys.*, **56**, 1444 (1972).
(22) (a) J. Laane, "Vibrational Spectra and Structure", Vol. 1, J. R. Durig, Ed., Marcel Dekker, New York, N.Y., 1972, p 25; (b) C. S. Blackwell and R. C. Lord, *ibid.*, p 1.
(23) J. P. Chesick, *J. Am. Chem. Soc.*, **84**, 3250 (1962).
(24) (a) T. B. Malloy, Jr., F. Fisher, J. Laane, and R. M. Hedges, *J. Mol. Spectrosc.*, **40**, 239 (1971); (b) J. R. Durig, Y. S. Li, and L. A. Carreira, *J. Chem. Phys.*, **57**, 1896 (1972).
(25) (a) J. R. Durig, G. L. Coulter, and D. W. Wertz, *J. Mol. Spectrosc.*, **27**, 285 (1968); (b) H. Kim and W. D. Gwinn, *J. Chem. Phys.*, **51**, 1815 (1969).
(26) V. T. Aleksanyan, *Izv. Akad, Nauk. SSSR, Ser. Khim.*, 1999 (1974).

Carbon-13 Chemical Shifts of Butenes Adsorbed on Silica and Sodium-Treated Silica

Ian D. Gay* and J. F. Kriz

Department of Chemistry, Simon Fraser University, Burnaby, British Columbia, Canada V5A 1S6 (Received April 17, 1975)

Publication costs assisted by the National Research Council of Canada

The ^{13}C chemical shifts of all of the isomeric butenes adsorbed on SiO_2 have been measured. The trend of shifts is very similar to that observed by other workers in zeolites. Experiments with sodium doped and thermally dehydroxylated silicas indicate that neither surface OH nor Na^+ can account for the observed trends of chemical shift.

Introduction

Recently Michel has published ^{13}C chemical shifts relative to the liquid for all of the isomeric butenes sorbed in a Na-Y zeolite.[1] These results are in qualitative agreement with previous measurements in this laboratory of shifts for the 2-butenes adsorbed on silica.[2] Michel has interpreted these shifts as arising from interaction of the olefin with Na^+ in the zeolite structure, as contrasted with our previous proposal that the shifts arose from interaction with surface OH groups. In order to elucidate the situation, we have extended our measurements to include all of the butenes on pure silica and on a silica which has a substantial surface concentration of Na.

Experimental Section

All spectra were measured at 25.2 MHz with a Varian XL-100 spectrometer incorporating a TTI Fourier transform modification. Most spectra were obtained under proton noise decoupled conditions, using an external ^{19}F lock, or using a concentric sample tube containing D_2O in conjunction with the internal ^2H lock circuitry. Line widths were typically of the order of 10–20 Hz and lock stability over the duration of an experiment of the order of ±1 Hz, making it possible to determine chemical shifts to ±0.1 ppm. Shifts were referenced to a separate liquid sample of the appropriate butene in each case. Diamagnetic susceptibility corrections were applied by observing the ^1H resonance of $Si(CH_3)_4$ physically adsorbed on samples of the same adsorbent, the assumption being made that at high coverage the proton shifts do not differ intrinsically from those in the liquid state. This procedure enables us to obtain a shift correction which incorporates both the usual diamagnetic effect, together with a correction for the error which arises from differential shielding of the external lock sample by experimental samples of differing diamagnetic susceptibilities.[3] The latter correction amounts to as much as 0.2 ppm on the XL-100 spectrometer[3] and must therefore be applied for accurate shift measurements between separate samples using the external lock. The corrections obtained by the above method agree to ±0.05 ppm with those calculated from the molar susceptibility of SiO_2[4] together with the bulk density of our adsorbent and an independent measurement of lock perturbation using the spectrometer's linear field sweep unit.[3] We therefore believe that our shifts of adsorbed butenes relative to liquid butenes are correct to ±0.1 ppm.

Samples were prepared by vacuum degassing of the adsorbate, followed by adsorption of butene from the gas phase, the quantity adsorbed being measured as previously described.[2] Samples were degassed at various temperatures from 150 to 700°C as noted below. In the case of pure silica this causes a variation of the surface OH concentration from 7 to 2 $\mu mol/m^2$.[5] Whether similar variation occurs with Na-treated silica is not known. Results of acetone adsorption experiments (see below) suggest some differences in surface chemistry.

Surface areas were obtained by BET measurements using N_2 at 77 K, and an assumed area of 16.2 A^2 per molecule. Monolayer coverages of 1-butene and cis-2-butene were determined by the BET method using these gases as adsorbates at a temperature of 273 K. These differed by about 10 and 2% respectively from values obtained from the liquid density assuming a spherical shape. The calculated values were therefore used for trans-2-butene and 2-methylpropene, since for these equally compact molecules the approximation should be as good as with cis-2-butene.

All adsorption measurements and spectrum accumulation were performed at 33 ± 1°C.

Materials. The silica used in our previous experiments[2] from Matheson Coleman and Bell could not be used for measurements on 1-butene and 2-methylpropene, since it catalyzed the isomerization and polymerization, respectively, of these two molecules at inconveniently rapid rates at room temperature. This is presumably due to the presence of surface impurities.[6] We have therefore used Baker and Adamson Chromatographic grade silica which is free of these unwanted catalytic effects. Its surface properties seem otherwise to be similar, as chemical shifts for 2-butenes and acetone are in reasonably good agreement with our previous results.[2] The present silica has a surface area of 253 m^2/g and a bulk density of 0.36 g/cm^3.

Sodium treated silica was prepared by soaking SiO_2 in 0.1 M NaOH, filtering, titration of the residual solution to determine the amount of Na incorporated, and drying the filtered solid. The samples used contained 2.3 μmol of Na/m^2. The results of Malinowski et al.[7] show that the Na is uniformly dispersed in catalysts prepared with aqueous NaOH, in that catalytic activity increases linearly with incorporated Na, and that surface base sites are available to acidic reagents in the expected numbers. These workers suggest that the sodium is incorporated as Si–O–Na groups, although there is no direct structural evidence on this point. The Na-treated SiO_2 had an area of 177 m^2/g.

The butenes used were CP grade gases from Matheson of Canada Ltd., and were vacuum distilled before use.

TABLE I: Chemical Shifts^a for 1-C$_4$H$_8$ on Pure SiO$_2$

Coverage, μmol/m^2	Fractional coverage	Degassing temp, °C	H$_2$C=	=CH–	–CH$_2$–	–CH$_3$
0.68	0.20	250	+0.7	–3.1	+0.6	+1.6
1.77	0.53	250	+0.6	–2.8	+0.5	+1.6
2.33	0.70	250	+0.7	–2.5	+0.5	+1.5
3.31	0.99	250	+0.6	–2.3	+0.6	+1.6
2.04	0.61	150	+0.6	–2.6	+0.5	+1.5
2.04	0.61	350	+0.7	–2.5	+0.6	+1.6
2.05	0.61	500	+0.8	–2.3	+0.6	+1.4
2.08	0.62	700	–0.1	–2.6	+0.5	+1.3

^{a} In this and subsequent tables, chemical shifts are in ppm with respect to the neat liquid, and are corrected as indicated in the text. Positive shifts are to high field.

TABLE II: Chemical Shifts for Other Butenes on SiO$_2$

Molecule	Coverage, μmol/m^2	Fractional coverage	Degassing temp, °C	C atom	Shift, ppm
t-2-C$_4$H$_8$	1.4	0.39	500	–CH$_3$	+1.5
				=CH–	–1.1
	2.76	0.80	250	–CH$_3$	+1.4
				=CH–	–1.4
c-2-C$_4$H$_8$	2.79	0.80	250	–CH$_3$	+1.5
				=CH–	–1.3
CH$_2$=C(CH$_3$)$_2$	1.8	0.50	500	–CH$_3$	+1.5
				=CH$_2$	+1.2
				=C–	–4.1
	1.96^a	0.54	700	–CH$_3$	+1.8
				=CH$_2$	–0.2
				=C–	–5.0
	2.39	0.66	250	–CH$_3$	+1.0
				=CH$_2$	+1.3
				=C–	–4.7

^{a} Partially dimerized when spectrum recorded.

Results

All of our results are presented as chemical shifts relative to the same molecule in the pure liquid phase. These have been corrected for susceptibility differences and instrumental effects as noted above. The necessary corrections are –0.3 ppm when using an external lock and –0.5 ppm when using concentric samples and the internal lock. A typical spectrum is shown in Figure 1.

Our most complete investigation has been made for 1-butene, and our results for chemical shifts on pure SiO$_2$, as a function of coverage and of degassing temperature, are shown in Table I. Our results for the other butenes on pure SiO$_2$ are shown in Table II, and results for the Na-treated SiO$_2$ in Table III.

We previously found[2] that the carbonyl chemical shift for adsorbed acetone can be used to monitor the surface concentration of OH, at least on pure SiO$_2$. We have made

TABLE III: Chemical Shifts for Butenes on Na-Treated SiO$_2$

Molecule	Coverage, μmol/m^2	Fractional coverage	Degassing temp, °C	C atom	Shift, ppm
1-C$_4$H$_8$	1.8	0.53	400	=CH$_2$	+1.5
				=CH–	–2.9
				–CH$_2$–	+0.4
				–CH$_3$	+1.6
t-2-C$_4$H$_8$	2.0	0.56	300	=CH–	–1.1
				–CH$_3$	+1.7
CH$_2$=C(CH$_3$)$_2$	2.0	0.56	150	=CH$_2$	+1.5
				=C–	–4.9
				–CH$_3$	+1.1
	2.0	0.56	300	=CH$_2$	+1.4
				=C–	–4.4
				–CH$_3$	+1.1

Figure 1. (a) ^{13}C spectrum of 1-C$_4$H$_8$ on pure SiO$_2$ degassed at 250°C. Fractional coverage 0.70. 8192 scans. (b) ^{13}C spectrum of liquid 1-C$_4$H$_8$. Single scan.

measurements for acetone on our pure and Na-treated samples, and these are shown in Table IV.

For at least one sample of each butene, we have measured a spectrum without proton decoupling. This enables the direct-bonded C–H coupling constants to be determined. We have not found any change in these values upon adsorption. Longer-range couplings are not resolved in our adsorbed samples.

Since the liquid-phase chemical shifts of –CH$_2$– and –CH$_3$ in 1-butene do not appear to have been reported in the literature as yet,[8] we have measured these relative to Si(CH$_3$)$_4$ using a saturated solution of 1-butene in the latter compound. The observed shifts are –27.1 ppm for –CH$_2$– and –13.3 ppm for –CH$_3$. The corresponding results for H$_2$C= and =CH– are –113.3 and –140.1 ppm, respectively. The last is in good agreement with the previously reported value,[8] the former is 0.5 ppm to lower field.

Discussion

As can be seen from Tables I and II, a range of chemical shift variations occurs for the various carbons of various

TABLE IV: Chemical Shifts of Acetone on Pure and Na-Treated SiO_2

SiO_2	Fractional coverage	Degassing temp, °C	CO shift	CH_3 shift
Pure	0.80	250	−6.7	+1.0
Pure	0.80	500	−3.7	+1.2
Na-treated	0.77	250	−6.7	+1.1
Na-treated	0.82	500	−5.1	+1.1

olefins on pure SiO_2. The trend throughout is for the less protonated carbons to move downfield on adsorption and the more protonated carbons to move upfield with respect to the liquid. The extreme range of shifts is from −4 to −5 ppm for the nonprotonated carbon of 2-methylpropene to +1.5 to +2.0 ppm for various methyl groups. These trends display a remarkable parallelism to those observed by Michel[1] in Na-Y zeolite, but are on the whole of about one-half the magnitude. This parallelism casts doubt on Michel's interpretation of such shifts as arising from interaction with Na^+.

It can be seen from Table I that the shift of the =CH– carbon of 1-butene has a regular dependence on coverage, whereas the shifts of the other carbons do not. This result suggests that this carbon is involved in a fairly specific interaction with a relatively small number of localized sites on the surface, the average shift decreasing as further noninteracting molecules are added.

As can be seen from Tables I and II, the only marked effect of strong dehydroxylation (heating to 700°C) is to remove the upfield shifts of the =CH_2 groups in 1-butene and 2-methylpropene, bringing the carbon in question to approximately its liquid phase value. This suggests an interaction of such carbons with surface OH leading to upfield shifts. Unfortunately this interpretation is complicated in the case of 2-methylpropene by the fact that heating at 700°C developed some activity for 2-methylpropene polymerization, and we were unable to obtain a spectrum free of lines arising from the dimer. Thus our interpretation may be confused by a coverage dependence in this case.

A comparison of Table III with Tables I and II shows that Na substitution of the surface has little effect on the shifts. The only clear change seems to be an upfield shift of the =CH_2 group in 1-butene. This effect is not reproduced, however, with 2-methylpropene. Thus it again appears that

$Na+$ is not important to the establishment of overall patterns of shift on adsorption.

Table IV shows the shifts observed for acetone on pure and Na-treated SiO_2. The results for pure SiO_2 are in good agreement with our previous correlation[2] between carbonyl shift and degassing temperature (and hence by implication[5] with surface hydroxyl concentration). In the case of Na–SiO_2 heated at 250°C, the shift is the same as with pure SiO_2, whereas at 500°C, a larger C=O shift is recorded. If these data are interpreted at face value they would imply that Na treatment increases the thermal stability of surface OH groups. This interpretation is rather tentative, however, as little is known of the surface chemistry of Na-treated SiO_2. Malinowski's results[7a] indicate, for example, that a catalyst of Na content similar to ours has, after heating to 120°C, about three-quarters of the acidic surface OH concentration possessed by pure silica.

In conclusion, we have shown that the various isomeric butenes adsorbed on pure SiO_2 show a range of ^{13}C chemical shift behavior which is quite parallel to, but smaller than, results obtained[1] in Na-Y zeolite. Modification of the surface by Na addition or OH removal has little effect on any of these shifts, except for small variations in the =CH_2 groups. The hypotheses that the shift patterns arise mainly from interactions with OH or Na^+ do not therefore seem to be sustainable. One is therefore left with the conclusion that they arise from interaction with some other component of the lattice, possibly O atoms whose degree of ionicity might differ appreciably between SiO_2 and molecular sieve. We hope to elucidate this point by further investigations on other pure oxides.

References and Notes

(1) D. Michel, *Surf. Sci.*, **42**, 453 (1974).
(2) I. D. Gay, *J. Phys. Chem.*, **78**, 38 (1974).
(3) A. G. Whitney, Thesis, Simon Fraser University, 1975.
(4) "Handbook of Chemistry and Physics", 50th ed, Chemical Rubber Co., Cleveland, Ohio.
(5) V. Ya. Davydov, A. V. Kiselev, and L. T. Zhuravlev, *Trans. Faraday Soc.*, **60**, 2254 (1964).
(6) P. B. West, G. L. Haller, and R. L. Burwell, Jr., *J. Catal.*, **29**, 486 (1973).
(7) (a) S. Malinowski and S. Szczepanska, *J. Catal.*, **2**, 310 (1963); (b) S. Malinowski, S. Basinski, S. Szczepanska, and W. Kiewlicz, *Proc. Int. Congr. Catal.*, *3rd*, 441 (1965).
(8) J. B. Stothers, "Carbon-13 NMR Spectroscopy", Academic Press, New York, N.Y., 1972.

Carbon-13 Nuclear Magnetic Resonance Studies of Organo Alkali
Metal Compounds. Models of Polymerization Systems

S. Bywater, P. Lachance, and D. J. Worsfold*

Division of Chemistry, National Research Council of Canada, Ottawa, Canada K1A 0R9 (Received March 10, 1975)

^{13}C NMR spectra have been measured of normal, *sec-*, and *tert-*butyllithium, and of isopropyllithium as representative of alkyllithiums. Spectra have also been measured of two allyllithium compounds and three benzyl alkali metal compounds as typical compounds where delocalized carbanions might be expected. All these compounds are typical of those found in anionic polymerization systems. Although it was found that the benzyl compounds behaved as if the charge was largely delocalized, and the C_α had an sp^2 character, the allyl compounds were found in hydrocarbon solvents to have a less extreme character.

Introduction

NMR investigations have been carried out on three types of organo alkali metal compounds. First, the lithium alkyls used as initiators in anionic polymerization, secondly the adducts of *tert-*butyllithium with butadiene and isoprene which model the active chain end in the polymerization of these monomers, and finally benzylic alkali-metal compounds which correspond to the propagating species in the polymerization of styrene and its derivatives. The three types of compound form a series where the bonding probably changes from highly ionic (benzyl compounds) to nearly covalent (lithium alkyls). None of these compounds however form simple covalent structures. All in hydrocarbon solvents form aggregates and the lithium alkyls are associated even in donor solvents. These latter compounds in the solid state still show aggregated structures which are commonly supposed to result from multicenter bonding. Interesting variations are observed in the ^{13}C NMR spectra which could lead to an increased understanding of the bonding properties.

Experimental Section

^{13}C spectra were measured either on a Varian CFT20 spectrophotometer at 20 MHz, or on a Varian XL100 instrument at 25.2 MHz. The polymers were in C_6D_6 or C_4D_8O solution. All δ values given are ppm downfield from TMS.

Isopropyl, *sec-*, and *tert-*butyllithium were prepared by allowing the appropriate aliphatic chloride to react with finely dispersed lithium. A petrolatum dispersion of lithium (2% Na) from Lithium Corp. was freed of petrolatum by rinsing with a heptane solution of *n-*butyllithium in an all glass vacuum apparatus fitted with breakseals and a glass filter. The lithium was filtered and rinsed many times by condensing the heptane onto it and filtering. Finally the heptane was distilled back on to the lithium and the portion of the apparatus containing the residues sealed off and removed. The alkylchloride was slowly distilled onto the stirred lithium suspension at 15° from an evacuated side arm after a restraining breakseal had been broken. When the reaction was completed the lithium alkyl solution was filtered through the glass filter and sealed off. The solvent was then removed, the alkyllithium given a short path distillation in the case of *sec-*butyllithium or a sublimation in

the case of the other two, still in the vacuum apparatus. The product was dissolved in C_6D_6 from a breakseal fitted side arm and sealed in an NMR tube. The *n-*butyllithium was a commercial sample.

The adduct of *tert-*butyllithium and butadiene was prepared directly as before.[1] The product appeared free of any product containing two butadiene units. The corresponding adduct of isoprene prepared in this fashion always contains some of the two unit addition product which complicates the ^{13}C spectrum.[2] A purer product was obtained from the corresponding mercury compound. First an isoprene solution in heptane was added, under N_2, to an equimolar solution of *tert-*butyllithium in pentane, cooled below room temperature. After allowing the mixture to react for 1 hr, HgCl$_2$ (0.4 mol based on *tert-*butyllithium) in THF solution was added slowly at 0°. After 0.5 hr, water was added carefully to destroy the remaining organo lithium compounds and to dissolve the salts. The organic layer was washed, dried, and freed of solvent. The residual organo mercury compound was given a molecular distillation under high vacuum up to a temperature of 60°, the middle third being retained.

The product gave the NMR spectrum expected of a mixture of *cis-* and *trans-*di(2,5,5-trimethylhexen-2-yl)mercury. This compound was then allowed to react in a benzene solution in a vacuum apparatus with finely divided lithium as described above, and filtered into the NMR tube. Neither the ^{13}C or ^{1}H NMR spectra showed any evidence of the addition product with two isoprene molecules.

The potassium salt of the dimer of α-methylstyrene and the addition product of *tert-*butyllithium and α-methylstyrene were prepared as described before.[3] The lithium dimer was prepared from the potassium compound by adding dry LiBr to its solution in THF in a vacuum apparatus. KBr precipitates leaving the lithium dimer in solution in the presence of excess LiBr.[4]

Results

The spectra of the four lithium alkyls are shown in Figure 1. The peak positions are abstracted and compared with those of the parent hydrocarbon in Table I. The most significant difference between the spectra is the absence of ^{13}C–^{7}Li coupling in *n-*butyllithium. The *tert-*butyllithium spectrum shows a multiplet containing an odd number of lines with 11 appearing above the noise, Figure 2. The most
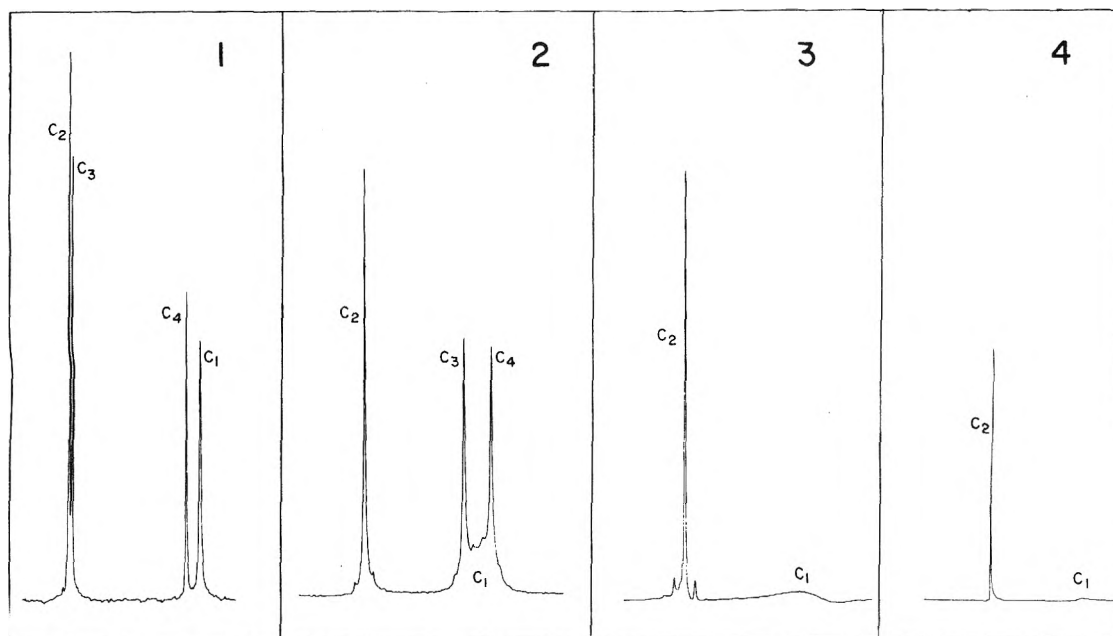
Figure 1. ^{13}C NMR spectra of (1) n-butyllithium, (2) sec-butyllithium, (3) isopropyllithium, (4) $tert$-butyllithium. Solvent C_6D_6, proton decoupled, room temperature. The carbon numbering is as in Table I.
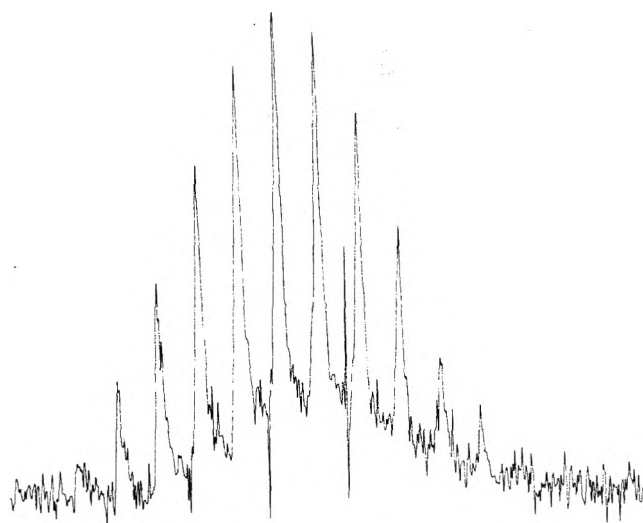
Figure 2. ^{13}C coupling pattern of C_1 of $tert$-butyllithium.

direct interpretation of this spectrum is that each carbon is interacting with four equivalent lithium atoms. This would give a 13 line spectrum, but the outside pair would be lost in the noise. A comparison of the intensities, found and calculated, is given in Table II.

Such analysis is not possible in the case of sec-butyllithium and isopropyllithium. What is assumed to be the absorption due to the carbon α to the lithium, only appears as a broad unresolved band. It is possible that at lower temperatures the resolution would have improved if the broadening was caused by the onset of intermolecular exchange, but as the solvent was benzene the temperature range was restricted.

The spectra of the addition products of $tert$-butyllithium with butadiene and isoprene are given in Figure 3, and the relevant shifts compared with the parent compounds in Tables III and IV. The shifts of 5,5-dimethylhexene-2 were calculated by means of the formula given recently by Rob-

TABLE I: ^{13}C Shifts of Alkyllithium in Benzene Solution[a]

	Li $CH_2CH_2CH_2CH_3$				Li $CH_3CHCH_2CH_3$				Li $(CH_3)_2CH$		Li[b] $(CH_3)_3C$	
	1	2	3	4	3	1	2	4	2	1	2	1
δ_1	11.8					(17)			10.2		10.5	
Δ_1	−1.4					(−8)			−5.9		−10.7	
δ_2	31.9					31.3			23.7		33.3	
Δ_2	+6.9					+6.3			+8.1		+9.0	
δ_3	31.4					19.2						
Δ_3	+6.4					+6.0						
δ_4	13.9					15.8						
Δ_c	+0.7					+2.6						

[a] $\Delta_n = \delta_n$ RH − δ_n RLi, positive values downfield   [b] $J_{C-Li} = 10.7$ Hz.

TABLE II: Calculated and Measured Intensities of $^{13}C_n$ Lines Coupled with Four ^7Li in $tert$-Butyllithium

Calcd	0.023	0.09	0.23	0.45	0.71	0.90	1.00
Meas		0.14	0.21	0.47	0.73	0.92	1.00

erts et al.[5] The spectrum of 2,5,5-trimethylhexene-2 was measured before,[2] but the assignment of two carbons have been reversed to give agreement with the spectrum calculated as above.

The lithium compound from butadiene exhibits peaks from both the cis and the trans forms which coexist in benzene solution. The spectrum of 2,5,5-trimethylhexen-2-yllithium prepared by the new method is a great improvement over the previously published spectrum[2] containing the addition product with two isoprene molecules, and enables more of the peaks to be assigned. It is now possible to see that all carbons contribute simple peaks to the spectrum for both cis and trans forms, although Table III still lists two carbons where assignment is uncertain. It can be seen,
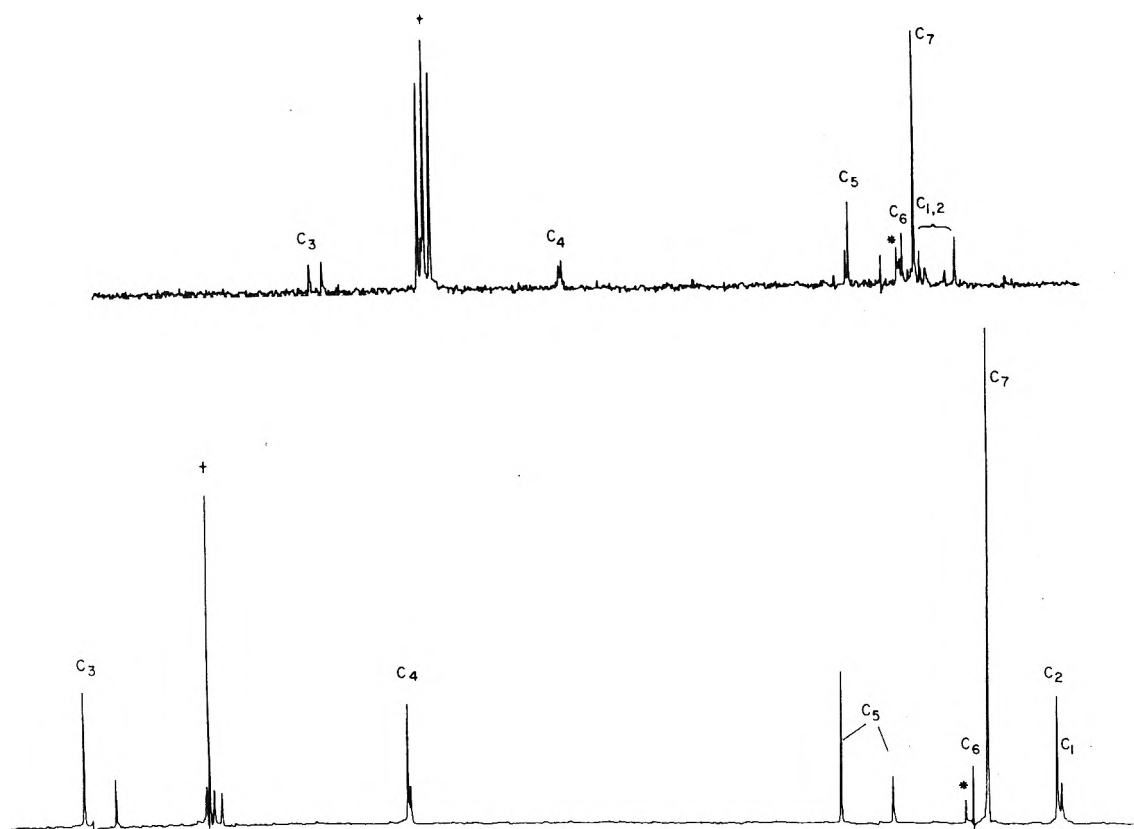
Figure 3. ^{13}C NMR spectra of (top) 2,5,5-trimethylhexenyl-2-lithium and (bottom) 5,5-dimethylhexenyl-2-lithium. Solvent C_6D_6, an asterisk indicates the methyl peak of *tert*-butyllithium a plus sign the C_6D_6 peaks plus some C_6H_6.

however, that in neither of these compounds does $^{13}C-^7Li$ coupling occur as was previously considered possible.

Three benzyl type compounds were studied, all in THF-d_8 solution because of their low solubility in benzene. First the potassium salt of the tail-to-tail dimer of α-methylstyrene, then the equivalent lithium compound, and lastly the adduct of *tert*-butyllithium with α-methylstyrene. The spectra of the potassium dimer, coupled and decoupled from ^1H, and of the parent hydrocarbon are shown in Figure 4. The uncoupled spectrum is readily assigned, with any doubts settled by the coupled spectrum. The relevant data are given in Table V. The ortho and para aromatic resonances are moved up field by the charge delocalized over the phenyl ring. Both ortho and meta resonances are double showing the absence of rotation of the phenyl rings as has been found from the proton NMR spectrum.[3]

The corresponding lithium compound gave a very poor spectrum at room temperature, although it was apparent that the doubling of the aromatic lines was absent. Some improvement was obtained at $-10°$ where once again the doubling of the aromatic lines was seen as in the potassium dimer. Evidently this temperature range marks the onset of rotation of the phenyl rings. This is seen more clearly in the behavior of the ortho protons in the ^1H spectra of this lithium compound in Figure 5. Probably the lithium dimer is less rigid than the potassium compound. There is also evidence for a smaller delocalization of the charge in the lithium compound as is shown in Table V, where the ring charges are calculated from the shifts in the ^{13}C spectrum compared with that of the parent, using the relationship 1ϵ = 160 ppm.[6] Also shown in the table are the corresponding values from the proton spectra, (1ϵ = 1.08 ppm). The two

give rather different values, particularly for the meta position.

The ^{13}C spectrum of the adduct of *tert*-butyllithium and α-methylstyrene was measured at $-5°$ as decomposition occurred at room temperature. The spectrum was good and the relevant data are given in Tables V and VI. At this temperature the ortho and meta aromatic carbon signals were doubled, as also was the case at room temperature, but proton studies have shown the onset of more rapid rotation above room temperature.[3]

Discussion

tert-Butyllithium is known to be tetrameric in benzene solution.[7] The presence of clearly defined coupling of the carbons with four lithium atoms in this compound clearly supports the suggestion that rapid intramolecular exchange of lithium atoms occurs. Such coupling was found in the ^7Li spectrum of ^{13}C enriched *tert*-butyllithium by Waack and McKeever,[8] but on the basis of intensities it was not possible to differentiate clearly between coupling with three Li for slow exchange (local environment hypothesis), or four Li for fast exchange. Previously Brown[9] had suggested that rapid intraaggregate exchange occurred in mixed *tert*-butyllithium–lithiomethyltrimethylsilane tetramers at room temperature.

Evidently $^{13}C-^7Li$ coupling also occurs in *sec*-butyllithium and isopropyllithium, but it is not possible to distinguish what form it takes. *n*-Butyllithium, however, shows no coupling, as also found by Waack and McKeever from the ^7Li spectrum.[8] Brown has suggested that intermolecular exchange may occur through the hexameric form.[10] Such exchange would, if fast enough, cause the coupling to

TABLE III: 13C Shifts for Allylic Compounds

	H $\diagdown$ $C\!=\!C$ $\diagup$ CH_2X / $(CH_3)_3CCH_2$ CH_2Y			H $\diagdown$ $C\!=\!C$ $\diagup$ X / $(CH_3)_3CCH_2$ Y	
	7 65 4 3 $\frac{2}{1}$			7 65 4 3 $\frac{2}{1}$	
X =	H	H	Li(trans)	CH2Li(trans)	H
Y =	H	Li(cis)	H	H	CH2Li(cis)
δ_n					
1	18.0	23.6[a]	21.2[a]		20.0
2	26.3	27.4[a]	28.4[a]	20.7	
3	132.4	150.6	148.4	144.3	140.3
4	122.3	100.1	100.5	103.3	103.0
5	42.6	42.9	43.4	48.2	41.3
6	31.8	32.0	32.0	31.4	31.4
7	29.6	29.6	29.6	29.4	29.4

[a] The assignment of these four peaks is uncertain.

TABLE IV: 13C Shift Differences between Allyllithium Compounds and Parent Hydrocarbon[a]

	Solvent	α	β	γ
Butadienyl[b]	Benzene	5.3	16.2	−25.2
Isoprenyl[b]	Benzene	3.9	17.2	−21.6
Allyl[c]	THF	31.7	13.6	−64.8
Crotyl[b,c]	THF	17.0	19.5	−46.1
Allylsilicon[d]		6.7	−0.4	−1.9

[a] Positive sign downfield. [b] Average of cis and trans values. [c] Reference 16. [d] Reference 15.

disappear from the spectrum. Both tert-butyllithium and sec-butyllithium have been shown to be tetrameric, and hence intermolecular exchange may not be rapid enough. Isopropyllithium was shown by Brown[9] to be at least partly hexameric and hence would not be expected to show the coupling it does if Brown's hypothesis is correct.

The benzyllic compounds in THF must be considered as highly ionic. The electrical conductance of their solutions indicates that they exist principally as intimate ion pairs. Under these circumstances a largely delocalized benzyllic anion is to be expected. This is confirmed by the upfield shifts experienced for the aromatic absorptions in both the 13C and 1H spectra. The appreciable differences in the estimates of the ring charges calculated from the two types of spectrum indicate that these systems are more complex than the simple unsubstituted aromatic anions where proportionality between charge and NMR shift was measured. Little reliance can be placed on the absolute values given, but they indicate that at least half of the charge is on the ring, with the rest presumably residing on the α carbon.

Such delocalization of the charge would be expected from a sp^2-hybridized α carbon with the three bonds and the phenyl ring coplanar for maximum overlap. The 13C NMR absorption of the α carbon is then, relative to the parent compound, susceptible to the upfield shift caused by any charge residing on the carbon, and an opposing downfield shift caused by the change from sp^3 to sp^2 hybridization. The net result in the K dimer is a downfield shift of 37 ppm from the parent's C_α absorption (Table V). Allowing 100 ppm as a typical downfield shift for the sp^3–
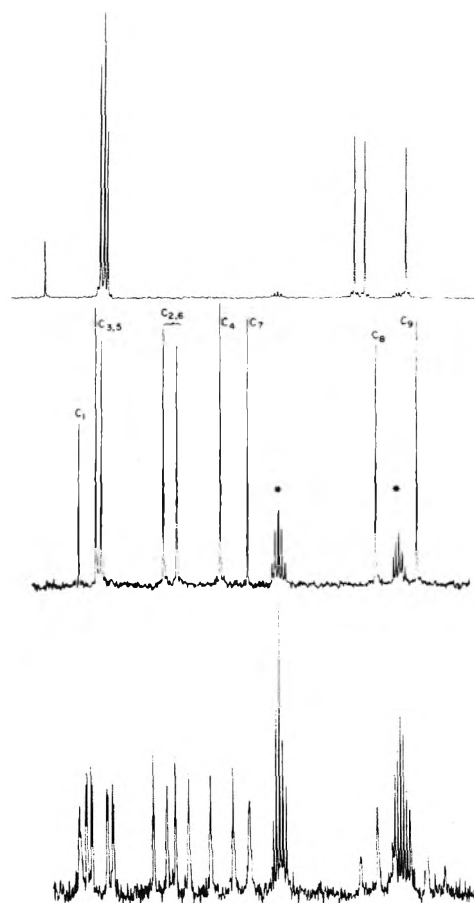
Figure 4. 13C NMR spectra of (top) 2,5-diphenylhexane (tail-to-tail dimer of α-methylstyrene), (middle) 2,5-diphenyl-2,5-dipotassiohexane, and (bottom) the same nonproton decoupled. An asterisk indicates the solvent THF-d_8 peaks.

sp^2 change, this gives about 63 ppm upfield shift caused by the charge. If the ϵ = 160 ppm ratio is still valid for nonring carbons[8] this would suggest a charge of 0.41ϵ on C_α, which matches well with the 0.57ϵ on the ring measured from the 13C shifts. Similar calculations give 0.44ϵ for the C_α of the

TABLE V: ^{13}C Chemical Shifts of Benzyl Compounds[a]

		Li or K dimer			B, Li adduct	
M =	H	Li	K (J_{CH})		H	Li
δ_n						
1	147.9	148.9	136.8		149.9	142.0
2	127.2	109.4	107.5 (154)		127.6	108.3
3	128.6	129.0	131.1 (146)		128.9	128.3
4	126.1	97.0	87.5 (160)		126.2	89.5
5	128.6	128.6	129.1 (149)		128.9	127.3
6	127.2	108.0	102.1 (153)		127.6	106.0
7	40.6	63.1	77.8		37.7	66.8
8	37.0	36.3	33.6 (116)		52.7	50.9
9	22.5	19.8	19.1 (122)		26.4	23.9
10					31.7	37.3
11					30.6	30.6

[a] Positions 2 and 6, 3 and 5 are arbitrary.
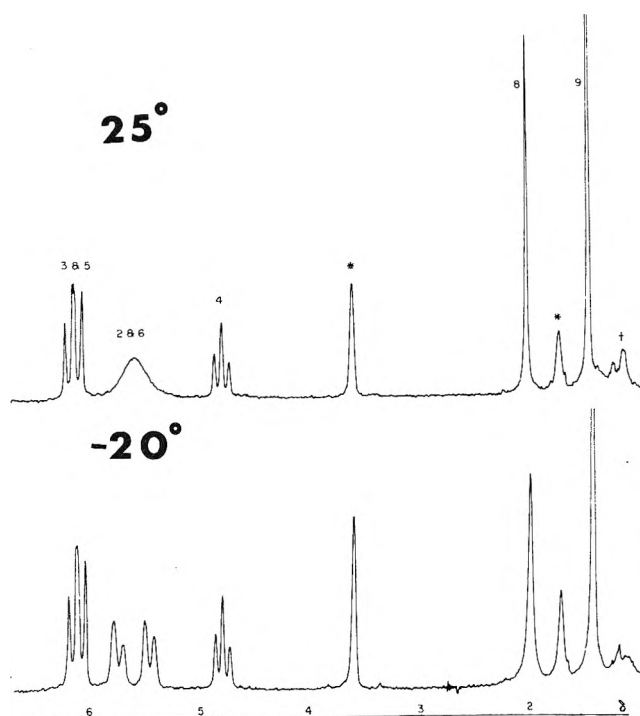
Figure 5. ^{1}H NMR spectra of 2,5-diphenyl-2,5-dilithiohexane. An asterisk shows the solvent THF-d_8 residual protons.

Li adduct compared with 0.56ϵ for the ring. The Li dimer gives 0.48ϵ and 0.42ϵ as the charges on C_α and ring, respectively. The sum is appreciably less than 1ϵ. Correspondingly, the Li dimer shows appreciable rotation of the phenyl rings at room temperature, which might suggest there may be less sp^2 character to the C_α, although the methylene protons remain equivalent suggesting C_α is still planar. From these rough calculations it would appear that the estimates of the ring charges from the ^{13}C measurements are self-con-

TABLE VI: Ring Charges of Benzyl Compounds from NMR Shifts

		1	Ortho	Meta	Para	Total
K dimer	^{13}C	−0.07	−0.14	+0.01	−0.24	−0.57
	^{1}H		−0.19	−0.11	−0.28	−0.88
Li dimer	^{13}C	+0.01	−0.13	+0.01	−0.19	−0.42
	^{1}H		−0.14	−0.09	−0.22	−0.68
Li adduct	^{13}C	−0.05	−0.13	−0.01	−0.24	−0.57
	^{1}H		−0.17	−0.10	−0.26	−0.80

sistent, and perhaps to be preferred to those from the ^{1}H measurements.

Waack and McKeever[11] considered on the basis of ^{13}C, ^{7}Li, and ^{1}H NMR data that in benzyllithium and 1,1-diphenylhexyllithium C_α had considerable sp^3 character. Alternative explanations for the results obtained have been given.[3,12] The results here for the K dimer, however, can be interpreted best as having a large degree of sp^2 character of the C_α as described earlier. Supporting evidence for the planar structure is the absence of separate absorptions of meso and racemic forms in the ^{13}C spectra of both dimers, the equivalence of the methylene protons in the ^{1}H spectrum, and of course the restricted rotation of the phenyl ring. Rapid inversion of the corresponding sp^3 forms could give some of these effects. It was noted, however, that the ^{1}H spectrum of the Li dimer showed appreciable broadening of the methylene peak at −60° while the methyl peak began to broaden at −90°. It is possible that slowing of inversion would cause both to broaden at the same temperature. If the broadening was merely caused by restriction of rotation in this stiff molecule, this could occur at different temperatures for different bonds. In view of the evidence from charge delocalization, at least the potassium dimer must be considered to have a fully sp^2 C_α, with the two lithium compounds very nearly so.

There is no evidence for coupling between C_α and Li in

the ^{13}C spectrum of the adduct of *tert*-butyllithium and α-methylstyrene. However as free exchange of the lithium ion is expected such coupling is not expected.

The addition compounds of *tert*-butyllithium and butadienes were studied in benzene solution as stability was poor in tetrahydrofuran at room temperature. In this latter solvent the ^{1}H NMR spectrum of allyllithium indicates[13] a symmetrical delocalized anion exists. The equivalence of α and γ positions are not interpretable in terms of rapidly interconverting covalent structures. The ^{13}C spectrum[14] can be used therefore to estimate the effects of charge and hybridization changes on chemical shifts. There is a net upfield shift of 64.8 ppm (Table IV) of the γ-carbon compared with the parent propene and hence a shift in this system of about 130 ppm per electron. (C_α and C_γ should have each nearly half an electronic charge.) This can be compared with the often suggested shift of 160 ppm per electron in aromatic systems. The shift of the α-carbon is 32.5 ppm downfield would result from the same 64.8-ppm upfield shift due to the charge plus a 96.7-ppm downfield shift caused by the change from sp^3 to sp^2 hybridization. This is in agreement with the conventionally suggested value (∼100 ppm) in aromatic and ethylenic compounds for such a hybridization change. It seems unlikely that alkyl substitution would significantly change the nature of such species but, for example, in crotyllithium the γ substituent will make this position less favorable for charge location. In the ^{13}C spectrum in tetrahydrofuran, the α and γ shift differences are −14.7 and +18.7 ppm less than in allyllithium. The nearly equal differences of opposite sign can be produced by an unequal charge distribution without change in hybridization. It is true that the coupling constant J_{C-H} at the α position drops to 132 Hz on methyl substitution, a value little above those normally obtained for sp^3 carbons, but since the β coupling constant is nearly unchanged at 137 Hz it must be concluded that as this carbon is in any case sp^2 that such arguments are not reliable in charged systems.

In benzene solution, the addition compounds of *tert*-butyllithium with isoprene and butadiene are tetrameric[15,16] as are some of the lithium alkyls. No coupling between carbon and lithium is evident which could indicate a difference in bonding. The absence of coupling in some of the alkyls however suggests that differences in intermolecular exchange rates may be at least as important. These compounds show typical near-uv absorption bands both in benzene and in tetrahydrofuran[17] in the region 270–320 nm expected of allylic anions. The ^{13}C spectra do however show evidence for further charge transfer away from the γ carbon (Table IV) leaving only about one third that in the corresponding position in the allyl anion. Correspondingly the lower downfield shift at the α carbon compared with the parent is consistent with increased charge at this position. Decreased sp^2 character could also explain the α-carbon shift. Preliminary ^{1}H experiments on 2-*tert*-butylcrotyllithium and 2-*tert*-butylallyllithium (soluble in benzene unlike the unsubstituted compounds)[18] suggests that charge redistribution away from the more substituted carbon is an important phenomenon. The latter compound shows only one ^{1}H absorption for the two CH$_2$ groups, as expected from delocalization to an ionic species, at a position intermediate between those of the α and γ carbons of the former.

References and Notes

(1) S. Bywater, D. J. Worsfold, and G. Hollingworth, *Macromolecules*, **5**, 389 (1972).
(2) S. Brownstein, S. Bywater, and, D. J. Worsfold, *Macromolecules*, **6**, 715 (1973).
(3) S. Bywater and D. J. Worsfold, *J. Organometal. Chem.*, **33**, 273 (1971).
(4) M. Schlosser and J. Hartmann, *Angew. Chem., Int. Edit Engl.*, **12**, 508 (1973).
(5) D. E. Doorman, M. Jautelat, and J. D. Roberts, *J. Org. Chem.*, **36**, 2757 (1971).
(6) H. Speisecke and W. G. Schneider, *Tetrahedron Lett.*, 468 (1961).
(7) H. L. Lewis and T. L. Brown, *J. Am. Chem. Soc.*, **92**, 4664 (1970).
(8) L. D. McKeever and R. Waack, *Chem. Commun.*, 750 (1969).
(9) G. E. Hartwell and T. L. Brown, *J. Am. Chem. Soc.*, **88**, 4625 (1966).
(10) T. L. Brown, *J. Pure Appl. Chem.*, **23**, 447 (1970).
(11) L. D. McKeever and R. Waack, *J. Organometal. Chem.*, **28**, 145 (1971).
(12) J. R. Murdock and A. Streitwieser, *Intra-Sci. Chem. Rep.*, **7**, 45 (1973).
(13) P. West, J. I. Purmont, and S. V. McKinley, *J. Am. Chem. Soc.*, **90**, 797 (1968).
(14) J. P. C. M. VanDongen, H. W. D. Van Dijkman, and M. J. A. de Bie, *Recl. Trav. Chim. Pays-Bas*, **93**, 29 (1974).
(15) KH. B. Tsvetanov, V. N. Zgonnik, B. L. Yerusalimskii, I. M. Panaiotou, and N. I. Nikolayev, *Vysokomol. Soedin., Ser. A*, **15**, 2116 (1973).
(16) D. J. Worsfold and S. Bywater, *Macromolecules*, **5**, 393 (1972).
(17) S. Bywater and D. J. Worsfold, *Polym. Prep.*, **15**, 153 (1974).
(18) P. Lachance, unpublished data.

Longitudinal Relaxation Rates of Lanthanum-139 in Aqueous Salt Solutions

Jacques Reuben

Department of Isotope Research, The Weizmann Institute of Science, Rehovot, Israel   (Received March 14, 1975)

Longitudinal relaxation rates of lanthanum-139 at 8.4 MHz are reported for aqueous solutions of $LaCl_3$ and $La(ClO_4)_3$ in the concentration range 0.1–1.7 M. The effects of added NaCl, $LiClO_4$, and $LiNO_3$ have also been investigated. It is found that the ^{139}La relaxation in aqueous chloride solutions is well described by the classical theory of a moving rigid sphere in a viscous medium. The relaxation rate at infinite dilution is $1/T_1{}^0 = 277$ sec^{-1} and the quadrupole coupling constant of ^{139}La in the aquo-ion is 3.1 MHz. Departures from the classical theory are observed in the presence of excess perchlorate, which are explained by the formation of outer-sphere ion pairs. The effect on the relaxation rate of inner-sphere complex formation with nitrate is much larger.

Introduction

A large volume of data on the thermodynamic and transport properties of aqueous solutions of rare earth salts, recently augmented by X-ray and Raman spectral studies, has been interpreted by Spedding and his coworkers in terms of the structure and microdynamic behavior of the aquo complexes.[1,2] The interpretation of the partial molal heat capacities has been subjected to some criticism by Grenthe et al.[3] A more direct way to look into this problem is by nuclear magnetic resonance in general and nuclear relaxation rates in particular.[4] Work in this laboratory has focused in the past on the proton and oxygen-17 NMR of the solvent and anion nuclei.[5,6] Advantage was taken of the fact that most of the trivalent lanthanides are paramagnetic and exert their influence on nuclei in their vicinity through the electron–nuclear hyperfine interaction. Among the trivalent rare earth ions only lanthanum and lutetium are diamagnetic and it appears that lanthanum-139, a nucleus of spin 7/2 with a natural abundance of 99.91% and NMR sensivity (relative to that of protons) of 5.92%, is suitable for NMR experiments. Attempts to observe the nuclear resonance of lutetium-175 failed probably because its quadrupole moment[7] is a factor of 10 larger, leading to two orders of magnitude faster relaxation.

Presented here are the results of a preliminary study of the longitudinal relaxation rates of lanthanum-139 in aqueous solutions of the chloride and perchlorate salts. The effects of added excess of chloride (as NaCl), perchlorate (as $LiClO_4$), and nitrate (as $LiNO_3$) were also investigated in order to clarify some of the observed phenomena. Line widths of lanthanum-139 in ionic aqueous solutions have previously been reported by Nakamura and Kawamura.[8] While the general appearance of the present results resembles that of the line widths, there are some differences in the detailed features leading to different conclusions. A comment regarding the possible sources of these discrepancies is given in the Experimental Section. The theoretical background forming the basis of the present work is summarized for convenience in the following paragraphs.

Theoretical Background

Lanthanum-139 possesses a quadrupole moment, the interaction of which with intramolecular electric field gradients modulated by molecular motion gives rise to pronounced relaxation effects. These effects may serve in turn

to monitor both the changes in the immediate environment of the ion and its microdynamic behavior. The longitudinal relaxation rate, $1/T_1$, of a quadrupole nucleus in the case of rapid tumbling (extreme narrowing) is given by[9]

$$\frac{1}{T_1} = \frac{3(2I+3)}{40I^2(2I-1)}\left(\frac{e^2Qq}{\hbar}\right)^2 \tau_c \qquad (1)$$

where eQ is the quadrupole moment of the nucleus of spin I, eq is the electric field gradient, τ_c is the correlation time characteristic of the motion for molecular reorientation, and the usually negligible contribution of an asymmetry factor has been omitted. An analogous equation governs the transverse relaxation rate.[9] The quantity e^2Qq/h, which has frequency units, is referred to as the quadrupole coupling constant, K. Thus for lanthanum-139 we obtain

$$1/T_1 = 0.403K^2\tau_c \qquad (2)$$

The chemical environment is reflected in the magnitude of K and the microdynamic behavior in τ_c. Assuming that the molecular motion is described by the diffusion equation of Stokes, i.e., that the complex may be regarded as a rigid sphere of radius r moving in a medium of viscosity η, the correlation time may be expressed as[10]

$$\tau_c = 4\pi r^3\eta/3kT \qquad (3)$$

Equations 2 and 3 predict a proportionality between the relaxation rate and the viscosity for constant K.

If several complexes are present in solution with rapid chemical exchange between them, the observed relaxation rate will be given by the weighted average

$$1/T_{1,\text{obsd}} = \sum_i P_i/T_{1i} \qquad (4)$$

where P_i is the relative abundance of the ith species, the relaxation rate of which is $1/T_{1i}$.

Experimental Section

Stock solutions (2–2.5 M) of the chloride and perchlorate salts of lanthanum were prepared by allowing La_2O_3 (Fluka AG) to react with the appropriate stoichiometric amounts of hydrochloric or perchloric acids, respectively. Concentrations were determined by EDTA titrations using Arsenazo I as the end point indicator. Dilutions were made volumetrically. In order to eliminate the possible effects of hydrolysis all solutions were made 0.01 M in hydrochloric

or perchloric acid. The samples, ca. 0.5 ml in volume, were contained in 10-mm o.d. tubes. Measurements were done at the ambient probe temperature of $23 \pm 2°$.

The lanthanum-139 magnetic resonance was observed at 8.4 MHz (magnetic field of ca. 14 kG) with a Bruker 322S pulsed NMR spectrometer equipped with a Hewlett-Packard Model 5480A signal analyzer. Longitudinal relaxation rates, $1/T_1$, were determined by the 180–90° pulse method, by which the magnetization amplitude, A, is measured as a function of the time interval, t, between the two pulses and the relaxation rate obtained from the relation

$$A = A_0[1 - 2\exp(-t/T_1)] \qquad (5)$$

where A_0 is the amplitude in the absence of the 180° pulse.[9] Typical runs are shown in Figure 1. It is seen that the magnetization difference, $A_0 - A$, decays as a single exponent over the whole concentration range investigated as predicted by eq 5. The uncertainty in the $1/T_1$ values obtained in the present work is estimated to be less than $\pm 3\%$.

A Comment on the Lanthanum-139 Line Widths. Pulse methods can be employed in principle to measure transverse relaxation rates. An alternative and experimentally more convenient way is to obtain them from the line width at half-height of the continuous wave absorption mode spectrum. This approach has been used by Nakamura and Kawamura who, in addition, used audio frequency modulation and observed the derivative of the absorption mode.[8] The lines obtained in this way are distorted and corrections have to be applied in order to account for the broadening due to the finite modulation amplitude. These corrections have been shown to be a nonlinear function of the ratio between the true line width and the modulation amplitude.[11,12] However, in the above-mentioned line width study, the corrections have been done by linear extrapolation to zero modulation amplitude.[8] It has been our experience, and it can be shown by a calculation,[11,12] that in this way narrower lines are "under-corrected" and broader lines are "over-corrected". Another possible source of "instrumental" broadening, particularly at the lower concentrations, is partial saturation due to the higher radiofrequency power that might have been necessary in order to observe the weaker signals. It is not surprising therefore that the transverse relaxation rates reported by Nakamura and Kawamura[8] are higher at the lower concentrations and slightly lower at the higher concentrations than the longitudinal relaxation rates obtained in the present work, although it is anticipated on theoretical grounds[4,9] that $1/T_2 = 1/T_1$ in this system.

Results

Longitudinal relaxation rates, $1/T_1$, of lanthanum-139 were measured in solutions of $LaCl_3$ in the concentration range 0.1–1.7 M. Already from the decays of the magnetization difference, shown in Figure 1, it is seen that the relaxation is faster at higher concentrations. The relaxation rates are plotted as a function of the concentration in Figure 2. Over the concentration range covered the relaxation rate increases by a factor of ca. 3 in a way similar to that of the macroscopic viscosity.[13] Spedding and Pikal have shown[13] that the relative viscosity, η_r, of lanthanide chloride solutions is well described by the modification of Vand's equation of the form[14]

$$\ln \eta_r = A_3 c/(1 - Q'c) \qquad (6)$$
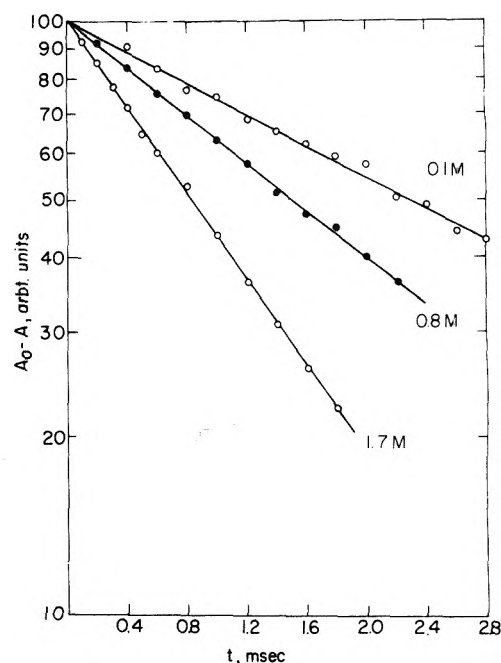
Figure 1. The exponential decay of the magnetization difference (in normalized arbitrary units) of ^{139}La in $LaCl_3$ solutions as a function of the time interval, t, between the 180 and 90° pulses.
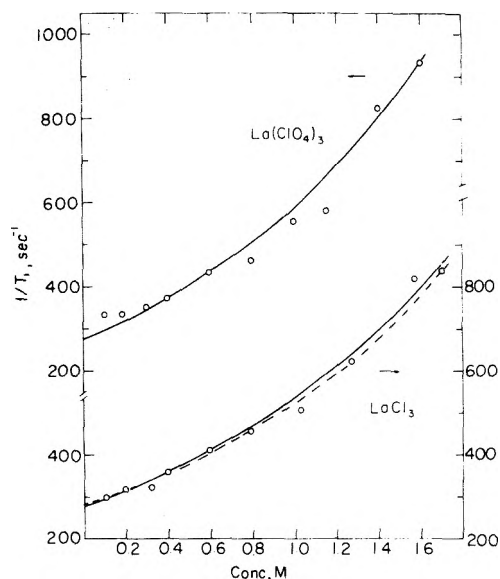
Figure 2. Longitudinal relaxation rates of ^{139}La in aqueous solutions of $LaCl_3$ and $La(ClO_4)_3$ as a function of concentration. Ordinates are displaced for clarity. Curves are calculated (see text).

where c is the molar concentration and A_3 and Q' are adjustable parameters. Thus, if the relaxation rates do follow the viscosity they should be of the form

$$1/T_1 = \eta_r/T_1{}^0 \qquad (7)$$

where $1/T_1{}^0$ is the relaxation rate extrapolated to zero concentration. The results were fitted to eq 6 and 7 (the solid curve in Figure 2) and the parameters obtained are $A_3 = 0.653$ M^{-1}, $Q' = 0.008$ M^{-1}, and $1/T_1{}^0 = 277$ $\sec^{-1}$ with a standard deviation of 4.26%. The broken line in Figure 2 shows the fit to the experimental viscosities reported by Spedding and Pikal[13] with $1/T_1{}^0 = 284$ $\sec^{-1}$. The agreement between the two sets is excellent. The quadrupole coupling constant was calculated from eq 2 with $1/T_1 = 277$
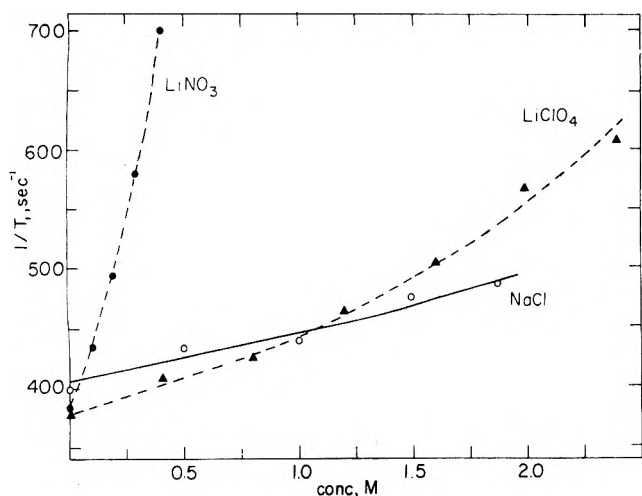
Figure 3. Longitudinal relaxation rates of ^{139}La as a function of added salt concentration: (▲) $LiClO_4$, (●) $LiNO_3$, (O) NaCl. Concentrations of $La(ClO_4)_3$ were 0.3, 0.315, and 0.375 M, respectively. The solid curve is calculated (see text).

sec^{-1} and $\tau_c = 7 \times 10^{-11}$ sec (as previously determined from proton relaxation rates in dilute $GdCl_3$ solutions[15]) and found to be $K = 3.1$ MHz.

The effects of added NaCl on the relaxation rates of a 0.375 M $La(ClO_4)_3$ solution are shown in Figure 3. The solid curve was calculated from eq 6 and 7 using the parameters A_3 and Q' for NaCl given by Robinson and Stokes.[14] Again the fit is excellent.

The relaxation rates in solutions of $La(ClO_4)_3$ are shown on the upper part of Figure 2. The curve was calculated with eq 6 and 7 and the parameters obtained are $A_3 = 0.75$ M^{-1}, $Q' = 0.013$ M^{-1}, and $1/T_1^0 = 275$ sec^{-1} with a standard deviation of 6%. However the relaxation rates here are faster than those in $LaCl_3$ solutions although the viscosities of lanthanide perchlorates are known to be lower than those of the corresponding chlorides in this concentration range.[2] In order to test the effect of excess perchlorate, the relaxation rate of a 0.3 M $La(ClO_4)_3$ solution was measured as a function of added $LiClO_4$. The results are shown in Figure 3. Again the relaxation rate increases with increasing concentration faster than anticipated from the viscosity change. In going from 0 to 2.4 M $LiClO_4$ the relaxation rate increases from 380 to 610 sec^{-1}, whereas the relative viscosity of $LiClO_4$ solution increases from 1 to 1.25 over the same concentration range.[16]

In order to obtain the effect of inner-sphere complex formation the relaxation rate of a 0.315 M $La(ClO_4)_3$ solution was measured as a function of added $LiNO_3$. Already at 0.4 M $LiNO_3$ an approximately twofold increase in the relaxation rate is observed (see Figure 3), whereas the relative viscosity of $LiNO_3$ solutions in this concentration range should have increased by not more than 5%. An order of magnitude calculation with eq 4 and 2 using 0.5 M^{-1} as the formation constant of the mononitrato complex[6] shows that the ^{139}La quadrupole coupling constant in the complex has increased by a factor of nearly 3 over that of the aquo-ion.

Discussion

The longitudinal relaxation rates of lanthanum-139 in solutions of chloride salts are well represented by the macroscopic viscosity. This finding provides additional support to the classical view of Stokes that the viscosity of electro-

lyte solutions is a measure of the hydrodynamic effect arising from the distortion of streamlines by particles larger than water molecules.[14,17] No evidence is found in the present work for an equilibrium between different hydrated forms of the lanthanum ion as has been previously been invoked on the basis of ^{139}La NMR line widths.[8] It now seems that that interpretation may have resulted from instrumental artifacts (see Experimental Section). Our findings are in agreement with the recent X-ray work of Spedding et al.[1] who observed that in a saturated $PrCl_3$ solution nine water molecules are coordinated to the lanthanide cation.

Nitrate ions are known, e.g., from previous oxygen-17 NMR studies,[6] to form inner-sphere complexes with lanthanides. The present findings of the effect of added $LiNO_3$ on the ^{139}La relaxation rates concur with the intuitive expectation that in the nitrato complex a higher electric field gradient is imposed on the lanthanum nucleus. On the other hand, it has previously been shown that perchlorate ions do not penetrate the first coordination sphere of lanthanides.[6] The unexpected relaxation effects of perchlorate observed in the present work seem to reflect the formation of an outer-sphere ion pair between the lanthanum aquo-ion and perchlorate. The ^{139}La relaxation rate in the ion pair should be faster than that of the aquo-ion since in addition to size effects on the correlation time (see eq 3) there will be a considerably larger electric field gradient imposed on the lanthanum nucleus by the nearby perchlorate anion. This interpretation is in agreement with the transport and Raman spectral data of Spedding et al.[1,2,18] In particular water molecules shared between cations and anions, i.e., belonging to an ion pair, have been observed in the Raman spectra of concentrated lanthanide perchlorate solutions.[18-20]

Conclusions

The longitudinal relaxation rates of lanthanum-139 in aqueous chloride solutions are well described by the classical theory of a moving rigid sphere (the aquo-ion) in a viscous medium. In solutions of $La(ClO_4)_3$ as well as in the presence of excess perchlorate an outer-sphere ion pair is formed leading to relaxation effects larger than anticipated from the viscosity changes. Stable inner-sphere complexes, e.g., the nitrato complex, have much more pronounced effects on the relaxation rates. Thus ^{139}La relaxation rates may serve to monitor complex formation as well as to study the microdynamic behavior in solution.

References and Notes

(1) A. Habenschuss and F. H. Spedding, *Proc. Rare Earth Res. Conf., 11th,* 909 (1974), and references cited therein.
(2) J. A. Rard and F. H. Spedding, *Proc. Rare Earth Res. Conf., 11th,* 919 (1974), and references cited therein.
(3) I. Grenthe, G. Hessier, and H. Ots, *Acta Chem. Scand.,* **27**, 2543 (1973).
(4) For a review of NMR studies of the microdynamic behavior of liquids see H. G. Hertz, *Prog. Nucl. Magn. Reson. Spectrosc.,* **3**, 159 (1967).
(5) J. Reuben and D. Fiat, *Chem. Commun.,* 729 (1967).
(6) J. Reuben and D. Fiat, *J. Chem. Phys.,* **51**, 4909, 4918 (1969).
(7) K. Murakawa and T. Kamei, *Phys. Rev.,* **105**, 671 (1957).
(8) K. Nakamura and K. Kawamura, *Bull. Chem. Soc. Jpn.,* **44**, 330 (1971).
(9) A. Abragam, "The Principles of Nuclear Magnetism", Oxford University Press, London, 1961.
(10) W. Bloembergen, E. M. Purcell, and R. V. Pound, *Phys. Rev.,* **73**, 679 (1948).

(11) H. Wahlquist, *J. Chem. Phys.*, **35**, 1708 (1961).
(12) G. W. Smith, *J. Appl. Phys.*, **35**, 1217 (1964).
(13) F. H. Spedding and M. J. Pikal, *J. Phys. Chem.*, **70**, 2430 (1966).
(14) R. A. Robinson and R. H. Stokes, "Electrolyte Solutions", 2nd ed (revised), Butterworths, London, 1965, Chapter 11.
(15) J. Reuben, *Biochemistry*, **10**, 2834 (1971).
(16) H. Hognas, *Suomen Kemi.*, **40**, 130 (1967).
(17) R. H. Stokes in "The Structure of Electrolyte Solutions", W. J. Hamer, Ed., Wiley, New York, N.Y., 1959, p 298.
(18) L. Gutierrez, W. C. Mundy, and F. H. Spedding, *J. Chem. Phys.*, **61**, 1953 (1974).

(19) The detailed results of the viscosities of La(ClO₄)₃ solutions became available to the author after the manuscript of this paper was submitted for publication. It can be shown that the relaxation rates of the lanthanum-139 in La(ClO₄)₃ solutions conform to the macroscopic viscosities; however, the relaxation rate at infinite dilution, $1/T_1^0$, obtained from a fit to eq 7, is $312\ sec^{-1}$, which is considerably higher than the value of $1/T_1^0 = 277\ sec^{-1}$ obtained for chloride solutions. Thus our conclusion regarding the formation of outer-sphere ion pairs with perchlorate ions receives further support.
(20) F. H. Spedding, L. E. Shiers, and J. A. Rard, *J. Chem. Eng. Data*, **20**, 66 (1975).

Crystal Structures of Hydrated and Dehydrated Potassium-Exchanged Zeolite A

Peter C. W. Leung, Kevin B. Kunz, Karl Seff*

Chemistry Department, University of Hawaii, Honolulu, Hawaii 96822

and I. E. Maxwell

Koninklijke/Shell-Laboratorium, Amsterdam, The Netherlands   (Received March 3, 1975)

The crystal structures of hydrated ($a = 12.301$ (2) Å) and vacuum-dehydrated ($a = 12.309$ (2) Å) potassium-exchanged zeolite A have been determined by single-crystal X-ray diffraction techniques in the cubic space group $Pm3m$. In each case all 12 potassium ions per unit cell were located, and the structures refined to final conventional R indices of 0.114 and 0.057, respectively. In the dehydrated structure, three equivalent K⁺ ions lie near the centers of the oxygen 8-rings. Another six equivalent K⁺ ions lie on three of the four threefold axes opposite 6-rings in the large cavity, in an eightfold equipoint. The three remaining K⁺ ions are nonequivalent, and lie along the remaining threefold axis, two inside the sodalite unit and one recessed far into the large cavity. *It is most unique that this latter K⁺ ion is not within contact distance of any atom or ion; it occupies a relatively shallow energy minimum in the electrostatic field of the remainder of the structure.* In the hydrated structure, eight K⁺ ions are found inside the large cavity on the threefold axes near the 6-oxygen rings; three more lie near the centers of the 8-rings but somewhat off those planes; the twelfth is located near the center of the unit cell. Twelve water molecules bridge between the eight threefold axis K⁺ ions along the edges of the cube. Three of these twelve can also be close to the twelfth K⁺ ion near the center of the large cavity. The sodalite unit contains eight water molecules which hydrogen bond to each other and to framework oxygens.

Introduction

The K⁺ positions in potassium-exchanged zeolite A, K-A,[1] are likely to be similar, except for the effect of ionic radius, to those of the Na⁺ ions in Na-A. The position of the twelfth K⁺ ion, if it could be determined, would be of interest in the hydrated structure because it would suggest which of the possible positions previously determined[2] for a twelfth Na⁺ ion is correct and would serve to complete the structure of hydrated Na-A, the form in which zeolite A is synthesized. In the dehydrated case, a position opposite a 4-oxygen ring was noted in dehydrated Na-A;[3] the larger X-ray scattering factor of K⁺ might have allowed a strong confirmation of the previous result. An ion populating such a site at high temperature in this or another zeolite would be particularly available to sorbed molecules, would be particularly coordinatively or associatively unsaturated, and could be a site of high catalytic activity. Such a site has been shown to be sensitive to sorbate content.[3]

Recent ir studies of hydrated monovalent cation-exchanged zeolite A have led, using large-ring vibrational assignments,[4] to specific conclusions about the placement of K⁺ ions in the zeolite. The work reported herein was undertaken in part to test the validity of these assignments and the conclusions based upon them.

Experimental Section

Crystals of zeolite 4A were prepared by a modification of Charnell's method,[5] including a second crystallization using seed crystals from the first synthesis. Ion exchange with 0.2 N aqueous KCl solution, conducted for 1 week at 28° with daily agitation and renewal of solution, yielded clear and colorless crystals. A flame test of these crystals indicated, by the absence of the yellow sodium D line, that the exchange was complete. Later, a separate batch of crystals was similarly prepared with 0.2 N aqueous KOH solution to discourage any possible hydrogen ion exchange into the zeolite. Subsequent crystallographic analysis indicated the presence of 12 K⁺ ions per unit cell in each sample.

A crystal 0.08 mm on an edge, exchanged in KCl solution, was dehydrated by a procedure[3] similar to that used

TABLE I: Positional, Thermal,[a] and Occupancy Parameters for K-A

	Wyckoff position	x	y	z	β_{11} or B_{iso}	β_{22}	β_{33}	β_{12}	β_{13}	β_{23}	Occupancy factor
					(a) Dehydrated						
(Si, Al)	24(k)	0	1886(3)	3774(2)	14(2)	16(2)	19(2)	0	0	2(4)	1[b]
O(1)	12(h)	0	2457(8)	1/2	41(9)	22(8)	13(7)	0	0	0	1
O(2)	12(i)	0	2833(6)	2833(6)	44(9)	26(5)	26(5)	0	0	31(15)	1
O(3)	24(m)	1111(4)	1111(4)	3597(6)	41(4)	41(4)	46(4)	33(13)	-9(8)	-9(8)	1
K(1)	8(g)	2311(4)	2311(4)	2311(4)	49(3)	49(3)	49(3)	50(8)	50(8)	50(8)	3/4
K(2)	12(i)	0	4770(25)	4770(25)	61(13)	93(30)	93(30)	0	0	-45(55)	1/4
K(3)	8(g)	3557(62)	3557(62)	3557(62)	833(183)	833(183)	833(183)	-611(247)	-611(247)	-611(247)	1/8
K(4)	8(g)	1306(24)	1306(24)	1306(24)	4(1)						1/8
K(5)	8(g)	1849(34)	1849(34)	1849(34)	7(2)						1/8
					(b) Hydrated						
(Si, Al)	24(k)	0	1825(2)	3712(2)	16(2)	16(2)	10(2)	0	0	5(3)	1[b]
O(1)	12(h)	0	2228(11)	1/2	151(20)	16(8)	14(7)	0	0	0	1
O(2)	12(i)	0	2941(7)	2941(7)	32(8)	18(4)	18(4)	0	0	19(10)	1
O(3)	24(m)	1113(6)	1113(6)	3437(11)	32(4)	32(4)	92(11)	23(10)	36(10)	36(10)	1
O(4)	12(j)	2683(21)	2683(21)	1/2	387(71)	387(71)	93(27)	-599(156)	0	0	1
O(5)	8(g)	978(15)	978(15)	978(15)	103(11)	103(11)	103(11)	-26(25)	-26(25)	-26(25)	1
K(1)	8(g)	2585(4)	2585(4)	2585(4)	56(2)	56(2)	56(2)	26(5)	26(5)	26(5)	1
K(2)	24(m)	795(56)	4460(34)	4460(34)	8(1)						1/8
K(3)	24(m)	3828(141)	4621(81)	4621(81)	8(5)						1/24

[a] Positional and anisotropic thermal parameters are given $\times 10^4$; isotropic thermal parameters are in Å^2. Numbers in parentheses are the estimated standard deviations in the least significant digits. See Figure 1 for the identities of the atoms. The anisotropic temperature factor = $\exp[-(\beta_{11}h^2 + \beta_{22}k^2 + \beta_{33}l^2 + \beta_{12}hk + \beta_{13}hl + \beta_{23}kl)]$. [b] Occupancy for (Si) = 1/2; occupancy for (Al) = 1/2.

for dehydrating zeolite 4A, Na-A. The Pyrex capillary containing the crystal was sealed off by torch under vacuum after 48 hr of dehydration at 300° and 10^{-6} Torr, and was mounted on a goniometer head. The crystal remained clear and colorless.

Another crystal from the same exchange, also 0.08 mm on an edge, was mounted on the tip of a fine glass fiber and was left exposed to the atmosphere (relative humidity 30%) during data collection. Subsequent diffraction intensities for both crystals were collected at 20°. Two crystals prepared from KOH solution, also both 0.08 mm on an edge, were treated similarly.

The cubic space group $Pm3m$ (no systematic absences) appeared to be appropriate.[3,6-9] A Syntex four-circle computer-controlled diffractometer with a graphite monochromator and a pulse-height analyzer was used throughout for preliminary experiments and for the collection of diffraction intensities. Molybdenum radiation ($K\alpha_1$, λ 0.70926 Å; $K\alpha_2$, λ 0.71354 Å) was used throughout. In each case, the cell constant, a = 12.309 (2) Å for the dehydrated crystal (prepared from 0.2 N KOH solution) and a = 12.301 (2) Å for the hydrated crystal (prepared from 0.2 N KCl solution), was determined by a least-squares treatment of 15 intense reflections for which $2\theta < 24°$. (As will be discussed later, only the results for these two of the four data sets are presented.)

The $2\theta-\theta$ scan technique was employed at a constant scan rate of 0.5°/min (in 2θ). The scan range varied from 2.0° at 2θ = 3° to 2.5° at 2θ = 70°. One-half of the total scan time was spent counting background at each end of the scan range. All unique reciprocal lattice points (889 for each crystal) below a maximum 2θ value of 70° were examined. The high upper limit for 2θ was chosen to maximize the size of the data sets, even though few reflections with

large 2θ values showed significant intensity. Three check reflections, monitored in each data collection after every 100 reflections, indicated no significant variation in intensity.

Standard deviations were assigned according to the formula:

$$\sigma(I) = [\omega^2\{CT + 0.25(t_c/t_b)^2(B_1 + B_2)\} + (pI)^2]^{1/2}$$

where ω is the scan rate, CT is the total integrated count obtained in a scan time, t_c, B_1, and B_2 are the background counts each obtained in time t_b, and I = $\omega[CT - 0.5(t_c/t_b)(B_1 + B_2)]$. A value of 0.02 was assigned to the empirical parameter p[10] to account for instrumental instability. The net counts were then corrected[11] for Lorentz and polarization effects, including that of the monochromator crystal which was assumed to be half perfect and half mosaic in character. An absorption correction was not necessary–the transmission coefficients are estimated to range within 0.6% of their average values.

Only those reflections in each data set for which the net counts exceeded three times the corresponding esd's were used in structure solution and refinement. This amounted to 214 and 374 unique reflections for the dehydrated and hydrated crystals, respectively.

Structure Determination

Dehydrated K-A. Full-matrix least-squares refinement of dehydrated $K[AlSiO_4]$-A,[1c] or K-A (exchanged using KCl), began using the cation coordinates (adjusted to account for the differing ionic radii) and framework positions of thallium-exchanged zeolite A.[8] Isotropic refinement converged quickly to an R_1 index, $(\Sigma|F_o - |F_c|)/\Sigma F_o$, of 0.095 and an R_2 weighted index, $(\Sigma w(F_o - |F_c|)^2/\Sigma wF_o^2)^{1/2}$, of 0.101. Anisotropic refinements of all framework atoms with

TABLE II: Selected Interatomic Distances (Å) and Angles (deg)[a]

(a) Dehydrated K-A

(Si, Al)-O(1)	1.676(5)	O(1)-(Si, Al)-O(2)	108.5(4)
(Si, Al)-O(2)	1.660(3)	O(1)-(Si, Al)-O(3)	111.0(4)
(Si. Al)-O(3)	1.668(2)	O(2)-(Si, Al)-O(3)	107.9(4)
		O(3)-(Si, Al)-O(3)	110.2(4)
K(1)-O(3)	2.620(7)	(Si, Al)-O(1)-(Si, Al)	128.5(6)
K(1)-O(2)	2.986(3)	(Si, Al)-O(2)-(Si, Al)	178.4(5)
K(2)-O(1)	2.861(30)	(Si. Al)-O(3)-(Si, Al)	153.7(5)
K(2)-O(2)	3.372(45)		
K(3)-O(3)	4.257(10)	O(3)-K(1)-O(3)	111.3(4)
K(4)-O(3)	2.840(25)	O(1)-K(2)-O(1)	101.4(10)
K(5)-O(3)	2.505(9)	O(2)-K(2)-O(2)	96.1(8)
		O(1)-K(2)-O(2)	50.7(6)
		O(3)-K(3)-O(3)	119.4(29)
		O(3)-K(4)-O(3)	99.2(8)

(b) Hydrated K-A

(Si, Al)-O(1)	1.660(5)	O(1)-(Si, Al)-O(2)	107.3(6)
(Si, Al)-O(2)	1.668(4)	O(1)-(Si. Al)-O(3)	110.6(6)
(Si, Al)-O(3)	1.660(3)	O(2)-(Si, Al)-O(3)	108.6(4)
		O(3)-(Si, Al)-O(3)	111.1(9)
K(1)-O(3)	2.768(11)	(Si, Al)-O(1)-(Si, Al)	145.2(9)
K(1)-O(4)	2.975(5)	(Si, Al)-O(2)-(Si. Al)	159.3(6)
K(2)-O(1)	2.99(4)	(Si, Al)-O(3)-(Si, Al)	146.0(9)
K(2)-O(2)	2.82(6)		
K(3)-O(4)	2.81(12)	O(3)-K(1)-O(3)	93.9(4)
K(1)-O(5)	3.425(33)	O(4)-K(1)-O(4)-	85.3(11)
K(1)-O(2)	3.240(4)	K(1)-O(4)-K(1)	173.3(2)
O(5)-O(5)	2.40(4)	O(4)-K(3)-O(4)	91.7(38)
O(5)-O(2)	3.62(2)	O(1)-K(2)-O(1)	107.6(19)
O(4)-O(1)	3.35(1)	O(2)-K(2)-O(2)	98.1(10)
		O(1)-K(2)-O(2)	54.9(11)
		O(2)-K(1)-O(2)	104.3(5)
		O(3)-O(5)-O(3)	83.4(5)
		O(1)-O(4)-O(1)	71.0(12)

[a] The numbers in parentheses are the estimated standard deviations in the units of the least significant digit given for the corresponding parameter.

seven K(1)'s (see Table I), three K(2)'s, and a single potassium ion between K(4) and K(5) lowered the error indices to 0.072 and 0.073, respectively. The occupancy of K(2) refined well to one ion per 8-ring (three per unit cell).

Since the twelfth K^+ ion could not be located on subsequent refinements, the previous exchange of one hydrogen ion per unit cell was suspected. For this reason a new data set was collected using a crystal exchanged with aqueous KOH. Full-matrix least-squares refinement of the structure model of the previous paragraph converged with the error indices R_1 = 0.058 and R_2 = 0.050. A subsequent difference Fourier map revealed five small peaks (1.3 to 2.6 e Å^{-3} in height) at (0, 0, 0), (0, 0, 0.16), (0, 0, 0.40), (0.14, 0.14, 0.14), and (0.23, 0.5, 0.5). The first three were unstable in least-squares refinement. The fourth peak, in subsequent refinements, indicated the presence of two nonequivalent potassium ions, K(4) and K(5), since the thermal ellipsoid of a single potassium ion placed at an intermediate position became very elongated and then nonpositive definite in refinement. The fifth peak refined well with a single potassium ion to the final R_1 and R_2 values of 0.057 and 0.044, respectively. The close approach distances between K(1) and K(4), and K(1) and K(5), can be dismissed as virtual if no two ions are simultaneously assigned to the same 6-ring. Furthermore, by the same reasoning, K(4) and K(5) must be placed on the same threefold axis but on opposite

sides of the origin, and K(3) must be placed on the opposite side of a 6-ring from K(4). Thus the final model has six K(1)'s, three K(2)'s, and one ion at each of the positions, K(3), K(4), and K(5).

Finally, this 12 K^+ model was refined using the data set for KCl-exchanged K-A, to R_1 = 0.072 and R_2 = 0.071. The presence of 12 K^+ ions per unit cell was indicated in KCl-exchanged K-A. The structure does not depend, then, on the exchanging solution, so only the better data set, which happened to be that of the KOH-exchanged crystal, and its structure, are reported.

The standard deviation of the electron density on the Fourier function was 0.1 e Å^{-3}. The goodness-of-fit, $(\Sigma w (F_o - |F_c|)^2/(m - s))^{1/2}$, is 1.65; m is the number of observations (214), and s (37) is the number of variables in least squares. All shifts in the final cycle of refinement were less than 1% of their corresponding esd's. Calculated and observed structure factors are available.[11] The final structural parameters are presented in Table Ia, and selected bond lengths and bond angles are given in Table IIa.

Hydrated K-A. Least-squares refinement of hydrated K-A (KCl exchanged) was commenced using the parameters of the dehydrated structure. After several trials, eight ions at K(1) and three at K(2) were located (see Table Ib) with R_1 = 0.21 and R_2 = 0.20. Successive Fourier syntheses and least-squares refinements served to reveal the posi-

tions of 20 water molecules, which fully occupy two equipoints: O(4) (Wyckoff 12(j)) within the large cavity, and O(5) (Wyckoff 8(g)) within the sodalite unit. The inclusion of these water molecules (as isotropic oxygen atoms) further reduced R_1 and R_2 to 0.118 and 0.112, respectively.

Since again, the twelfth potassium ion was not located, a new data set was collected for a KOH-exchanged K-A crystal. Least-squares refinement using the model derived from the KCl-exchanged K-A crystal led to R_1 and R_2 indices of 0.126 and 0.158. A subsequent Fourier difference function revealed three peaks: (0, 0, 0; 2.3 e Å^{-3}), (0.18, ½, ½; 2.5 e Å^{-3}), and (0.39, ½, ½; 3.0 e Å^{-3}). Only the last refined well at a position compatible with the rest of the structure. An ion at that position, K(3), was reasonably distant (3.2 Å) from three O(4)'s related by the threefold axis; its inclusion in refinement allowed R_1 and R_2 to reach 0.119 and 0.124, respectively; actually a position just off the fourfold axis refined slightly better and is reported.

Subsequent least-squares refinement using the same model with the KCl-exchanged K-A data set resulted in error indices of 0.114 and 0.107, and a substantially lower goodness-of-fit value, so only this latter data set and its corresponding structure, which as before does not differ from the structure based on data collected with the otherwise-exchanged crystal, is reported.

The standard deviation of the electron density of the Fourier function is 0.15 e Å^{-3}. The goodness-of-fit is 2.37; $R_1 = 0.114$; $R_2 = 0.107$; the total number of observations (m) is 374; and the number of variables in least squares was 39. The large error indices suggest that a few additional water molecules, perhaps near the center of the large cavity near K(3), may exist per unit cell, and were not located in this work; also O(4) appears to be an average position.

All shifts in the final cycle of refinement were less than 1% of their corresponding esd's. Calculated and observed structure factors are available.[11] The final structural parameters are presented in Table Ib, and selected bond lengths and bond angles are given in Table IIb.

The full-matrix least-squares program used[12] in all structure determinations minimized $\Sigma w (\Delta |F|)^2$; the weights (w) were the reciprocal squares of σ, the standard deviation of each observation. Atomic scattering factors for K^+,[13] O,[13] O^-,[14] and $(Si,Al)^{1.75+}$ were used. The function describing $(Si,Al)^{1.75+}$ is the mean of the Si^0, Si^{4+}, Al^0, and Al^{3+} functions.[14] The scattering factors for K^+ and $(Si,Al)^{1.75+}$ were modified to account for the real component $(\Delta f')$ of the anomalous dispersion correction.[15]

Discussion

In the dehydrated structure (see Tables Ia, IIa, III, and Figures 1 and 2), 9 of the 12 K^+ ions per unit cell are distributed over four nonequivalent threefold axis equipoints (Wyckoff 8(g)), while the remaining three lie in the plane of the 8-oxygen rings (Wyckoff 12(i)).

The first nine K^+ ions, K(1), K(3), K(4), and K(5), have occupancies, per unit cell, of 6, 1, 1, and 1 ions, respectively. The most populated position, K(1), is located in the large cavity, 0.79 Å above the O(3) plane of the oxygen 6-rings. While two nonequivalent K^+ ions, K(4) and K(5), are located inside and very near to the surface of the sodalite unit, respectively (1.35 and 0.19 Å from the [111] plane at O(3)), the ninth K^+ ion was found deep within the large cavity (3.45 Å from the O(3) plane). K(1), K(4), and K(5) are trigonally coordinated to their respective sets of three framework O(3)'s at 2.62, 2.84, and 2.50 Å. Because of disorder,

TABLE III: Deviations of Atoms (Å) from Planes[a]

Dehydrated K-A		Hydrated K-A	
	(a) From the (111) Plane at O(3)		
K(1)	0.79	K(1)	1.49
K(3)	3.45	K(3)	5.26
K(4)	-1.35	O(4)	3.34
K(5)	-0.19	O(5)	-1.94
	(b) From the (100) Plane at O(1) and O(2)		
		K(1)	3.18
		K(2)	0.98
		K(3)	4.71

[a] A negative deviation indicates that the atom lies on the same side of the plane as the origin. The numbers in parentheses are the estimated standard deviations in the units of the least significant digit given for the corresponding parameter.
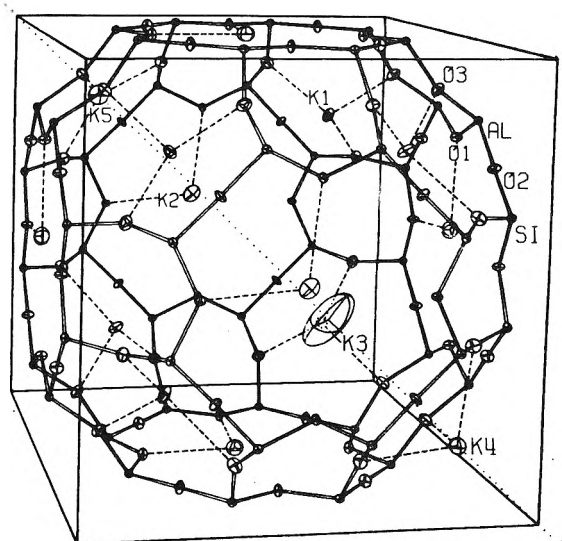
DEHYDRATED ZEOLITE K-A

Figure 1. The dehydrated K-A zeolite unit cell is shown[12] with potassium ions placed statistically within each of the five equipoints so as to minimize intercationic repulsions. Closest ionic approaches to framework oxygens are indicated by broken lines. The unique threefold axis on which K(3), K(4), and K(5) lie is indicated by a dotted line. Ellipsoids of 20% probability are shown.

only the average O(3) positions could be calculated. However, the framework 6-rings should be nonequivalent, depending on which kind of K^+ ion is nearest. For this reason, the short K(5)–O(3) distance of 2.505(9) Å (Table IIa) is likely to be virtual.

To minimize K^+–K^+ repulsions, it is necessary that K(3), K(4), and K(5) be on the same threefold axis (that is, associated with two opposite 6-rings of the large (or small) cavity), while the six K(1)'s fully occupy the six remaining 6-oxygen rings per unit cell. Furthermore, the two K^+ ions in the sodalite unit at K(4) and K(5) must be on opposite sides of the origin, and K(3) and K(4) must be on opposite sides of the same 6-ring, so that the actual intercationic distances are as large as possible: K(3)–K(4), 4.80 Å; K(4)–K(5), 6.73 Å; and K(3)–K(5), 9.79 Å.

It is most interesting to observe the position of the K^+ ion at K(3). *It is not in ionic contact with any other ion or atom in the structure.* Instead, it lies at a position relative-

DEHYDRATED ZEOLITE K-A

DEHYDRATED ZEOLITE K-A
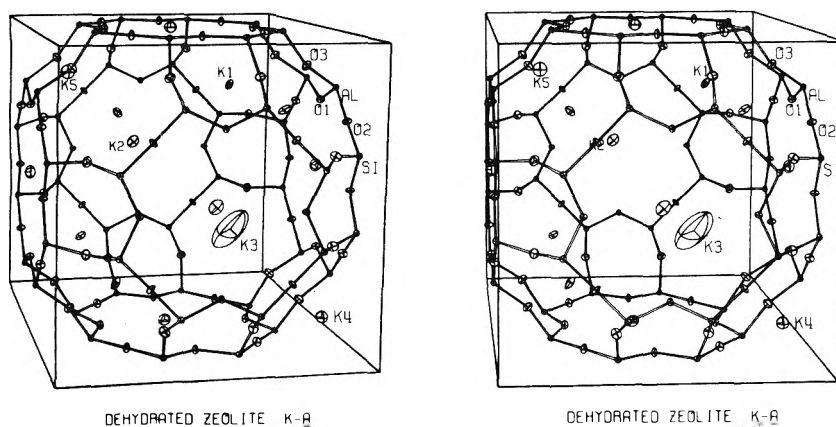
Figure 2. Stereoview[12] of dehydrated K-A. Ellipsoids of 20% probability are shown.

HYDRATED ZEOLITE K-A

HYDRATED ZEOLITE K-A
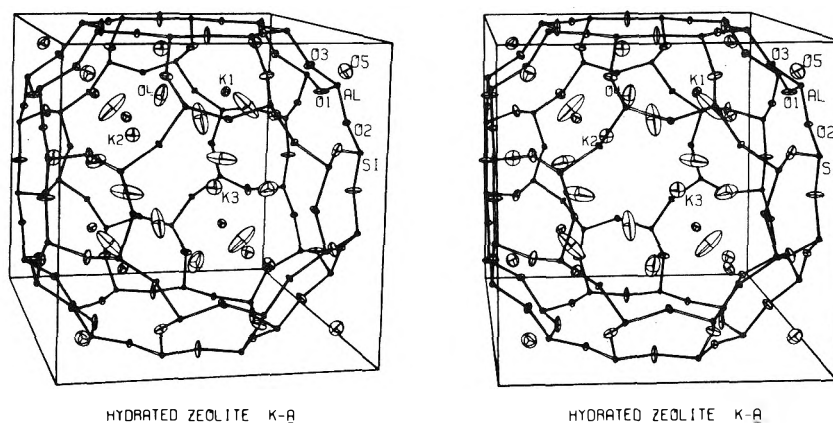
Figure 3. Stereoview[12] of the large cavity of hydrated K-A. Ellipsoids of 20% probability are shown.

K-A HYDRATED SODALITE CAGE

K-A HYDRATED SODALITE CAGE
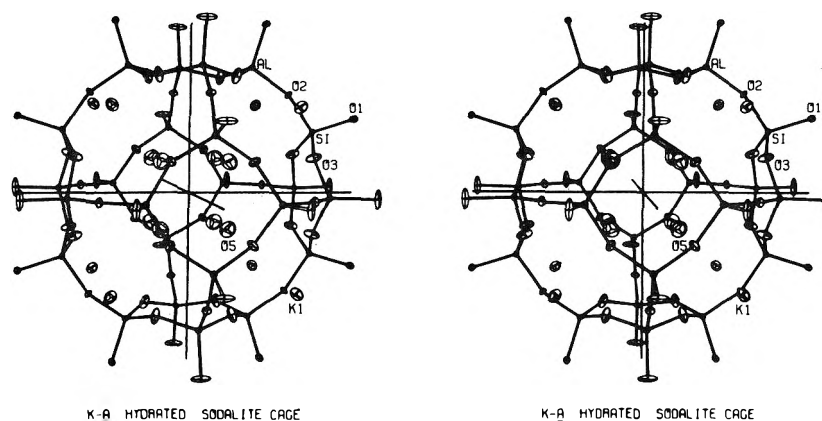
Figure 4. Stereoview[12] of the sodalite cavity of hydrated K-A. Ellipsoids of 20% probability are shown.

ly loosely defined by the electrostatic field of the framework and the other K^+ cations. Its nearest neighbors, all part of the nearest 6-ring or arranged symmetrically about it, are three O(3)'s at 4.26 Å, three O(2)'s at 4.56 Å, the single K(4) at 4.80 Å, six O(1)'s at 4.91 Å, and three K(1)'s at 5.53 Å. Its broad oblate thermal ellipsoid appears to be consistent with the maintenance of the distance between K(3) and its nearest neighbors at O(3), O(2), and K(4). The K(3) thermal parameters do not depend upon the exchanging solutions, aqueous KCl, or KOH, and presumably are not artificially large for reasons for partial occupancy because of possible partial proton ion exchange. These large thermal parameters indicate instead the relative shallow-

ness of the electrostatic minimum, and appear to be reasonable.

Lastly, the K(2)'s are located in the planes of the 8-rings, 2.86 Å from two adjacent O(1)'s and 3.37 Å from the nearest O(2). If the K(2)'s were located at the centers of the 8-rings, the K^+–O atomic distances would have been 3.13 Å to all four O(1)'s, and 3.77 Å to all O(2)'s, each far greater than the K(1)–O(3) distance of 2.62 Å (which is near to the sum of the ionic radii[16] of K^+ and O^{2-}, 1.33 + 1.32 = 2.65 Å). Accordingly, it is reasonable that the K(2)'s are not found at the centers of the 8-rings.

Upon hydration, the positions of the framework atoms remain almost unchanged, but those of the cations are

modified (see Tables Ib, IIb, and III, and Figures 3 and 4). First, the partially occupied nonequivalent K(1), K(4), and K(5) positions become a fully occupied K(1) position. No K$^+$ ions are found inside the sodalite unit in hydrated K-A.

The K(1)–O(3) distance increases by 0.15 Å and the K(1)'s are found recessed 0.70 Å further into the large cavity from the [111] plane at O(3), nearly doubling the distance. The solitary K(3) ion in the large cavity shifts away from Wyckoff (8(g)) to a 24 (m) position, to associate with two of the twelve O(4)'s, so that the shortest K(3)–O(4) distance becomes 2.81 Å. Again, the K(1)–O(4) distance (2.98 Å) must be regarded as an average distance, since the K(3) position has caused the O(4)'s to become nonequivalent. The K(1)'s are each associated with three O(3)'s and three O(4)'s in a distorted (but eclipsed) trigonal trapezoidal (C_{3v} = 3m) arrangement.

The eight O(5)'s, hydrogen bonded to each other within the sodalite unit, form a cube which can accommodate up to 12 of the 16 hydrogen atoms in hydrogen bonding along its edges. The remaining four or more hydrogen atoms can hydrogen bond to 6-ring oxygens, probably O(2).

Upon hydration, the three K(2) ions at the 8-rings shift off those planes, and the K(2)–O(1) and K(2)–O(2) distances become 2.99 and 2.82 Å, respectively. This could result in part from a strong interaction between each K(2) and two of the twelve O(4)'s. The O(4) position determined should then be the average of two nonequivalent sets of six oxygens each, one set associated with the three K(2)'s and the other not. The K(2)–O(4) distance determined could be too long because it is to the average O(4) position, so that the actual K(2)–O(4) distance would be closer to the sum of their respective ionic radii, 2.65 Å.[16] The unusually large O(4) "thermal" parameters of Table Ib support this suggestion.

The water molecules at O(4) can form two long (3.35 Å) equivalent "hydrogen bonds" to two O(1) atoms of the nearest 4-ring. The "hydrogen bond" angle (OH–O) is approximately 155°. Perhaps the O(4) oxygens find minimum energy positions somewhat off the diagonal mirror planes where one better hydrogen bond could form.

An attempt to reduce the symmetry of the O(4) position to Wyckoff (24(l)), as suggested by the elongated O(4) thermal ellipsoid, was not successful. Although the O(4) positions off the diagonal mirror plane appear to be reasonable (0.2511, 0.2861, ½), perhaps so as to allow one good linear hydrogen bond 3.17 Å in length to form between O(4) and one O(1), no significant lowering of the error indices is observed.

Only the single ion at K(3) does not associate with a framework oxygen ion. Its position is 2.81 Å from two O(4)'s, perhaps accounting for its much lower thermal parameter (see Table IIb) as compared to that of K(3) in the dehydrated structure.

It is unique to the K-A system, of results reported to date, that the cell constant does not decrease upon dehydration. In zeolite systems, the removal of all ligand (sorbed) molecules generally results in a smaller unit cell volume. In dehydrated K-A, the K$^+$ ions appear to be involved in a sufficient number of repulsive interactions to counteract this effect.

A comparison of the (Si,Al)–O–(Si,Al) angles between the two structures indicates large angular changes upon dehydration of −17° at O(1) and +19° at O(2) (see Table II).

The change at O(3) is much less, +8°. Somewhat smaller changes (all of opposite sign!) are observed in Tl-A,[8] and a much smaller deformation is noted in Na-A,[3] upon dehydration.

In conclusion, the structures of K-A (hydrated and dehydrated) are surprisingly different from those of Na-A.[2,3] In the hydrated structure, the arrangement of water molecules is completely different in the large cavity. In the dehydrated structure, the twelfth K$^+$ ion cannot approach a 4-oxygen ring because its approaches to two K(1) ions would be too close, so it must occupy an unusual site remote from the zeolite framework. That twelfth K$^+$ ion should be particularly sensitive and available to sorbed molecules, and suggests that dehydrated K-A could be an ionic superconductor. The position of K(1) in the hydrated case is consistent with the conclusion,[4] based on ir studies, that 8 of the 12 K$^+$ ions are firmly bonded to the zeolite 6-rings.

Supplementary Material Available. Listings of the observed and calculated structure factors of both structures (supplementary Tables I and II) will appear following these pages in the microfilm edition of this volume of the journal. Photocopies of the supplementary material from this paper only or microfiche (105 × 148 mm, 24× reduction, negatives) containing all of the supplementary material for the papers in this issue may be obtained from the Business Office, Books and Journal Division, American Chemical Society, 1155 16th St., N.W., Washington, D.C. 20036. Remit check or money order for $4.00 for photocopy or $2.50 for microfiche, referring to code number JPC-75-2157.

References and Notes

(1) A discussion of zeolite nomenclature is available: (a) L. Broussard and D. P. Shoemaker, *J. Am. Chem. Soc.*, **82**, 1041 (1960); (b) Reference 3; (c) R. M. Barrer, Zeolite Nomenclature Committee, informally presented at the Third International Conference on Molecular Sieves, Zurich, Switzerland, 1973.
(2) V. Gramlich and W. M. Meier, *Z. Kristallogr.*, **133**, 134 (1971).
(3) R. Y. Yanagida, A. A. Amaro, and K. Seff, *J. Phys. Chem.*, **77**, 805 (1973).
(4) I. E. Maxwell and A. Baks, *Adv. Chem. Ser.*, No. **121**, 87 (1973).
(5) J. F. Charnell, *J. Cryst. Growth*, **8**, 291 (1971).
(6) K. Seff, *J. Phys. Chem.*, **76**, 2601 (1972).
(7) R. Y. Yanagida and K. Seff, *J. Phys. Chem.*, **76**, 2597 (1972).
(8) P. E. Riley, K. Seff, and D. P. Shoemaker, *J. Phys. Chem.*, **76**, 2593 (1972).
(9) P. E. Riley and K. Seff, *J. Am. Chem. Soc.*, **95**, 8180 (1973).
(10) S. W. Peterson and H. A. Levy, *Acta Crystallogr.*, **10**, 70 (1957).
(11) See paragraph at end of text regarding supplementary material.
(12) Principal programs used in this study were: LP-73 data reduction program, T. Otterson, University of Hawaii, 1973; full-matrix least-squares, P. K. Gantzel, F. A. Sparks, and K. N. Trueblood, UCLALS4, American Crystallographic Association Program Library (old) No. 317 (modified); Fourier, C. R. Hubbard, C. O. Quicksall, and R. A. Jacobson, Ames Laboratory Fast Fourier, Iowa State University, 1971, modified; C. K. Johnson, ORTEP, Report ORNL-3794, Oak Ridge National Laboratory, Oak Ridge, Tenn., 1965.
(13) P. A. Doyle and P. S. Turner, *Acta Crystallogr., Sect A*, **24**, 329 (1968).
(14) "International Tables for X-ray Crystallography", Vol. III, Kynoch Press, Birmingham, England, 1962, p 202.
(15) "International Tables for X-ray Crystallography", Vol. III, Kynoch Press, Birmingham, England, 1962, p 215.
(16) "Handbook of Chemistry and Physics", Chemical Rubber Co., Cleveland, Ohio, 1968, p F152.

Hydrated and Dehydrated Crystal Structures of Seven-Twelfths Cesium-Exchanged Zeolite A

T. Blake Vance, Jr., and Karl Seff*

Chemistry Department, University of Hawaii, Honolulu, Hawaii 96822 (Received March 20, 1975)

The crystal structures of hydrated (a = 12.320 (2) Å) and vacuum-dehydrated (a = 12.158 (2) Å) seven-twelfths Cs^+-exchanged synthetic molecular sieve zeolite A, $Cs_{0.58}Na_{0.42}[AlSiO_4]$-A, stoichiometry Cs_7-$Na_5Al_{12}Si_{12}O_{48}$ per unit cell, have been determined from three-dimensional X-ray diffraction data gathered by counter methods. The structures were solved in the cubic space group $Pm3m$ and refined to final R (unweighted) indices of 0.098 and 0.090, respectively. Cesium ions are located at three distinct crystallographic sites in each structure. Three Cs^+ ions lie at the centers of the 8-oxygen rings at sites of D_{4d} symmetry, filling that equipoint; these ions are approximately 0.3 Å further from their nearest framework oxygen neighbors than the sum of the appropriate ionic radii would indicate. The remaining four Cs^+ ions are associated with the 6-oxygen rings and lie on unit cell threefold axes. Because each Cs^+ ion is too large to lie in the plane of its nearest 6-ring neighbors, all four are found near but off that position. Three Cs^+ ions are recessed approximately 2.0 Å into the large cavity from that plane, and one is located in the sodalite unit approximately 2.15 Å from the plane of its nearest framework oxygen neighbors. To minimize electrostatic repulsions, these latter four Cs^+ ions are probably associated with four tetrahedrally placed 6-rings in each unit cell or sodalite unit; the exchange limit observed appears to be related to this structural feature. In each structure, positions for only four of the five Na^+ ions were found; these are near the centers of those remaining four 6-rings not associated with Cs^+ cations. In the hydrated material, water molecules were not located.

Introduction

Complete exchange of Li^+ [1,2] (ionic radius = 0.60 Å),[3] of Ag^+ [2,4] (ionic radius = 1.26 Å),[3] of K^+ [1,2,5] (ionic radius = 1.33 Å),[3] and of Tl^+ [1,2,4] (ionic radius = 1.40 Å)[6] for 12 Na^+ (ionic radius = 0.95 Å)[3] ions per unit cell has been reported in zeolite A at room temperature. With Rb^+ (ionic radius = 1.48 Å),[3] only 8.3[7] or 8.4[1] of the 12 Na^+ ions per unit cell have been reported to be exchangeable, and with Cs^+ (ionic radius = 1.69 Å)[3] the exchange limit is apparently less. Previous studies of partially Cs^+-exchanged sodium zeolite A have been carried out with 6.1,[7] 5.4,[1] and 3.8[8] Cs^+ ions per unit cell. This work was undertaken in part to determine the exchange limit of Cs^+ for Na^+ at room temperature, and to learn the structural basis for that limit.

This work was also undertaken to test the validity of the infrared methods[9] which have been used[7] to establish the ring associations and therefore the approximate positions of some large univalent cations in zeolite A and X. By that procedure, it has been concluded that only loosely bound Na^+ ions can be exchanged by Rb^+ or Cs^+, that these large ions interact relatively weakly with the zeolite framework, and that they tend not to be associated with the 6-rings of the zeolite framework.[7]

Selective sorption measurements on zeolite A containing K^+ and Zn^{2+} have indicated that K^+ ions occlude 8-oxygen rings preferentially over 6-oxygen rings,[10] although the latter are unoccupied and are available to K^+. Although this specific problem is now under investigation in this laboratory, the placement of the large Cs^+ ions in dehydrated partially Cs^+-exchanged zeolite A was expected to indicate siting preferences for the larger ion in the activated zeolite.

General discussions of the structure of zeolite A and of the terms used in its description are available.[8,11,12]

Experimental Section

Single crystals of zeolite 4A, $Na[AlSiO_4]$-A[13] (exclusive of water molecules) and subsequently referred to as Na_{12}-A, or $Na_{12}Al_{12}Si_{12}O_{48}\cdot27H_2O$ per unit cell, were grown as clear colorless cubes by the method of Charnell.[14] Approximately 0.1 g of zeolite A was allowed to exchange at 28° with 10 ml of aqueous 1.0 M CsCl, a large ionic excess of Cs^+, and was periodically agitated to ensure a uniform Cs^+ ion concentration in the vicinity of the crystals. Ion exchange for 1 month, with renewal of exchanging solution to pure aqueous CsCl approximately weekly, yielded crystals unaltered in appearance.

Wet-chemical analysis was not attempted because difficulties were anticipated, and because least-squares refinement of the occupancy parameters of the Cs^+ ions (large scatterers) at their position(s) in the dehydrated structure was expected to yield a definitive result. This expectation was fulfilled (see Structure Determination section). The zeolite has the formal name[13] $Cs_{0.58}Na_{0.42}[AlSiO_4]$-A, with a unit cell composition exclusive of water molecules of $Cs_7Na_5Si_{12}Al_{12}O_{48}$, and will be subsequently referred to as Cs_7Na_5-A.

A relatively large cubic single crystal 0.08 mm on an edge was mounted at the tip of a glass fiber and maintained at 19° and a relative humidity of 30%. Diffraction intensities were collected using graphite-monochromatized Mo $K\alpha$ radiation ($K\alpha_1$, λ 0.70926 Å; $K\alpha_2$, λ 0.71354 Å). A second crystal, also 0.08 mm on an edge, was dehydrated by a procedure similar to that employed before with Na_{12}-A (zeolite 4A):[12] the capillary containing the single crystal was sealed off under vacuum after a 24-hr dehydration period at 350° and 4 × 10⁻⁶ Torr. The crystal remained colorless upon dehydration. Subsequent diffraction intensities were collect-

TABLE I: Positional, Thermal, and Occupancy Parameters for Cs$_7$Na$_5$-A^a

	Wycoff position	x	y	z	β_{11} or B_{iso}	β_{22}	β_{33}	β_{12}	β_{13}	β_{23}	Occupancy factor
				(a) Dehydrated							
(Si, Al)	24(k)	0	1814(9)	3697(9)	24(9)	38(9)	48(10)	0	0	7(16)	1[b]
O(1)	12(h)	0	2248(28)	1/2	60(40)	86(35)	16(28)	0	0	0	1
O(2)	12(i)	0	3016(16)	3016(16)	59(33)	40(23)	40(23)	0	0	-177(54)	1
O(3)	24(m)	1124(13)	1124(13)	3348(17)	47(13)	47(13)	57(24)	20(34)	-22(23)	-22(23)	1
Cs(1)	3(c)	0	1/2	1/2	143(15)	78(7)	78(7)	0	0	0	1
Cs(2)	8(g)	2825(9)	2825(9)	2825(9)	110(8)	110(8)	110(8)	-8(17)	-8(17)	-8(17)	3/8
Cs(3)	8(g)	847(37)	847(37)	847(37)	197(38)	197(38)	197(38)	-103(73)	-103(73)	-103(73)	1/8
Na	8(g)	1960(51)	1960(51)	1960(51)	131(44)	131(44)	131(44)	350(94)	350(94)	350(94)	1/2
				(b) Hydrated							
(Si, Al)	24(k)	0	1832(3)	3714(2)	19(2)	13(2)	9(2)	0	0	4(3)	1[b]
O(1)	12(h)	0	2239(12)	1/2	92(14)	25(8)	8(7)	0	0	0	1
O(2)	12(i)	0	2944(8)	2944(8)	36(9)	18(5)	18(5)	0	0	32(12)	1
O(3)	24(m)	1104(6)	1104(6)	3437(8)	31(4)	31(4)	48(7)	34(10)	15(8)	15(8)	1
Cs(1)	3(c)	0	1/2	1/2	302(14)	112(4)	112(4)	0	0	0	1
Cs(2)	8(g)	2841(3)	2841(3)	2841(3)	60(2)	60(2)	60(2)	-4(4)	-4(4)	-4(4)	3/8
Cs(3)	8(g)	872(18)	872(18)	872(18)	142(12)	142(12)	142(12)	-25(30)	-25(30)	-25(30)	1/8
Na	8(g)	2166(40)	2166(40)	2166(40)	194(40)	194(40)	194(40)	302(95)	302(95)	302(95)	1/2

^{a} Positional and anisotropic thermal parameters are given $\times 10^4$; isotropic thermal parameters are given in Å^2. Numbers in parentheses are the estimated standard deviations in the last significant digits. See Figure 1 for the identities of the atoms. The anisotropic temperature factor = $\exp[-(\beta_{11}h^2 + \beta_{22}k^2 + \beta_{33}l^2 + \beta_{12}hk + \beta_{13}hl + \beta_{23}kl)]$. ^{b} Occupancy for (Si) = 1/2; occupancy for (Al) = 1/2.

ed at 19° for 0° < 2θ < 70°. The space group $Pm3m$ (no systematic absences) was used instead of $Fm3c$ for reasons discussed earlier.[12,15,16]

A Syntex four-circle computer-controlled diffractometer with a pulse height analyzer was used throughout for preliminary experiments and for the collection of diffraction intensities. In each case the cubic cell constants, a = 12.320 (2) Å for the hydrated crystal and a = 12.158 (2) Å for the dehydrated one, were determined by a least-squares treatment of 15 intense reflections for which 20° < 2θ < 24°.

The θ–2θ scan technique was employed at a fixed rate of 0.5°/min in 2θ. All unique reciprocal lattice points (891 and 857 for the hydrated and dehydrated crystals, respectively) for which 2θ < 70° were examined. The high upper limit was chosen for 2θ to maximize the size of the data sets even though few reflections with large 2θ values showed significant intensity. One-half of the total scan time for each reflection was spent counting background at each end of the scan range, which varied from 2.0° at 2θ = 3° to 2.5° at 2θ = 70°. Three check reflections, monitored after every 100 reflections during the course of data collection, showed no significant trends in intensity.

Standard deviations were assigned according to the formula:

$$\sigma(I) = [\omega^2\{CT + 0.25(t_c/t_b)^2(B_1 + B_2)\} + (pI)^2]^{1/2}$$

where CT is the total integrated count obtained in a scan time of t_c, B_1 and B_2 are the background counts each obtained in time t_b, and $I = \omega[CT - 0.5(t_c/t_b)(B_1 + B_2)]$. A value of 0.02 was assigned to the empirical parameter p[17] to account for instrumental variabilities. The net counts were then corrected for Lorentz and polarization effects. Absorption corrections were not applied: μ = 39.3 and 40.3 cm^{-1} for the hydrated and dehydrated crystals, respectively, and transmission coefficients ranged from 0.735 to 0.768, and from 0.716 to 0.750, respectively.

Structure Determination

Dehydrated Cs$_7$Na$_5$-A. Initial full-matrix least-squares refinement of the dehydrated Cs$_7$Na$_5$-A zeolite using the framework and anisotropic Cs$^+$ ion parameters from the hydrated structure, which was determined first, quickly converged at an R_1 index, $(\Sigma|F_o - |F_c||/\Sigma F_o)$, of 0.090 and a corresponding weighted R_2 index, $(\Sigma w(F_o - |F_c|)^2/\Sigma w F_o^2)^{1/2}$, of 0.077.

Occupancy parameter refinement indicated 3.0 Cs(1)'s, 2.9 Cs(2)'s, 1.1 Cs(3)'s, and 3.4 Na$^+$'s per unit cell. These values constitute crystallographic verification of the presence of seven Cs$^+$ ions per unit cell and were fixed at the integers 3, 3, 1, and 4, respectively, the latter to fill the remaining 6-windows. The final R values remained unchanged.

The goodness-of-fit, $(\Sigma w(F_o - |F_c|)^2/(m - s))^{1/2}$, is 1.57; m (123) is the number of observations, and s (32) is the number of variables in least squares. All shifts in the final cycle of least-squares refinement were less than 1% of their corresponding esd's. The final structural parameters are presented in Table Ia and a listing of the observed and calculated structure factors is available.[18] The structure is shown in Figures 1 and 2. Those 123 reflections for which $I_0 > 3\sigma(I_0)$ were used throughout.

For dehydrated Cs$_7$Na$_5$-A, the largest peak on the final difference Fourier function, whose estimated standard deviation is 0.14 e$^-$/Å^3, was 2.0 e$^-$/Å^3 in height and was located at (½, ½, ½). Five other peaks with heights between 1.1 and 1.5 e$^-$/Å^3 appeared also, at (0.10, 0.10, 0.22), (0.11, 0.28, 0.28), (0.14, ½, ½), (0.22, 0.22, 0.22), and (0.25, ½, ½). All six of the above peaks were unusually narrow with an approximate width at half height of 0.2 to 0.6 Å, or irregular, and hence, in addition to being weak, apparently not indicative of new atomic positions. The final difference function was particularly featureless at and near (0, ½, ½).
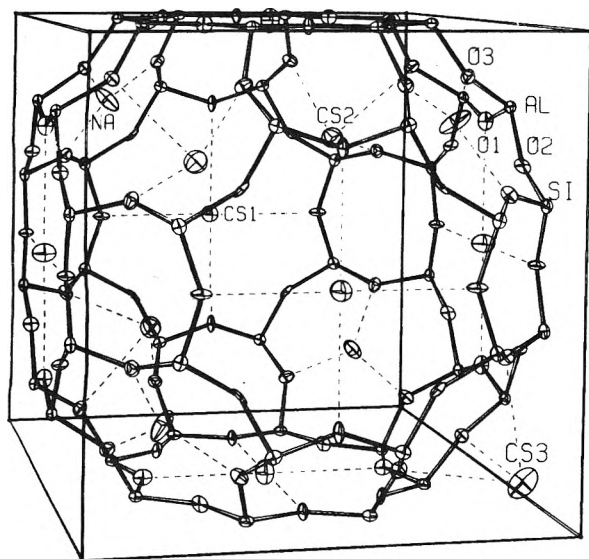
DEHYDRATED CS-EXCHANGED ZEOLITE A

Figure 1. The dehydrated Cs_7Na_5-A unit cell is shown with Cs^+ and Na^+ ions placed statistically within their four equipoints. Positions of partial occupancy are represented so as to maximize the approach distances between cations. Closest ionic approaches to framework oxygens are indicated. Ellipsoids of 20% probability are shown.[20]
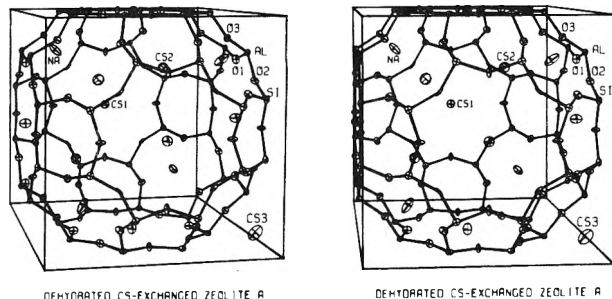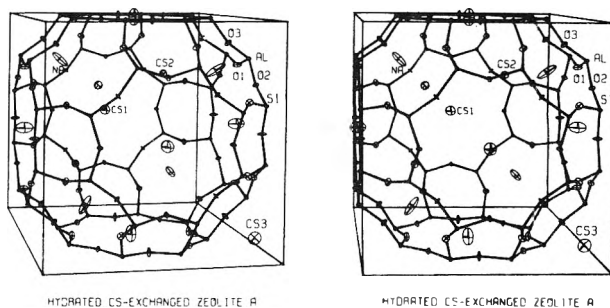

DEHYDRATED CS-EXCHANGED ZEOLITE A   DEHYDRATED CS-EXCHANGED ZEOLITE A

Figure 2. A stereoview[20] of the dehydrated Cs_7Na_5-A unit cell is shown. Ellipsoids of 20% probability are used. To produce a physically meaningful drawing, the thermal parameters β_{23} for O(2) and β_{12} for Na^+ are reduced by 2.0σ.

Hydrated Cs_7Na_5-A. Using framework parameters of hydrated three-quarters Mn(II)-exchanged zeolite 4A,[19] initial full-matrix least-squares refinement of hydrated Cs_7Na_5-A zeolite quickly converged to R_1 and R_2 indices of 0.37 and 0.36, respectively. Successive difference Fourier syntheses and least-squares refinement served to reveal the positions of the seven Cs^+ ions distributed among three equipoints, three at $(0, \frac{1}{2}, \frac{1}{2})$, three at $(0.28, 0.28, 0.28)$, and one at $(0.09, 0.09, 0.09)$. Four Na^+ ions were located at $(0.20, 0.20, 0.20)$.

The final values of R_1 and R_2 are 0.098 and 0.086, and the goodness-of-fit is 2.22. All 323 reflections which were significant at the 3σ level were used throughout; the number of variables in least squares was 32. The final structural parameters are presented in Table Ib, and a listing of the observed and calculated structure factors is available.[18] The structure is shown in Figure 3.

The two largest peaks on the final difference Fourier function for hydrated Cs_7Na_5-A, whose esd was calculated to be 0.16 $e^-/Å^3$, were 2.4 $e^-/Å^3$ in height and were located at $(0.12, 0.12, 0.12)$ and $(0.26, 0.26, \frac{1}{2})$. Four other peaks of height 1.3 to 1.7 $e^-/Å^3$ were also present.

HYDRATED CS-EXCHANGED ZEOLITE A   HYDRATED CS-EXCHANGED ZEOLITE A

Figure 3. A stereoview[20] of the hydrated Cs_7Na_5-A unit cell is shown. Ellipsoids of 20% probability are used.

In hydrated Cs_7Na_5-A (Table IB AND Figure 3), acceptable positions for water molecules were not established. Two peaks located on a final difference Fourier function refined satisfactorily with nine oxygen atoms at 0.27, 0.27, $\frac{1}{2}$ (Wyckoff position 12(j)) and $B = 12$ $Å^2$, and three oxygen atoms at 0.11, 0.11, 0.11 (Wyckoff position 8(g)) and $B = 5$ $Å^2$. Although the inclusion of these atoms caused the error indices to decrease to $R_1 = 0.078$ and $R_2 = 0.071$, plausible distances to established atoms were lacking, and water oxygens were not assigned to these positions in the final model.

The full-matrix least-squares program[20] used in both structure determinations, UCLALS4, minimizes $\Sigma w(\Delta|F|)^2$; the weights (w) were the reciprocal squares of σ, the standard deviation of each observation. Atomic scattering factors[21] for Cs^+, Si^{2+}, $Al^{1.5+}$, Na^+, and O^- were used. The first was corrected for the real part of anomalous dispersion,[22] and the second two were averaged to describe the (Si,Al) disordered position. The final cycles of least-squares refinement of the dehydrated structure were repeated using NUCLS[20] and including the imaginary part of the anomalous dispersion correction[22] for Cs^+, but no significant change in any structural parameter resulted.

Discussion

In the dehydrated structure (Table Ia and Figures 1 and 2), three Cs^+ ions at $Cs(1)$ are located in the middle of the 8-oxygen rings at sites of D_{4d} symmetry, 3.35 Å from four O(1) oxygens and 3.41 Å from four O(2)'s. The remaining Cs^+ ions, at $Cs(2)$ and $Cs(3)$, and the four Na^+ ions which could be located, are on threefold axes and are associated with 6-oxygen rings. The ions at $Cs(2)$ and the Na^+ ions are recessed into the large cavity by 2.02 and 0.20 Å, respectively, from the [111] plane at O(3). The ion at $Cs(3)$ is 2.14 Å from the same plane but in the sodalite unit, perhaps to better distribute the charge with respect to the anionic zeolite framework. The ions at $Cs(2)$ and $Cs(3)$, and Na^+, are all three-coordinate, approaching their respective sets of three framework O(3)'s at 2.99 (3), 3.08 (6), and 2.22 (2) Å.

One would expect the conformation of a particular 6-oxygen ring to depend upon the identity and position of the cation associated with it. In this work, only the average conformation over eight such rings has been determined, and small errors in Cs–O distances due to this disorder are expected.

The lack of agreement between the sum of the ionic radii of Cs^+ and O^{2-}, 3.09 Å,[3] and those observed, 2.99 and 3.08 Å; and between Na^+ and O^{2-}, 2.35 Å,[3] and the observed value of 2.22 Å, is presumably a result of the unusually low

TABLE II: Selected Interatomic Distances (Å) and Angles (deg)[a]

	Cs_7Na_5-A (hydr)	Cs_7Na_5-A (dehydr)
(Si, Al)–O(1)	1.662(5)	1.670(15)
(Si, Al)–O(2)	1.666(4)	1.679(13)
(Si, Al)–O(3)	1.665(3)	1.659(9)
Cs(1)–O(1)	3.401(14)	3.346(34)
Cs(1)–O(2)	3.582(13)	3.412(27)
Cs(2)–O(3)	3.114(11)	2.992(26)
Cs(3)–O(3)	3.187(28)	3.077(58)
Na–O(3)	2.424(24)	2.216(23)
O(1)–(Si, Al)–O(2)	107.1(7)	101.1(15)
O(1)–(Si, Al)–O(3)	111.0(4)	113.7(8)
O(2)–(Si, Al)–O(3)	109.0(6)	108.3(10)
O(3)–(Si, Al)–O(3)	109.6(7)	111.0(15)
(Si, Al)–O(1)–(Si, Al)	144.9(10)	143.2(23)
(Si, Al)–O(2)–(Si, Al)	159.4(9)	149.1(20)
(Si, Al)–O(3)–(Si, Al)	147.0(7)	140.2(14)
O(3)–Cs(2)–O(3)	81.5(2)	79.4(7)
O(3)–Cs(3)–O(3)	79.3(6)	76.8(15)
O(3)–Na–O(3)	113.9(35)	119.2(48)

[a] Numbers in parentheses are the estimated standard deviations in the last significant digits.

association number (ligancy) of the cations in the dehydrated structure.

The differences between the hydrated and dehydrated structures are limited to moderate positional shifts, as can most easily be seen in the distances given in Tables II and III. The Na^+–O(3) distance decreases by 0.21 Å (Table II) upon dehydration, corresponding to the movement of Na^+ to a position closer to the plane of its nearest O(3) neighbors, and to conformational changes in the 6-oxygen rings. Lesser changes upon dehydration include the corresponding movement of the Cs(2) and Cs(3) ions toward their O(3) neighbors. Similar decreases in distance are found between Cs(1) and its O(1) and O(2) neighbors, and may contribute to the contraction of the unit cell edge length.

In general, the (Si,Al)–O–(Si,Al) framework bond angles of hydrated Cs_7Na_5-A (see Table IV) are very similar to those in hydrated Na_{12}-A,[23] hydrated K_{12}-A,[5] and hydrated Tl_{11}-A,[15] and can be considered the "relaxed" or least-strained framework conformation. Upon dehydration, however, relatively large changes (see Table IV) are observed which can be compared with those found in Na^+-,[12] K^+-,[5] and Tl^+-exchanged[15] zeolite A. It is surprising that the framework conformations of these dehydrated structures are so different.

In neither structure could the fifth Na^+ ion be located. It is likely, since the other eleven ions per unit cell are each associated with one of the eleven 6- and 8-rings, that this remaining Na^+ ion occupies a new equipoint and has a low occupancy. A site in the large cavity near a 4-ring, such as that found in dehydrated Na_{12}-A,[12] is available in dehydrated Cs_7Na_5-A between a Na^+-containing 6-ring and the 6-ring associated with Cs(3), which is located within the sodalite unit. The structures of hydrated Na_{12}-A[23] and K_{12}-A[5] suggest that the fifth Na^+ ion in hydrated Cs_7Na_5-A is in the large cavity, associated entirely with water molecules and not in ionic contact with the zeolite framework.

All of the 8-rings, but only half of the 6-rings, are occupied by Cs^+ ions. This indicates either that Cs^+ prefers 8-

TABLE III: Deviations of Atoms (Å) from the (111) Plane at O(3)[a]

	Cs_7Na_5-A (hydr)	Cs_7Na_5-A (dehydr)
Cs(2)	2.05	2.02
Cs(3)	-2.16	-2.14
Na	0.61	0.20
O(2)	0.17	0.30

[a] A negative deviation indicates that the atom lies on the same side of the plane as the origin.

TABLE IV: (Si,Al)–O–(Si,Al) Angles[a] at Various Oxygen Positions

	O(1)	O(2)	O(3)
(a) Hydrated			
Na_{12}-A[b]	146	160	144
K_{12}-A[c]	145	159	146
Tl_{11}-A[d]	148	161	144
Cs_7Na_5-A	145	159	147
(b) Dehydrated			
Na_{12}-A[e]	145	166	146
K_{12}-A[c]	128	178	154
Tl_{11}-A[d]	162	144	138
Cs_7Na_5-A	143	149	140

[a] Esd's are 2° or less. [b] Reference 23. [c] Reference 5. [d] Reference 15. [e] Reference 12.

ring sites, into which it fits better, or that Na^+ prefers 6-rings for analogous reasons, or both. This is consistent with the conclusion[10] of Takaishi et al. based upon sorption measurements in the Zn,K-A system, that K^+ ions locate preferentially in the 8-rings instead of available 6-rings, and with that of Maxwell and Baks[7] that 6-rings associate preferentially with Na^+ ions instead of the much larger Cs^+ ions.

This structure agrees generally with that predicted by Maxwell and Baks[7] on the basis of infrared correlations of spectra with position. However, Cs^+ ions are less reluctant to associate with 6-rings than suggested.[7] Only two Cs^+ ions were located in 6-rings by infrared methods in Cs_6Na_6-A; presumably had an additional Cs^+ ion been present as was the case in this work (Cs_7Na_5-A), it would have been sited in a 6-ring to give an assignment of three such Cs^+ ions per unit cell, one less than is found crystallographically. The four "loosely bound and readily exchangeable"[7] positions in the large cages in hydrated Na_{12}-A[23] must be those in the planes of the 8-rings (three ions) and in the vicinity of the center of the large cavity (one ion). Upon seven-twelfths Cs^+ exchange, no Cs^+ ion is located near the center of the large cavity. All are associated with the zeolite framework, although the 8-ring Cs^+ ions are further from the framework oxygens by approximately 0.3 Å (see Table II), and their interaction should be correspondingly weaker, than those of the 6-ring Cs^+ ions. There are, then, only three "loosely bound" Cs^+ positions according to this work, not four,[7] per unit cell.

The coalescence of the four potential minima (at 0, z, z; 0, $1 - z$, z; 0, z, $1 - z$; and 0, $1 - z$, $1 - z$) found for Na^+,[12,23] K^+,[5] and Tl^+ [15] ions in an 8-ring to one (at 0, ½, ½) for Cs^+, keeps the shortest Cs^+ approach to the frame-

work at 3.40 Å (Cs(1)–O(1), hydrated) or 3.35 Å (dehydrated), *substantially longer* than the sum of the corresponding ionic radii, 3.09 Å.[3] The apparent absence of direct ionic contact between Cs(1) and the zeolite is the structural basis of the observation[7] that Cs(1) has a weak interaction with the zeolite framework, while nearly all Na^{+}, K^{+}, and Tl[+] ions have strong interactions in their corresponding hydrated structures.[7]

The weak interaction observed between some Rb^{+} ions[7] and the zeolite implies that these are also located at Wyckoff 3(c), at the very centers of the 8-rings, so that an even greater disparity, of approximately 0.5 Å, between the Rb^{+}–O(1) distance and the sum of the corresponding ionic radii should exist. (The value 0.5 is the approximate sum of the disparity in this work, 0.31 Å, and the difference in the ionic radii of Cs^{+} and Rb^{+}, 0.21 Å. Expected changes in zeolite framework conformation are likely to cause the true disparity to be somewhat different from that sum.) A critical monovalent cation radius for the occupation of Wyckoff 3(c) between that of Tl[+] (1.40 Å) and Rb^{+} (1.48 Å) is indicated, although the possibly more covalent bonding by Tl[+] may confuse this result. Tl[+] ions are strongly bound[7] and do not occupy the Wyckoff 3(c) equipoint.[15] It appears that these 8-ring Cs^{+} and Rb^{+} ions are further examples of ions which occupy positions of minimum electrostatic energy whose centers are not within an ionic contact distance of any other ion or atom in the dehydrated structures, although the Cs^{+} ion is approximately one root mean square thermal vibration amplitude from each of four such contacts, as Rb^{+} is likely to be. A much clearer example of an isolated ion was reported for a K^{+} ion in dehydrated K-A.[5]

Supplementary Material Available. Listing of the observed and calculated structure factors for both structures (supplementary Tables I and II) will appear following these pages in the microfilm edition of this volume of the journal. Photocopies of the supplementary material from this paper only or microfiche (105 × 148 mm, 24× reduction, negatives) containing all of the supplementary material for the papers in this issue may be obtained from the Business Office, Books and Journals Division, American Chemical Society, 1155 16th St., N.W., Washington, D.C. 20036. Remit check or money order for $4.00 for photocopy or $2.50 for microfiche, referring to code number JPC-75-2163.

References and Notes

(1) R. M. Barrer, L. V. C. Rees, and D. J. Ward, *Proc. R. Soc., Ser. A*, **273**, 180 (1963).
(2) D. W. Breck, "Zeolite Molecular Sieves", Wiley, New York N.Y., 1974, p 541.
(3) L. Pauling, "The Nature of the Chemical Bond", 3rd ed, Cornell University Press, Ithaca, N.Y., 1960, p 514.
(4) H. S. Sherry and H. F. Walton, *J. Phys. Chem.*, **71**, 1457 (1967).
(5) P. C. W. Leung, K. B. Kunz, I. E. Maxwell, and K. Seff, *J. Phys. Chem.*, preceding paper in this issue.
(6) Reference 4, p 518.
(7) I. E. Maxwell and A. Baks, *Adv. Chem. Ser.*, **No. 121**, 87 (1973).
(8) D. W. Breck, W. G. Eversole, R. M. Milton, T. B. Reed, and T. L. Thomas, *J. Am. Chem. Soc.*, **78**, 5963 (1956).
(9) E. M. Flanigen, H. A. Szymanski, and H. Khatami, *Adv. Chem. Ser.*, **No. 101**, 201 (1971).
(10) T. Takaishi, Y. Yatsurugi, A. Yusa, and T. Kuritomi, *J. Chem. Soc., Faraday Trans.*, **71**, 97 (1975).
(11) L. Broussard and D. P. Shoemaker, *J. Am. Chem. Soc.*, **82**, 1041 (1960).
(12) R. Y. Yanagida, A. A. Amaro, and K. Seff, *J. Phys. Chem.*, **77**, 805 (1973).
(13) Nomenclature informally presented by R. M. Barrer, Third International Conference on Molecular Sieves, Zurich, 1973.
(14) J. F. Charnell, *J. Cryst. Growth*, **8**, 291 (1971).
(15) P. E. Riley, K. Seff, and D. P. Shoemaker, *J. Phys. Chem.*, **76**, 2593 (1972).
(16) P. E. Riley, K. B. Kunz, and K. Seff, *J. Am. Chem. Soc.*, **97**, 537 (1975).
(17) S. W. Peterson and H. A. Levy, *Acta Crystallogr.*, **10**, 70 (1957).
(18) See paragraph at end of text regarding supplementary material.
(19) R. Y. Yanagida, T. B. Vance, Jr., and K. Seff, *Inorg. Chem.*, **13**, 723 (1974).
(20) Principal computer programs used in this study were: T. Ottersen, LPCOR data reduction program, University of Hawaii, 1973; P. K. Gantzel, R. A. Sparks, and K. N. Trueblood, UCLALS4, full-matrix least-squares, American Crystallographic Association Program Library (old) No. 317 (modified by K. Seff); C. R. Hubbard, C. O. Quicksall, and R. A. Jacobson, Ames Laboratory Fast Fourier, Iowa State University, 1971; C. K. Johnson, ORTEP, Report ORNL-3794, Oak Ridge National Laboratory, Oak Ridge, Tenn., 1965; J. A. Ibers, NUCLS, Northwestern University, Evanston, Ill., full-matrix least-squares, based on ORFLS by W. R. Busing and H. A. Levy.
(21) "International Tables for X-ray Crystallography", Vol. III, Kynock Press, Birmingham, England, 1962, p 212.
(22) C. H. Dauben and D. H. Templeton, *Acta Crystallogr.*, **8**, 841 (1955).
(23) V. Gramlich and W. M. Meier, *Z. Kristallogr.*, **133**, 134 (1971).

Friction and Partition in Membranes

J. A. M. Smit,* J. C. Eijsermans, and A. J. Staverman

Gorlaeus Laboratories of the State University of Leiden, Leiden, The Netherlands (Received November 7, 1974: Revised Manuscript Received June 30, 1975)

Nonelectrolytic transport through a membrane has been described in terms of the friction formalism of nonequilibrium thermodynamics. The assumption of constancy of the friction coefficients along the transport direction in the membrane leads to linear concentration profiles in the stationary state. The dependence on concentration of measurable resistance coefficients can be predicted and allows the evaluation of partition coefficients. Experimental data obtained in a number of systems, consisting of a sugar as solute, water as solvent, and porous glass (Vycor) as membrane, support the theory.

1. Introduction

Transport processes involving membranes have been successfully described hitherto by nonequilibrium thermodynamics. Two main approaches can be distinguished: the continuum theory and the black-box theory. In the latter theory the membrane separates two bulk phases and maintains discrete differences between the state variables in those phases. Going from one bulk phase to the other and considering the membrane a black box one has a discontinuous change in the state variables. In the continuum theory the membrane appears as a separate phase, in which the state variables are continuous functions of space coordinates and time. Consequently, the black-box theory requires a minimum of information about the membrane itself and provides us with a very general description of the transport process, irrespective of the membrane model adopted. On the contrary, the continuum theory covering the phenomena occurring locally within the membrane supposes detailed knowledge of what happens in its interior.

In this respect two extreme situations can be distinguished.[1-3] If the membrane pores have dimensions much larger than the mean free path of the permeating molecules the membrane participates only marginally in the transport process. If, however, the membrane pores are of the same order of magnitude as the mean free path of the permeating molecules the membrane is involved intimately in the transport process at a molecular level. Frequently one meets this distinction between two membrane models in the literature, here referred to as "pore model" and "gel model", concurring with respectively the former and the latter case discussed before.

In the pore model the membrane consists of a number of uniform cylindrical pores crossing an impermeable barrier.[2,4] In that case the characteristics of the transport process are implied in the transport properties of a single macroscopic capillary of which an analysis has been given.[1] In the pore liquid there is in the isothermal case a local entropy production, which contains diffusive terms but also terms due to viscous flow. In the steady state the pressure gradients are maintained by forces caused by viscous drag. The influence of the membrane is restricted to a small part of the pore liquid which is in contact with the wall of the capillary. Contrary to this the membrane participates more intensively in the transport process when the gel model applies. It contributes as a specific component in the local entropy production. In the steady state at mechanical equi-

librium the pressure gradients are balanced by the external forces exerted on the components (the membrane included). This is the only difference with the situation met in freely diffusing liquid mixtures or solutions, where pressure is uniform because of the absence of external forces. Hence, one can make fruitful use, dealing with the gel model, of the many available theories on liquid mixtures.[5-8]

The theory to be discussed here applies to a continuum and starts from the gel model since we consider the membrane (pore radius about 20×10^{-10} m) to be interspersed at a molecular level among the permeating molecules. Following the pathways of nonequilibrium thermodynamics we derive phenomenological force-flow equations for two different choices of the frame of reference with respect to which the velocities of the components are counted. By taking the membrane itself as a reference component we arrive at phenomenological relations in which the so-called resistance coefficients R_{ik} appear as transport coefficients. The other reference scheme is found by taking into consideration only the relative velocities between two individual components, leading to the so-called friction coefficients r_{ik}. The latter coefficients are well-defined physical quantities,[5-8] being a measure for the friction between two different species having a relative motion to each other.

Further treatment has been focussed on the comparison of the concentration-dependent coefficients R_{ik} with the concentration-independent coefficients r_{ik}. As it appears information about partition and friction in the membrane is obtained in this way.

Apart from that an equivalent description of membrane phenomena in terms of frictions is well known and has been put forward first by Spiegler[9] and later on by Kedem and Katchalsky.[10] Their friction coefficients f_{ik} developed from a mechanical model differ by a concentration factor from the coefficients r_{ik}. However, we emphasize that nonequilibrium thermodynamics itself provides a framework for formulating a friction formalism, though it has been suggested otherwise.[11]

2. The Phenomenological Relations in the Gel Model

The system to be discussed here consists of a number of diffusing components i (i from 1 to m), which form the "membrane phase", i.e., the membrane including the pore liquid. The membrane phase is considered as a slab only normal to which transport can occur (x direction). The transport phenomenon will be treated as an isothermal unidirectional diffusion of a multi-component system, on the

understanding, however, that component m, being the membrane, is confined by a "wall potential" between two boundary surfaces and is made to form a lattice.

We start with the basic assumption that mechanical equilibrium has been established everywhere in the membrane phase. Let ∇P be the local pressure gradient in the x direction, c_i the local molar concentration of species i per unit of total volume of membrane phase, and F_i the external forces exerted on a mole of species i, then the equation of motion reduces at mechanical equilibrium to the following force equation[1]

$$0 = -\nabla P + \sum_{i=1}^{m} c_i F_i \tag{1}$$

in which accelerative and viscous contributions vanish.

When $\nabla \mu_i$ represents the local gradient of the chemical potential of species i into the x direction, ∇P can be related to these gradients by the Gibbs–Duhem equation according to

$$\sum_{i=1}^{m} c_i \nabla \mu_i = \nabla P \tag{2}$$

Introduction of eq 1 into eq 2 yields the equality

$$0 = \sum_{i=1}^{m} c_i (F_i - \nabla \mu_i) \tag{3}$$

Using a theorema due to Prigogine and the equality (3) De Groot and Mazur write for the local entropy production in the case of isothermal diffusion of m components[1]

$$\sigma_D = 1/T \sum_{i=1}^{m} c_i (u_i - u^a)(F_i - \nabla \mu_i) \tag{4}$$

with T the absolute temperature, u_i the local velocity of species i, and u^a an arbitrary reference velocity. Generally neither the flows $c_i(u_i - u^a)$ nor the forces $(F_i - \nabla \mu_i)$ in eq 4 are independent. In order to obtain independent flows and forces in eq 4, we simply put into eq 4

$$u^a = u_m \tag{5}$$

and we define the flows J_i, measured with respect to the membrane component, as

$$J_i = c_i(u_i - u_m) \tag{6}$$

which finally leads to

$$\sigma_D = 1/T \sum_{i=1}^{m} J_i (F_i - \nabla \mu_i) \tag{7}$$

For small deviations from the equilibrium state we assume that the forces are linearly related to the flows according to

$$F_i - \nabla \mu_i = \sum_{k=1}^{m-1} R_{ik} J_k \quad i = 1, 2, \ldots, m - 1 \tag{8}$$

where the coefficients of proportionality $R_{ik}(i \neq k)$ are subjected to the Onsager reciprocal relation

$$R_{ik} = R_{ki} \quad i \neq k; \; i, k = 1, 2, \ldots, m - 1 \tag{9}$$

because they relate independent flows to their conjugated independent forces.[1] From eq 8 and eq 3 we derive for the membrane component

$$F_m - \nabla \mu_m = -\sum_{j=1}^{m-1} \sum_{k=1}^{m-1} \frac{R_{jk} c_j}{c_m} J_k \tag{10}$$

The coefficients R_{ik} are called "resistance coefficients".

Upon inspection of eq 8 and eq 9 it is seen that a number of $\frac{1}{2}m(m - 1)$ is sufficient to determine the force-flow relations.

In the following we will show that an alternative description in terms of friction coefficients r_{ik} can be introduced in a formal way. By analogy to the derivation of eq 8 from eq 7 one can define starting from eq 4 linear relations between forces and flows

$$F_i - \nabla \mu_i = -\sum_{k=1}^{m} r_{ik} c_k (u_k - u^a) \quad i = 1, 2, \ldots, m \tag{11}$$

It must be noted that the coefficients r_{ik} in eq 11 are not uniquely defined because of the dependence of the forces expressed by eq 3. As we have seen the minimally required number of independent coefficients is equal to $\frac{1}{2}m(m - 1)$, so there remains among the m^2 coefficients r_{ik} a number of $\frac{1}{2}m(m + 1)$ restrictive relations. We arrive at these restrictive relations by confrontation of the set (11) with the eq 8 and 10. First the arbitrariness due to u^a in eq 11 can be completely removed by adopting m restrictive relations[5,8]

$$\sum_{k=1}^{m} r_{ik} c_k = 0 \quad i = 1, 2, \ldots, m \tag{12}$$

Then it follows by eliminating the coefficients r_{ii} from eq 11 and eq 12 that

$$F_i - \nabla \mu_i = \sum_{k=1}^{m} r_{ik} c_k (u_i - u_k) \quad i = 1, 2, \ldots, m \tag{13}$$

By means of eq 6 we rearrange eq 13 and obtain

$$F_i - \nabla \mu_i = \left[\sum_{k=1}^{m-1} \frac{r_{ik} c_k + r_{im} c_m}{c_i} \right] J_i - \sum_{k=1}^{m} r_{ik} J_k$$
$$i \neq k, \; i = 1, 2, \ldots, m - 1 \tag{14}$$

and with eq 12

$$F_m - \nabla \mu_m = -\sum_{k=1}^{m-1} r_{mk} J_k \tag{15}$$

It is clear that eq 14 and 15 essentially describe the same phenomena as eq 8 and 10. Comparing the coefficients of J_k in both sets, we have the following equalities

$$R_{ii} = \sum_{\substack{k=1 \\ k \neq i}}^{m-1} \frac{r_{ik} c_k + r_{im} c_m}{c_i} \quad i = 1, 2, \ldots, m - 1 \tag{16}$$

$$R_{ik} = -r_{ik} \quad i \neq k; \; i, k = 1, 2, \ldots, m - 1 \tag{17}$$

$$\sum_{k=1}^{m-1} \frac{R_{ki} c_k}{c_m} = r_{mi} \quad i = 1, 2, \ldots, m - 1 \tag{18}$$

From these relations by which the resistance coefficients $R_{ik}(i, k = 1, 2, \ldots, m - 1)$ are expressed in terms of the friction coefficients $r_{ik}(i, k = 1, 2, \ldots, m)$ it follows with the Onsager reciprocal relation (9) that

$$r_{ik} = r_{ki} \quad i \neq k; \; i, k = 1, 2, \ldots, m \tag{19}$$

A number of $\frac{1}{2}m(m - 1)$ cross relations appear in eq 19 among the coefficients $r_{ik}(i \neq k)$ which together with the m relations (12) amounts to the required number of $\frac{1}{2}m(m + 1)$ restrictive relations to which the elements of the matrix r_{ik} are subjected.

The treatment above shows that two equivalent descriptions are possible. One uses the symmetrical resistance matrix R_{ik} and is based on eq 8 and eq 9, the other one uses the symmetrical friction matrix r_{ik} and is based on eq 13 and eq 19. In the latter matrix the elements r_{ii} are not of interest, because they do not occur in eq 13 and eq 19. From a physical point of view it means that friction between particles within the same species does not enter into the transport equations because they cannot be distinguished from each other. However, by radioactive labeling of some of these particles, which makes them distinguishable, the friction within the same species can be made perceptible. In that case coefficients r_{ii} do appear in the transport equations.[12]

The description in terms of friction coefficients frequently met in literature[3,4,6,8-14] has often been put forward because of its alleged physical clarity. The interpretation of the coefficients r_{ik} as well-defined quantities describing the friction of 1 mol of species i with 1 mol of species k is closely connected to their supposed slight dependence or independence on concentration. In order to clarify this somewhat we develop the coefficients r_{ik} in a Taylor series with respect to the solute concentrations c_j (including the membrane)

$$r_{ik}(c_1, c_2, \ldots, c_j) = (r_{ik})_0 + \sum_{j=1} c_j \left[\frac{\partial r_{ik}}{\partial c_j} \right]_0 + \ldots$$
$$i \neq k; \quad i, k = 1, 2, \ldots, m \quad (20)$$

where the function values at the right member have been taken at zero solute concentrations and are subjected to the Onsager reciprocal relation. The coefficients r_{ik} do not vanish in the limit of zero solute concentrations but have a limiting value $(r_{ik})_0$.[15,16] In dilute solutions it is plausible to expect rather constant friction coefficients r_{ik} because they become approximately equal to the leading terms $(r_{ik})_0$ which are relatively large compared to the higher terms. However, in general the friction coefficients depend on composition, and only in cases in which no or little change in composition is involved does the concept of constant friction coefficients apply.

Also from Bearman's statistical mechanical approach[7] the coefficients r_{ik} emerge as quantities which generally depend on composition. The resulting phenomenological equations derived by him are identical with our eq 13, 16–19, if they are specified to the isothermal case (cf. eq 5.8 and 5.12 in the literature cited). Further Staverman[13] and Richardson[11] have presented results in agreement with our eq 14, although they do not take into account explicitly the external forces present in the system. Finally, by the replacement of

$$r_{ik} c_k = f_{ik} \quad i \neq k; \quad i, k = 1, 2, \ldots, m \quad (21)$$

into eq 13 and eq 19 we are led to the phenomenological equations derived by Spiegler[9] from a model of Newtonian frictions. The same replacement applied to eq 16 and eq 17 yields results identical with those obtained by Kedem and Katchalsky[10] (cf. eq 1–12 in the literature cited). Clearly the introduction of Spieglers friction coefficients f_{ik} is justified by the assumption that in the linear approach the forces will be proportional to the velocities. However, the coefficients f_{ik} do depend on the concentration c_k, eq 21 and are therefore less appropriate quantities for analysis of the concentration dependence of the resistance coefficients R_{ik}. Only in cases where this concentration does not change can they be used.

3. The Integral Phenomenological Relations for a Ternary Nonelectrolytic System

The system of interest here consists of a nonelectrolytic solvent, a nonelectrolytic solute, and a membrane component, respectively, indicated by 1, 2, m. The origin of the coordinate system is fixed in space. Within this coordinate system there is no movement of component m, being the membrane. So at every point x of the transport direction $u_m = 0$.

At the interfaces $x = 0$ and $x = l$ the membrane slab meets respectively the external bulk phases α and β which are kept at uniform pressure and composition. For the membrane phase $0 < x < l$, we may put, because of the absence of external forces acting on components 1 and 2

$$F_1 = 0$$
$$F_2 = 0 \quad (22)$$
$$F_m \neq 0$$

The inequality in eq 22 expresses that a reaction force F_m is present which as is seen from eq 1 maintains a pressure gradient.

Finally, the following conditions are assumed to be fulfilled.[13,17] (1) At the boundaries $x = 0$ and $x = l$ no jump in the chemical potentials of the components 1 and 2 exists, which means that

$$-\int_0^l \nabla \mu_i \, dx = \mu_i{}^\alpha - \mu_i{}^\beta = \Delta \mu_i \quad i = 1, 2 \quad (23)$$

Corresponding to the nonelectrolytic character of the components 1 and 2 $\Delta \mu_i$ can be written out in a concentration dependent and a pressure dependent part as

$$\Delta \mu_i = \Delta \mu_i{}^c + v_i \Delta P \quad i = 1, 2 \quad (24)$$

(2) The flows $J_i (i = 1, 2)$ are independent of x within the membrane, i.e., a steady state is assumed in which neither accumulation nor depletion of any species may occur locally in the membrane.

Using the symbol $\langle \ \rangle$ for the averaging operation $1/l \int_0^l (\ ) \, dx$ we find from eq 8, 9, 22–24

$$\frac{\Delta \mu_1{}^c}{l} + v_1 \frac{\Delta P}{l} = \langle R_{11} \rangle J_1 + \langle R_{12} \rangle J_2$$
$$\frac{\Delta \mu_2{}^c}{l} + v_2 \frac{\Delta P}{l} = \langle R_{21} \rangle J_1 + \langle R_{22} \rangle J_2 \quad (25)$$

with $\langle R_{12} \rangle = \langle R_{21} \rangle$.

Along the same lines of reasoning we derive from eq 14, 19, 21–24

$$\frac{\Delta \mu_1{}^c}{l} + v_1 \frac{\Delta P}{l} = \left\langle \frac{r_{12} c_2 + f_{1m}}{c_1} \right\rangle J_1 - \langle r_{12} \rangle J_2$$
$$\frac{\Delta \mu_2{}^c}{l} + v_2 \frac{\Delta P}{l} = \left\langle \frac{r_{21} c_1 + f_{2m}}{c_2} \right\rangle J_2 - \langle r_{21} \rangle J_1 \quad (26)$$

with $\langle r_{12} \rangle = \langle r_{21} \rangle$.

Force-flow eq 25 and 26 are identical with the relations originating from the black-box theory, but have been found here as a result of the integration of the local equations of the continuum theory. By comparing the set (25) with the set (26) we have the following equalities:

$$\langle R_{11} \rangle = \left\langle \frac{r_{12} c_2 + f_{1m}}{c_1} \right\rangle$$

$$\langle R_{22} \rangle = \left\langle \frac{r_{21} c_1 + f_{2m}}{c_2} \right\rangle \quad (27)$$

$$\langle R_{12} \rangle = -\langle r_{12} \rangle = -\langle r_{21} \rangle = \langle R_{21} \rangle$$

The average resistance coefficients appearing in the left-hand side of eq 27 can be evaluated from experimental data. The same applies to the average friction coefficient $\langle r_{12} \rangle$ which accounts for the friction between solvent and solute. Contrary to this the friction coefficients $f_{1m}(=r_{1m}c_m)$ and $f_{2m}(=r_{2m}c_m)$ involving the membrane are not simply determinable without auxiliary assumptions. The basic assumption underlying the further development starts from constancy of r_{12}, r_{1m}, and r_{2m} with respect to x. This needs some explanatory remarks. As follows from eq 20 r_{12}, r_{1m}, and r_{2m} generally depend on the composition of the system expressed by c_2 and c_m. However, the dependence on c_m is irrelevant in the transport direction in which c_m may be supposed constant. The remaining dependence on c_2 disappears in the limit of dilute solution and, more generally, when the concentration gradients in the membrane are too small to change the friction coefficients. The constancy of the friction coefficients enables us to specify the concentration profiles within the membrane as shown in the following. Finally, it leads to a prediction of the dependence on concentration of the average resistance coefficients, which can be tested experimentally.

4. The Solute Concentration Profile within the Membrane under Steady State Conditions

We shall calculate the concentration profile of the solute $c_2(x)$ for the simple ternary system defined above. Once it is known, the profile of the solvent concentration $c_1(x)$ follows by taking into account the interdependence of the concentrations within the membrane, reading

$$c_1 v_1 + c_2 v_2 + \phi_m = 1 \qquad (28)$$

where ϕ_m represents the volume fraction of the membrane species, supposed to be uniform everywhere in the membrane phase. Assuming that r_{12}, f_{1m}, f_{2m}, and ϕ_m do not depend on x and dealing with dilute solutions ($c_2 v_2 \ll c_1 v_1$) it can be shown (see paragraph at end of text regarding supplementary material) that the function $c_2(x)$ turns out to be

$$c_2 = c_2' + \frac{c_2'' - c_2'}{e^{zl} - 1}(e^{zx} - 1) \qquad (29)$$

where the prime and double prime refer to concentrations within the membrane at the interfaces at $x = 0$ and $x = l$ and z represents a reciprocal characteristic diffusion length defined by

$$z = \frac{\ln(\gamma_2'/\gamma_2'')}{l} + \frac{r_{12}(1 - \phi_m) + f_{1m}v_2}{v_1(1 - \phi_m)RT}J_v \qquad (30)$$

with γ_2 the activity coefficient of the solute and J_v the total volume flow given by

$$J_v = J_1 v_1 + J_2 v_2 \qquad (31)$$

For small values of zl the exponents appearing in eq 29 can be developed into a series, which is broken off after two terms, giving

$$c_2 = c_2' + \frac{c_2'' - c_2'}{l}x \qquad (32)$$

The linear concentration profile suggested by eq 32 may be expected for small values of z, i.e., for small volume flows J_v and for cases where $\gamma_2' \simeq \gamma_2''$. The latter situation arises when the solute concentrations in the outer bulk phases do not differ too much. In that case a single partition coefficient K couples the solute concentrations inside and outside the membrane at the interfaces according to

$$c_2' = Kc_2^\alpha(1 - \phi_m) \qquad x = 0$$
$$c_2'' = Kc_2^\beta(1 - \phi_m) \qquad x = l \qquad (33)$$

where c_2^α and c_2^β represent the external concentrations in respectively the α phase and the β phase. In the ideal case that neither adsorption nor depletion of the solute occurs within the membrane at the boundaries $K = 1$ and the external concentrations c_2^α and c_2^β are equal to respectively $c_2'/(1 - \phi_m)$ and $c_2''/(1 - \phi_m)$ being the solute concentrations per unit of pore volume of the membrane at the boundaries. If $K > 1$, this is an indication of adsorption of the solute, whereas $K < 1$ indicates the occurrence of depletion of the solute. Summarizing one may expect linear concentration profiles according to eq 32 in the nonelectrolytic system described above, if the volume flow J_v is rather small and the ratio c_2^α/c_2^β does not deviate much from unity. Actually these requirements were fulfilled in our experiments.

5. The Relations between the Friction Coefficients and the Resistance Coefficients

Relationships 27 between $\langle R_{11} \rangle$, $\langle R_{22} \rangle$, $\langle R_{12} \rangle$ and r_{12}, f_{1m}, f_{2m} can be worked out further if the latter coefficients do not depend on x. In that case eq 27 become

$$\langle R_{11} \rangle = r_{12}\left\langle \frac{c_2}{c_1} \right\rangle + f_{1m}\left\langle \frac{1}{c_1} \right\rangle$$

$$\langle R_{22} \rangle = r_{12}\left\langle \frac{c_1}{c_2} \right\rangle + f_{2m}\left\langle \frac{1}{c_2} \right\rangle \qquad (34)$$

$$\langle R_{12} \rangle = -r_{12}$$

From eq 34 it is clear that if the assumption of constant friction coefficients is valid the coefficients $\langle R_{11} \rangle$ and $\langle R_{22} \rangle$ are functions of the concentrations of the solute and the solvent as distinct from $\langle R_{12} \rangle$. Evaluation of the terms between brackets on the right-hand side of eq 34 requires specific knowledge of the concentration profiles within the membrane. Assuming that the solute concentration c_2 is a linear function of x according to eq 32, that the membrane volume fraction ϕ_m does not depend on x, and that a single partition coefficient relates the internal solute concentration to the external one according to eq 33, we calculate the following average quantities:

$$\left\langle \frac{1}{c_1} \right\rangle = \frac{v_1 \ln\left[\dfrac{1 - Kv_2c_2^\alpha}{1 - Kv_2c_2^\beta}\right]}{K(1 - \phi_m)v_2(c_2^\beta - c_2^\alpha)} \simeq$$

$$\frac{v_1}{1 - \phi_m}\{1 + \tfrac{1}{2}Kv_2(c_2^\alpha + c_2^\beta)\}$$

$$\left\langle \frac{1}{c_2} \right\rangle = \frac{\ln[c_2^\alpha/c_2^\beta]}{K(1 - \phi_m)(c_2^\alpha - c_2^\beta)}$$

$$\left\langle \frac{c_2}{c_1} \right\rangle = \frac{v_1}{v_2}\left\{\frac{\ln[(1 - Kv_2c_2^\alpha)/(1 - Kv_2c_2^\beta)]}{Kv_2(c_2^\beta - c_2^\alpha)} - 1\right\} \simeq$$

$$\tfrac{1}{2}Kv_1(c_2^\alpha + c_2^\beta) \qquad (35)$$

$$\left\langle \frac{c_1}{c_2} \right\rangle = \frac{v_2}{v_1}\left[\frac{\ln[c_2^\alpha/c_2^\beta]}{Kv_2(c_2^\alpha - c_2^\beta)} - 1\right]$$

Insertion of eq 35 into 34 leads to

$$\langle R_{11} \rangle = v_1\left(r_{12} + \frac{f_{1m}v_2}{1 - \phi_m}\right)K\tfrac{1}{2}(c_2^\alpha + c_2^\beta) + \frac{f_{1m}v_1}{1 - \phi_m} \qquad (36)$$

$$\langle R_{22} \rangle = \frac{1}{K}\left(\frac{r_{12}}{v_1} + \frac{f_{2m}}{1 - \phi_m}\right)\frac{\ln(c_2^\alpha/c_2^\beta)}{c_2^\alpha - c_2^\beta} - r_{12}\frac{v_2}{v_1} \qquad (37)$$

$$\langle R_{12} \rangle = -r_{12} \qquad (38)$$

The merit of eq 36–38 is that by measuring $\langle R_{11}\rangle$, $\langle R_{22}\rangle$, $\langle R_{12}\rangle$, and $(1 - \phi_m)$ the coefficients r_{12}, f_{1m}, f_{2m}, and K can be determined.

It turns out that $\langle R_{11}\rangle$ increases linearly with the average concentration $\frac{1}{2}(c_2{}^{\alpha} + c_2{}^{\beta})$ and that $\langle R_{22}\rangle$ decreases linearly in a rather good approximation with the reciprocal average concentration $2/(c_2{}^{\alpha} + c_2{}^{\beta})$. The latter can be seen by developing the concentration function in eq 37 which series expansion reduces to the desired form when $c_2{}^{\alpha} \simeq c_2{}^{\beta}$.[3,18] Under the assumptions adopted $\langle R_{12}\rangle$ must remain constant with respect to the average solute concentration. It must be noted, however, that without making any assumptions one can always evaluate $\langle r_{12}\rangle$ using eq 27. The assumptions made in the derivation of eq 36–38 are necessary to evaluate the remaining coefficients f_{1m}, f_{2m}, and K.

6. The Experimental Quantities

Experimentally we have observed the permeation of the successive solutes pentaerythritol ($C_5H_{12}O_4$; mol wt 136.15), mannitol ($C_6H_{14}O_6$; mol wt 182.17), sucrose ($C_{12}H_{22}O_{11}$; mol wt 342.30), and raffinose ($C_{18}H_{32}O_{16}$; mol wt 504.44) and the solvent water through a Vycor glass membrane at 25°C. Four experimental quantities have been determined: the filtration coefficient L_p, the solute permeability ω, and the reflection coefficients σ and σ'. They are defined by the experimental equations due to Staverman[14,19-21] and to Kedem and Katchalsky[18,22] as

$$J_2 = \omega\Delta\Pi + \bar{c}_2(1 - \sigma')J_v \qquad (39)$$

$$J_v = L_p(\Delta P - \sigma\Delta\Pi) \qquad (40)$$

where $\Delta\Pi$ represents the ideal osmotic pressure difference across the membrane given by

$$\Delta\Pi = -\Delta\mu_1{}^{c}/v_1 \qquad (41)$$

and $\bar{c}_2$ represents an effective concentration defined by[24,14]

$$\bar{c}_2 = \frac{1}{v_2 - (\Delta\mu_2{}^{c}/\Delta\mu_1{}^{c})v_1} \qquad (42)$$

However, to evaluate the coefficients $\langle R_{12}\rangle$, $\langle R_{11}\rangle$, and $\langle R_{22}\rangle$ only three experimental quantities L_p, ω, and σ are necessary because of the Onsager reciprocal relation $\sigma = \sigma'$. The latter equality has been verified experimentally for the systems mentioned above.[23,33]

By confronting eq 39 and 40 with the set (25) using eq 41 and 42 we can express the resistance coefficients in terms of the experimental quantities. This yields

$$\langle R_{12}\rangle = \frac{v_1 v_2}{l L_p} - \frac{(1 - \sigma)\{1 - (1 - \sigma)\bar{c}_2 v_2\}v_1}{l\omega} \qquad (43)$$

$$\langle R_{11}\rangle = \frac{v_1{}^2}{l L_p} + \frac{(1 - \sigma)^2\bar{c}_2 v_1{}^2}{l\omega} \qquad (44)$$

$$\langle R_{22}\rangle = \frac{v_2{}^2}{l L_p} + \frac{\{1 - (1 - \sigma)\bar{c}_2 v_2\}^2}{l\omega\bar{c}_2} \qquad (45)$$

As is seen from eq 43–45 the determination of the resistance coefficients involves, besides the measurement of σ, L_p, and ω, the measurement of the partial molar volumes of the solute and the solvent and the geometry of the membrane. The practical data of the coefficients $\langle R_{ik}\rangle$ for mannitol as solute have been compiled in Figure 1. (Additional figures for the three remaining solutes are available on microfilm.) They were obtained from experiments where the ratio $c_2{}^{\alpha}/c_2{}^{\beta}$ was about 2.5 and the volume flows J_v were very small.
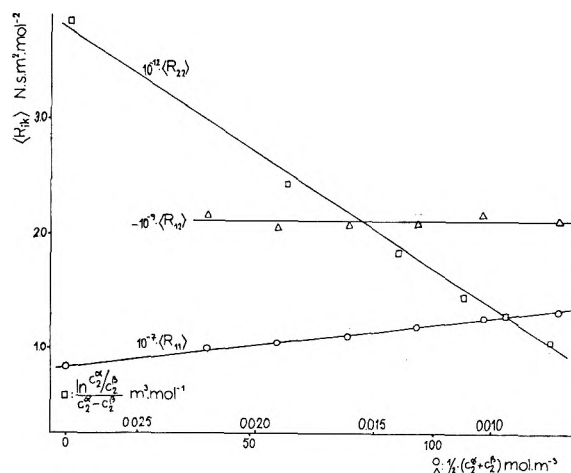
mannitol

Figure 1. Resistance coefficients as a function of external concentrations in the case of mannitol as solute, water as solvent, and porous glass as a membrane at 25°C.

7. Experimental Section

Measurements have been performed with an improved version[25] of an osmometer described earlier.[26] This full glass osmometer consists of an α compartment (20 × 10⁻⁶ m³) and a β compartment (250 × 10⁻⁶ m³) separated by a porous glass membrane (Vycor, Corning Glass Works, Corning, N.Y.). In both compartments a stirring mechanism is present. Leaky joints frequently met in osmometers with clamped membranes have been excluded here, as the membrane was fused to the α compartment. The porous glass phase consists of about 96% silica glass[27] with a pore radius which proved to be 20–30 × 10⁻¹⁰ m. The geometry of the membrane has been determined with a cathetometer and by measuring the upward force in a submersion experiment. The values found for the different membranes do not vary much. The membrane surface is about 25 × 10⁻⁴ m, the membrane thickness l about 1.4 × 10⁻³ m. For detailed data we refer to the literature cited.[25] The water content of the membrane has been measured by weighing it in the wet state as well as in the dry state. From this the pore volume fraction $(1 - \phi_m)$ has been calculated for a membrane containing only water (Tables I and II). It is supposed that this pore volume fraction remains unchanged in case a dilute solution is introduced in the membrane. The pore volume fraction defined in this way need not be identical with a pore volume fraction determined in an inert gas. The partial molar volumes v_1 and v_2 have been evaluated from density data obtained by pycnometry. By means of regulating manostats the pressure difference between the two osmometer compartments could be varied from 0 to 80 × 10⁻² m water or from 0 to 76 × 10⁻² mHg. The resulting flow J_v has been measured by following the descending meniscus in a capillary with a calibrated uniform diameter and connected to the α compartment. At the beginning and the end of each experiment the concentrations $c_2{}^{\alpha}$ and $c_2{}^{\beta}$ were analyzed with a Rayleigh interferometer (Zeiss). Moreover, the concentration $c_2{}^{\beta}$ could be followed continuously during the experiments by circulating the solution in the β compartment through a differential refractometer (Waters R4).

The transport phenomena were studied by two types of

TABLE I: Friction Coefficients f_{ik} (N sec m^{-1} mol^{-1}) and the Partition Coefficient K in the Glass Membrane at 25°C

Solute/ membrane	$1 - \phi_m$	$10^{-13}\, f_{21}$	$10^{-13}\, f_{2m}$	$10^{-11}\, f_{1m}$	$10^{-11}\, f_{12}$, c_2 in 10 or 50 mol m^{-3}		K
					10	50	
Pentaerythritol/M4	0.352	2.71	0.36	1.22	0.14	0.70	1.03
Mannitol/M5	0.309	3.61	0.26	1.44	0.21	1.06	0.92
Sucrose/M5	0.324	5.40	1.50	1.33	0.30	1.51	1.06
Raffinose/M6	0.288	5.85	2.67	1.25	0.37	1.85	1.02

TABLE II: Friction Coefficients r_{12} and r_{12}^f (N sec m^2 mol^{-2}) Successively in the Glass Membrane and in Free Solution at 25°C

Solute/ membrane	$1 - \phi_m$	$10^{-9}\, r_{12}$	$10^{-7}\, r_{12}^f$	$\dfrac{r_{12}^f/r_{12}}{(1 - \phi_m)} = \theta^2$
Pentaerythritol/M4	0.352	1.39	5.89	0.12
Mannitol/M5	0.309	2.11	6.72	0.10
Sucrose/M5	0.324	3.01	8.57	0.09
Raffinose/M6	0.288	3.67	10.28	0.10
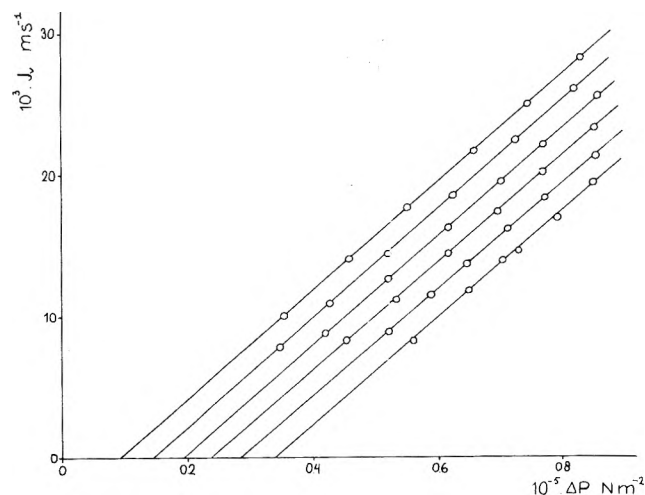
Figure 2. The dynamic measurement of the experimental osmotic pressure $\sigma\Delta\Pi$ in an an osmotic experiment with various solutions of mannitol in water and a glass membrane. The intersections with the ΔP axis represent the value of $\sigma\Delta\Pi$.

measurements: the dynamic experiment and the relaxation experiment. In the dynamic experiments a rather constant solute concentration difference between both compartments could be maintained over a period of about 4 hr due to the slowness of the transport process and the relatively large osmometer compartments. By varying ΔP and measuring the corresponding J_v, perfect linear relations have been found between J_v and ΔP according to eq 40, as shown in Figure 2 for mannitol as solute. From the slopes and intercepts the reflection coefficients σ and the filtration coefficient L_p have been calculated. In the relaxation experiments the system was subjected for about 30 hr to a hydrostatic pressure difference approximately equal to $\sigma\Delta\Pi$. In this manner the resulting volume flow J_v was kept

practically equal to zero. By analyzing the composition of the solution in both osmometer compartments at the beginning and at the end of the experiment the solute permeability ω has been measured on the base of eq 39 specified to the case $J_v = 0$. The procedure described above and detailed numerical data have been presented elsewhere.[25]

8. Results and Interpretation

The discussion of the results centers around the application of eq 36, 37, and 38. From these equations one expects linear graphs when the coefficients $\langle R_{ik}\rangle$ are plotted against the appropriate concentration functions and the assumption of constant friction and partition coefficients is true. This expectation is confirmed by the experimental results shown. From the slopes and intercepts of the lines r_{12}, f_{1m}, f_{2m}, and K have been calculated. One can immediately conclude from eq 38 and the figures that r_{12} is constant with respect to external concentrations. The constancy of r_{12} and the linearity of the graph of $\langle R_{11}\rangle$ vs. $\frac{1}{2}(c_2^\alpha + c_2^\beta)$ implies a constancy of f_{1m} and K. Finally, the constancy of f_{2m} is reflected by the linear plot of $\langle R_{22}\rangle$ vs. $(\ln c_2^\alpha/c_2^\beta)/(c_2^\alpha - c_2^\beta)$. A general view of the friction and partition coefficients present in the system has been given in Table I. From the coefficient r_{12} two friction coefficients f_{21} and f_{12} have been derived, successively equal to $r_{21}c_1$ and $r_{12}c_2$. The solvent concentration c_1 being nearly constant in the membrane has been approximated by $(1 - \phi_m)/v_1$, whereas for the solute concentration c_2, having a gradient in the membrane, two representative values have been chosen.

From Table I the following conclusions may be drawn. (a) $f_{21} > f_{2m}$. One mole of the solute (2) undergoes more friction from the solvent (1) than from the membrane species (m) during permeation. Both friction coefficients increase with larger molecular weight of the solute. (b) $f_{2m} \gg f_{1m}$. The membrane exerts more friction on 1 mol of the solute (2) than on 1 mol of the solvent (1). In the sequence mannitol, sucrose, and raffinose this effect is stronger as the molecular weight increases. The relative large value of f_{2m} in the case of pentaerythritol might be an indication of adsorption of this solute. However, a significantly higher value of K has not been found. (c) $f_{1m} > \simeq f_{12}$. In the concentration range used 1 mol of the solvent (1) undergoes friction from the membrane (m) which is of the order or larger than the friction from the solute (2). The influence of the solute becomes larger according as its molecular weight and its concentration increase. (d) The discrepancies between the different f_{1m} values can be reduced by considering f_{1m}/ϕ_m, by which the influence of the different concentrations c_m is eliminated. The remaining discrepancies must be ascribed to differences in the average pore radius. (e) The partition coefficients turned out to be about unity. The standard deviations, about 5%, make a conclusion concerning the occurrence of adsorption ($K > 1$) or depletion ($K < 1$) difficult. Nevertheless, the fact that the values of K center around unity indicates that the membrane is chemically inert. In the case of mannitol we have performed another independent measurement of K by equilibrating the membrane in contact with a solution containing radioactive tracers of this solute. This static procedure yields a value of 0.98 for K in conformity with the value found from the dynamic measurements mentioned in Table I. The main aspect emerging especially from conclusion e is that we are dealing with membranes showing a neutral behavior ($K = 1$) with respect to the solute molecules despite the fact that their small pore dimensions

might enhance interactions of the membrane matrix with these molecules.

In order to get a more complete picture it is worth drawing the coefficient r_{12}^f found in free solution into our consideration and comparing it with the coefficient r_{12} found within the membrane. It has been pointed out[3] that when $K = 1$ the ratio r_{12}^f/r_{12} turns out to be a purely geometrical factor which is independent of the solute chosen, but does depend on the porosity of the membrane $(1 - \phi_m)$ and the tortuosity of the channels inside it. In the case considered we may write

$$r_{12}^f = (1 - \phi_m)\theta^2 r_{12} \qquad (46)$$

where θ represents the so-called tortuosity factor.

In Table II the data for the coefficients r_{12} and r_{12}^f have been compiled. These coefficients are calculated from the mutual diffusion coefficient in free solution.[28-31] The last column of Table II shows a reasonable constant value for the different solutes in agreement with eq 46 and demonstrating the chemical inertness of the membrane. The deviation found in the case of pentaerythritol might be a corollary of an adsorption phenomenon reflected by a relative high value of f_{2m}, although such a significant conclusion cannot be drawn from the value of K in this case.

Inspection of Table II shows that values of θ have been found in the range of 0.30–0.36, whereas for comparable but not identical porous glass species values in the range 0.39–0.42 have been reported[32] using an expression for Knudsen flow of a gas. Debye and Cleland[34] predict a value of θ equal to 0.5 for a porous system with random oriented pore segments.

Clearly the fact that permeation behavior of four different solutes leads to values of K centering around unity as well as to relatively constant values of θ^2 suggests that the friction between solute and solvent is not remarkably influenced by chemical factors in the glass membranes discussed here and does not differ in this respect with the corresponding friction found in free solution.

Symbols

c_i	concentration of species i in the membrane, mol m^{-3}
c_2', c_2''	concentrations of the solute (2) in the membrane at the boundaries $x = 0^{(\prime)}$ and $x = l^{(\prime\prime)}$, mole m^{-3}
c_2^α, c_2^β	concentrations of the solute (2) in the stirred bathing solutions facing the membrane at $x = 0(\alpha)$ and $x = l(\beta)$, mol m^{-3}
$\bar{c}_2$	concentration of the solute averaged according to eq 42 over c_2^α and c_2^β, mol m^{-3}
F_i	external force exerted on a mole of species i, N mol^{-1}
f_{ik}	friction coefficient coupling the driving force $F_i - \nabla\mu_i$ with the relative velocity $u_i - u_k$, N sec m^{-1} mol^{-1}
J_i	flux of species i equal to $c_i u_i$, mol m^{-2} sec^{-1}
J_v	total volume flow per unit area of the membrane, m sec^{-1}
K	partition coefficient relating c_2' to c_2^α and c_2'' to c_2^β according to eq 33
l	thickness of the membrane, m
L_p	filtration coefficient, N^{-1} m^3 sec^{-1}
P	pressure, N m^{-2}
R	universal gas constant, N m mol^{-1} K^{-1}

R_{ik}	resistance coefficient coupling the driving force $F_i - \nabla\mu_i$ to the flux J_k, N m^2 sec mol^{-2}
r_{ik}	friction coefficient coupling the driving force $F_i - \nabla\mu_i$ to the diffusional flow $c_k(u_i - u_k)$, N m^2 sec mol^{-2}
r_{ik}^f	the corresponding friction coefficient r_{ik} in free solution
T	absolute temperature, K
u_i	local velocity of species i, m sec^{-1}
u^a	arbitrary local velocity, m sec^{-1}
v_i	partial molar volume of species i, m^3 mol^{-1}
x	transport direction normal to the membrane, m
z	reciprocal characteristic diffusion length defined by eq 30, m^{-1}
γ_2', γ_2''	activity coefficients referring to the solute (2) at $x = 0^{(\prime)}$ and $x = l^{(\prime\prime)}$ in the membrane
ϕ_i	volume fraction of species i
μ_i	chemical potential of species i, N m mol^{-1}
μ_i^c	concentration dependent part of μ_i, N m mol^{-1}
ω	solute permeability, N^{-1} sec^{-1} mol
Π	osmotic pressure, N m^{-2}
σ, σ'	reflection coefficients
σ_D	local entropy production, N m^{-2} sec^{-1} K^{-1}
θ	tortuosity factor

Operators

∇Q	local gradient of Q normal to the membrane: $\nabla Q = \partial Q(x)/\partial x$
ΔQ	difference of Q between the external phases: $\Delta Q = Q^\alpha - Q^\beta$
$\langle Q \rangle$	average of Q in the membrane: $\langle Q \rangle = 1/l \int_0^l Q(x)\,dx$

Indices

i,j,k	1,2, m in the ternary system: 1 refers to the solvent, 2 refers to the solute, m refers to the membrane species

References and Notes

(1) S. R. de Groot and P. Mazur. "Non-equilibrium Thermodynamics", North Holland Publishing Co., Amsterdam, 1962.
(2) D. C. Mikulecky and S. R. Caplan, *J. Phys. Chem.*, **70**, 3049 (1966).
(3) J. A. M. Smit, Thesis, Chapter 3, Leiden, 1970.
(4) R. L. Cleland, *Trans. Faraday Soc.*, **62**, 350 (1966).
(5) L. Onsager, *Ann. N.Y. Acad. Sci.*, **46**, 241 (1945).
(6) A. Z. Klemm, *Z. Naturforsch. A*, **8**, 397 (1953).
(7) R. Bearman and J. G. Kirkwood, *J. Chem. Phys.*, **28**, 136 (1958).
(8) R. W. Laity, *J. Phys. Chem.*, **63**, 80 (1959).
(9) K. S. Spiegler, *Trans. Faraday Soc.*, **54**, 1409 (1958).
(10) O. Kedem and A. Katchalsky, *J. Gen. Physiol.*, **45**, 143 (1961).
(11) I. W. Richardson, *J. Memb. Biol.*, **4**, 3 (1971).

(12) W. Dorst, A. J. C. Hoeve, and A. J. Staverman, *Trans. Faraday Soc.*, **59**, 2415 (1963).
(13) A. J. Staverman, C. A. Kruissink, and D. T. F. Pals, *Trans. Faraday Soc.*, **61**, 2805 (1965).
(14) A. J. Staverman, *J. Electroanal. Chem.*, **37**, 233 (1972).
(15) H. Schonert, *J. Phys. Chem.*, **73**, 62 (1969).
(16) C. Elata, *Desalination*, **6**, 1 (1969).
(17) J. G. Kirkwood in "Ion Transport across Membranes", H. T. Clarke, Ed., Academic Press, New York, N.Y., 1954.
(18) A. Katchalsky and P. F. Curran, "Non-equilibrium Thermodynamics in Biophysics", Harvard University Press, Cambridge, Mass., 1965, Chapter 10.
(19) A. J. Staverman, *Recl. Trav. Chim. Pays Bas*, **70**, 344 (1951).
(20) A. J. Staverman, *Recl. Trav. Chim. Pays Bas*, **71**, 176 (1952).
(21) A. J. Staverman, *Trans. Faraday Soc.*, **48**, 623 (1952).

(22) O. Kedem and A. Katchalsky, *Biochim. Biophys. Acta*, **27**, 229 (1958).
(23) J. A. M. Smit and A. J. Staverman, *J. Phys. Chem.*, **74**, 966 (1970).
(24) J. A. M. Smit, Thesis, Appendix I, Leiden, 1970.
(25) J. A. M. Smit, Thesis, Chapter 4, Leiden, 1970.
(26) J. L. Talen and A. J. Staverman, *Trans. Faraday Soc.*, **61**, 2794 (1965).
(27) M. E. J. Nordberg, *J. Am. Ceram. Soc.*, **27**, 299 (1944).
(28) F. J. Kelly, R. G. Mills, and J. M. Stokes, *J. Phys. Chem.*, **64**, 1448 (1960).
(29) P. J. Dunlop, *J. Phys. Chem.*, **69**, 4276 (1965).
(30) L. J. Gosting and M. S. Morris, *J. Am. Chem. Soc.*, **71**, 1998 (1949).
(31) P. J. Dunlop, *J. Phys. Chem.*, **60**, 1464 (1956).
(32) R. L. Cleland, J. K. Brinck, and R. K. Shaw, *J. Phys. Chem.*, **68**, 2779 (1964).
(33) J. A. M. Smit, Thesis, Chapter 5, Leiden, 1970.
(34) P. Debye and R. L. Cleland, *J. Appl. Phys.*, **30**, 84 (1959).

A Kinetic Study of the Rest Potential on a Platinum │Oxygen Diaphragm Electrode

James P. Hoare

Electrochemistry Department, Research Laboratories, General Motors Corporation, Warren, Michigan 48090
(Received February 27, 1975)

The rest potential of the front side of Pt foil diaphragm was recorded as a function of pH and P_{O_2} before and after the back side of the foil had been strongly anodized. The rest potential is a mixed potential and the local cell involved consists of the cathodic reduction of oxygen coupled with the anodic oxidation of the Pt. From an analysis of the kinetics of the proposed local cell model, calculated values for the coefficients, $\partial E/\partial$pH and $\partial E/\partial \log P_{O_2}$, were found to agree well with the experimentally determined values. An expression for the mixed potential (E_m) may be written as $E_m = E_m° - 0.048$ pH $+ 0.012 \log P_{O_2}$.

Introduction

For a number of years, a certain amount of controversy has existed[1] concerning the nature of the electrode reactions which determine the rest potential of a Pt electrode in contact with an oxygen-saturated, acid solution, although it is generally agreed[2-10] that this potential is a mixed potential.[11] It was proposed[1,5] that the local cell is composed of the cathodic reduction of O_2

$$O_2 + 4H^+ + 4e^- \rightleftarrows 2H_2O \qquad (1)$$

and the anodic oxidation of Pt

$$Pt + H_2O \rightleftarrows Pt\text{-}O + 2H^+ + 2e^- \qquad (2)$$
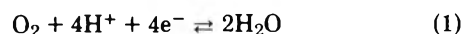
The direction of the local cell is such that a layer of adsorbed oxygen, Pt–O, is formed on the Pt surface. As pointed out by Wroblowa et al.,[7] the local cell action would cease to exist if the Pt surface became covered with the protective, conducting layer of Pt–O. Under these conditions, the rest potential would be determined solely by eq 1 and an open circuit potential of 1.229 V (the reversible O_2 potential) would be observed. This behavior is contrary to experimental observation, since the rest potential of a prereduced Pt│O_2 electrode is observed to reach values no higher than about 1.06 V in 2N H_2SO_4 solution (pH ~0) saturated with O_2 at $P_{O_2} = 1$.

To bring the mechanism in line with experimental fact requires a steady-state coverage of Pt–O which is less than a monolayer, and this requirement is met by the dissolution of adsorbed oxygen into the bulk metal. When the rate of formation of Pt–O by local cell action equals the rate of dissolution into the Pt lattice, a steady-state coverage of about 30% of a monolayer[12] and a rest potential value of 1.06 V are reached. The Pt lattice acts as a vast reservoir for dissolved oxygen. It was calculated[13] that it would require about 190,000 days to saturate 1 cm^3 of Pt (one face exposed to the anodic current) with dissolved oxygen at the experimentally determined[14,15] local cell current density of about 10^{-7} A/cm^2. Consequently, the rest potential appears to remain at the steady-state value indefinitely.

It has been found[12,13,16] that large amounts of dissolved oxygen can be obtained in Pt by strong anodization of the Pt electrode. When the back side of a Pt foil diaphragm, which was mounted between two halves of a two-compartmented Teflon cell, was anodized, it was observed[13] that the rest potential on the front side approached the reversible oxygen potential (within 50 mV). This behavior was explained as follows. Anodization of the back side of the Pt diaphragm nearly saturates the Pt lattice with dissolved oxygen. As a result, the rate of dissolution of dissolved oxygen, Pt–O, is greatly reduced and the Pt–O layer grows, approaching the value of a monolayer. The observed fact that the rest potential increases linearly with increasing coverage, θ, of the surface with adsorbed oxygen[12,14,17,18] accounts for the value of 1180 mV observed on the front side of the diaphragm.

The kinetics of the local cell reaction which determines the rest potential has never before been set down. It

seemed desirable to assume a specific mechanism for the cathodic and anodic processes making up the local cell. An equation for the potential is derived from which the coefficients for the dependence of pH and partial pressure of O_2, P_{O_2}, can be calculated. The calculated values of these coefficients are compared with the experimentally determined coefficients as a check on the validity of the assumed mechanism. This report is an account of such a procedure.

Theory

Consider the local cell diagram sketched in Figure 1a. The local cell polarization curves for the reduction of O_2 are represented by curves A_1 to A_3 for decreasing values of P_{O_2}. The Nernst equation for the reversible oxygen reaction may be written as

$$E = 1.229 - 0.059 \text{ pH} + 0.015 \log P_{O_2} \tag{3}$$

Curve B represents the polarization curve for the oxidation of Pt (eq 2) and is independent of P_{O_2}. Since the metal surface is an equipotential surface, the observed rest potential, which is a mixed potential, is the potential value where the B curve crosses the A curves. When P_{O_2} is 1 atm (curve A_1), the rest potential is the observed value of 1.06 V, the polarizing local cell current is 3.2×10^{-7} A/cm^2 [15] and θ is 0.3. The reversible potential for eq 2 was found[5] to be 0.88 V. From Figure 1a, the dependence of the mixed potential on P_{O_2} is about the same as that for the reversible oxygen potential. In the literature,[5,19,20] values for $\partial E / \partial \log P_{O_2}$ for a Pt|O_2 electrode at steady state range between 0.011 and 0.015 V.

The first step in the reduction of oxygen in acid solution at a Pt electrode is the adsorption of O_2 molecules from solution by dissociative adsorption[7,21,22] on the Pt surface.

$$O_2 \overset{k_1}{\underset{k_{-1}}{\rightleftharpoons}} 2O_{ads} \tag{4}$$

With the discharge of an electron, an adsorbed O^- ion is formed and it is this step that is considered to be the rate-determining step.

$$2O_{ads} + 2e^- \overset{k_2}{\rightarrow} 2O_{ads}^- \tag{5}$$
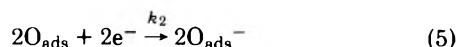
Following this rate-limiting step, the reaction with H^+ ions and the discharge of another electron complete the reduction of O_2 to H_2O.

$$2O_{ads}^- \overset{2H^+}{\rightleftharpoons} 2OH_{ads} \overset{2e^-}{\rightleftharpoons} 2OH_{ads}^- \overset{2H^+}{\rightleftharpoons} 2H_2O \tag{6}$$

The rate of the cathodic reaction, v_c, is

$$v_c = k_2(O_{ads}) e^{-\alpha(E - E_0^c)F/RT} \tag{7}$$

where α is the symmetry factor and E_0^c is the equilibrium potential of the O_2–H_2O reaction, eq 1. At steady state, the concentration of all intermediates is constant with time so that

$$\frac{\partial(O_{ads})}{\partial t} = 0 =$$

$$k_1(O_2) - k_2(O_{ads})^2 e^{-2\alpha(E - E_0^c)F/RT} - k_{-1}(O_{ads})^2 \tag{8}$$

From eq 8

$$(O_{ads})^2 = \frac{k_1(O_2)}{k_2 e^{-2\alpha(E - E_0^c)F/RT} + k_{-1}} \tag{9}$$
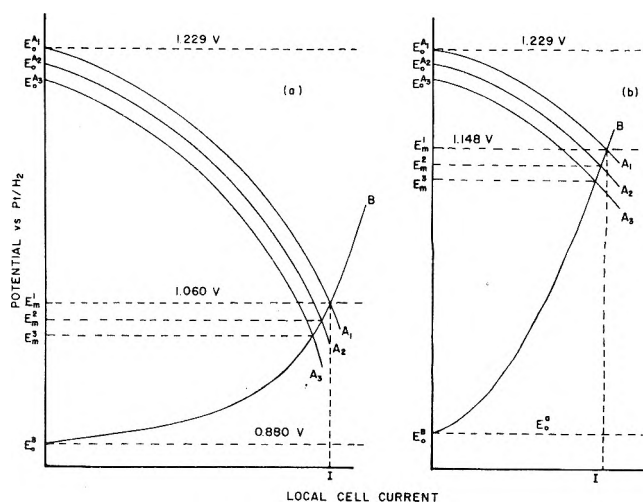
Figure 1. (a) A sketch of the local cell determining the rest potential at a Pt|O_2 electrode with curve B representing the polarization curve for the anodic oxidation of Pt and curves A_1 to A_3 those for the cathodic reduction of O_2 for decreasing values of P_{O_2}. Where the curves cross, one obtains the mixed potential (rest potential), E_m, and the corrosion current, I. (b) A sketch of the local cell determining the rest potential at a Pt–O alloy|O_2 electrode. The notation is the same as in (a).
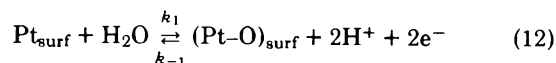
However $k_2 \ll k_{-1}$ so

$$(O_{ads}) = (k_1/k_{-1})^{1/2}(O_2)^{1/2} \tag{10}$$

Finally, after substitution of eq 10 into eq 7

$$v_c = k_2(k_1/k_{-1})^{1/2}(O_2)^{1/2} e^{-\alpha(E - E_0^c)F/RT} \tag{11}$$

Damjanovic and coworkers[7,21,22] found a square root relationship between P_{O_2} and (O_{ads}) as expressed by eq 10.

For the anodic reaction, "bare" Pt surface sites, Pt_{surf}, react with H_2O to produce adsorbed oxygen atoms, $(Pt-O)_{surf}$.

$$Pt_{surf} + H_2O \overset{k_1}{\underset{k_{-1}}{\rightleftharpoons}} (Pt-O)_{surf} + 2H^+ + 2e^- \tag{12}$$

Certain $(Pt-O)_{surf}$ sites can flip over by a place exchange mechanism[23] to form dermasorbed[24] oxygen, $(Pt-O)_{derm}$

$$(Pt-O)_{surf} \overset{k_2}{\rightarrow} (Pt-O)_{derm} \tag{13}$$
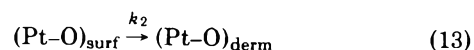
and it is this reaction that is considered to be rate determining. The dermasorbed oxygen can then migrate into the bulk metal as adsorbed oxygen, O_{abs}

$$(Pt-O)_{derm} \overset{k_3}{\underset{k_{-3}}{\rightleftharpoons}} Pt_{surf} + O_{abs} \tag{14}$$
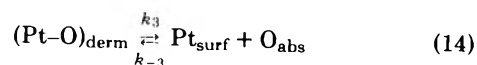
with the regeneration of Pt_{surf} sites which can react with H_2O again by eq 12 to maintain the local cell action.

The rate of the anodic reaction is

$$v_a = k_2(Pt-O)_{surf} \tag{15}$$

At steady state the rate of change of $(Pt-O)_{surf}$ with time is zero.

$$\frac{\partial(Pt-O)_{surf}}{\partial t} = 0 = k_1(Pt_{surf})(H_2O)e^{2(1-\alpha)(E - E_0^a)F/RT} -$$

$$k_2(Pt-O)_{surf} - k_{-1}(Pt-O)_{surf}(H^+)^2 e^{-2\alpha(E - E_0^a)F/RT} \tag{16}$$

where E_0^a is the equilibrium potential of the Pt|Pt–O reaction, eq 2. From eq 16, we obtain

$$(Pt-O)_{surf} = \frac{k_1(Pt_{surf})(H_2O)e^{2(1-\alpha)(E-E_0^a)F/RT}}{(k_2 + k_{-1})(H^+)^2 \, e^{-2\alpha(E-E_0^a)F/RT}} \quad (17)$$

By substituting eq 17 into eq 15 with the condition that $k_2 \ll k_1$, we find

$$v_a = \left(\frac{k_1 k_2}{k_{-1}}\right) \frac{(Pt_{surf})(H_2O)}{(H^+)^2} e^{2(E-E_0^a)F/RT} \quad (18)$$

When the local cell has reached steady state, E becomes the mixed potential, E_m, the activity of H_2O is unity, and the total cathodic current, I_c, equals the total anodic current, I_a, which equals the local cell current, I, in Figure 1a. In other words, the rate of the cathodic reaction equals that of the anodic reaction, $v_c = v_a$, since v and I are directly related. Consequently

$$K(O_2)^{1/2} e^{-\alpha(E_m-E_0^c)F/RT} = K' \frac{(Pt_{surf})}{(H^+)^2} e^{2(E_m-E_0^a)F/RT} \quad (19)$$

After rearranging

$$e^{-(2+\alpha)E_m F/RT} e^{(\alpha E_0^c + 2E_0^a)F/RT} = \frac{K''(Pt_{surf})}{(O_2)^{1/2}(H^+)^2} \quad (20)$$

and taking logarithms of both sides, we have

$$\alpha E_0^c + 2E_0^a - (2 + \alpha)E_m = \frac{2.3RT}{F} \log (Pt_{surf}) -$$

$$\frac{2.3RT}{F} \log (O_2)^{1/2} - \frac{2.3RT}{F} \log (H^+)^2 + \frac{2.3RT}{F} \log K'' \quad (21)$$

Then

$$\frac{\partial E_m}{\partial \log P_{O_2}} = (1/2) \frac{2.3RT}{F}\left(\frac{1}{2+\alpha}\right) = 0.012 \text{ V} \quad (22)$$

for $\alpha = 1/2$ and $T = 25°$. Similarly

$$\frac{\partial E_m}{\partial pH} = \frac{4.6RT}{F}\left(\frac{1}{2+\alpha}\right) = 0.048 \text{ V} \quad (23)$$

Note that the α appearing in eq 21 is the α_c associated with the cathodic reaction since α_a associated with the anodic reaction drops out of the expression for α_a (eq 18).

Experimental Section

A Pt foil (0.00127 cm thick, 2.03 cm^2 in area, and 99.99% pure) was prepared and clamped between the compartments of a clean Teflon cell as described earlier.[13] After the two compartments were filled with a 2 N H$_2$SO$_4$ solution, testing for leaks around or through the Pt diaphragm and purification of the electrolyte were carried out by procedures presented elsewhere.[13]

The partial pressure of O$_2$ was varied by mixing the streams of O$_2$ and N$_2$ (both purified in a multistaged purification train) in a long spiral of polypropylene tubing before entering the cell. The relative gas flows were determined with rotameters and the P_{O_2} of the exit gas from the cell was measured with the polarographic sensing unit of a Beckman oxygen analyzer. Because $\partial E/\partial \log P_{O_2}$ shifts from about 0.015 V at high values of P_{O_2} to 0.060 V at low values,[7,25,26] measurements were only made in the vicinity of 1 atm. This change from a 0.015-V slope to a 0.060-V slope may involve a change in mechanism of the O$_2$ electrode at low P_{O_2} or it may occur because of changes in the polarization of the local cell reduction of O$_2$ (p 36 of ref 1).

Since changes of a few thousandths of a volt must be measured at potentials over 1 V, the potential of a standard cell was used to buck the potential of the test cell so that a
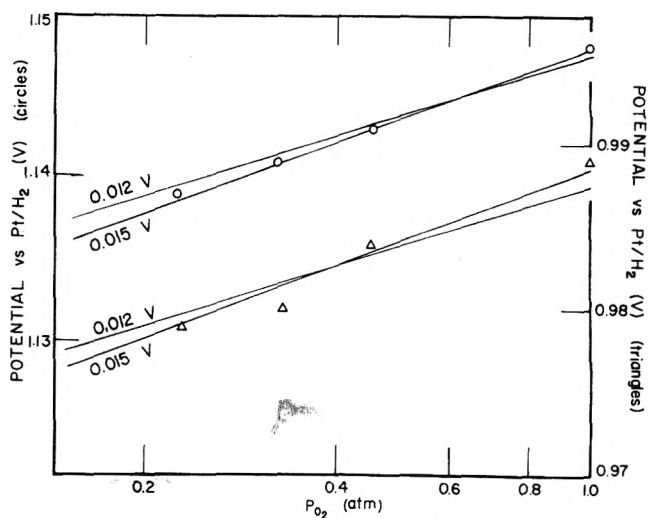

Figure 2. Plots of the rest potential at a Pt|O$_2$ (triangles) and a Pt-O alloy|O$_2$ (circles) electrode as a function of the log of P_{O_2}. Lines with slopes of 0.012 and 0.015 V are drawn through the data points to show that the data are consistent with 0.012 V $< \partial E/\partial \log P_{O_2} <$ 0.015 V for each electrode.

lower and more expanded scale could be used on the electrometer. A saturated calomel reference electrode (SCE) was used and the potential values are recorded with respect to a Pt|H$_2$ electrode in the same solution.

Measurements were made at three values of the pH according to the following procedure. After the potential on the front side of the Pt foil diaphragm was recorded in the O$_2$-stirred approximately 2 N H$_2$SO$_4$ solution, the O$_2$ was replaced with H$_2$ and the potential of the SCE was recorded against a Pt|H$_2$ gauze auxiliary electrode in the front compartment of the cell. The H$_2$ stirring was replaced with O$_2$ stirring until the potential of the Pt diaphragm had returned to the value before H$_2$ stirring was begun. Using a cleaned hypodermic syringe, exactly 6 ml of solution was removed from the front compartment through the gas exit tube and exactly 6 ml of triply distilled water was added. The total volume of solution in the compartment was 13.5 ml. When the rest potential of the front side of the Pt foil had come to a virtually steady value, this potential was recorded along with the potential of the SCE vs. Pt|H$_2$ as detailed above. By removing another 6 ml of solution and replacing with triply distilled water, a third pH measurement was obtained by repeating the above procedure. The pH of these three solutions was determined from pH-potential (SCE vs. Pt|H$_2$) tables.

Procedure and Results

With purified O$_2$ bubbling in the front compartment and purified N$_2$ bubbling in the back compartment, the rest potential of the front side of the Pt foil diaphragm was permitted to reach a steady value (after 16 hr). The P_{O_2} was varied by first lowering the P_{O_2} and then increasing it back to 1 atm. During two complete cycles of P_{O_2} variation the data were reproducible within ± 1 mV and are plotted in Figure 2 (triangles).

In the manner described before,[13] the back side of the Pt diaphragm was anodized (E_a = 2.05 V; i_a = 6.1 mA/cm^2) until the rest potential of the front side had risen to 1.148 V (after 2 days). Again, the P_{O_2} was varied and the data are presented in Figure 2 (circles). A Pt diaphragm which had been strongly anodized such as this one will be referred to as a Pt-O alloy diaphragm.
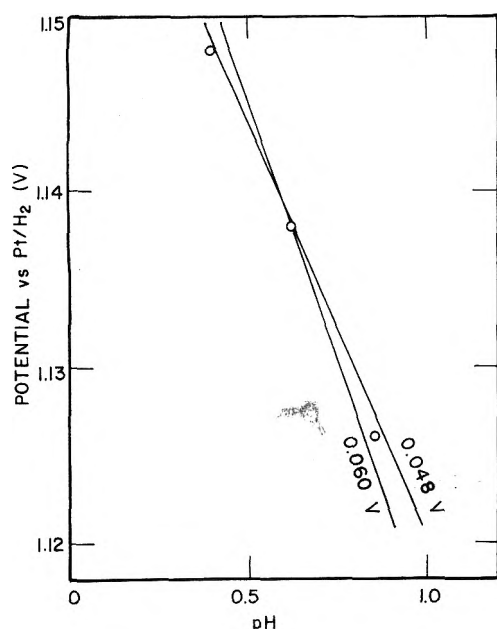
Figure 3. Plot of the rest potential of a Pt–O alloy | O_2 electrode as a function of pH. Lines with slopes of 0.048 and 0.050 V were drawn through the data points to show that the data are consistent with 0.048 V $< \partial E/\partial$ pH < 0.060 V.

A plot of the rest potential on the front side of the Pt–O alloy diaphragm as a function of pH for the three solutions studied is given in Figure 3.

Discussion

In Figure 2, lines with slopes of 0.012 and 0.015 V have been drawn through the points to show that the data are not really inconsistent with either value of $\partial E/\partial P_{O_2}$. If the value of α is less than 0.5, $\partial E/\partial P_{O_2}$ can have values between 0.012 and 0.015 V. The data in Figure 2 are in good agreement with the literature value of $\partial E/\partial P_{O_2}$,[5,19,20] which range between 0.011 and 0.015 V. Should equal confidence be placed on each data point for the Pt | O_2 electrode (triangles in Figure 2), the least-squares analysis of the data yields a value of 0.015 V for $\partial E/\partial P_{O_2}$ ($\sigma = 0.70$ mV).

Therefore, for a Pt | O_2 electrode at steady state in a given acid solution, the potential is determined by the local cell mechanism sketched in Figure 1a and eq 21 can account for the dependence of the rest potential on P_{O_2}.

When the data in (7) are analyzed, a value for $\partial E/\partial$ pH is found to be 0.052 V. This same value was also recorded[5] earlier and is in excellent agreement with eq 23 showing that eq 21 can also account for the dependence of the rest potential on a steady-state Pt | O_2 electrode.

As the Pt | O_2 electrode is converted to a Pt–O alloy | O_2 electrode by strong anodization of the back side of the Pt foil diaphragm,[13] the concentration of absorbed (dissolved) oxygen, O_{abs}, is increased. This action drives eq 14 to the left and increases the concentration of (Pt–O)$_{derm}$ sites with the consumption of Pt_{surf} sites. Because of the increase in (Pt–O)$_{derm}$ sites, the rate-determining step, eq 13, will be slowed down and the local cell current will be diminished. For given values of P_{O_2} and pH, eq 21 shows that E_m is inversely proportional to the log of Pt_{surf}, thus accounting for the increase in the rest potential as the Pt lattice is charged with dissolved oxygen (decrease in Pt_{surf}).

Experimentally, it was found that the local cell current (rate of oxygen dissolution) fell,[13] the coverage of the Pt

surface with (Pt–O)$_{surf}$ increased,[18] and the rest potential shifted to more noble values[13] as the Pt lattice was charged with dissolved oxygen. In this case, the local cell mechanism is sketched in Figure 1b. Here, $E_0{}^a$ for Pt–O alloy

$$PtOPt + H_2O \rightleftharpoons PtOPt{-}O + 2H^+ + 2e^- \qquad (24)$$
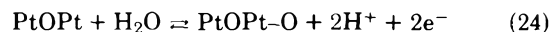
is most likely not the same as for eq 2 (0.880 V).

The Pt–O_2 system is said to be a local cell under anodic control (27, p 359 of ref 1).

From Figure 2 (circles) is is seen that the data for the dependence of the rest potential on a Pt–O alloy | O_2 electrode on P_{O_2} is consistent with a value of $\partial E/\partial$ log P_{O_2} ranging between 0.012 and 0.015 V. The least-squares analysis of these data yields a value of 0.0137 V. ($\sigma = 0.14$ mV). In Figure 3, lines having slopes of 0.048 and 0.060 V are drawn through the points. A least-squares analysis of these data gives a value for $\partial E/\partial$ pH of 0.047 V ($\sigma = 0.25$ mV). The good agreement between the experimental and the calculated values of the coefficients suggests that eq 21 can account for the dependence of the rest potential of a Pt–O alloy | O_2 electrode on both P_{O_2} and pH and for the shift in the rest potential toward more noble values as the Pt lattice is charged with dissolved oxygen.

If it were possible to saturate the Pt metal with dissolved oxygen, then all of the Pt_{surf} sites would be converted to (Pt–O)$_{derm}$ sites. Under these conditions the anodic reaction, eq 12, would cease, the local cell current would go to zero, and the surface would be covered with a complete layer of Pt–O. The only potential-determining reaction would be the O_2–H_2O reaction (eq 1) occurring on the conducting Pt–O layer, and the reversible O_2 potential (1.229 V) would be observed. Experimentally, the closest approach to this ideal situation was a Pt–O alloy diaphragm which reached a rest potential of 1.188 V. As noted before,[13] there is always some leakage of dissolved oxygen to the atmosphere from the exposed edges of the foil in the cell used in these investigations, thus preventing complete saturation of the lattice.

Since steady-state rest potentials on a Pt | O_2 electrode in acid solution lie between 1.0 and 1.06 V[1,5,7] and since they are determined by the local cell described in Figure 1 and by eq 21, oxygen must begin to dissolve in the Pt lattice in the potential range 1.0 V $< E_m < 1.06$ V as required for steady-state conditions. Although oxygen should not dissolve in Pt below 1.1 V as interpreted[28] from potential sweep traces and although one may associate certain intermediate stoichiometries for hydrated Pt–O as the Pt–O layer grows,[28] the fact remains from the data presented here that oxygen begins to dissolve in the Pt lattice when the potential reaches values 1.0 $< E_m < 1.06$ V.

Some evidence in favor of the mechanisms described by Figure 1 exists in the literature where Damjanovic and Brusic[20] measured $\partial E/\partial$ log P_{O_2} on freshly prepared (<1 hr in contact with O_2-saturated acid solution) and aged (17 hr in contact with O_2-saturated acid solution) Pt | O_2 electrodes. The fresh electrode exhibited a rest potential of 0.98 V and $\partial E/\partial$ log P_{O_2} of 0.06 V, whereas the aged electrode exhibited 1.03 V and <0.015 V, respectively. An explanation other than theirs may be made in the light of the work presented here. The freshly prepared Pt | O_2 electrode is not at steady state; and during the determination of the P_{O_2} measurements, the rest potential is drifting to more noble values, causing the value for $\partial E/\partial$ log P_{O_2} to be too high. After aging the Pt | O_2 electrode for 17 hr, a virtual steady-state condition is reached at 1.03 V, and the value

for $\partial E/\partial \log P_{O_2}$ can be determined without the drift error. In this case, the low value of slope is recorded.

It is interesting that Rand and Woods,[29] in a recent article, suggest that oxygen is not dissolved in Pt which had been preanodized at 1.23 V for about 14 hr because the traces obtained from triangular potential sweeps applied to the electrode were identical during the first ten cycles. On the contrary, such data provide excellent evidence that oxygen does dissolve in the Pt during anodization. As noted by these authors as well as by others,[30,31] the potential sweep traces obtained on prereduced Pt electrodes display large changes in shape between the first ten cycles of polarization. It is suggested here that it requires from five to ten cycles of polarization to build up the dermasorbed oxygen concentration in the surface layers of the Pt metal so that a stable, reproducible, steady-state surface can be generated. Certainly, anodization of Pt at 1.23 V for 14 hr will generate such a steady-state surface and no changes in the shape of the potential sweep traces would be expected in the first ten cycles of polarization.

In summary, it is concluded that the steady-state rest potential of a Pt|O_2 electrode is a mixed potential and the potential-determining process is a local cell composed of the cathodic reduction of O_2 (eq 1) and the anodic oxidation of Pt (eq 2). The mixed potential is determined by eq 21, which may be simplified to

$$E_m = E_m^\circ - 0.048 \text{ pH} + 0.012 \log P_{O_2}$$

At a Pt|O_2 bead electrode in 2 N H_2SO_4 solution stirred with purified O_2 at 1 atm, $E_m^\circ = 1.060$ V.[5] If the Pt lattice could be saturated with dissolved oxygen, the Pt surface would become covered with a conducting layer of Pt–O, the anodic oxidation of Pt would cease, the local cell process would disappear, and the rest potential would be the reversible O_2 potential determined solely by the O_2–H_2O reaction, eq 1. The reason why the reversible potential of 1.229 V cannot be observed on prereduced Pt electrodes is the fact that Pt is not inert in O_2-saturated electrolytes. The corrosion of Pt sets up a local cell and the rest potential is shifted from the reversible value. When the Pt surface is protected by a passive layer of conducting Pt–O or PtO_2,[18,19,32–35] the reversible potential is observed.

References and Notes

(1) J. P. Hoare, "The Electrochemistry of Oxygen", Interscience, New York, N.Y., 1968, pp 15–46.
(2) T. P. Hoar, *Proc. R. Soc., Ser. A*, **142**, 628 (1933).
(3) J. Giner, *Z. Elektrochem.*, **63**, 386 (1959).
(4) D. S. Gnanamuthu and J. V. Petrocelli, *J. Electrochem. Soc.*, **114**, 1036 (1967).
(5) J. P. Hoare, *J. Electrochem. Soc.*, **109**, 858 (1962).
(6) D. Winkelmann, *Z. Elektrochem.*, **60**, 731 (1956).
(7) H. Wroblowa, M. L. B. Rao, A. Damjanovic, and J. O'M. Bockris, *J. Electroanal. Chem.*, **15**, 139 (1967).
(8) V. I. Nesterova and A. N. Frumkin, *Zh. Fiz. Khim.*, **26**, 1178 (1952).
(9) A. J. Appleby, *J. Electrochem. Soc.*, **117**, 328, 641 (1970).
(10) R. Kh. Burshtein, M. R. Tarasevich, and V. A. Bogdanovskaya, *Elektrokhimya*, **8**, 1542 (1972).
(11) C. Wagner and W. Traud, *Z. Elektrochem.*, **44**, 391 (1938).
(12) R. Thacker and J. P. Hoare, *J. Electroanal. Chem.*, **30**, 1 (1971).
(13) J. P. Hoare, *J. Electrochem. Soc.*, **121**, 872 (1974).
(14) K. J. Vetter and D. Berndt, *Z. Elektrochem.*, **62**, 378 (1958).
(15) J. P. Hoare, *J. Electrochem. Soc.*, **112**, 602 (1965).
(16) J. P. Hoare, *J. Electrochem. Soc.*, **116**, 612 1390 (1969).
(17) W. Bold and M. W. Breiter, *Electrochim. Acta*, **5**, 145 (1961).
(18) J. P. Hoare, R. Thacker, and C. R. Wiese, *J. Electroanal. Chem.*, **30**, 15 (1971).
(19) J. O'M. Bockris and A. K. M. S. Huq, *Proc. R. Soc., Ser. A*, **237**, 277 (1956).
(20) A. Damjanovic and V. Brusic, *J. Electroanal. Chem.*, **22**, Appendix 1 (1969).
(21) M. L. B. Rao, A. Damjanovic, and J. O'M. Bockris, *J. Phys. Chem.*, **67**, 2508 (1963).
(22) A. Damjanovic, M. L. B. Rao, and M. Genshaw, ASTIA Report No. AD-405675, Nov 1962.
(23) N. Sato and M. Cohen, *J. Electrochem. Soc.*, **111**, 512 (1964); B. E. Conway and S. Gottesfeld, *J. Chem. Soc., Faraday Trans. 1*, **69**, 1090 (1973).
(24) S. Schuldiner and T. B. Warner, *J. Electrochem. Soc.*, **112**, 212, 853 (1965).
(25) M. A. V. Devenathan and M. L. B. Rao, ASTIA Report No. AD-291763, Nov 1962.
(26) S. Schuldiner, T. B. Warner, and B. J. Piersma, *J. Electrochem. Soc.*, **113**, 573 (1966); **110**, 1142 (1963).
(27) U. R. Evans, "The Corrosion and Oxidation of Metals", Arnold, London, 1960, p 875.
(28) H. Angerstein-Kozlowska, B. E. Conway, and W. B. A. Sharp, *J. Electroanal. Chem.*, **43**, 9 (1973).
(29) D. A. J. Rand and R. Woods, *J. Electroanal. Chem.*, **47**, 353 (1973).
(30) M. W. Breiter, *J. Electroanal. Chem.*, **8**, 230 (1964).
(31) W. G. French and T. Kuwana, *J. Phys. Chem.*, **68**, 1279 (1964).
(32) J. P. Hoare, *J. Electrochem. Soc.*, **110**, 1019 (1963); **112**, 849 (1965).
(33) N. Watanabe and M. A. Devnathan, *J. Electrochem. Soc.*, **111**, 613 (1964).
(34) G. Bianchi, F. Mazza, and T. Mussini, *Electrochim. Acta*, **11**, 1509 (1966).
(35) R. Kh. Burshtein, M. R. Tarasevich, and V. A. Bogdanovskaya, *Elektrokhimya*, **8**, 1542 (1972).

Density, Viscosity, and Conductance of Molten Ca(NO₃)₂·3.99H₂O–KCNS Systems

N. Islam* and Ismail K

Department of Chemistry, Aligarh Muslim University, Aligarh, 202001, India (Received February 25, 1975)

Density, viscosity, and conductance measurements of molten $Ca(NO_3)_2$·3.99H₂O and its mixtures with KCNS were made as functions of temperature and composition. Densities were least-square fitted to an equation of the form, $\rho = a - bt(°C)$. Fluidity, ϕ, and equivalent conductance, Λ, data were fitted to the equations, $Y(\phi,\Lambda) = A_{\phi,\Lambda} T^{-1/2} \exp[-k_{\phi,\Lambda}/(T - T_{0,\phi,\Lambda})]$ and $Y(\phi,\Lambda) = A_{\phi,\Lambda}' \exp[-B_{\phi,\Lambda}'/(V - V_{0,\phi,\Lambda})]$ based on the free volume model. $A_{\phi,\Lambda}$, $k_{\phi,\Lambda}$, $T_{0,\phi,\Lambda}$, $A_{\phi,\Lambda}'$, $B_{\phi,\Lambda}'$, and $V_{0,\phi,\Lambda}$ are empirical parameters. Almost identical values of $V_{0,\phi}$ and $V_{0,\Lambda}$, as well as those of $T_{0,\phi}$ and $T_{0,\Lambda}$ were found. Composition dependences of the empirical parameters have been discussed. The molal volume, V_m, and intrinsic volume, V_0, were found to be additive in nature. The glass transition temperature, T_0, has been found to increase linearly with composition. The ratio of the activation energies, E_ϕ/E_Λ, has been found as 1.26 ± 0.03. The low values of the product of the ratio of critical void volume, v^*, to average molecular (ionic) volume, $\bar{v}_m$, and a geometric factor, γ, $\gamma v^*/\bar{v}_m$ viz., 0.31 and 0.25 obtained from fluidity and conductance data, respectively, both in the cases of $Ca(NO_3)_2$·3.99H₂O ($\alpha = 4.6 \times 10^{-4}$) and its mixtures with KCNS ($\alpha = 4.5 \times 10^{-4}$), indicate that a random distribution of free volume is apparently not obtained in molten salts.

Introduction

Hydrated melts allow the exploration of their properties at relatively lower temperatures than those in the corresponding anhydrous melts. A direct consequence of these low liquidus temperatures is that the temperature dependence of the transport properties of various hydrated melts,[1-4] e.g., $Ca(NO_3)_2$·4H₂O, $Mg(NO_3)_2$·4H₂O, $Na_2S_2O_3$·5H₂O, $Ca(NO_3)_2$·4H₂O–$Cd(NO_3)_2$·4H₂O, $Ca(NO_3)_2$·4H₂O–KNO_3, is non-Arrhenius and is well described by an equation of the form

$$Y(\phi,\Lambda) = A_{\phi,\Lambda} T^{-1/2} \exp[-k_{\phi,\Lambda}/(T - T_0)] \qquad (1)$$

where Y is equivalent conductance, Λ, or fluidity, ϕ; A and k are constants characteristic of the transport process and the chemical system. T_0, on the other hand, is a constant of the chemical system alone provided the external pressure is held constant. Equation 1 may be derived from theories which take the free volume or the configurational entropy as the important quantity in setting the temperature dependence of the liquid transport properties. T_0 has been called the "zero mobility" or "ideal glass transition" temperature at the specified composition and interpreted as the temperature below which no further changes in internal energy by means of rearrangements of particles into configurations of lower potential energy are possible. In most cases where the glass transition can be observed as an experimental phenomenon the transition temperature, T_g, is found to lie slightly above T_0. Empirically it is found that the non-Arrhenius behavior implicit in eq 1 is observed in the temperature interval T_0 to $2T_0$.

Doolittle[5] suggested empirically an exponential relation of the form

$$\phi = A_1 \exp[-B_1 v_0/v_f] \qquad (2)$$

for the dependence of viscosities of normal alkanes on free volume. A_1 and B_1 are the empirical constants. The free volume was defined as $v_f = v - v_0$, where v is the specific volume of the liquid at any temperature and v_0 is the specific volume of liquid extrapolated to absolute zero without change of phase. Later Cohen and Turnbull[6] derived theoretically such an equation based on a "hard-sphere" model. Recently Doolittle's expression was found to hold well in glass-forming anhydrous melts[7] also. An attempt has been made here to apply Doolittle's expression to aqueous melts of calcium nitrate tetrahydrate. However, in doing so the expression has been modified to

$$Y(\phi,\Lambda) = A_{\phi,\Lambda}' \exp[-B_{\phi,\Lambda}'/(V - V_0)] \qquad (3)$$

in which A' and B' are empirical parameters, V is the molal volume at any temperature, and V_0 is the intrinsic volume or the molal volume at T_0.

The hydrated cation of fixed stoichiometry with larger effective size is taken as a fundamental component in hydrated melts and also in their solutions with salts having cations of low charge/radius ratios as evidenced by spectral,[8,9] conductance,[1,4] and density[10] studies. However, many measurements,[11,12] especially those in which the water concentration is an independent variable, show such an assumption to be untenable. For example, kinetically, there is no stoichiometry such that the transference number of water relative to calcium ion is zero. Similarly, the formation of associated species suggest a competition between hydration and ion association rather than a fixed stoichiometry.

Density, viscosity, and conductance measurements of binary solutions of molten calcium nitrate tetrahydrate and potassium thiocyanate are made. The applicability of the above models (eq 1 and 3) has been examined, and the significance of the computed parameters emphasized.

Experimental Section

Commercial calcium nitrate tetrahydrate (BDH) was used as solvent in the molten state. Potassium thiocyanate (BDH) was recrystallized twice from double-distilled water.

Several samples of $Ca(NO_3)_2$·4H₂O–KCNS were prepared at ~60°. $Ca(NO_3)_2$·4H₂O was found to dissolve up to ~65 mol % of KCNS.

All measurements were performed in a manner as described earlier[13] except for the differences in the dimen-

sions of the viscometer (6.26 cSt/sec) and conductivity cell $(0.76027 \text{ cm}^{-1})$.

Results

No reaction has been found to occur between KCNS and molten calcium nitrate tetrahydrate unlike those in the molten KNO_3–$NaNO_3$ system.[14]

The measured densities of calcium nitrate tetrahydrate at 25° are found to be 0.012 and 0.14% higher than those reported by Ewing and Mikovsky[15] and Moynihan,[2] respectively. On the basis of the density comparison, the actual H_2O/Ca mole ratio has been corrected to 3.99 ± 0.01. Density data for each melt were least-squares fitted to a linear function of the form $\rho = a - bt(°C)$, and the molal volumes, V_m, along with thermal expansivities, α, were computed (Table I).

The measured viscosities and conductances of pure $Ca(NO_3)_2 \cdot 3.99H_2O$ at 40° differ by ~8–10% when compared (Figure 1)[16] with those reported by Moynihan[2] for $Ca(NO_3)_2 \cdot 4.04H_2O$. This may be attributed to a difference in the water content in the two cases. A 2% difference in our results for every 0.01 change in the H_2O/Ca ratio is consistent with those of Moynihan et al.[3]

The molal volume of pure KCNS at 50° has been obtained as 57.5 cm^3/mol by the extrapolation of molal volume isotherm and this almost coincides with that calculated from its density data,[17] viz., 57.25 cm^3/mol. The viscosity has been found to increase slightly from 0 to 20 mol % KCNS and then increases linearly with composition. However, no such regularity has been found in the case of the conductance isotherm. The additive nature of fluidity and conductance data could not be estimated accurately because it involves a 100°K extrapolation of literature data[17] for pure KCNS to lower temperatures.

The conductance and fluidity data (Table II)[16] show non-Arrhenius behavior and are therefore least-squares fitted to eq 1. The empirical parameters along with the standard deviations in ln Λ and ln ϕ are given in Table III. The

linear plots (Figure 2) of log $\Lambda T^{1/2}$ and log $\phi T^{1/2}$ vs. $[1/(T - T_0)]$ also signify the applicability of eq 1 based on the free volume model in explaining the transport behaviors in molten $Ca(NO_3)_2 \cdot 3.99H_2O$–KCNS systems.

The conventional activation energies, E_Λ and E_ϕ, were computed from the corresponding derivatives and their corrected values were obtained (Table IV)[16] as $E_{corr} = E_{\Lambda,\phi} + (1/2)RT$.

Further, values of Λ and ϕ plotted (Figure 3) against those of $(V - V_0)$ tend to be nonlinear signifying the inability of the Hildebrand[18] equation, $Y(\Lambda,\phi) = B(V - V_0)/V_0$, to explain the transport behavior in the present system. However, linear plots (Figure 4) of log Λ and log ϕ vs. $[1/(V - V_0)]$ demonstrate a better fit of these data (Table V) to eq 3.

Discussion

The parameters A, k, and T_0 do not vary significantly with composition unlike those expected. There are a number of A–k–T_0 sets which may adequately describe the results. As an example, the fluidity data for X_{KCNS} (mole fraction) = 0.2 may be fitted to eq 1 with a standard deviation of 0.0165 in ln ϕ, i.e., twice that for the best fit for $T_{0,\phi}$ anywhere in the range 206.6–209.0. The corresponding ranges in A_ϕ and k_ϕ are 8845–7917 and 676–648, respectively. It appears likewise, from this example, that the parameter T_0 is the one most precisely determined by the curve fitting procedure and that small variations in it will produce much larger variations in A and k. Consequently, one does not expect a large composition dependence of T_0 while no meaningful trends are apparent in the composition dependences of A and k terms.

Recently Angell and Brassel[19] considered k as nearly constant multiples of T_0 in aqueous melts of calcium nitrate tetrahydrate and substituted DT_0 for k in eq 1 where D is independent of composition. However, such a variation in k with composition has not been observed in the present case. This has been supported by an empirical rule[1,4,20] which states that the k term is composition independent for systems in which the composition changes do not alter the melt structure in too radical a fashion as found in a large variety of fused nitrates and chlorides and concentrated aqueous solutions.

Therefore, the parameters A and T_0 were computed by using almost constant values of k by the method adopted by Moynihan et al.[3] The standard deviations for the fits with equal k terms are slightly larger than the best fit standard deviations (Table VI).[16] However, such a fit gives $T_{0,\phi}$ values approximately equal to $T_{0,\Lambda}$ values within ±2° as expected. A gradual increase in A and T_0 values with composition has been observed (Table III).

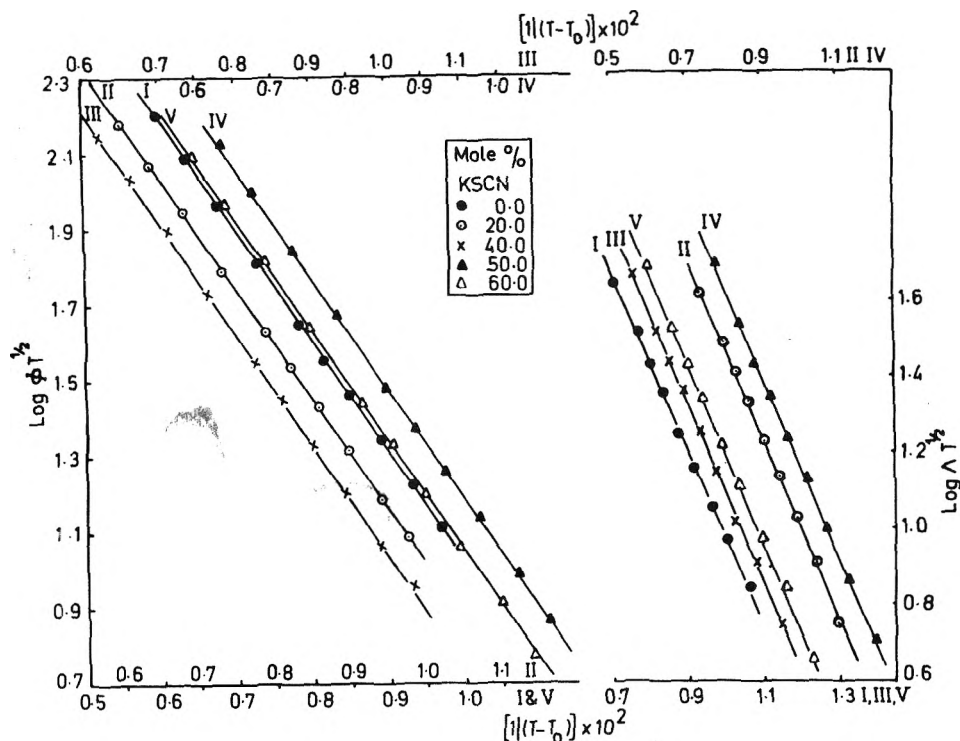A constant value for k is also expected in the light of

TABLE I: Densities, Molal Volumes, and Expansivities for $Ca(NO_3)_2 \cdot 3.99H_2O$–KSCN Melts[a]

Cation fraction Ca^{2+}	a	$10^3 b$	V_m at 50°, cm^3/mol	$10^4 \alpha$ at 50°, deg^{-1}
1.000	1.7694	0.80853	136.863	4.6763
0.800	1.7627	0.78832	120.941	4.5743
0.600	1.7592	0.78733	105.019	4.5778
0.500	1.7570	0.78662	97.057	4.5795
0.400	1.7543	0.78570	89.096	4.5811

[a] The density equation is $\rho(g/cm^3) = a - bt(°C)$.

TABLE III: Parameters for Eq 1 for the Fluidity and Electrical Conductance of $Ca(NO_3)_2 \cdot 3.99H_2O$–KSCN Melts Selected to Give Almost Constant k_ϕ and k_Λ Values

Cation fraction K^+	A_ϕ	k_ϕ	$T_{0,\phi}$	Std dev in ln ϕ	A_Λ	k_Λ	$T_{0,\Lambda}$	Std dev in ln Λ
0.0	8579.9	671.16	205.50	0.00919	2120.1	542.53	203.40	0.0308
0.2	8684.4	673.38	206.51	0.00887	2406.2	547.69	206.98	0.0163
0.4	9360.0	676.50	211.74	0.00817	2912.1	545.00	210.60	0.0192
0.5	9430.2	675.50	215.00	0.01994	3367.3	544.30	214.31	0.0159
0.6	9617.5	676.00	217.50	0.00709	3583.9	542.00	216.44	0.0187

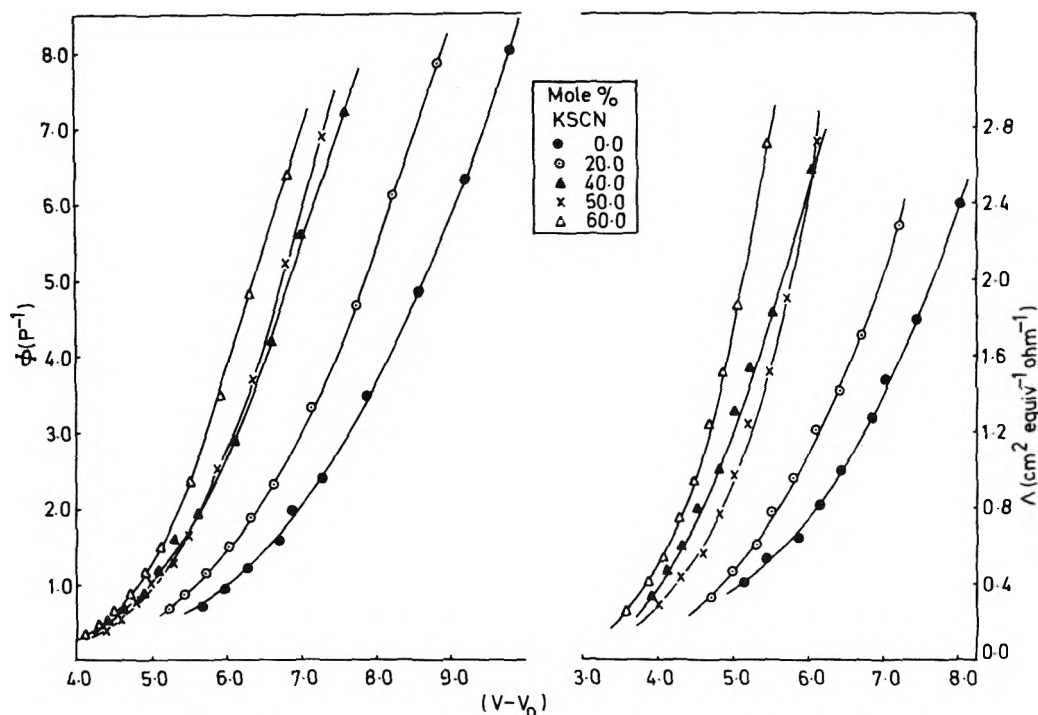**Figure 2.** Plots of log $Y(\phi,\Lambda)T^{1/2}$ vs. $[1/(T - T_0)]$ for molten $Ca(NO_3)_2 \cdot 3.99H_2O$–KCNS systems

Figure 3. Plots of $Y(\phi,\Lambda)$ vs. $(V - V_0)$ for molten $Ca(NO_3)_2 \cdot 3.99H_2O$–KCNS systems.

Cohen and Turnbull's "hard-sphere" model[6] in which $k = \gamma v^*/\alpha \bar{v}_m$, where α is taken as the mean value of the expansion coefficient for a temperature change from T_0 to T and γ is geometric factor to correct for the overlap of free volume in the calculation of the probability of occurrence of a critical void. On the basis of this model the diffusion coefficient of solutes, e.g., KCNS in this case, will be governed by the molecular size. If the solute molecule is smaller than

the solvent molecule it will diffuse at the same rate as that of solvent since the diffusive transport is completed only by the jumping of a neighboring solvent molecule into the void. In the case of conductance $Ca(H_2O)_4{}^{2+}$ may act as a solvent cation of larger size. No doubt, the rate of diffusion will decrease by the addition of solutes due to a decrease in the average free volume per molecule. Consequently the critical void volume, v^*, should remain the same both in

TABLE V: Best Fit Parameters for Eq 3 for the Fluidity and Equivalent Conductance of Ca(NO₃)₂·3.99H₂O–KSCN Melts[a]

Cation fraction K*	A_ϕ'	B_ϕ'	$V_{0,\phi}$	Std dev in ln φ	A_Λ'	B_Λ'	$V_{0,\Lambda}$	Std dev in ln Λ	$V_{0,\text{extrap}}$
0.0	220.03	32.47	130.23	0.0166	52.656	25.308	130.04	0.0502	129.25
0.2	271.43	31.42	114.86	0.0110	84.210	26.000	114.79	0.0219	114.30
0.4	311.88	28.35	99.90	0.0167	123.040	23.016	99.98	0.0408	99.50
0.5	474.85	30.90	92.02	0.0147	177.500	26.000	91.79	0.0589	92.00
0.6	631.57	30.90	84.38	0.0265	224.18	24.357	84.42	0.0359	84.75

[a] $V_{0,\text{extrap}}$ is obtained by extrapolating the plot of V vs. T to T_0.
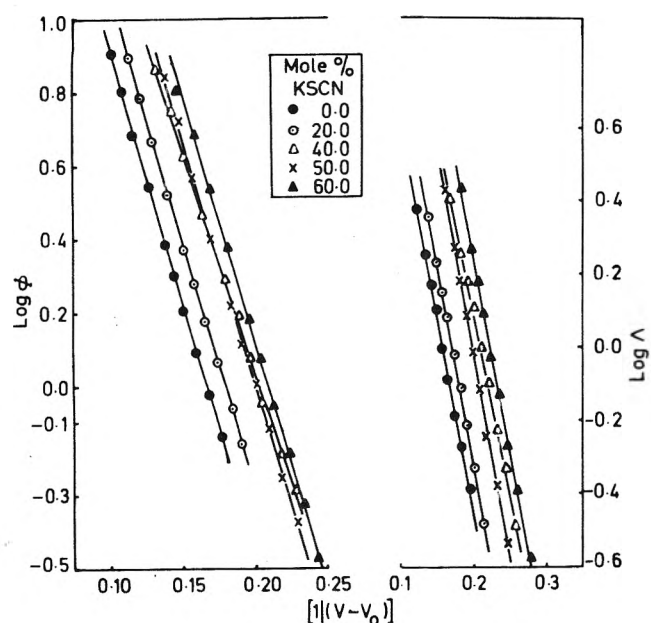
Figure 4. Plots of log $Y(\phi,\Lambda)$ vs. $[1/(V - V_0)]$ for molten Ca(NO₃)₂·3.99H₂O–KCNS systems.

the cases of solvent and the molten mixture containing solutes of smaller molecular size. Since α varies by about 2% in the composition range studied, $\gamma v^*/\bar{v}_m$ (or k) itself must be substantially independent of composition. The value of $k_\phi = 676°$K conforms with the value obtained by Moynihan[2] for Ca(NO₃)₂·4.04H₂O and that of $k_\Lambda = 542°$K is somewhat lower. The $\gamma v^*/\bar{v}_m$ values are found to be 0.31 and 0.25 in the cases of fluidity and conductance, respectively, both for Ca(NO₃)₂·3.99H₂O ($\alpha = 4.6 \times 10^{-4}$) and its mixtures with KCNS ($\alpha = 4.5 \times 10^{-4}$). The value 0.25 seems to coincide with those for anhydrous melts[20] obtained from conductance study. The ratio $k_\phi/k_\Lambda = 1.24$ is very close to those reported by others,[21] viz., 1.18–1.2. The higher value of k_ϕ than k_Λ appears to originate from the differences in E_ϕ and E_Λ which have actually been observed here.

The corrected activation energies for fluidity and conductance, E_{corr}, are tested for linearity with the function $[T/(T - T_0)]^2$ for the most appropriate choice of T_0. The values of $k_{\phi,\Lambda}$ for different compositions have been calculated from the slopes of such plots: for example, $k_\phi(X_{\text{KCNS}} = 0.0) = 670.8$, $k_\phi(X_{\text{KCNS}} = 0.2) = 671.0$, $k_\phi(X_{\text{KCNS}} = 0.4) = 670.8$, $k_\phi(X_{\text{KCNS}} = 0.5) = 676.1$, and $k_\phi(X_{\text{KCNS}} = 0.6) = 679.2$. Similar constancy in the values of k_Λ has also been observed. This further signifies that $k_{\phi,\Lambda}$ remains almost

independent of composition for the system under consideration.

From the activation energy isotherms (Figure 5)[16] it is apparent that changes in E_ϕ and E_Λ with composition are considerably less in the low concentrated region and become larger at higher concentrations. At low temperatures activation energies for fluidity and conductance are comparatively larger and the isotherms become more and more steep. According to the free volume model[6] average free volume per molecule decreases with increasing composition and the molecules get closer and closer resulting in high intermolecular forces. Consequently, in the concentrated region the flowing entities appear to involve clusters which evidently need higher energy to flow as compared to simple entities. As the temperature increases the free volume increases due to thermal expansion which causes a decrease in the intermolecular forces. This helps in bringing down the height of the potential energy barrier for viscous flow. Similar explanation also holds good for the conductance of ions. The ratios of the activation energies, E_ϕ/E_Λ (Table VII), are found to be ≈1.26 ± 0.03 which is close to those reported earlier[13] in the cases of MCl₂ (M = Mn²⁺, CO²⁺, Ni²⁺) -rich mixtures of Bu₄NCl where $E_\phi/E_\Lambda \approx 1.30 \pm 0.10$. This ratio was found to be greater than unity in ionic melts also. Hence it is apparent that migration of molecular species requires higher activation energy to surmount the energy barriers for fluidity than those required for ionic conductance.

The glass transition temperature, T_0, increases linearly with composition (Figure 6). This observation is similar to those in molten Ca(NO₃)₂·4H₂O + KNO₃ systems.[4] A correlation has been found[22] between T_g (or T_0) and the characteristic Debye temperature, θ_D which, in turn, shows an $m^{-1/2}$ dependence on the effective masses of the component particles of the amorphous phase. Consequently, the increase in T_0 observed here may be due to a decrease in the average molecular mass by the addition of KCNS. Qualitatively T_0 of a particular system refers to the extent of cooling required to reach the glass transition region. Since the free volume decreases with increase in composition, less cooling is required for supercooling the material at higher concentrations than those at lower concentrations and accordingly this may result in an increase in T_0 with composition. On extrapolation of the T_0 isotherm one obtains $T_0 = 225°$K for pure KCNS. However recently from electrical conductance data[23] the value of T_0 for KCNS has been reported as equal to 203°K. This restricts such an extrapolation as was also the case in alkali metal + divalent metal nitrate systems.[24]

Looking to the components embodied in $A_{\phi,\Lambda}$ terms it is clear that $A_{\phi,\Lambda}$ is directly related to $m^{-1/2}$. Hence one can

TABLE VII: The Ratio E_ϕ/E_Λ as a Function of Temperature for $Ca(NO_3)_2 \cdot 3.99H_2O$–KSCN Melts

T, °K	E_ϕ/E_Λ				
	0.0 mol% KSCN	20.0 mol % KSCN	40.0 mol % KSCN	50.0 mol % KSCN	60.0 mol % KSCN
313.0	1.2963	1.2258	1.2778	1.2663	1.2828
318.0	1.2949	1.2268	1.2772	1.2660	1.2821
323.0	1.2938	1.2280	1.2767	1.2658	1.2815
328.0	1.2927	1.2291	1.2763	1.2658	1.2810
333.0	1.2917	1.2302	1.2761	1.2659	1.2807
343.0	1.2902	1.2324	1.2758	1.2662	1.2806
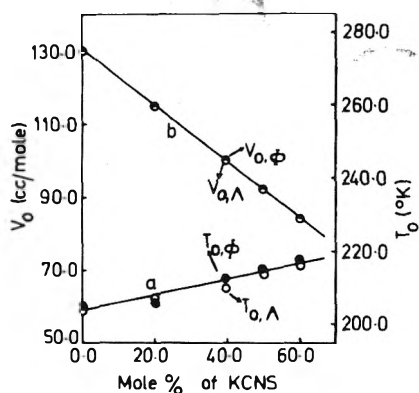
Figure 6. Variation of (a) $T_{0,\phi,\Lambda}$ and (b) $V_{0,\phi,\Lambda}$ with composition for molten $Ca(NO_3)_2 \cdot 3.99H_2O$–KCNS systems.

predict that the increase in $A_{\phi,\Lambda}$ with increasing X_{KCNS} is due to the lower molecular mass of KCNS. However, such a prediction fails in the case of $Ca(NO_3)_2 \cdot 4.09H_2O$–$Cd(NO_3)_2 \cdot 4.07H_2O$ melts[3] where A increases with increasing mole fraction of Cd^{2+} having larger mass. Moynihan et al.[3] presumed that this discrepancy may be due to the fact that the composition dependence of A is also related to differences in the lability of water or nitrate ions in the coordination shells of Ca^{2+} and Cd^{2+}.

A comparison of the plots (Figures 2 and 4) suggests a similarity in the "hard-sphere" and the Doolittle models. Higher standard deviations in ln ϕ and ln Λ in Doolittle's fit may apparently be due to the absence of $T^{-1/2}$ in the preexponential term although its effects are insignificant even in Cohen and Turnbull's expression. Furthermore, B' in the exponential term is related to γv^* per mole and remains composition independent like that of Cohen and Turnbull's k as supported by the least-squares fit and the slopes of the linear plots (Figure 4) of log ϕ and log Λ vs. $[1/(V - V_0)]$. Similarly, A' is expected to depend on composition as is the case with A. $V_{0,\phi}$ is found to be nearly equal to $V_{0,\Lambda}$ as $T_{0,\phi}$ and $T_{0,\Lambda}$.

It is interesting to note that the V_0 obtained from the extrapolation of the V–T plots (Figure 7)[16] to T_0 are almost similar to those obtained from the least-squares fit (Table V). This emphasizes the view[6,25] that the origin of free volume is not at 0°K but T_0.

In order to account for the deviation in normal alkanes from Doolittle's expression at low temperatures Miller[25] reasoned that the intrinsic volume, V_0, is dependent on temperature. No such deviation within the experimental range of temperature is observed in the present case. This

may be predicted presuming that V_0 remains independent of temperature for a hard-sphere model while it becomes temperature dependent for more complex and linear molecules such as normal alkanes.

However, V_0 has been found to decrease linearly with composition as apparent from Figure 6. On extrapolation of this plot to 0 mol % $Ca(NO_3)_2 \cdot 3.99H_2O$ one obtains the V_0 for pure KCNS as 54 cm³/mol. V_0 is found to be additive and can be given by the relation $V_{0,x_i} = \sum_i X_i V_{0,i}$ where V_{0,x_i} is the intrinsic volume of the melt with x_i as the mole fraction of the ith component. This additive nature of V_0 may also be due to the ideal behavior of the system with respect to the molal volume. V_0 appears to show a direct dependence on m unlike T_0 (Figure 6).

It is important to note here that, even though the free volume model seems to be a useful and successful representation of the present data, the empirical parameters may not be quantitatively interpreted in terms of the structure of the system. Especially during the study[26-28] of the effect of pressure on viscosity or T_g and on electrical conductivity the free volume theory fails badly. The Rice–Allnatt theory,[29,30] based upon Kirkwood's hypothesis[31] in which the dissipative forces are divided into components arising from the long- and short-range parts of the intermolecular pair potential, was extended to molten salts by Berne et al.[32] and Rice[33] and has been found to be a more promising quantitative theory of transport in ionic melts. Recent examination of some fundamental simplifying approximations made in the Rice–Allnatt theory[29,30] by Smedley and Woodcock[34] using Monte Carlo and molecular dynamics computational results[35-38] has indicated the cooperative nature of transport and the distribution of relaxation times. Moreover such an analysis reflects that cross correlations between hard and soft forces are important which implies that the simple two-event mechanisms for momentum transfer is not suitable to real liquids. Secondly, coulombic forces are found to make an appreciable contribution to the dissipation of energy in ionic liquids largely through cross correlations with the short-range repulsions and, therefore, the transport properties of the melt are largely determined by short-range forces. Lastly, the relaxation time characteristic of the dispersion (soft) forces is distinctly less than that due to the repulsive (hard) forces in ionic melts.

From the molal volume and equivalent conductance isotherms (Figure 8)[16] it is apparent that $\Delta V^E = 0$, but $\Delta \Lambda^E \neq 0$. This reflects that the system is not strictly ideal in thermodynamic properties and the additivity of molal volumes is not a very rigorous test of ideal mixing. Such behaviors are also observed in AgCl + AgBr and $PbCl_2$ + $PbBr_2$ melts.[39] Λ appears to decrease with composition over the temperature range 298–308°K, even though, the decrease is negligible from $X_{KCNS} = 0.2$ to $X_{KCNS} = 0.4$. It seems that the isotherm passes through a maximum at $X_{KCNS} = 0.4$ over the range 313–328°K and, further, this maximum appears to shift to $X_{KCNS} = 0.5$ in the range 333–343°K. Throughout the temperature scan there is a decrease in Λ from $X_{KCNS} = 0.0$ to $X_{KCNS} = 0.2$. Here the substitution of the more highly conducting K^+ for $\frac{1}{2}Ca^{2+}$ causes a decrease in conductance instead of the anticipated increase. This phenomenon is found to be common to many binary systems, e.g., $MgCl_2$ + KCl, $CdCl_2$ + KCl, AlF_3 + NaF. At the moment we are not able to explain why conductance isotherms show such behaviors. However, in the region 0.0–0.2 mole fraction of KCNS the decrease in conductance

may be due to the suppression of the mobility of K^+ ions by the steric hindrance of hydrated cations of the solvent which are in excess. Consequently the decrease in the average free volume per ion by the addition of solute causes a decrease in the conductance. As cited earlier, the rate of diffusion of the smaller solute cation becomes similar to that of the solvent cation and the lower value of E_ϕ/E_Λ for $X_{KCNS} = 0.2$ provide further support for the above view.

Supplementary Material Available. Tables II, IV, and VI and Figures 1, 5, 7, and 8 will appear following these pages in the microfilm edition of this volume of the journal. Photocopies of the supplementary material from this paper only or microfiche (105×148 mm, 24X reduction, negatives) containing all of the supplementary material for the papers in this issue may be obtained from the Business Office, Books and Journal Division, American Chemical Society, 1155 16th St., N.W., Washington, D.C. 20036. Remit check or money order for $4.00 for photocopy or $2.50 for microfiche, referring to code number JPC-75-2180.

References and Notes

(1) C. A. Angell, *J. Phys. Chem.*, **70**, 3988 (1966).
(2) C. T. Moynihan, *J. Phys. Chem.*, **70**, 3399 (1966).
(3) C. T. Moynihan, C. R. Smalley, C. A. Angell, and E. J. Sare, *J. Phys. Chem.*, **73**, 2287 (1969).
(4) C. A. Angell, *J. Electrochem. Soc.*, **112**, 1225 (1965).
(5) A. K. Doolittle, *J. Appl. Phys.*, **22**, 1471 (1951).
(6) M. H. Cohen and D. Turnbull, *J. Chem. Phys.*, **31**, 1164 (1959).

(7) N. Islam, M. R. Islam, S. Ahmad, and B. Waris, *Appl. Spectrosc.*, **29**, 68 (1975).
(8) C. T. Moynihan and A. Fratiello, *J. Am. Chem. Soc.*, **89**, 5546 (1967).
(9) E. J. Sare, C. T. Moynihan, and C. A. Angell, *J. Phys. Chem.*, **77**, 1869 (1973).
(10) J. Braunstein, L. Orr, and W. Macdonald, *J. Chem. Eng. Data*, **12**, 415 (1967).
(11) R. W. Laity et al., Electrochemical Society Symposium, Chicago, Extended Abstracts, Vol. 73-1, 1973.
(12) H. Braunstein, J. Braunstein, and P. T. Hardesty, *J. Phys. Chem.*, **77**, 1907 (1973).
(13) N. Islam, M. R. Islam, S. Ahmad, and B. Waris, *J. Am. Chem. Soc.*, **97**, 3026 (1975).
(14) M. E. Martins, A. J. Calendra, and A. J. Arvia, *J. Inorg. Nucl. Chem.*, **36**, 1705 (1974).
(15) W. W. Ewing and R. J. Mikovsky, *J. Am. Chem. Soc.*, **72**, 1390 (1950).
(16) See paragraph at end of text regarding supplementary material.
(17) G. J. Janz, F. W. Dampier, G. R. Lakshminarayanan, P. K. Lorenz, and R. P. T. Tomkins, *Natl. Stand. Ref. Data Ser., Natl. Bur. Stand.*, **No. 15**, 105 (1968).
(18) J. H. Hildebrand and R. H. Lamoreaux, *J. Phys. Chem.*, **77**, 1471 (1973).
(19) C. A. Angell and R. D. Brassel, *J. Phys. Chem.*, **76**, 3244 (1972).
(20) C. A. Angell, *J. Phys. Chem.*, **68**, 1917 (1964).
(21) C. A. Angell and C. T. Moynihan, "Transport Processes in Low-Melting Molten Salt Systems" in "Molten Salts", G. Mamantov, Ed., Marcel Dekker, New York, N.Y., 1969, pp 315-375.
(22) C. A. Angell, *J. Am. Ceram. Soc.*, **51**, 117 (1968).
(23) P. Dulieu and P. Claes, *Bull. Soc. Chim. Belg.*, **82**, 639 (1973).
(24) O. J. Kleppa and L. S. Hersh, *Discuss. Faraday Soc.*, **32**, 99 (1962).
(25) A. A. Miller, *J. Phys. Chem.*, **67**, 1031 (1963).
(26) M. Goldstein, *J. Chem. Phys.*, **39**, 3369 (1963).
(27) J. M. O'Reilly, *J. Polym. Sci.*, **57**, 429 (1962).
(28) B. Cleaver, S. I. Smedley, and P. N. Spencer, *J. Chem. Soc., Faraday Trans. 1*, **68**, 1720 (1972).
(29) S. A. Rice and A. R. Allnatt, *J. Chem. Phys.*, **34**, 2144 (1961).
(30) A. R. Allnatt and S. A. Rice, *J. Chem. Phys.*, **34**, 2156 (1961).
(31) J. G. Kirkwood, *J. Chem. Phys.*, **14**, 180 (1956).
(32) B. Berne and S. A. Rice, *J. Chem. Phys.*, **40**, 1347 (1964).
(33) S. A. Rice, *Trans. Faraday Soc.*, **58**, 499 (1962).
(34) S. I. Smedley and L. V. Woodcock, *J. Chem. Soc., Faraday Trans. 2*, **70**, 955 (1974).
(35) K. Singer and L. V. Woodcock, *Trans. Faraday Soc.*, **67**, 12 (1971).
(36) L. V. Woodcock, *Chem. Phys. Lett.*, **10**, 257 (1971).
(37) L. V. Woodcock, *Adv. Molten Salt Chem.*, **3**, 1 (1974).
(38) L. V. Woodcock, *J. Chem. Soc., Faraday Trans. 2*, **71**, 41 (1975).
(39) H. Bloom, "The Chemistry of Molten Salts", W. A. Benjamin, New York, N.Y., 1967, p 61.

Heats of Mixing of Polyelectrolyte Solutions Having a Common Polyion. I.
Polystyrenesulfonic Acid with Its Magnesium Salt

J. Škerjanc

Department of Chemistry, University of Ljubljana, 61000 Ljubljana, Yugoslavia (Received April 14, 1975)

Publication costs assisted by the Department of Chemistry, University of Ljubljana

The heats of mixing of aqueous solutions of polystyrenesulfonic acid with solutions of its magnesium salt of the same concentration have been measured at 25° at two polyelectrolyte concentrations, 0.0600 and 0.00811 mono$M$. The heat effects are endothermic; the maxima of the curves, ΔH_m vs. equivalent fraction of the acid, decrease with increasing polyelectrolyte concentration. The experimental values have been compared with those predicted by the cell model with cylindrical symmetry. Reasonable agreement between theory and experiment has been found.

Introduction

Most of the research work in the field of synthetic polyelectrolytes has thus far been concerned with the properties of a single polyelectrolyte in a pure solution or in a solution containing an excess of simple electrolyte. Studies of such properties are essential to an understanding of the interionic forces which distinguish polyelectrolyte solutions from ordinary polymer solutions. Usually only one counterionic species has been present in pure polyelectrolyte solutions. However, few studies have been reported on solutions containing mono- as well as divalent counterions.

Studies of such mixed polyelectrolyte solutions are attractive not only per se but also in the perspective of their extension to solutions of naturally occurring polyelectrolytes, i.e., proteins and nucleic acids, which very often contain as counterions ionic species differing in valency.

The equilibrium properties of these mixed polyelectrolyte solutions which have been studied thus far are the osmotic[1] and activity coefficients,[2] heat of dilution,[3] and volume change on dilution.[4] Among other thermodynamic properties of interest are the enthalpy and volume changes on mixing. These two properties have been extensively investigated with solutions of simple electrolytes and ordinary polymers, but as far as we could ascertain no such studies have been performed with solutions of polyelectrolytes. Therefore, this work has been undertaken. Measurements have been made of the enthalpy change ensuing from mixing an aqueous solution of polystyrenesulfonic acid with a solution of its magnesium salt of the same concentration. An interpretation of the results with a theoretical treatment based on the cell model will be attempted.

Experimental Section

Sodium polystyrenesulfonate, NaPSS (mol wt, 100,000; degree of sulfonation, 1.00) obtained from Polysciences Inc. (Rydal, Pa.) was used as starting material. The polymer was purified by repeated slurring and filtering with a methanol–water solution (10:1) and finally by exhaustive dialyzing of a polymer solution against water. The dialyzed NaPSS solution was converted to the acid solution by ion exchange and its concentration was determined by potentiometric titration. The magnesium salt was prepared from the acid solution as described previously.[5]

Calorimetric measurements were carried out at 25° using an LKB 10700-2 batch microcalorimeter with golden reaction cells.

Results and Discussion

The heats of mixing, ΔH_m, in the present study were obtained in experiments in which the solution of polystyrenesulfonic acid was mixed with the solution of its magnesium salt of the same concentration. By mixing appropriate amounts of these solutions the dependence of ΔH_m on the equivalent fraction of the acid, $\bar{N}_1$, was obtained. It is convenient to express the results of mixing processes in calories per monomole of polyelectrolyte in the resulting mixture. Then ΔH_m is related to the enthalpies of the mixed and both single solutions, containing 1 monomole of polyelectrolyte, by

$$\Delta H_m = H_{mixed\ soln} - \bar{N}_1 H_1 - (1 - \bar{N}_1)H_2 \qquad (1)$$

The calorimetric results for two polyelectrolyte concentrations are shown in Figure 1. It may be seen that the enthalpy change is positive and that the skewness of the curves is more pronounced at lower polymer concentration. Similar behavior of the ΔH_m curve is predicted by the cell model.[6] According to this model the cylindrical polyion of radius a and length h carries ν negative charges and is enclosed by a larger concentric cylinder of radius R which contains all the counterions. In our previous paper[3] this model has been applied to a polyelectrolyte solution containing a mixture of mono- and divalent counterions and the electrostatic internal energy of the solution, E_e, has been calculated. Expressed per monomole of polyelectrolyte it reads[3]
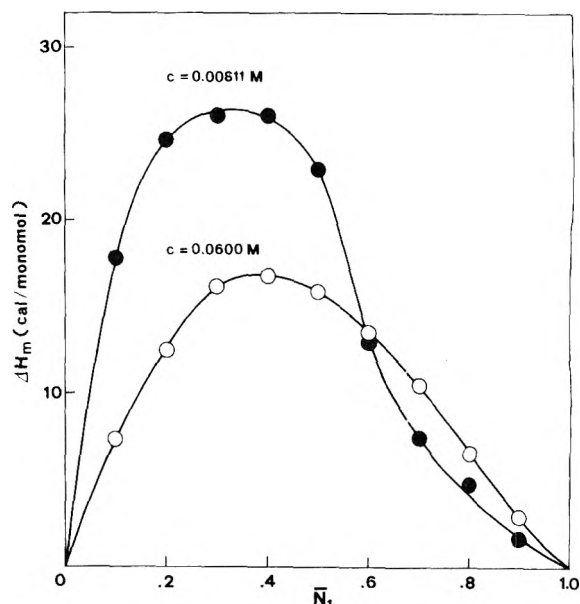
Figure 1. Heats of mixing of polystyrenesulfonic acid with its magnesium salt in water at 25° for two polyelectrolyte concentrations as a function of the equivalent fraction of the acid.
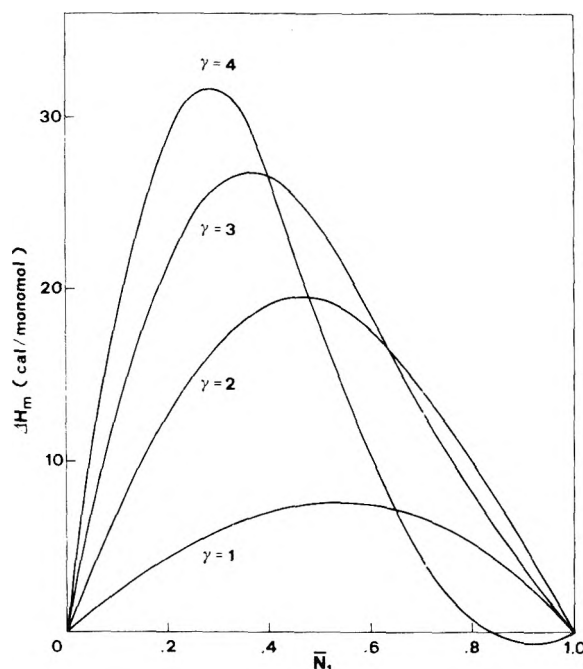

Figure 2. Theoretical curves calculated for $\lambda = 2.83$ and for various values of γ.

$$E_e = \frac{\Re T}{4\lambda}\left(1 + \frac{d \ln \epsilon}{d \ln T}\right) I$$

$$I = \int_0^\gamma \left(\frac{d\phi}{dt}\right)^2 dt \qquad (2)$$

$$- e\psi/kT = \phi, r = a \exp(t), R = a \exp(\gamma)$$

where ψ is the electrostatic potential, r the distance from the polyion axis, e the positive charge within the limits $0 \leq e \leq e_0$, where e_0 is the protonic charge, k is the Boltzmann constant, ϵ the dielectric constant of the solvent, $\Re$ the gas constant, T the absolute temperature, and the charging parameter λ has been defined[6a] by

$$\lambda = \nu e_0^2 / \epsilon k T h \qquad (3)$$

The heat of mixing, ΔH_m, defined by eq 1, may be formally split into two terms

$$\Delta H_m = \Delta H_m{}^0 + \Delta H_{m,e} \qquad (4)$$

where ΔH^0 is the nonelectrostatic and ΔH_e the electrostatic contribution. In the present calculation $\Delta H_m{}^0$ is assumed to be much smaller than $\Delta H_{m,e}$ and is therefore neglected. It is seen from eq 4 that for comparison of experimental and theoretical results we would actually need an expression for the electrostatic enthalpy of the solution, H_e. However, the difference $H_e - E_e$ is small at moderate concentrations[7] and consequently we may use eq 2 as a reasonable approximation for H_e. From eq 1 and 2 we thus obtain

$$\Delta H_m = \frac{\Re T}{4\lambda} \left(1 + \frac{d \ln \epsilon}{d \ln T}\right) \times$$
$$[I(\bar{N}_1) - \bar{N}_1 I(\bar{N}_1 = 1) - (1 - \bar{N}_1) I(\bar{N}_1 = 0)] \qquad (5)$$

The theoretical curves, calculated according to this equation, are presented in Figure 2. For the charging parameter its structural value[8] was used ($\lambda = 2.83$ at 298.15 K with $\epsilon = 78.54$ and $h/\nu = 2.52$ Å) and for the coefficient $d \ln \epsilon/d \ln T$ the value[9] for water, -1.368, was taken. For the evaluation of the integral I we have to solve the Poisson–Boltzmann equation for the fully charged system. A detailed description[3] of the numerical calculation and the computed values[4] of the integral have been given previously. The concentration parameter γ, defined by eq 2, is related to the monomolar concentration, c. The values of $\gamma = 1, 2, 3,$ and

4 for polystyrenesulfonates ($a = 8$ Å) correspond to 0.443, 0.0600, 0.00811, and 0.00110 monomolar solutions, respectively. The concentration of the theoretical curves for $\gamma = 2$ and $\gamma = 3$ correspond thus to the concentrations of both experimental curves. It may be seen that although the agreement between calculated and theoretical values is only semiquantitative, the concentration dependence of ΔH_m is properly predicted. This finding is in general accord with the results of previous studies[1-5,8,10] and may be considered as additional support for the applicability of the cell model for those systems in which no significant specific binding of counterions to the polyion has been detected.

References and Notes

(1) D. Dolar and D. Kozak in "Abstracts of the IUPAC Symposium on Macromolecules, Leiden", Vol. 1, Inter Scientias, The Hague, 1970, p 363.
(2) M. Rinaudo and B. Loiseleur, *Bull. Soc. Chim. Fr.*, 1241 (1973); *J. Chim. Phys.*, **69**, 1606 (1972).
(3) D. Dolar and J. Škerjanc, *J. Chem. Phys.*, **61**, 4106 (1974).
(4) J. Škerjanc and D. Dolar, *J. Chem. Phys.*, **63**, 515 (1975).
(5) J. Škerjanc, *J. Phys. Chem.*, **77**, 2225 (1973).
(6) (a) R. M. Fuoss, A. Katchalsky, and S. Lifson, *Proc. Natl. Acad. Sci. U.S.*, **37**, 579 (1951); (b) T. Alfrey, Jr., P. W. Berg, and H. Morawetz, *J. Polym. Sci.*, **7**, 543 (1951).
(7) J. Škerjanc, D. Dolar, and D. Leskovšek, *Z. Phys. Chem. (Frankfurt am Main)*, **56**, 208 (1967).
(8) A. Katchalsky, Z. Alexandrowicz, and O. Kedem, "Polyelectrolyte Solutions", in "Chemical Physics of Ionic Solutions", B. E. Conway and R. G. Barradas, Ed., Wiley, New York, N.Y., 1966, p 295.
(9) B. B. Owen, R. C. Miller, C. E. Milner, and H. L. Cogan, *J. Phys. Chem.*, **65**, 2065 (1961).
(10) A. Katchalsky, *Pure Appl. Chem.*, **26**, 327 (1971).

Mercury-Photosensitized Production of Free Radicals in Organic Glasses[1]

N. Bremer, B. J. Brown, G. H. Morine, and J. E. Willard*

Department of Chemistry, University of Wisconsin, Madison, Wisconsin 53706 (Received May 12, 1975)

Trapped free radicals are produced by Hg-photosensitized reactions when 3-methylpentane (3MP), CH_3OH, C_2H_5OH, or C_3H_7OH glasses containing dissolved or vapor deposited Hg are exposed to 254- or 185-nm light at 77 K. During illumination at 254 nm the uv absorption peak of the Hg in the region of 250–260 nm decreases while the radical concentration grows to a plateau. Subsequent steady illumination with broad band uv light regenerates part of the original Hg absorbance and is accompanied by continuing growth in radical concentration with a yield of many radicals per dissolved Hg atom. A search for ESR and optical absorption lines of HgH in samples from which the Hg absorbance has been bleached has yielded negative results. The optical absorption spectrum of the radicals produced in 3MP is reported.

Introduction

Trapped electrons and free radicals produced in organic glasses by ionizing radiation have been extensively investigated.[2] The purpose of the experiments reported here has been to determine whether these species can be formed by photoionization or photosensitization reactions of mercury dispersed in such matrices at 77 K. Production in this way would allow them to be studied in the absence of interfer-

ing species which accompany formation by ionization radiation.

Mercury-photosensitized decomposition of hydrocarbons has been investigated in the gas[3] and liquid phases[4] by determination of the stable reaction products. The free radical products from 11 gaseous alkanes have been determined by $^{14}C_2H_5$ radical scavenging.[3c] Transient radicals produced have also been observed by mass spectrometry.[5] In-

sofar as we are aware, no mercury-sensitized reactions have been studied in the solid phase, although photosensitized radical production in solid hydrocarbons has been observed with aromatic molecules as sensitizer.[6] Uv irradiation of sodium dispersed in 3-methylpentane glass at 77 K yields both trapped electrons and 3-methylpentyl radicals.[7]

Experimental Section

Sample Preparation and Measurement. Dispersions of Hg in 3MP glass have been prepared by dissolving liquid mercury in purified degassed 3MP followed by quench cooling in liquid N_2 and by deposition of Hg and 3MP vapors onto a cold finger using an apparatus of the type illustrated in Figure 1. The solubility of Hg in n-hexane has been determined[8a] to be 6.3×10^{-6} M at 25°C and 15×10^{-6} M at 40°C with the aid of radiomercury. The absorption spectrum is a broad doublet with a maximum absorption at ~257 nm. The solubility in 3MP has not been directly determined but is assumed to be 5×10^{-6} M at 25°C from data[8] on other branched hydrocarbons. A fivefold increase in concentration (to ~25×10^{-6} M) has been obtained in the present work by shaking of Hg with the solvent for a few minutes at ~55°C. Solutions saturated at room temperature or above and quenched to 77 K show similar spectra and nearly the same concentration as at the saturation temperature, but with a small blue shift, giving a maximum absorption at ~255 nm. The spectra in the glassy state at 77 K were measured using two 2.5-cm^2 fused silica cells in series to give a light path of 5 cm. The cells were mounted under liquid nitrogen in a styrofoam box provided with Suprasil light pipes from the cell face to the outside of the box. The light pipes prevented bubbles in the liquid nitrogen from causing fluctuations in the analyzing light beam from the Cary spectrophotometer. When samples of 3MP–Hg glass at 77 K are warmed slowly to room temperature without shaking, very little Hg remains in solution, indicating that solubility equilibrium is achieved at low temperatures during the warm-up. The origin of the structure of the Hg absorption band in the liquid has been considered extensively.[9]

To prepare 3MP–Hg samples with the apparatus of Figure 1, the temperature of the 3MP reservoir (F) was maintained at ca. −80°C (vapor pressure of 3MP 0.2 Torr). The temperatures used for the Hg reservoir, and the corresponding vapor pressures, were 25°C, 1.8×10^{-3} Torr; 0°C, 1.3×10^{-4} Torr; −80°C $<10^{-7}$ Torr. When the dewar (A) was filled with liquid nitrogen and stopcocks H, I, and J were opened, a nearly uniform thickness of an opaque 3MP-Hg mixture was deposited in a band 3–4 cm high on all sides of the 3-mm i.d., 4-mm o.d. central finger (K). This was white for pure 3MP but became grey with increasing Hg concentration. About 30 min was required to prepare a 0.5 mm thickness of deposit. The tube (L) was then moved up with the aid of the sliding vacuum seal (C) until the sample deposit was near the bottom of the tube. (L) was then introduced into the cavity of the ESR spectrometer. Deposition of 3MP on all sides of the cold finger indicates considerable reflection of molecules from the walls of the outer tube. In the following text the deposits are arbitrarily designated by the ratio of the vapor pressures, e.g., "Hg/3MP" = $1:10^3$. At constant incident light intensities the rates of growth of radicals as indicated by ESR peak heights were the same ($\pm 10\%$) for samples with the same Hg:3MP ratio but differed for different ratios.
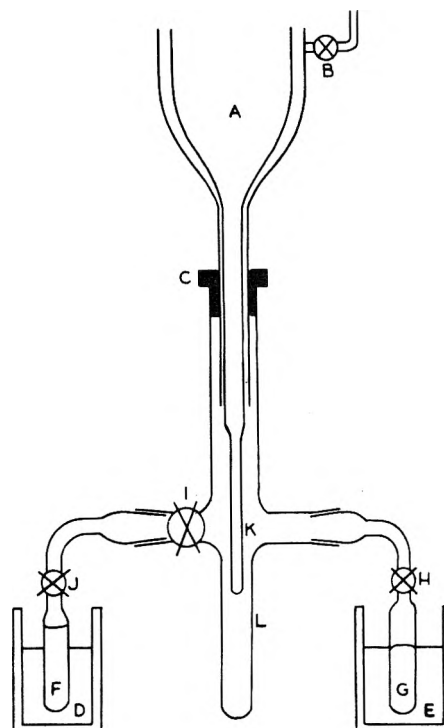
Figure 1. Apparatus for vapor deposition and ESR examination of Hg–3MP mixtures: (A) liquid nitrogen dewar assembly; (B) stopcock–vacuum line connection; (C) movable O-ring vacuum seal; (D, E) temperature baths; (F) 3-methylpentane reservoir; (G) Hg reservoir; (H, I, J) stopcocks; (K) 3 × 4 mm Suprasil cold finger; (L) 11-mm o.d. Suprasil outer tube.

Suprasil and Vycor spiral low-pressure Hg lamps, a Hanovia end window SC2537 low-pressure Hg lamp, a collimated beam from a quartz-jacketed GE AH4 medium-pressure Hg lamp, and a Chromatix tunable dye laser were used as light sources, with filters noted later in the text. The intensities were measured with a power meter or estimated from earlier chemical actinometry. For illuminations with the spiral lamps, the finger of the Varian ESR dewar holding the sample under liquid nitrogen was positioned in the center of the spiral. All other illuminations in the ESR experiments were made with the sample in the Varian V-4531 cavity of a Varian 4501 ESR spectrometer. An open waveguide in the cavity wall admitted the beam. The spectra were taken in the X band, using 100-kHz modulation, powers of 40–500 μW for radical signals and of 10–40 μW to look for trapped electron signals. Absolute spin concentrations were determined by comparison with solutions of known concentration of the stable free radicals DPPH and galvinoxyl by comparison of the double integral values of the first-derivative spectra using a Northern Scientific Co. signal averager data processor. All ESR measurements for absolute spin determinations were made in 2- or 3-mm i.d. calibrated Suprasil tubes containing a small droplet of Hg for saturating the purified degassed liquid at room temperature.

Phillips Pure Grade 3MP was further purified by standing over Linde 13X molecular sieve, passage through 2 m of freshly activated silica gel, degassing by freeze–pump–thaw cycles, and storage over a sodium mirror under vacuum. Methanol (Mallinkrodt AR, anhydrous), ethanol (AR, absolute), and propanol (Fisher Certified Reagent) were purified by treatment with 2,4-dinitrophenylhydrazine.[10]
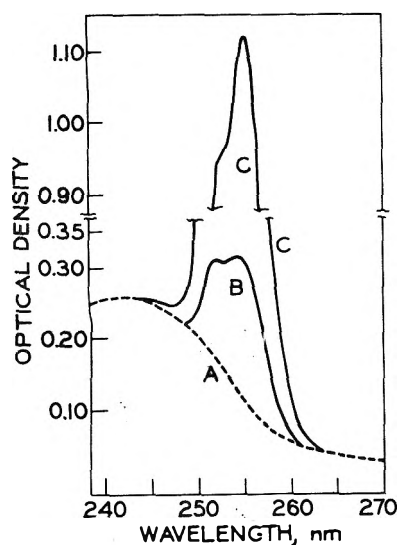
Figure 2. Optical spectra of Hg in 3MP glass at 77 K (5-cm pathlength in two 2.5-cm² quartz cells): (A) spectrum of quartz cell walls; 3MP is transparent in this region; (B) 3MP saturated with Hg at 25°C and quenched to 77 K; (C) 3MP saturated with Hg at ~55°C and quenched to 77 K.
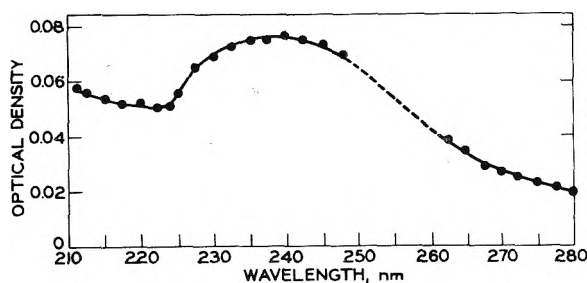

Figure 3. Optical spectrum produced by Hg-photosensitized decomposition of 3MP glass at 77 K, obtained by subtracting absorption before illumination from absorption after illumination. Same conditions as for Figure 2B.

Results

Effect of Illumination on Optical Spectrum. 3MP glass containing ~2.5 × 10^{-5} M Hg in two 2.5-cm square quartz cells in series was exposed at 77 K to a Hanovia end window SC2537 low-pressure Hg lamp which had 85% of its emission at 254 nm and no other significant output below 310 nm. This caused the absorbance due to Hg (Figure 2) to decrease to a steady state value equal to ~2% of that before illumination. Subsequent exposure to the full emission of the quartz-jacketed AH4 medium-pressure Hg lamp regenerated Hg absorbance to a steady state value of ~7% of the original. During both these illuminations, a broad absorption (Figure 3), believed to be due primarily to 3-methylpentyl radicals, grew in. Exposure for several minutes to the AH4 lamp, filtered (25 mm of 0.17 g of KI/100 ml of H_2O) to remove >99% of the 254-nm radiation while passing wavelengths greater than 260 nm, regenerated the Hg to 11% of its initial absorbance and longer illumination might have increased it further. A small increase in broad background absorption for λ <240 nm accompanied the regeneration of the Hg absorption. Light from the AH4 lamp filtered by 6 mm of Pyrex (OD > 2 at <300 nm) did not regenerate mercury atom absorption.

In a sample where the broad absorption below 280 nm was generated by bleaching an initial Hg concentration of
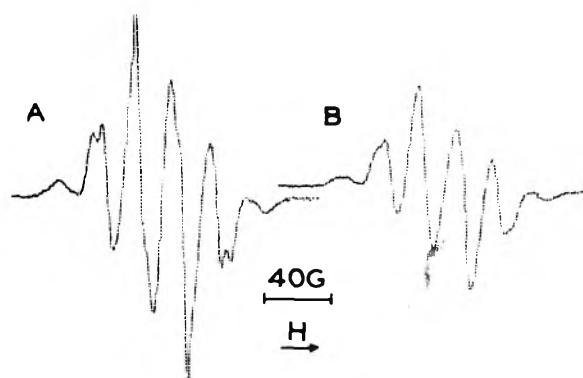
Figure 4. ESR spectra of radicals produced by exposure of vapor deposited 3MP–Hg at 77 K to full light from quartz-jacketed AH4 lamp (Hg:3MP = 1:10^3): (A) 3MP radicals after ~2-hr photolysis; (B) 3MP radicals after ~2-hr photolysis and 7-hr thermal decay. Spectra taken at 500-μW microwave power, modulation amplitude 2 G.
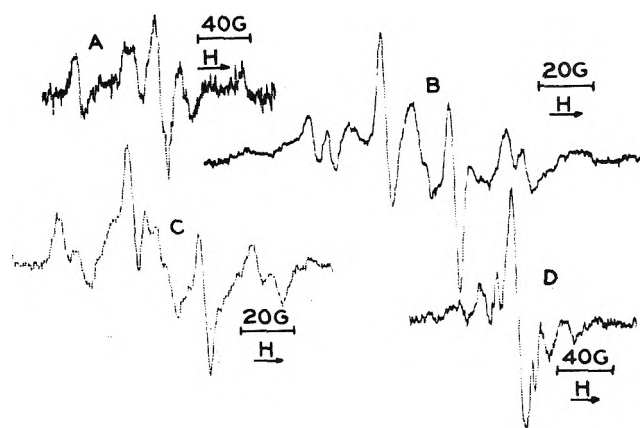

Figure 5. ESR spectra of radicals produced by exposure of vapor deposited Hg–alcohol mixtures at 77 K to full light of quartz-jacketed AH4 lamp: (A) Hg:MeOH = 1:1.5 × 10^4, 5-hr photolysis; (B) Hg:EtOH = 1:10^4, 1 hr; (C) Hg:n-PrOH = 1:5 × 10^3, 3 hr; (D) sample B after ~1-hr thermal decay following photolysis. Microwave power, 40 μW, modulation amplitude, 2 G. A was recorded at 1.6 times the sensitivity used for the other spectra.

~5 × 10^{-6} M for 4 min with the AH4 lamp, the absorption had decreased by ~60% after 3 days in the dark. On warming to room temperature the species responsible for this absorption disappeared.

Radicals Produced. When 3MP–Hg glass prepared by either of the methods described in the Experimental Section is exposed to light from the AH4 medium-pressure Hg lamp, radicals giving the ESR spectrum of Figure 4A are produced. Similar illumination of pure 3MP produces no ESR signal. Figure 4B is the spectrum of the same sample after an additional six hr at 77 K in the dark. It is similar to that found in γ-irradiated pure 3MP glass, which is due predominantly to secondary 3-methylpentyl radicals.[11] The latter is converted to a spectrum similar to that of Figure 4A by 254-nm irradiation[12,13] without significant change in total spin concentration and reverts to that of Figure 4B on standing in the dark.

Vapor-deposited dispersions of Hg in methanol, ethanol, and propanol have been prepared in the apparatus of Figure 1 and exposed to the full light of the AH4 lamp. In each case radicals were produced (Figure 5A–C). After decay at 77 K for 1 hr the initial ethanol spectrum (Figure 5B) changed to the spectrum of 5D.

Factors Determining Radical Growth Rates. When vapor-deposited samples with "Hg:3MP" ratios of $1:10^5$, $1:10^3$, and $1:150$ were exposed while in the ESR cavity to the full light of the AH4 lamp, the ESR signal as measured by the vertical distance from the maximum of peak 3 on the low-field side to the minimum of peak 5 (Figure 4) grew linearly after an apparently faster initial growth. The rate was higher for the $1:10^3$ sample than the $1:10^5$ sample, but that for the $1:150$ sample was much lower, presumably because of Hg agglomeration. A sample prepared by dispersion of Hg in 3MP with an ultrasonic microprobe (70 W cm^{-2}) in air, followed by quenching at 77 K, gave about the same growth rate as the $1:10^5$ vapor deposited sample. Rough estimates indicated quantum yields of 0.1 to 1 based on the light absorbed by the Hg.

Beam-expanded laser light falling on vapor deposited samples ("Hg:3MP" = $1:10^3$) in the ESR cavity showed no radical production at either 392 nm ($\sim 4 \times 10^{14}$ photons sec^{-1} on portion of sample in sensitive region of cavity) or 265 nm ($\sim 3 \times 10^{14}$ photons sec^{-1}). Similarly exposure to the AH4 lamp with Corning Glass Co. 7-39 and 7-37 filters which gave about 3×10^{14} photons sec^{-1} between 300 and 400 nm but negligible intensity below 300 nm, produced no radical signal. In experiments using the AH4 lamp without a filter, with a Vycor filter, and with a Corning 7-54 filter the peak heights of the radical ESR signal grew at rates proportional to the estimated light intensity in the 250–265-nm region.

Samples of degassed 3MP saturated with Hg at 25°C and quenched to 77 K showed the radical growth indicated in Figure 6 when exposed to the Vycor spiral lamp. The periods of illumination were alternated with dark intervals of ~ 4 min for measurement in the ESR cavity. The concentrations were determined by double integration of the first derivative ESR signals. When a sample which had reached the plateau of Figure 6 was then exposed to the AH4 lamp, the radical concentration again increased as shown by the dashed lines of Figure 6. The lower dashed line is for an AH4 illumination that was started after a sample had undergone a 30-min period of dark decay after reaching the plateau. Figure 7 shows the radical growth (based on the double integral of the spectrum) for a similar sample during continuous illumination by the AH4 lamp, without prior illumination with the low-pressure Hg lamp. Growth curves similar to these for radical production in 3MP have been found on illumination of Hg in 3-ethylpentane glass. It is estimated that the absolute radical concentrations given in Figures 6 and 7 are accurate to ±20%.

Electrons, H Atoms, and HgH. In none of these experiments have we found any evidence for the ESR singlet typical of trapped electrons,[2] for the doublet of ~ 500-G splitting characteristic of trapped H atoms in 3MP,[14] or for ESR or optical spectra indicative of HgH.

The search for electron production has included illumination of vapor-deposited 3MP ("Hg:3MP" = $1:10^3$) in the center of the spiral Suprasil low-pressure Hg lamp through interference filters which gave a ratio of intensity at 185 nm to 254 nm of 16 with an incident intensity on a 1 cm height of the sample of $\sim 2 \times 10^{15}$ photons sec^{-1} at 185 nm. The sample, in the apparatus of Figure 1, was transferred to the ESR cavity and a spectrum taken within 5 min after a 5-min irradiation. All ESR measurements in search of trapped e^- were made at an ESR power of 10–40 μW. The rate of radical production by the spiral lamp was similar to that by the unfiltered AH4. The absence of a trapped-elec-
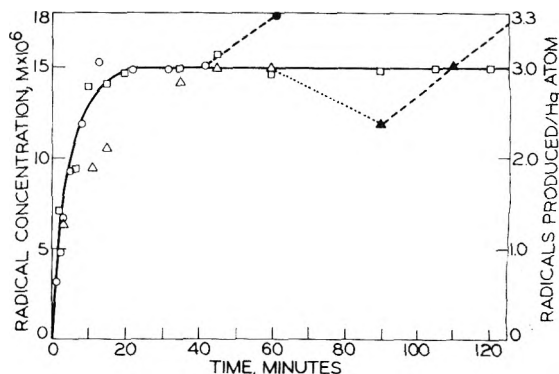

Figure 6. Hg-photosensitized production of radicals in 3MP glass at 77 K. Open points (three different exposures) and solid line show results of exposure to Vycor low pressure Hg lamp; closed points and — lines show results of exposure to AH4 lamp. The absolute values of concentration and [R·]/[Hg] shown on the ordinate scales refer to the experiment with points indicated by the □. The data for the two other exposures were normalized at the plateau. The dotted line indicates a dark period.
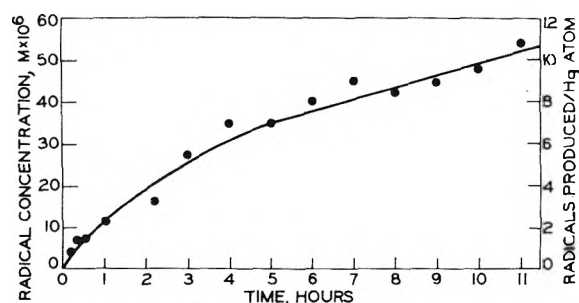

Figure 7. Hg-photosensitized production of radicals in 3MP glass at 77 K using quartz-jacketed AH4 medium-pressure Hg lamp.

tron signal indicates that the gas phase ionization potential of Hg (10.4 eV) is not lowered sufficiently in the glass to allow photoionization by 185-nm (6.5 eV) light. Previous work has shown that photoionization of Na in similarly vapor deposited Na–3MP matrices produces readily observable trapped electrons.[7]

The search for HgH by ESR included scanning of the region from 2750 to 4350 G and multiple scanning at high sensitivity with signal averaging of the region from 3400 to 2900 G where the most intense ESR lines from HgH in Ar matrices have been found.[15] Microwave powers from 0.3 to 8.5 mW were tested.
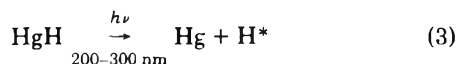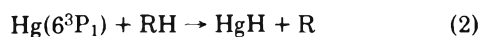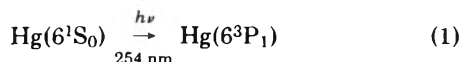
Numerous optical emission lines from HgH have been reported[16,17] from 161 to 452 nm. Absorption lines of ground state HgH in band systems in the region of 280–450 nm have also been reported.[18] In the present work, no absorption was found in the 300–420-nm region, using a 5-cm pathlength of 3MP glass at 77 K from which the absorption due to an initial Hg concentration of $\sim 2.5 \times 10^{-5}$ M had been bleached. There also was no structure attributable to HgH on the broad free radical absorption at wavelengths below 300 nm.

Discussion

Mechanism of Radical Formation. The disappearance of the Hg optical absorption (Figure 3 as compared to Figure 2) during 254-nm irradiation of 3MP–Hg glasses and the accompanying decrease in rate of radical production (Figure 6) imply that the formation of the radicals is accompanied by formation of an Hg compound which is not rapidly

decomposed at this wavelength, presumably because of a relatively low extinction coefficient. The regeneration of the Hg with light at wavelengths in the 260–300-nm range indicates that the compound absorbs in this region. Its absorption has not been resolved from the broad band believed to be the spectrum of trapped radicals, nor are any lines attributable to it resolved from the ESR spectrum.

The only Hg compounds which might account for the observations seem to be HgH, HgC$_6$H$_{13}$, and Hg(C$_6$H$_{13}$)$_2$. Assuming for the purpose of illustration the compound is HgH, a plausible mechanism for radical production may be represented as

$$Hg(6^1S_0) \xrightarrow[254 \text{ nm}]{h\nu} Hg(6^3P_1) \qquad (1)$$

$$Hg(6^3P_1) + RH \rightarrow HgH + R \qquad (2)$$

$$HgH \xrightarrow[200–300 \text{ nm}]{h\nu} Hg + H^* \qquad (3)$$

$$H^* + RH \rightarrow H_2 + R \qquad (4)$$

According to this sequence of reactions, the initial rapid rise in radical concentration in the experiment of Figure 6 is attributable to reactions 1 and 2. When the Hg concentration has been depleted, radical growth becomes slow, but is increased when the AH4 which provides a band of wavelengths absorbed by HgH is used. Radical production continues by the reaction sequence 3 + 4, and by reactions 1 and 2 utilizing the Hg produced in reaction 3.

HgH is known to be produced with significant yield when Hg is activated by 254-nm light in the presence of gaseous H$_2$, CH$_4$, C$_2$H$_6$, C$_3$H$_8$, or C$_4$H$_{10}$.[17-19] It has only a transitory lifetime as a gas, but has been postulated to be an intermediate which persists for several minutes in a liquid alkane.[4b] If it is formed in the glassy systems and has a still longer lifetime, a repeated utilization of an Hg atom with radical formation both by Hg excitation and by hot H atoms from HgH activation seems possible. The energy of the hot hydrogen atoms, H*, produced by reaction 3 would be >50 kcal mol^{-1} for the wavelengths available. The probability for such a hydrogen atom to be thermalized before abstraction of H from 3MP in the glass at 77 K is low.[20] Although H atoms can be thermalized and trapped in perdeuterated hydrocarbons at <50 K, they are not found in protiated glasses even at 4 K.[14]

Direction dissociation of C–H bonds by energy transfer from Hg(6^{3}P$_1$) atoms (Hg(6^{3}P$_1$) + RH → Hg(^{1}S$_0$) + R + H), in contrast to HgH formation, could account for the behavior observed if some of the Hg atoms combine with radicals to form HgR and the H atoms abstract H from other molecules to yield more radicals. In this case the HgC$_6$H$_{13}$ must be decomposed by light in the 260–300-nm region in a reaction analogous to (3). HgC$_6$H$_{13}$ is expected[21] to have a bond energy of ~3 kcal mol^{-1}, sufficient for stability at 77 K. Hg(C$_6$H$_{13}$)$_2$ would be expected to be stable even at room temperature. It is unlikely that it contributes significantly to the primary disappearance of the Hg because it could only be formed by sequential processes involving diffusion (Hg + R → HgR, HgR + R → Hg$_2$R$_2$, or 2HgR → HgR$_2$ + Hg).

Radical Tracks. In the experiment of Figure 7, the ratios of number of radicals present at the end of the experiment to number of Hg atoms initially present was 11 and other experiments with the AH4 lamp regularly showed similarly

high ratios, indicating that on the average each Hg atom must have absorbed many photons and caused the decomposition of many 3MP molecules. For these radicals to be observable, sufficient Hg atom diffusion must occur during the period of illumination to allow the radicals to be spaced at distances great enough so that they do not react with each other rapidly. The diffusion coefficient of C$_6$H$_{13}$ radicals in 3MP at 77 K has been estimated as 9 × 10^{-20} cm^2 sec^{-1}.[12] Estimating the diffusion coefficient of Hg atoms to be 2 × 10^{-19} cm^2 sec^{-1}, on the basis of the relative radii, it may be estimated that such atoms undergo an average displacement of 0.07 Å sec^{-1} (using the relation $\bar{X}^2 = 2Dt$ where X = the displacement in centimeters, D the diffusion coefficient, and t the time). Each Hg atom in an ESR sample absorbing 10^{11} to 10^{12} photons sec^{-1} from the AH4 lamp absorbs a photon about once in every few hundred seconds. Assuming these estimates, the average displacement between photon absorptions is several tens of ångströms or several molecular diameters. It would be of interest to determine radical yields per mercury atom at lower temperatures, where diffusion is very slow. If this did not decrease the radical yields per Hg atom at the same intensity, it would suggest that radicals may be formed by energy transfer at several molecular diameters from the Hg atoms.

Radical Spectra. The six-line ESR spectrum of Figure 4B is similar to the spectra obtained in 3MP glass following γ radiolysis,[11] abstraction by hot H atoms from the photolysis of HI,[20] and photosensitization by benzene.[6] Systems exposed to 254-nm light give the sharp spectrum of Figure 4A which reverts to the broader spectrum (4B) in the dark, with relatively little change in concentration. The sharpening on illumination (which has also been observed for the radicals in γ-irradiated 3-ethylpentane glass, 3-methylheptane glass, and polycrystalline n-hexane)[13] must result from an isomerization or change to a hindered configuration of the radical made possible by the energy of the absorbed photon. It is not known whether the radicals produced by the Hg photosensitization are born in this configuration or promoted to it by subsequent absorption of a 254-nm photon.

The optical spectrum of the radicals formed by Hg photosensitized decomposition of 3MP glass shown in Figure 3 is a composite of the spectrum of the sec-3-methylpentyl radicals which give the ESR spectra of Figure 4 and any absorption contributed by the Hg compound which is responsible for the disappearance of the Hg spectrum of Figure 2. Figure 3 is similar to recently reported absorption spectra for C$_5$ and C$_6$ alkyl radicals, produced by electron pulse radiolysis in the liquid phase[22,23] and proton pulse radiolysis in the gas phase.[24]

Spectra of Alcohol Radicals. The spectra of the radicals produced in vapor deposited Hg–CH$_3$OH and Hg–C$_2$H$_5$OH mixtures by illumination with the AH4 source (Figure 5) are similar to those reported for the illumination of alcohols with a low-pressure Hg lamp with Vycor filter (to remove light below 210 nm), and ascribed to methyl and ethyl radicals, respectively.[25] The large singlet in the spectrum from C$_2$H$_5$OH after 1-hr decay (Figure 5D) is probably due to the ethoxy (C$_2$H$_5$O) radical. The prominent line in the center of the spectrum from CH$_3$OH (Figure 5A) is presumably due to methoxy radicals. By analogy, the spectrum observed after photolysis of Hg–C$_3$H$_7$OH (Figure 5C) is attributed to propyl and propoxy radicals. In contrast to the spectrum of Figure 5B, γ-radiolysis of ethanol glass

produces a clean five-line spectrum of the CH_3CHOH radical.[26]

Since the absorption band of highest wavelength in the pure alcohols occurs below 200 nm,[27] the earlier workers[25] suggested the possibility that the photolytic radical production which they observed might be due to trace impurities. However, their results were unaffected by added oxygen and its reaction products. It may be speculated that the radicals reported were produced by Hg-photosensitized reactions as in the present work. The solubility of Hg, and the extinction coefficient for the $Hg(6^1S_0) \rightarrow Hg(6^3P_1)$ transition, in liquid alcohols is about the same as that in hydrocarbons.[8]

References and Notes

(1) This work has been supported in part by the U.S. Atomic Energy Commission under Contract No. AT(11-1)-1715 and by the W. F. Vilas Trust of the University of Wisconsin.

(2) See for examples and references: A. Ekstrom, *Radiat. Res. Rev.*, **2**, 381 (1970); J. E. Willard, *Science*, **180**, 553 (1973); L. Kevan in "Advances in Radiation Chemistry", Vol. 4, M. Burton and J. L. Magee, Ed., Wiley-Interscience, New York, N.Y., 1973.

(3) For reviews of Hg-photosensitization reactions refer to (a) J. G. Calvert and J. N. Pitts, "Photochemistry", Wiley, New York, N.Y., 1966, Chapter 2, p 27; (b) R. J. Cvetanovic, *Prog. React. Kinet.*, **2**, 39 (1964); (c) R. A. Holroyd and G. W. Klein, *J. Phys. Chem.*, **67**, 2273 (1963).

(4) (a) M. K. Phibbs and B. de B. Darwent, *J. Chem. Phys.*, **18**, 679 (1950); (b) R. R. Kuntz and G. J. Mains, *J. Am. Chem. Soc.*, **85**, 2219 (1963).

(5) F. P. Lossing, D. G. H. Marsden, and J. B. Farmer, *Can. J. Chem.*, **34**, 701 (1956).

(6) N. N. Bubnov, N. M. Bazhin, and V. V. Voevodskii, *Kinet. Katal.*, **5**, 357 (1964).

(7) S. C. Srinivasan and J. E. Willard, *J. Phys. Chem.*, **77**, 2171 (1973); B. J. Brown and J. E. Willard, unpublished.

(8) (a) J. N. Spencer and A. F. Voigt, *J. Phys. Chem.*, **72**, 464 (1968); (b) R. R. Kuntz and G. J. Mains, *ibid.*, **68**, 408 (1964).

(9) For discussion and references see S. N. Vinogradov and H. E. Gunning, *J. Phys. Chem.*, **68**, 1962 (1964).

(10) J. H. Baxendale and F. W. Mellows, *J. Am. Chem. Soc.*, **83**, 4720 (1961).

(11) D. J. Henderson and J. E. Willard, *J. Am. Chem. Soc.*, **91**, 3014 (1969).

(12) M. A. Neiss and J. E. Willard, *J. Phys. Chem.*, **79**, 783 (1975).

(13) E. D. Sprague and J. E. Willard, *J. Chem. Phys.* in press.

(14) D. Timm and J. E. Willard, *J. Am. Chem. Soc.*, **91**, 3406 (1969); M. Long and J. E. Willard, *J. Phys. Chem.*, **74**, 1207 (1970).

(15) L. B. Knight, Jr., and W. Weltner, Jr., *J. Chem. Phys.*, **55**, 2061 (1971).

(16) "Berkeley Analyses of Molecular Spectra", Vol. 2, J. G. Phillips and S. P. Davis, Ed., University of California Press, Berkeley, Calif., 1968.

(17) A. B. Callear and R. E. M. Hedges, *Trans. Faraday Soc.*, **66**, 615 (1970).

(18) A. B. Callear and P. M. Wood, *J. Chem. Soc., Faraday Trans. 2*, **68**, 302 (1972).

(19) A. C. Vikis and D. J. LeRoy, *Can. J. Chem.*, **50**, 595 (1972); **51**, 1207 (1973).

(20) L. Perkey and J. E. Willard, *J. Chem. Phys.*, **60**, 2732 (1974).

(21) M. Krech and S. J. Price, *Can. J. Chem.*, **41**, 224 (1964).

(22) L. W. Burggraf and R. F. Firestone, *J. Phys. Chem.*, **78**, 508 (1974).

(23) R. H. Schuler and L. K. Patterson, *Chem. Phys. Lett.*, **27**, 369 (1974).

(24) H. Christensen, G. Nilsson, K. Thuomas, and T. Reitberger, *Chem. Phys. Lett.*, **22**, 533 (1973).

(25) P. J. Sullivan and W. S. Koski, *J. Am. Chem. Soc.*, **84**, 1 (1962); **86**, 159 (1964).

(26) S. Fujii and J. E. Willard, *J. Phys. Chem.*, **74**, 4318 (1970).

(27) A. J. Harrison, B. J. Cederholm, and M. A. Teruilliger, *J. Chem. Phys.*, **30**, 355 (1959); A. J. Harrison and D. R. W. Price, *ibid.*, **30**, 357 (1959).

On the Use of Structural Probe Ions for Relaxation Studies in Glasses. I. Spectroscopic Properties of Cobalt(II) in Chloride-Doped Potassium Nitrate–Calcium Nitrate Glasses

A. Barkatt* and C. A. Angell

Department of Chemistry, Purdue University, Lafayette, Indiana (Received April 9, 1975)

As a preliminary to studies of the relaxation kinetics of processes involving temperature-induced coordination changes for transition metal ions dissolved in glasses, it has been necessary to determine the equilibrium spectroscopic and structural characteristics of these systems. For the particular case of the equilibrium between the tetrahedral and dodecahedral forms of Co(II) in 3:2 KNO_3–$Ca(NO_3)_2$ glasses containing 0–9 mol % KCl, the enthalpy change is found to be (5.2 ± 0.2) kcal/mol. Decreases in temperature and increases in KCl content shift the equilibrium in favor of more tetrahedral Co(II) formation. The molar absorptivities of the two forms were determined. Preliminary relaxation measurements indicate that at the glass transition temperature the relaxation time of the local Co(II) environment is of the same order as the structural relaxation time characteristic of the whole system.

Introduction

Recently there has been much interest in characterizing the time scales on which inorganic glasses and supercooled liquids respond to different types of perturbation from their equilibrium states. For instance (average) relaxation times for electrical field perturbations, determined by conductivity relaxation studies[1] prove in some cases to be many orders of magnitude shorter than the (average) relaxation times for shear stress perturbations as determined by

shear viscosity and ultrasonic absorption studies.[2] Volume and enthalpy relaxation studies[3] using refractive index, light scattering, dilatometry, and differential scanning calorimetry techniques have yielded relaxation times that agree with each other within a factor of 2 but which are an order of magnitude or more longer than the shear relaxation times. It is the volume and enthalpy relaxations which determine the temperature at which the so-called "glass transition" occurs, and these processes would appear to

provide the best measure of the rate at which general structural reorganizations occur at constant pressure and temperature in the vitreous quasi-lattice. The different characteristics of the conductivity relaxation process have naturally been ascribed to the quasi-independent motion of charge-carrying species in the glass. In the two types of glass on which these recent measurements have been concentrated, $Na_2O \cdot 2SiO_2$ and $6KNO_3 \cdot 4Ca(NO_3)_2$, the mobile species are assumed to be Na^+ and K^+ ions, respectively.

The independence of such relaxation processes has prompted us to inquire into the possibility of studying relaxation processes in glasses by techniques which follow specifically the structural equilibration of single elements of the glass structure. It would seem quite possible that such measurements could reveal the presence of a number of separable relaxation processes which occur sequentially in the overall process of structural equilibration, particularly in a multicomponent glass, in which case the total process will only be properly understood when its elements have been individually elucidated. The existence of structural elements with different relaxation times has in fact been proposed as one possible explanation of the finding that the relaxation process in viscous liquids can only rarely be described in terms of a single relaxation time. Spectroscopic studies, which can follow changes in the local structure around specific ions in the glass, would seem to offer an excellent means of examining this question since a series of structure-sensitive probes, each with different charge and/or shape characteristics, can in principle be studied in a single base glass.

It has been known qualitatively for a long time that temperature-induced coordination changes for transition metal ions dissolved in various types of glasses are arrested near the ordinary glass transition temperature,[4] and we have therefore decided to investigate this time-dependent structural equilibrium quantitatively in order to determine its relaxation kinetics. This type of process is easily followed spectroscopically since the d–d electronic transition energies of 3d cations depend sensitively on the chemical nature and geometrical arrangement of the nearest neighbors. When these change with time, the absorption coefficient at the wavelength of a chosen transition will reflect that change and, in favorable cases, very small perturbations from equilibrium will be detectable.

Since it is clearly desirable to carry out such measurements on systems which have already been characterized with respect to other relaxation processes, we have investigated the possibility of studying the structural relaxation of Co(II) ions in what are essentially $60KNO_3 \cdot 40Ca(NO_3)_2$ base glasses. To establish a temperature-dependent structural equilibrium involving Co(II) ions in these glasses it is necessary to add a small mole fraction (0.01–0.04) of chloride ions. Co(II) is then observed to coordinate selectively with the chloride ions to yield the tetrahedral ($CoCl_4$) group in proportions which increase with decreasing temperature. The small chloride additions have only minor effects on the glass transition temperature, as documented below, and it is probable that the relaxation times for the processes already studied in these glasses[1,2,5] will be little affected by the composition modification. As a preliminary to relaxation studies, it has been necessary to determine such equilibrium spectroscopic and structural characteristics of the system as the molar absorptivities of the high and low temperature coordination states, the enthalpy change for the coordination equilibrium, and the nature of

the centers responsible for these spectra. The present paper reports the results of such studies, and some very preliminary results on the structural relaxation process at long relaxation times.

The use of Co(II) as a spectroscopic structural probe has been based on the fact that its visible absorption spectrum is very sensitive to changes in environment. In basic media, such as $ZnCl_2$ glass,[6] borate,[7-11] silicate,[7-9] and phosphate[12] glasses with a high alkali oxide or alkali halide content, and chloride melts (LiCl–KCl,[13] NH_4NO_3–$LiNO_3$–NH_4Cl,[13] pyridine hydrochloride,[13] KCl–$AlCl_3$,[14] CsCl,[15] $ZnCl_2$[15]), most of the Co(II) is present in tetrahedral coordination, with a spectrum characterized by three strong bands peaking at or about 690, 660, and 623 nm, respectively. The weak absorption band around 570 nm due to Co(II) in acid (low-alkali) oxide glasses[7-12] as well as in certain salt mixtures and molecular solutions, e.g., the sulfates (K_2SO_4–$ZnSO_4$,[6,11] $NaHSO_4$–$KHSO_4$,[16] H_2SO_4[16]) and the acetates ($Pb(OAc)_2$,[17] $HOAc$[18]), has been attributed to octahedrally coordinated Co (II). The effect of distortions of these two symmetries on the spectra has been discussed.[6] However, in order to account for the single, relatively strong peak around 550 nm due to Co(II) in the 3:2 KNO_3–$Ca(NO_3)_2$ glass a third type of symmetry, viz. dodecahedral coordination, has been proposed[19] on account of the similarity between this absorption spectrum and those observed in solutions of the $[Co(NO_3)_4]^{2-}$ and $[Co(CF_3COO)_4]^{2-}$ ions and of $[CoL_2(NO_3)_2]$ complexes where the eightfold coordination has been established using X-ray techniques.[20-22] The spectra of Co(II) in a $LiNO_3$–KNO_3 melt,[13] in KCl–$ZnSO_4$–$ZnCl_2$ glass,[6,19] and in LiOAc–NaOAC glass or melt[18] are very similar to the spectrum observed in KNO_3–$Ca(NO_3)_2$ glass, and have been interpreted in the same way.[18,19]

Experimental Section

a. Composition. Most of the measurements were carried out on 2:3 $Ca(NO_3)_2$–KNO_3 glasses, containing a small amount (8×10^{-3} mol %) of $CoCl_2$ or $Co(NO_3)_2$ and varying amounts (0–9 mol %) of KCl. Leaving the chloride out of consideration, these glasses contained 40.00 mol % or 51.97 wt % $Ca(NO_3)_2$.

A few measurements were carried out on 1.83:3 $Ca(NO_3)_2$–KNO_3 glasses (37.90 mol % or 49.76 wt % $Ca(NO_3)_2$).

b. Method of Preparation and Stability. The desired amounts of $Ca(NO_3)_2 \cdot 4H_2O$, KNO_3, and KCl (Mallinckrodt, AR) were weighed and shaken together. A solution (1 ml, of $CoCl_2 \cdot 6H_2O$ or $Co(NO_3)_2 \cdot 6H_2O$ (Baker, AR) in deionized water, of a desired concentration, was added. The mixture was heated over a bunsen flame until completely dissolved, and heating was continued until most of the water was expelled. Thereafter the melt was bubbled with N_2 in an aluminum block at a constant temperature of 500°K for 30 min to remove the rest of the water, and kept at this temperature for 15 min more to expel N_2 bubbles. This last stage was very effective in preventing the appearance of cracks when the glass was later cooled to the vicinity of T_g. (Trapped N_2 bubbles also appeared to promote devitrification.) Excessive heating was avoided so as to prevent the irreversible decomposition of the Co(II) salt to form gray CoO.

Glass samples (2:3 $Ca(NO_3)_2$–KNO_3) prepared by this procedure and containing 0–5 mol % KCl did not undergo crystallization at any temperature in the 320–500°K range for at least 1 hr. Samples containing 9 mol % KCl under-

went crystallization if maintained for more than about 20 min at temperatures in the 360–440°K range.

1.83:3 Ca(NO₃)₂–KNO₃ glasses were less stable, samples containing 4.5 mol % KCl displaying the same tendency to crystallize as 9 mol % KCl 2:3 Ca(NO₃)₂–KNO₃ samples. Only samples containing 0–2.5 mol % KCl were stable for >1 hr in the least favorable temperature ranges.

c. *Densities.* The densities needed to convert absorbances to molar absorptivities were obtained with sufficient accuracy for present purposes (±0.5%) using a simple volumetric technique.

d. *Spectra.* Absorption spectra of Co(II)-containing solutions of interest were obtained using a Cary 14R recording spectrophotometer. Samples were contained in 1.0-cm Pyrex glass cells mounted in a cartridge-heated aluminum block, the temperature of which was controlled to ±0.1° by means of a Dohrmann EP ProportioNull 1300 controller. The temperature was determined using a sheathed Cu–constantan thermocouple which dipped into the solution just outside the light path. The absorption of the Co(II)-containing solution was determined against the absorption of a solution of the same composition without Co(II).

Results and Discussion

a. *Glass Transition.* The glass transition temperature of 2:3 Ca(NO₃)₂–KNO₃, measured by means of a Perkin-Elmer DSC-2 differential scanning calorimeter operated at 10 deg/min, was (341.5 ± 0.5)°K, in agreement with previous results.[23]

Increasing KCl concentrations caused a slight decrease in T_g. (In the presence of 4.6 mol % KCl, T_g = (340.0 ± 0.5)°K; in the presence of 8.8 mol % KCl, T_g = (338.5 ± 0.5)°K.)

1.83:3 Ca(NO₃)₂–KNO₃ glasses (chloride-free) also had a slightly lower T_g, (339.0 ± 0.5)°K.

b. *Densities.* Densities of the KNO₃–Ca(NO₃)₂ solutions agreed with those of Dietzel and Poegel[24] within the expected limits except at temperatures outside the range in which spectral data were taken. Our data yield a smaller expansion coefficient, $\alpha \approx 5.5 \times 10^{-4}$ deg⁻¹. Addition of 4.5 mol % KCl caused only marginal density changes (≈0.2% decrease).

c. *Molar Absorptivities of Tetrahedral and Dodecahedral Co(II).* Absorbances determined for Co(II) in various media (see Experimental Section) were converted, using the appropriate composition and density data, to molar absorptivity units (M^{-1} cm⁻¹). The results are shown in Figure 1. Curve A is the spectrum of Co(II) present in 0.77 mM concentration in a saturated aqueous solution of pyridine hydrochloride at 294.7°K (ρ = 1.163 g ml⁻¹), where Co(II) is expected to be present in a tetrahedral configuration. Curves B, C, and D are the spectra of Co(II) (1.35 mM concentration) in 2:3 Ca(NO₃)₂–KNO₃ + KCl glasses. Curve B is the spectrum in a 8.85 mol % Cl⁻ glass at 343.0°K, where the tetrahedral form predominates. Curve C is the spectrum in the chloride-free glass, where only dodecahedral Co(II) is present, at a temperature of 343.0°K. Curve D is the spectrum in a 0.81 mol % Cl⁻ glass at 340.9°K, where the tetrahedral and dodecahedral forms are present in comparable concentrations. Note that the three curves intersect at a common point (580 nm), suggesting that only two species are involved in the equilibrium.

The molar absorptivities at the absorption maxima are summarized in Table I and compared with previous results obtained in media where a major fraction of the Co(II) was
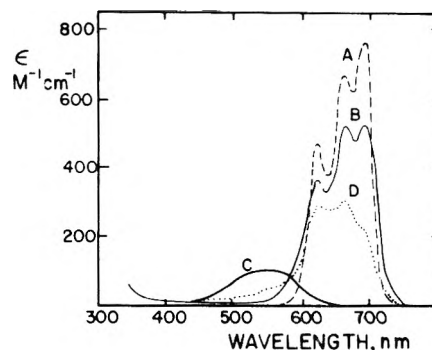
Figure 1. Absorption spectra of Co(II) in various media (for explanation of different curves see text).

considered to be present either in a tetrahedral or in a dodecahedral coordination.

d. *The Temperature Dependence of the* $Co(II)_{dod} \rightleftarrows Co(II)_{tet}$ *Equilibrium.* The position of the $Co(II)_{dod} \rightleftarrows Co(II)_{tet}$ equilibrium in mixed nitrate solutions was studied as a function of composition (0–9 mol % KCl) and temperature (325–510°K) by measuring the absorbance of the Co(II)-doped solution (against that of the same solution without Co(II)) at two wavelengths: the Co(II)_{tet} absorption maximum at 660 nm and the Co(II)_{dod} maximum at 550 nm. Results obtained for the temperature dependence of the Co(II) absorption spectrum in the presence of an intermediate concentration of chloride are presented in Figure 2. The approximate isobestic point at ≈580 nm is consistent with the participation of only two species in the exchange.

Denoting the concentrations of Co(II)_{tet}, Co(II)_{dod}, and total Co(II) by [T], [D], and [S], respectively, we have

$$[T]/[D] = K$$
$$[T] + [D] = [S] \qquad (1)$$

Hence

$$\frac{[S]}{[T]} - 1 = \frac{[D]}{[T]} = \frac{1}{K}$$

Substituting

$$d \ln K/dT = \Delta H/RT^2$$

between any two temperatures, we obtain

$$\ln\left(\frac{[S]_1}{[T]_1} - 1\right) - \ln\left(\frac{[S]_2}{[T]_2} - 1\right) =$$
$$\ln\frac{K_2}{K_1} = \frac{\Delta H}{R}\left(\frac{1}{T_1} - \frac{1}{T_2}\right) \quad (2)$$

([S]₂ may be slightly different from [S]₁ for the same sample because of the temperature dependence of the density.)

ΔH may therefore be calculated from the slope of the plot of $\ln [([S]/[T]) - 1]$ vs. $1/T$.

[T] and [D] are found from the spectra (where the optical pathlength is 1 cm):

$$D_{660} = \epsilon_{660}^T[T] + \epsilon_{660}^D[D]$$
$$D_{550} = \epsilon_{550}^T[T] + \epsilon_{550}^D[D]$$

Therefore

TABLE I: Molar Absorptivities of Co(II) in Various Ionic Media

| Composition | Medium | T, °K | Predominant Co(II) coordination | ϵ, M^{-1} cm^{-1} | | | | Ref |
				690 nm	660 nm	623 nm	550 nm	
KNO_3–$Ca(NO_3)_2$–KCl	Glass	343.0	Tetrahedral	531	525	368	14	This work (B)
NH_4NO_3–$LiNO_3$–NH_4Cl	Melt	433	Tetrahedral	433	454	376	18	13
KCl–$AlCl_3$	Melt	573	Tetrahedral	406	395	250	16	14
CsCl	Melt	973	Tetrahedral	406	394	250	22	15
$ZnCl_2$	Glass	≈300	Tetrahedral	622	489	335	<14	6
Pyridine·HCl–H_2O	Concn soln	294.7	Tetrahedral	745	640	436	<3	This work (A)
Pyridine·HCl	Melt	433	Tetrahedral	634	574	378	8	13
KNO_3–$Ca(NO_3)_2$–KCl	Glass	340.9	Tet–dod mixture	221	305	293	50	This work (D)
$LiNO_3$–KNO_3–LiCl–KCl	Melt	433	Tet–dod mixture	272	327	268	43	13
KNO_3–$Ca(NO_3)_2$	Glass	343.0	Dodecahedral	0.4	0.7	12	99	This work (C)
KNO_3–$Ca(NO_3)_2$	Glass	≈300	Dodecahedral	1	2	12	75	19
$LiNO_3$–KNO_3	Melt	433	Dodecahedral	1	4	21	89	13
LiOAc–NaOAc	Glass	≈300	Distorted dod	5	14	73	156	18
KCl–$ZnSO_4$–$ZnCl_2$	Glass	≈300	Distorted dod (mixed ligands)	37	85	130	92	6
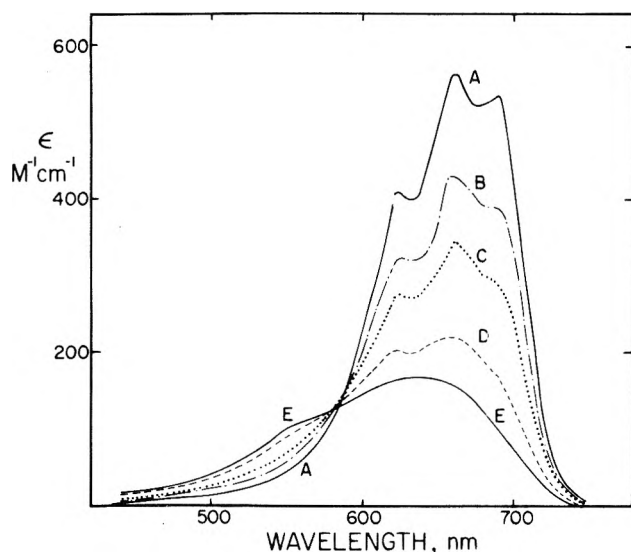
Figure 2. Absorption spectra of Co(II) in 2:3 Ca(NO$_3$)$_2$–KNO$_3$, 2.41 mol % KCl, 8 × 10^{-3} mol % Co(II) (composition E, Table II) at different temperatures: (A) 339.9°K; (B) 377.4°K; (C) 414.6°K; (D) 454.5°K; (E) 502.5°K.

$$[T] = \frac{D_{660} - (\epsilon_{660}{}^{D}D_{550}/\epsilon_{550}{}^{D})}{\epsilon_{660}{}^{T} - (\epsilon_{550}{}^{T}\epsilon_{660}{}^{D}/\epsilon_{550}{}^{D})} = \frac{D_{660} - 0.007D_{550}}{525} \quad (3)$$

$$[D] = \frac{D_{550} - (\epsilon_{550}{}^{T}D_{660}/\epsilon_{660}{}^{T})}{\epsilon_{550}{}^{D} - (\epsilon_{660}{}^{D}\epsilon_{550}{}^{T}/\epsilon_{660}{}^{T})} = \frac{D_{550} - 0.027D_{660}}{99} \quad (4)$$

The correction term (0.007D_{550}) in eq 3 due to the absorption of Co(II)$_{oct}$ at 660 nm is <1% when [T]/[S] > 0.14.

[S] can be calculated either from eq 1 or from the relation

$$[S] = \frac{n\rho(T)}{W} \quad (5)$$

where n is the total quantity of Co(II) present (in moles), W the weight of the sample, and $\rho(T)$ the density.

In the present measurements, very close agreement was found between [S] as calculated from eq 1 and from eq 5, and the small discrepancies between the values obtained by each of these methods did not exhibit any significant trend.
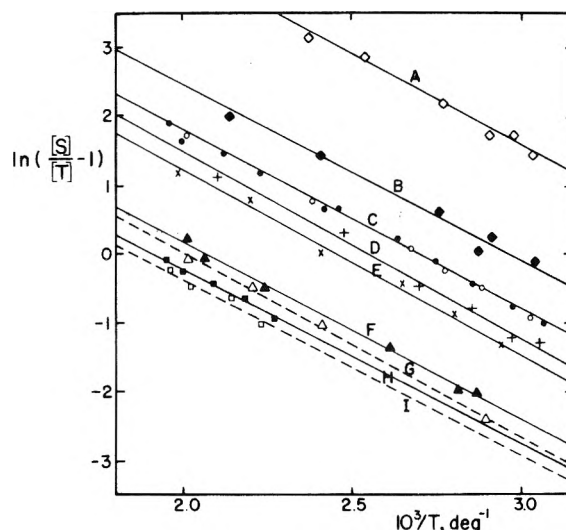

Figure 3. The dependence of the fraction of tetrahedral Co(II) on temperature and chloride content (for explanation of different curves see Table II).

Using eq 3 and 5, the fraction of tetrahedral Co(II), [T]/[S], was calculated as a function of temperature at various glass compositions. The results are shown in Figure 3. Glass compositions are given in Table II.

In the case of the chloride-rich compositions H and I no measurements could be carried out over the 360–440°K temperature range because of crystallization effects (see Experimental Section, b). In the case of the 2:3 Ca(NO$_3$)$_2$–KNO$_3$ glass (composition H) rapid cooling through this range made it possible to prevent crystallization and carry out measurements at 343°K (see above, c), but in the case of the less stable 1.83:3 Ca(NO$_3$)$_2$–KNO$_3$ glass (composition I) crystallization always proceeded too rapidly. The values of ln [([S]/[T]) − 1] were calculated for each composition and plotted against T^{-1} (see Figure 3). The corresponding values of ΔH were calculated according to eq 2 and recorded in the fifth column of Table II. From Figure 3 it was also possible to calculate T_e, the temperature at which [T] = [D] = [S]/2 and ln [([S]/[T]) − 1] = 0, for each

TABLE II: The $Co(II)_{dod} \rightleftharpoons Co(II)_{tet}$ Equilibrium at Various Glass Compositions

Composition	$Ca(NO_3)_2$–KNO_3 ratio	[KCl], mol %	Total [Co(II)], mol %	$-\Delta H$, kcal/mol	T_e, °K
A	2:3	0.30	8×10^{-3}	5.22	277[a]
B	2:3	0.81	8×10^{-3}	5.13	339
C·	2:3	1.21	8×10^{-3}	5.09	371
Co	2:3	1.21	16×10^{-3}	5.09	371
D	2:3	1.61	8×10^{-3}	5.43	394
E	2:3	2.41	8×10^{-3}	5.33	408.5
F	2:3	4.63	8×10^{-3}	5.13	484
G	1.83:3	4.78	8×10^{-3}	5.37	498
H	2:3	8.85	8×10^{-3}	5.00	524
I	1.83:3	9.13	8×10^{-3}	5.01	541.5

[a] Extrapolated.

of the glass compositions investigated. The dependence of T_e on the chloride content is shown in the last column of Table II and in Figure 4.

The results obtained can be summarized as follows. (1) In nitrate–chloride mixtures, low temperatures favor the four-coordinated tetrahedral arrangement [CoCl₄] as found earlier by Gruen et al. for alkali metal nitrate–chloride melts.[13] This is an interesting inversion of the natural tendency to higher coordination numbers at lower temperatures seen in most systems (both of mixed ligand type (e.g., H_2O + HCl) and single ligand type (e.g., $ZnCl_2$ + $AlCl_3$[15] or Na_2O + P_2O_5)).[25] (Actually if one considers only the number of *anions* in the coordination sphere, then no change in *coordination number* is involved in the process.) High-pressure studies will be needed to help decide whether the change occurs because of packing problems for the [Co(NO₃)]₄ group in the second coordination shell, because the Co^{2+}–Cl^- bond is substantially stronger than the Co^{2+}–NO_3^- bond, or because the stabilization energy for Co(II) in dodecahedral fields is comparatively small. (2) $-\Delta H$ = (5.2 ± 0.2) kcal/mol. This value is not affected by changing the Cl^- content over the range 0–9 mol % or changing the $Ca(NO_3)_2$–KNO_3 ratio from 2:3 to 1.83:3. (3) In the absence of Cl^- the coordination of Co(II) is dodecahedral independent of temperature in the range investigated. (4) At small Cl^- contents small additions of Cl^- cause large increases in the temperature, T_e, below which most of the Co(II) is in the CoCl₄ state. Above 5 mol % KCl the effect of Cl^- on T_e is slight. When a large excess of Cl^- is present, it is evidently the absolute concentration of Cl^- in the glass, rather than the Co^{2+}:Cl^- ratio that determines the value of T_e. This useful result is indicated in Figure 4 by the coincidence of points for the different Co(II) concentrations (8 × 10^{-3} and 16 × 10^{-3} mol %, respectively). It implies that, in relaxation studies, for which small heat capacities and rapid heat transfers are desirable, it will be possible to reduce sample thicknesses without changing the absorbance or the position of coordination equilibrium, simply by using increased concentrations of Co(II). (5) Changing the $Ca(NO_3)_2$–KNO_3 ratio from 2:3 to 1.83:3 brings about a small increase (10–20°) in T_e, i.e., favors the tetrahedral symmetry.

e. Preliminary Relaxation Time Measurements. The present results allow us to calculate the change in absorbance brought about by the sudden small change in system temperature employed in a T-jump type relaxation measurement. For instance, if it is assumed that for a certain glass composition at a temperature close to T_g, e.g.,
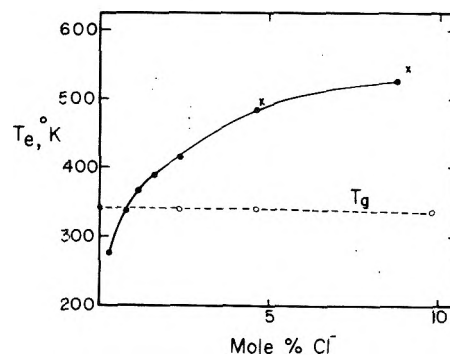

Figure 4. The dependence of the $Co(II)_{dod} \rightleftharpoons Co(II)_{tet}$ equimolar temperature T_e on glass composition. (T_g values indicated by dashed line.) (●) 2:3 $Ca(NO_3)_2$–KNO_3; (×) 1.83:3 $Ca(NO_3)_2$–KNO_3.

340.7°K, the fraction of Co(II)$_{tet}$, [T]/[S], is 0.5000, then a temperature jump of 1° will decrease [T]/[S] to 0.4944 when ΔH is 5.2 kcal/mol. With [S] = 1.35 mM (corresponding to 8 × 10^{-3} mol % Co(II)) and an optical pathlength of 1 cm, the resulting change in absorbance at 660 nm will be 0.0039. Such a change, although considerably less than one would freely choose for the purpose, should be sufficient to permit a reasonably accurate assessment of the average relaxation time and its distribution using the low noise Cary system with a 0–0.1 absorbance units slide wire, and a temperature jump of 1–2°.

Some preliminary measurements in the vicinity of T_g, using a 0–1.0 absorbance slide wire and larger temperature jumps of ~7°, have been made by the straightforward (but slowly responding) method of changing the temperature setting on the controller thermostatting the aluminum block cell holder. The changes in absorbance at 660 nm and in temperature were recorded simultaneously and are shown, for the most trouble-free run, in Figure 5. It is clear that at the temperature of this experiment, the absorbance equilibration lags far behind the temperature equilibration.

The approximate average relaxation time for the Co(II) environment could therefore be obtained by taking, as an initial absorbance, a value at any time after the temperature had reached its final equilibrium value, and finding the time required for the absorbance to undergo (1 − 1/e) of the change to the final equilibrium value. Several different values of the relaxation time could be obtained by taking different points on the absorbance–time curve as initial values. Using the data in Figure 3, each of these initial absorbance values could be associated with a temperature, T_f,
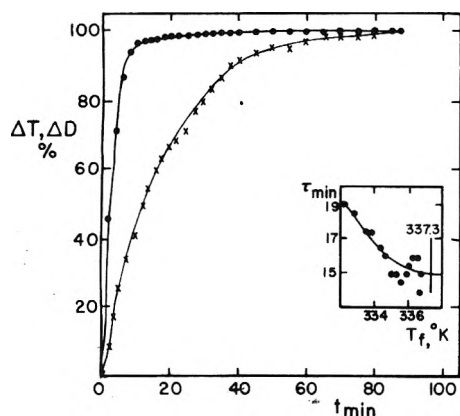
Figure 5. The dependence of the relaxation time on the structural equilibrium temperature of the glass T_f. 16×10^{-3} mol % Co(II) in a 2:3 Ca(NO$_3$)$_2$–KNO$_3$, 1.21 mol % KCl glass. Changes in absorbance measured at 660 nm: (●) ΔT, per cent of total (328.9°K → 337.3°K); (X) ΔD, per cent of total (1.415 → 1.356).

at which the system at equilibrium would have this absorbance. The relaxation time τ is plotted as a function of this "fictive" temperature in the inset to Figure 5, and the dependence is seen to be rather small. The limiting value $\tau \approx 15$ min for T_F → 337.3 (the final temperature) should correspond to the value of τ for very small temperature jumps, i.e., the "equilibrium" value, apart from errors introduced by the assumption that the relaxation curve for small perturbations is exponential in form.

The probe ion relaxation time, $\tau_{Co(II)}$, assessed in this way is almost two orders of magnitude larger than the shear relaxation time τ_s assessed from the viscosity η^5 by the Maxwell relation

$$\tau_s = \eta/G_\infty \tag{6}$$

where the limiting high-frequency shear modulus G_∞ is available from ultrasonic sound velocity data.[2,5] As noted earlier, the shear relaxation time is usually considerably smaller than the volume or enthalpy relaxation times and it is the latter which provide the best guide to the overall structural relaxation time. Unfortunately the latter times, whose relation to the Co(II) times is of greatest interest, have not yet been assessed for the nitrate glass. We may however turn to a second value of $\tau_{Co(II)}$, 240 sec, measured at T_g (10 deg min^{-1}), 341.5 K, and compare this with recently determined values of τ_H and τ_V for B$_2$O$_3$ and As$_2$S$_3$ at their T_g (10 deg min^{-1}).[3d,e] These values are all of the order of hundreds of seconds suggesting that $\tau_{Co(II)}$, while much longer than τ_s, may not be significantly longer than the overall structural relaxation time (and in fact may be directly determined by it through cooperative mechanisms).

In this case the small dependence of τ on fictive temperature, obtained on the assumption of exponential decay kinetics, must be suspect. It could be the fortuitous result of cancellation of effects due to actual nonexponential decays (which characterize the enthalpy and volume relaxations[3])

by opposing effects of nonlinear responses due to the relatively large displacements from equilibrium utilized in the present technique. This question will be resolved in future measurements.

The significant conclusions that we can draw at the present time are (1) the study of the kinetics of local structure rearrangements in glassy media by time-dependent spectrophotometry[26] is experimentally feasible; (2) the local structure equilibration time for a quite complex coordination shell rearrangement of a minor component in a mixed nitrate glass is probably little different from the overall vitreous quasi-lattice relaxation time.

References and Notes

(1) (a) P. B. Macedo, C. T. Moynihan, and R. Bose, *Phys. Chem. Glasses*, **13**, 171 (1972); (b) V. Provenzano, L. P. Boesch, V. Volterra, C. T. Moynihan, and P. B. Macedo, *J. Am. Ceram. Soc.*, **55**, 492 (1972); (c) F. S. Howell, R. A. Bose, P. B. Macedo, and C. T. Moynihan, *J. Phys. Chem.*, **78**, 639 (1974).
(2) (a) J. Tauke, T. A. Litovitz, and P. B. Macedo, *J. Am. Ceram. Soc.*, **51**, 158 (1968); (b) R. Weiler, R. Bose, and P. B. Macedo, *J. Chem. Phys.*, **53**, 1258 (1970).
(3) (a) L. Boesch, A. Napolitano, and P. B. Macedo, *J. Am. Ceram. Soc.*, **53**, 148 (1970); (b) J. A. Bucaro, H. D. Dardy, and R. D. Corsaro, *J. Appl. Phys.*, **46**, 741 (1975); (c) S. M. Rekhson and O. V. Mazurin, *J. Am. Ceram. Soc.*, **57**, 327 (1974); (d) C. T. Moynihan, P. B. Macedo, N. S. Saad, M. A. Debolt, B. E. Dom, A. J. Easteal, and J. A. Wilder, Proceeding of the VIth All-Union Conference on the Glassy State, Leningrad, USSR, to be published; (e) C. T. Moynihan, private communication.
(4) W. A. Weyl, "Colored Glasses", Society of Glass Technology, Sheffield, England, 1961.
(5) H. Tweer, N. Laberge, and P. B. Macedo, *J. Am. Ceram. Soc.*, **54**, 121 (1971).
(6) M. D. Ingram and J. A. Duffy, *J. Chem. Soc. A.*, 2575 (1968).
(7) A. A. Kefeli, *Dokl. Akad. Nauk SSSR*, **57**, 61 (1947); **58**, 1051 (1947).
(8) N. I. Vlasova, E. I. Galant, and A. A. Kefeli, *Proc. 3rd All-Union Conf. Glassy State*, **2**, 327 (1959).
(9) M. A. Aglan and H. Moore, *J. Soc. Glass Technol.*, **39**, 351 (1955).
(10) B. F. Dzhurinskii, *Izv. Akad. Nauk SSSR, Neorg., Mater.*, **1**, 272, 277 (1965).
(11) C. A. Angell, *J. Am. Ceram. Soc.*, **51**, 125 (1968).
(12) B. F. Dzhurinskii, *Izv. Akad. Nauk SSSR, Neorg. Mater.*, **1**, 434 (1965).
(13) D. M. Gruen, P. Graf, S. Fried, and R. L. McBeth, *Proc. Second Int. Conf. Peaceful Uses At. Energy*, **28**, 112 (1958).
(14) H. A. Oye and D. M. Gruen, *Inorg. Chem.*, **4**, 1173 (1965).
(15) C. A. Angell and D. M. Gruen, *J. Inorg. Nucl. Chem.*, **29**, 2243 (1967).
(16) J. A. Duffy, F. P. Glasser, and M. D. Ingram, *J. Chem. Soc. A*, 551 (1968).
(17) M. D. Ingram, G. G. Lewis, and J. A. Duffy, *J. Phys. Chem.*, **76**, 1035 (1972).
(18) J. A. Duffy and M. D. Ingram, *J. Chem. Soc. A*, 2398 (1969).
(19) J. A. Duffy and M. D. Ingram, *J. Am. Ceram. Soc.*, **51**, 544 (1968).
(20) F. A. Cotton, D. M. L. Goodgame, and R. H. Soderberg, *Inorg. Chem.*, **2**, 1162 (1963).
(21) F. A. Cotton and J. G. Bergman, Jr., *J. Am. Chem. Soc.*, **86**, 2941 (1964).
(22) J. G. Bergman, Jr., and F. A. Cotton, *Inorg. Chem.*, **5**, 1208, 1420 (1966).
(23) K. J. Rao, D. B. Helphrey, and C. A. Angell, *Phys. Chem. Glasses*, **14**, 26 (1973).
(24) A. Dietzel and H. P. Poegel, *Proc. Int. Glass Congr.*, **34d**, 219 (1953).
(25) A. Paul, *J. Non-Cryst. Solids*, **15**, 517 (1974).
(26) A reviewer has suggested the term "chronospectrophotometry" for this type of study.

COMMUNICATIONS TO THE EDITOR

The Chromatographic Technique of Diffusivity Measurement

Sir: Recently, Grushka and Kikta[1] have discussed an extension of the chromatographic broadening method to liquid phase diffusivity measurements. We too have developed this technique,[2] and are therefore prompted to comment on several points raised by Grushka and Kikta which may be misleading to potential users of the technique. In addition, we provide an example of a hitherto unreported application of the method.

First, Grushka and Kikta[1] have implied that fulfillment of the condition

$$\frac{R_0{}^2 \bar{U}}{D_{AB}L} \ll 0.1 \qquad (1)$$

is necessary for the measurement of molecular diffusivities by the chromatographic technique. Here, R_0 and L are the radius and length of the diffusion tube respectively, $\bar{U}$ is the average linear velocity of the flow, and D_{AB} the molecular diffusivity of species A and B.

At any instant of time the dispersing solute is normally distributed along the diffusion tube. However, observation of the eluted sample peak is necessarily carried out over a finite time at a fixed cross section so that the temporal variation of the solute concentration is not in general normal, because the diffusion process continues during the time of measurement. If the diffusion process is slow (i.e., condition 1 is satisfied) the skewness of the distribution is negligible[2,3] and graphical methods suffice to obtain the moments of the eluted peak from the recorded analog signal. However, condition 1 need not be fulfilled, provided that a means of digitally recording the solute concentration is available, because then all the moments of a peak can be constructed and the complete working expressions,[2-4] including the above-mentioned effects, may be used for the evaluation of the molecular diffusivity.

This relaxation of condition 1 is important in cases where the molecular diffusivity is low, so that fulfillment of (1) would require inordinately long experiment times.[4]

Grushka and Kikta[1] also discussed the influence of a coiled diffusion tube upon the dispersion process. They have speculated that the variation of the apparent molecular diffusivity with flow velocity, at high velocities, is a result of this coiling. In a recent publication,[4] we have shown that this is indeed the case, by means of a comparison of our experimental results with the theoretical analysis of Nunge et al.[5] We therefore suggest that the work of Nunge et al.[5] can be used to estimate the errors associated with the use of a coiled diffusion tube, and to ascertain the upper limit to the flow velocities to be employed for diffusivity measurements in particular cases. We are unable to

examine the work of Grushka and Kikta in this context, because the radius of curvature of their diffusion tube is not specified.

Grushka and Kikta[1] have also considerably underrated the potential of the chromatographic method for liquid phase diffusivity studies, in that they have suggested that only mutual diffusion coefficients at infinite dilution can be measured by this technique. Their conclusion was based upon the effect of changing the concentration of the solute in the injection pulse only. Taylor's original analysis of the problem[6] supports this view because, for the experimental conditions employed by Grushka and Kikta,[1] the maximum change of the mole fraction of chloroform when a pure sample of toluene is injected into it is only 8×10^{-3}. Thus, the diffusion process in such an experiment takes place in essentially pure solvent, and dilution of the solute in the injection pulse only serves to decrease the concentration perturbation. If much larger sample volumes were injected than those employed by Grushka and Kikta, so that the perturbation to the mole fraction of the flowing liquid was significant, then the diffusion process would take place over a wide and changing range of mixture composition. Thus the measured diffusion coefficient would correspond to a complicated average over the relevant composition range.

We, however, have developed an alternative scheme for the measurement of liquid phase diffusivities as a function of composition using the chromatographic technique.[2] Although Taylor's original analysis related to the dispersion of a δ function pulse of pure solute injected into a pure flowing solvent, the basic differential equation can easily be generalized to the case where the flowing fluid consists of a mixture of two species A and B, and where the injection is composed of a mixture with a slightly different composition. Then, the temporal variation of the mole fraction of species A at a distance L downstream from the point of injection, averaged over a cross section, is given by

$$\bar{x}_A = x_A + \frac{N}{2nV}\left[\frac{\pi D_{eff}t}{L^2}\right]^{-1/2} \exp\left[\frac{-(1 - \bar{u}t/L)^2}{4D_{eff}(t/L^2)}\right] \qquad (2)$$

where x_A is the initial mole fraction of A in the flowing mixture, n is the number density of molecules in the mixture, V the volume of the diffusion tube, N the excess number of molecules of A injected, and

$$D_{eff} = D_{AB}{}^{x_A} + \frac{R_0{}^2 \bar{u}^2}{48 D_{AB}{}^{x_A}} \qquad (3)$$

Here, $D_{AB}{}^{x_A}$ represents the mutual diffusion coefficient of species A and B at the composition of the flowing mixture, provided that the perturbation to the mole fraction of this mixture is small, which it is in all cases of practical interest.[2]

Thus, observation of the change in mole fraction of species A, from its value in the original mixture, allows de-
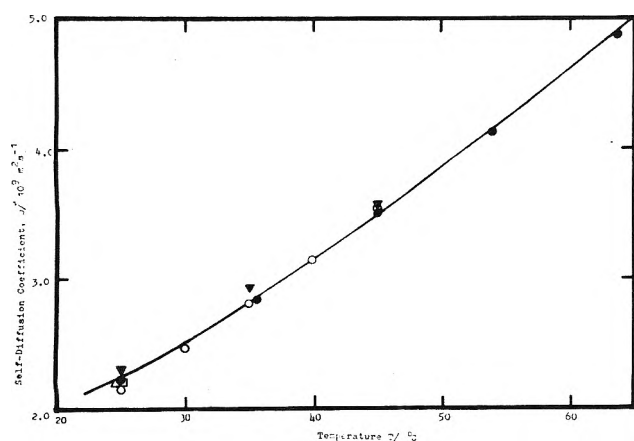
Figure 1. Self-diffusion coefficient for water: (●) present work; (▼) Mills;[7] (△) Gillen et al.;[8] (O) Simpson and Carr;[9] (□) O'Reilly and Peterson.[10]

termination of $D_{AB}{}^{x_A}$ at any desired composition. We have reported results obtained with this technique,[2] and have found good agreement with mutual diffusivities at varying mixture compositions obtained by other means. We may therefore conclude that our method allows determination of the mutual diffusion coefficient at a discrete mixture composition.

A further illustration of the wider application of the chromatographic broadening technique to the measurement of liquid phase diffusivities is provided by Figure 1,[11] where we have plotted data recently obtained for the self-diffusion coefficient of water by means of this method. These results were obtained by making injections of pure D_2O into a flowing stream of pure H_2O and, as Mills[7] has pointed out the tracer for the self-diffusion process is therefore HDO. The eluted peak was detected with a differential refractometer as in our earlier work which also contains the pertinent details of our experimental installation.[2] The raw diffusion coefficients obtained have been corrected to self-diffusion coefficients for H_2O according to the scheme suggested by Mills.[7] Figure 1 also contains reliable data for the same system[7-10] selected from the large body of results available in the literature. One set of results[7] was obtained with the diaphragm cell method, whereas the other sets[8-10] were obtained by NMR techniques. The satisfactory agreement obtained (within the mutual experimental uncertainty) establishes further confidence in the chromatographic method of measuring liquid phase diffusivities.

In principle, it should be possible to measure the two self-diffusion coefficients of a binary mixture by a similar technique. However the practical difficulties of preparing a flowing mixture and an injection mixture identical apart from the labeling of one constituent have thus far proved insuperable.

References and Notes

(1) E. Grushka and E. J. Kikta, Jr., *J. Phys. Chem.*, **78**, 2297 (1974).
(2) K. C. Pratt and W. A. Wakeham, *Proc. R. Soc., London, Ser. A*, **336**, 393 (1974).
(3) O. Levenspiel and W. K. Smith, *Chem. Eng. Sci.*, **6**, 227 (1957).
(4) K. C. Pratt and W. A. Wakeham, *Proc. R. Soc., London, Ser. A*, **342**, 401 (1975).
(5) R. J. Nunge, R. S. Lin, and W. N. Gill, *J. Fluid Mech.*, **51**, 363 (1972).
(6) G. I. Taylor, *Proc. R. Soc., London, Ser. A*, **219**, 186 (1953).
(7) R. Mills, *J. Phys. Chem.*, **77**, 685 (1973).
(8) K. T. Gillen, D. C. Douglass, and M. J. R. Hoch, *J. Chem. Phys.*, **57**, 5117 (1972).

(9) J. H. Simpson and H. Y. Carr, *Phys. Rev.*, **111**, 1201 (1958).
(10) D. E. O'Reilly and E. M. Peterson, *J. Chem. Phys.*, **55**, 2155 (1971).
(11) A tabular listing of the data contained in Figure 1 may be obtained by application to the authors.

Department of Chemical Engineering   **K. C. Pratt**
  and Chemical Technology   **W. A. Wakeham***
Imperial College
London SW7, England

On The Chromatographic Broadening Technique of Liquid Diffusivity Measurements

Sir: We are obviously in agreement with Pratt and Wakeham as to the potential of the chromatographic method in diffusion studies. We thus wish to make several comments concerning the communication by the above authors.[1] We do not feel that our paper[2] is misleading since, with one exception, all the points raised were actually discussed in our work.

Pratt and Wakeham[1] commented with regard to the limit

$$\frac{R_0{}^2 \bar{U}}{D_{AB} L} \ll 1 \tag{1}$$

where R_0 is the tube's radius, $\bar{U}$ is the solvent velocity, L is the column length, and D_{AB} is the diffusion coefficient, although they agree that in theory it is correct. Examination of their paper on the subject[3] (which incidentally we came across when our paper was in press) shows that they also used a time limit to obtain the diffusion coefficient:

$$t \geq \frac{50 R_0{}^2}{(3.8)^2 D_{AB}} \qquad \left(\text{note } t = \frac{L}{\bar{U}} \right) \tag{2}$$

In other words, the flow rate of the solvent in their system was so adjusted as to meet the condition set by eq 2, which, within a constant, is similar to eq 1. In reality, we did the same. Both their paper[3] and ours[2] show that the apparent diffusion coefficients become constants at a flow rate below a certain limit. Our data[2] were obtained at flow rates about that limit, which *emperically* is given by eq 2. We did not try to give the impression that one should wait infinitely long for diffusion measurements. The limit given in eq 1 is that required *theoretically* to approximate closely to eluted peak by the gaussian shape. Our measurements were done at a solvent velocity of about 0.5–0.6 cm/sec which corresponds closely to the upper limit of the 0.46 cm/sec used in Pratt and Wakeham's work.[3]

We feel that the important point is to ensure adequate sampling of all the streamlines in the solvent flow profile by the solute molecules. Otherwise, the observed diffusion coefficients, as obtained by the present method, will not have the correct magnitude and more complicated equations are needed in order to determine D. This point should be realized by all who use the method.

The authors did not indicate[1] how many moments they proposed to use, although for diffusion studies only the first and the second central moments are needed. We did use these quantities in our gaseous diffusion studies.[4,5] We did find, however, that least-squares fitting a gaussian gave more reliable results. When calculating moments, especial-

ly the higher ones, the error associated with the measurements must be recognized (see, for example, the papers by Cram and coworkers[6,7]). More important perhaps is the point that, using the present method, digitized data does not mean that diffusion measurement can be made at very fast flow rates, a point which the authors seem to imply in the present communication.[1]

Regarding the comments made on the effect of tube coiling it seems that both our groups are in agreement.

We do agree with Pratt and Wakeham that the method can be used at a wide concentration range and not only at infinite dilution. Indeed, the work of Pratt and Wakeham[3] elegantly demonstrates that possibility. In addition, the method can also be extended to three, or more, component analysis, a facet which we are investigating right now. In any event, we do not think that we considerably underrated the potential of the chromatographic method, and in a paper now being submitted[8] the utility of the technique in amassing, with ease, large quantities of data under various conditions is amply demonstrated. The application of the technique to self-diffusion[1] is an additional testimony to the versatility of the technique. In regard to self-diffusion, Pratt and Wakeham might wish to take notice of a recent paper by Hildebrand[9] where he questioned the validity of self-diffusion. [Since then, Hildebrand published several papers concerning the concept of fluidity.] In this particular case[1] the diffusion of HDO in H_2O can perhaps be regarded in terms of binary diffusion since the difference in molecular weights of the two species is significant ($\sim6\%$). Moreover, in view of Hildebrand's recent argument it would be interesting to see if the data in Figure 1 of ref 1 can be fitted to a straight line. As drawn there is a curvature in the line. Extrapolation of a straight line to zero D should be at T close to the freezing point.

References and Notes

(1) K. C. Pratt and W. A. Wakeham, J. Phys. Chem., preceding paper in this issue.
(2) E. Grushka and E. J. Kikta, Jr., J. Phys. Chem., 78, 2297 (1974).
(3) K. C. Pratt and W. A. Wakeham, Proc. R. Soc., London, Ser. A, 336, 393 (1974).
(4) E. Grushka and V. R. Maynard, J. Phys. Chem., 77, 1437 (1973).
(5) E. Grushka and P. Schnipelsky, J. Phys. Chem., 78, 1428 (1974).
(6) S. N. Chesler and S. P. Cram, Anal. Chem., 43, 1922 (1971).
(7) S. N. Chesler and S. P. Cram, Anal. Chem., 44, 2240 (1972).
(8) E. Grushka and E. J. Kikta, Jr., J. Am. Chem. Soc., in press.
(9) J. L. Hildebrand, Science, 174, 490 (1971).

Department of Chemistry   Eli Grushka*
State University of New York at Buffalo   Edward Kikta, Jr.
Buffalo, New York 14214

Inadequacy of the Ferrocene–Ferricinium Assumption for Estimating the Chemical Free Enthalpy (Gibbs Free Energy) of Transfer of Single Ions

Sir: Studies of recent literature[1-4] have disclosed that the ferrocene–ferricinium (Foc–Fic$^+$) assumption and the assumptions of the tetraphenylarsonium–tetraphenylborate

type (Ph$_4$As$^+$Ph$_4$B$^-$) lead to different values for the chemical free enthalpy of transfer of single ions from water to nonaqueous solvents ($\Delta G^\circ{}_{tr}$). Essentially, the two assumptions are similar. The Ph$_4$As$^+$Ph$_4$B$^-$ assumption derives from the work of Grunwald et al.,[5] who state that "the solvation of a large ion with very low density of surface charge closely resembles that of an uncharged molecule of equal size and structure".

The Foc–Fic$^+$ assumption is based on Strehlow et al.'s[6] "redox function". These authors postulate that if the oxidation and reduction ions of a redox couple are sufficiently large and of equal size (as in some metalorganic complexes) the contribution of short-range interactions to $\Delta G^\circ{}_{trox} - \Delta G^\circ{}_{trred}$ does not change, and the electrostatic contribution can be estimated by means of the Born equation. However, for such an estimation to be made it is essential that the charge be located in the center of the complex and be shielded by ligands.

Diggle and Parker[4] conclude that the Foc–Fic$^+$ assumption is at fault for several reasons, among which the relatively small radius of the ferricinium ion is quoted as the most important. This small radius should give rise to ion–dipole interaction and cause the solvent dipoles to orient toward the ion (solvation of the first kind). The ferrocene molecule should undergo only second kind of solvation in water. (Enhancement of the solvent structure by the presence of large hydrophobic solutes.) In ref 7 it was demonstrated already that, with water being used as the solvent, suppression of dielectric saturation calls for an ionic radius larger than 5 Å, the corresponding figure in the case of methanol being even larger than 15 Å. However, based as they are on rather old experimental evidence,[8] only semiquantitative significance should be assigned to these limit values. Still, they seem to suggest that even Ph$_4$As$^+$ and Ph$_4$B$^-$ should be subject to dielectric saturation. Admitting that the foregoing is a plausible explanation for the invalidity of the Foc–Fic$^+$ assumption, we still feel that the main cause has to be sought in the ferrocene molecule itself.

There is evidence showing that the electrons on the ferrocene molecule are unevenly distributed to the effect that the two rings carry a net electron charge of -0.35 and the Fe atom a charge of $+0.70$.[9-12] Owing to this distribution of charge, quadrupole–dipole interaction will occur between the ferrocene molecule and the solvent dipoles, which may account for the ferrocene having a higher solubility in (di)polar solvents than molecules of, e.g., noble gases and neopentane.

It also appears that the values of $\Delta G^\circ{}_{tr}$ for the transfer of ferrocene from water to methanol and other solvents differ from those to be expected in view of the radius. This is illustrated in Figure 1 of ref 2, where the $\Delta G^\circ{}_{tr}$ values for several compounds have been plotted vs. the respective radii. In the case of transfer from water to methanol, $\Delta G^\circ{}_{tr}$ for the ferrocene molecule is about 2.5 kcal/mol less negative than the expected value. This means that the solubilities of ferrocene in water and in methanol differ less than those of completely uncharged spherical particles of the same diameter. The influence of the quadrupole–dipole interaction will be more pronounced in water than in methanol, which is in agreement with the smaller radius of the water molecule.

A quantitative estimate of the influence of the quadrupole–dipole interaction can be made with the aid of the following model. The quadrupole is supposed to be linear, and the only significant contribution to the quadrupole–solvent

dipole interactions comes from solvent molecules on the top and the bottom of the yoyo-shaped ferrocene molecule. The ring charge (δ) is located in the center of the ring. Four solvent molecules are completely oriented on each ring. The solvent molecules are assumed to be spherical, with the dipoles being located in the centers. The dimensions of the ferrocene molecule have been taken from Stranks.[13] The dipole moments of H_2O and MeOH are 1.85 and 1.70 $\times$ 10^{-18} esu, and the molecular radii 1.4 and 1.95 Å, respectively.

The quadrupole–solvent dipole interaction energies in this model are U_{H_2O} = 21δ kcal/mol and U_{MeOH} = 10δ kcal/mol; U_{H_2O} − U_{MeOH} = 11δ kcal/mol $\approx$ 2.5 kcal/mol.[14] This gives $\delta \approx 0.25$, which is in fair agreement with the literature value of 0.35. It can be concluded, therefore, that the invalidity of the ferrocene–ferricinium assumption is caused mainly by the quadrupole moment of the ferrocene molecule. In ref 2 it is further shown that, as far as the value of $\Delta G°_{tr}$ for transfer from water to methanol is concerned, the ferricinium ion fits into the series of the univalent spherical cations, which means that the ferricinium ion does not interact differently with the solvent than other cations do. This accords with quantum-mechanical considerations to the effect that the ferricinium ion should not possess an appreciable quadrupole moment. Hence, there are several reasons why the ferrocene–ferricinium assumption should be rejected for estimating the chemical free enthalpy of transfer of single ions; these can be summarized as follows: the quadrupole–solvent dipole interaction on the order of several kilocalories exhibited by the ferrocene molecule does not occur in the interaction between the ferricinium ion and the solvent; the ferricinium ion is smaller than required by the condition that the electric field of the ionic charge must not cause orientation of the solvent dipoles.

It has proved possible to estimate the charge distribution on the ferrocene molecule with the aid of the solubility data for ferrocene in different solvents; these data can be easily obtained experimentally.

Reference and Notes

(1) I. M. Kolthoff and M. K. Chantooni, *J. Am. Chem. Soc.*, **93**, 7104 (1971).
(2) D. Bax, C. L. de Ligny, and M. Alfenaar, *Recl. Trav. Chim. Pays-Bas*, **91**, 452 (1972).
(3) B. G. Cox and A. J. Parker, *J. Am. Chem. Soc.*, **95**, 402 (1973).
(4) J. W. Diggle and A. J. Parker, *Electrochim. Acta*, **18**, 975 (1973).
(5) E. Grunwald, G. Baughman, and G. Kohnstam, *J. Am. Chem. Soc.*, **82**, 5801 (1960).
(6) H. M. Koepp, H. Wendt, and H. Strehlow, *Z. Elektrochem.* **64**, 483 (1960).
(7) M. Alfenaar and C. L. de Ligny, *Recl. Trav. Chim. Pays-Bas*, **86**, 929 (1967).
(8) J. Malsch, *Phys. Z.* **30**, 837 (1929).
(9) E. M. Shustorovich and M. E. Dyatkina, *Dokl. Akad. Nauk. SSR*, **128**, 1234 (1959).
(10) J. P. Dahl and C. J. Ballhausen, *Mater. Fys. Medd. Dansk. Vis. Selskab*, **33**, 5 (1961).
(11) A. T. Armstrong, D. G. Carroll, and S. P. MCGlynn, *J. Chem. Phys.*, **47**, 1104 (1967).
(12) R. D. Fischer, *Theor. Chim. Acta (Berlin)*, **1**, 418 (1963).
(13) D. R. Stranks, *Discuss. Faraday Soc.*, **29**, 73 (1960).
(14) These figures should be regarded as semiquantitative. The quadrupole–solvent interaction being of the same magnitude as $\frac{3}{2}RT$, some thermal distortion of the dipole orientation is to be expected. Further, when solvent dipole–dipole interactions are not taken into account, 0.25 must be considered as a lower limiting value for δ.

DSM Central Laboratory   **Marinus Alfenaar**
Geleen, Netherlands

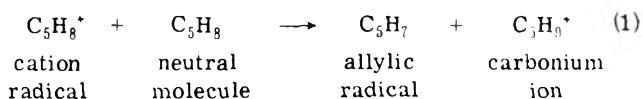## A Study of Chemical Reaction of Olefinic Radical Ions on H-Zeolon Surface

Sir: Both natural and synthetic zeolites adsorb hydrocarbon molecules. Spectroscopic methods such as ir, x-rays, and EPR can be employed to give useful information on the properties of zeolitic surface and modifications due to different activation treatments.[1] Changes in the spectra of adsorbed molecules on the zeolitic surface could yield additional knowledge about the interaction and chemical transformation of the reactive species.

Recently, we have performed extensive studies of various hydrocarbons chemisorbed on H-mordenite.[2] When the unsaturated molecules are encountered with intrinsic Lewis acid sites on zeolites, a charge-transfer mechanism takes place between the absorbate and solid. An electronic boundary layer is developed and it may result in a considerable rise in potential barrier for the ionic species to diffuse out of the zeolitic crystals.[3] With rigid channels of the solid and high heat of chemisorption of unsaturated molecules,[4] the hydrogen form of zeolites presents an excellent template to study the ion–molecule reactions in the solid surface.

In the present communication, we are reporting the first experimental results in which the chemisorbed cyclopentene cation radical ($C_5H_8^+$) presented at low temperature could transform into a neutral allylic radical (C_5H_7) at higher temperature inside the zeolitic crystals, observed by the change of ESR spectra under various conditions.

H-zeolon, obtained from the Norton Co., is calcined in oxygen at 500° to remove impurities, then activated under vacuum for 2 hr, and exposured to cyclopentene vapor at 77°K in a standard sample tube. ESR measurements were carried out on a Varian X-band 4502 spectrometer.

The ESR spectrum of adsorbed cyclopentene on H-zeolon at −185° consists of a quintet with 37.0-G separation and a triplet with 14.5-G spacing (Figure 1). With slowly increase in temperature, spectra change gradualy. In Figure 2, an ESR spectrum at 35° indicates a quintet with 25.2-G and a 14.5-G triplet. The quintet was assigned to the identical methylene groups. The splitting at 25.2 G is in reasonable agreement with those expected from cyclopentyl allylic type radicals (15.4 $\times$ 1.70 = 26.2 G), where 15.4 is the average value of the methyl splittings in allylic radical and the geometric factor 1.70 is taking the steric effect of the closed ring structure into account.[6] A 14.5-G triplet is assigned to two α hydrogens. Drastic changes in ESR spectra of cyclopentene adsorbed on H-zeolon revealed the presence of the following ion–molecule reactions on the zeolite surface:

$$C_5H_8^+ \quad + \quad C_5H_8 \quad \longrightarrow \quad C_5H_7 \quad + \quad C_5H_9^+ \qquad (1)$$

| cation radical | neutral molecule | allylic radical | carbonium ion |

The carbonium ion is expected to have the same order of electrostatic interaction energy with the zeolite as measured by the ion radicals (25–30 kcal/mol).[4] Hence, the neutral radical is in the vicinity of the carbonium due to influence of charge polarization effect, and may not have complete random motion as in liquid phase, as suggested in the observed intensity distribution.

The anomaly of the observed ESR spectrum is expected for radical species adsorbed on amorphous solid.[7] Neglecting four β protons and the α proton in the cyclopentyl allyl-
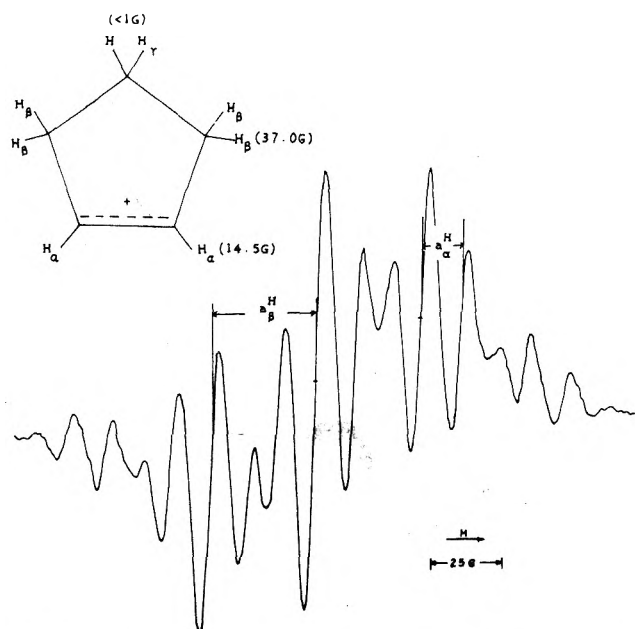
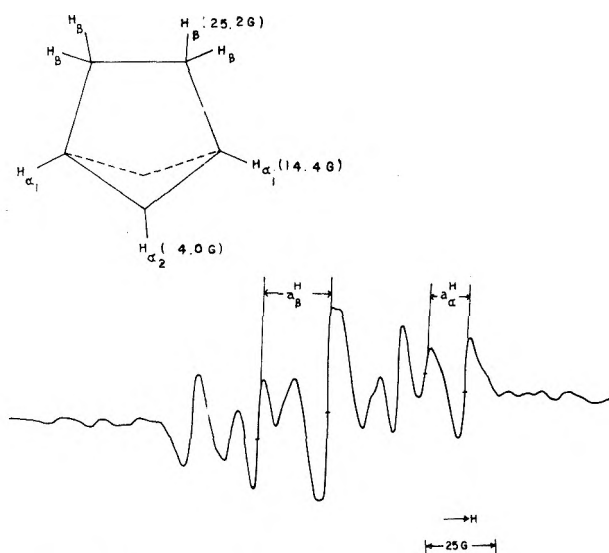**Figure 1.** ESR spectrum of cyclopentene cation radical generated on synthetic H-mordenite at −185°.

Figure 2. Esr spectrum of cyclopentyl allylic radical adsorbed on synthetic H-mordenite at 35°.

ic radicals due to small anisotropic contributions,[8] and we assume the known cyclopentene structure[9] with 36° separation for two α protons, a computer simulation program
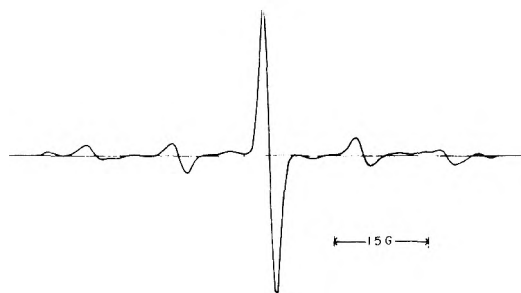

Figure 3. Computer simulated ESR spectrum at X-band for two α protons of cyclopentyl allylic radical rotating on zeolitic surface.

was used to study the outer wing of the observed ESR spectrum (Figure 3). With the right magnitude of proton hyperfine splittings and computer studies of line shape, we firmly established the existence of $\dot{C}_5H_7$ and their restricted motions on the H-zeolon surface.

Similar reactions were suggested in early work of radiolysis of alkenes at low temperatures. Smith et al.[10] observed the formation of neutral radicals in γ-irradiated vinylene and vinylidene alkenes. Shida and Hamill[11] also showed reaction 1 to be slightly endothermic ($\Delta H = 3$ kcal/mol) for vinylenes on the basis of thermochemistry. It is in excellent agreement with our observation that high temperature and trace amount of alkenes are required to promote reaction 1.

If alkenes are present inside the zeolites, this proton-transfer mechanism could play an important role in the synergistic effect on paraffin cracking reactions due to the presence of an olefinic initiator.[12]

Department of Chemical Engineering **Shawn Shih**
University of Southern California
Los Angeles, California 90007

References and Notes

(1) J. W. Ward, *J. Catal.*, **9**, 225, 396 (1967); *ibid.*, **11**, 238, 251, 259 (1968); A. E. Hirschler et al., *ibid.*, **4**, 628 (1965); D. H. Olson and E. Dempsey, *ibid.*, **13**, 221 (1969).
(2) P. L. Corio and S. Shih, *J. Catal.*, **18**, 126 (1970); *J. Phys. Chem.*, **75**, 3475 (1971); S. Shih, *J. Catal.*, accepted for publication.
(3) P. B. Weisz, *J. Chem. Phys.*, **21**, 1531 (1953).
(4) S. Shih, *J. Catal.*, accepted for publication.
(5) P. J. Krusic and J. K. Kochi, *J. Am. Chem. Soc.*, **90**, 7157 (1968).
(6) R. Dessau and S. Shih, *J. Chem. Phys.*, **57**, 1200 (1972).
(7) R. Lefebvre and J. Maruani, *J. Chem. Phys.*, **42**, 1480 (1965).
(8) W. Derbyshire, *Mol. Phys.*, **5**, 225 (1962).
(9) J. Lane and R. C. Lord, *J. Chem. Phys.*, **47**, 4941 (1967).
(10) D. R. Smith and J. J. Pieroni, *J. Phys. Chem.*, **70**, 2379 (1966).
(11) T. Shida and W. H. Hamill, *J. Am. Chem. Soc.*, **88**, 5376 (1966).
(12) P. B. Weisz, *Chem. Tech.*, **4**, 498 (1973); W. F. Pansing, *J. Phys. Chem.*, **69**, 392 (1965); J. N. Miale, N. Y. Chen, and P. B. Weisz, *J. Catal.*, **6**, 278 (1966).
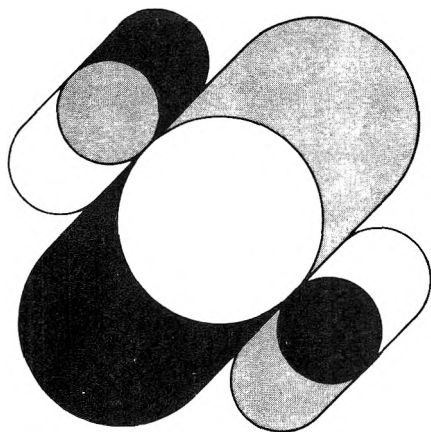
Nonequilibrium Systems In Natural Water Chemistry

ADVANCES IN CHEMISTRY SERIES No. 106

Thirteen papers from a symposium by the Division of Water, Air, and Waste Chemistry of the American Chemical Society, chaired by J. D. Hem.

Which is more important: efficient exploitation of our natural resources or a stable ecosystem? What is the relationship between a wide variety of life forms and a healthy environment? What do geology and groundwater flow patterns have to do with the chemical composition of water? How may one predict when a lake will reach equilibrium or tell how long it has supported life?

This volume features:

- principles of water pollution control
- methods of analysis for dissolved chemicals
- mathematical models
- discussion of stratified lakes
- chemical processes in a carbonate aquifer
- decomposition and racemization of amino acids

342 pages with index   Cloth   (1971) $11.00
Postpaid in U.S. and Canada; plus 40 cents elsewhere.
Set of L.C. cards with library orders upon request.

Other books in the ADVANCES IN CHEMISTRY SERIES on water chemistry include:

No. 105 Anaerobic Biological Treatment Processes
Nine papers survey the state of the art of this natural process for waste treatment, with three papers on methane fermentation, others on process control and design. Considers volatile acid formation, toxicity, synergism, antagonism, pH control, heavy metals, light metal cations.
196 pages with index   Cloth   (1971) $9.00

No. 79 Adsorption from Aqueous Solution
Fifteen papers discuss thermodynamic and kinetic aspects of adsorption phenomena and the results of studies on a variety of adsorbate-adsorbent systems.
212 pages with index   Cloth   (1968) $10.00

No. 73 Trace Inorganics in Water
Research reports; analytical developments including atomic absorption, flame emission, and neutron activation; and broad reviews, such as effects of trace inorganics on the ice-water system and the role of hydrous manganese and iron oxides on fixing metals in soils and sediments.
396 pages with index   Cloth   (1968) $12.50

No. 67 Equilibrium Concepts in Natural Water Systems
Sixteen papers represent the collaboration of aquatic chemists, analytical chemists, geologists, oceanographers, limnologists, and sanitary engineers, working with simplified models to produce fruitful generalizations and valuable insights into the factors that control the chemistry of natural systems.
344 pages with index   Cloth   (1967) $11.00

No. 38 Saline Water Conversion—II
Fourteen papers from two symposia; includes recovery of minerals from sea water, minimizing scale formation, wiped thinfilm distillation, diffusion still, solar flash evaporation, osmosis, electrodialysis (3 paper), research in Israel, hydrate process.
199 pages   Paper   (1963) $8.00

No. 27 Saline Water Conversion
Thermodynamics of desalting, solvent extraction, freezing, centrifugal phase barrier recompression distillation, multistage flash evaporation, ion exchange, osmosis, and electrochemical demineralization.
246 pages   Paper   (1960) $9.00

Order from: **Special Issues Sales, American Chemical Society
1155 Sixteenth St., N.W., Washington, D.C. 20036**